SYNTHESIS AND CHARACTERISATION OF CONJUGATED 4,8-BENZOBISTHIAZOLE DERIVATIVES FOR ORGANIC ELECTRONICS

Submitted by

Gary Conboy

A thesis submitted in fulfilment of the requirements for the degree of Doctor of Philosophy in

Department of Pure and Applied Chemistry, University of Strathclyde

2015

This thesis is the result of the author's original research. It has been composed by the author and has not been previously submitted for examination, which has led to the award of a degree.

Signed:

Date: 05-06-2015

Acknowledgement

I would like to thank EPSRC (EP/H004157/1) for funding my research and specifically, Prof. Peter Skabara for allowing me the opportunity to undertake the research under his continued supervision and support. I would like to thank collaborators at the University of St Andrews for photophysical studies and OPV measurements. I would also like to thank collaborators from Georgia Institute of Technology and specifically, Enrico Angioni for performing molecular modelling studies. I am very grateful to the groups of Prof. Iain McCulloch (ICL/KAUST) and Prof. Neil McKeown (Edinburgh) for generously performing GPC measurements for my work. I would like to say a big thank you to Dr. Alexander Kanibolotsky and Dr. Anto Regis Inigo for supporting me throughout my Ph.D. and never being too hard to reach when I needed a question answered. Similarly, many thanks to the entire Skabara group, past and present for making the lab such an enjoyable, supportive atmosphere in which to work.

Sincere thanks to all of the technical staff within the department, for their excellent support throughout my Ph.D. Thanks to Craig Irving for the NMR service, Pat Keating for Mass Spectrometry, Denise Gilmour and Alexander Clunie for elemental analysis, Lindsay McCulloch for TGA measurements, Gavin Bain for maintaining the SPS, Neil Hodgson for glass blowing services, John Dunseith for IT support and the staff from stores for ensuring a constant supply of consumables.

I would like to dedicate special thanks to Dr. Neil Findlay for his continuing help and support. From the very beginning he has been a friend and mentor, always approachable when needed. Also, for all of the corrections to countless documents over the years and the timely manner in which they were returned.

I would like to thank my Mum, Dad, Thomas and Sarah for supporting me throughout my study and providing a small escape from science when needed.

Finally, I would like to thank Kirsty, without whom I could not have done any of this. Thank you for the constant care and support needed to keep me on track and the sacrifices you have made because of it. I would not have made it without you being with me every step of the way.

Abstract

In recent years the field of organic semiconducting materials has seen rapid growth and development, with keen interest from both industrial and academic research. In the early stages of development, much of the performance improvements were due to increasingly complex device fabrication and processing methods. Research focused greatly on improving known semiconducting materials such as PPV, PT or PAC. Whilst these materials formed a strong foundation for early research, recent findings suggest that they do not possess the optimum chemical properties in order to achieve ultra-high efficiency devices. As such many research groups are now focusing efforts to develop sophisticated building blocks for incorporation into conjugated macromolecules and polymers. In order for these building blocks to find use as electronic materials, it is important to understand the intrinsic properties of each component and use these to derive effective structure-property relationships for use as tools in creating materials which are tailored to a particular role.

Chapter 1 includes a summarized description of band theory and the underlying physics of organic semiconducting materials, followed by a discussion of the recent technologies within the field, in particular donor-acceptor type macromolecules and polymers and their related device structures.

Chapters 2, 3 and 4 then present novel 4,8-benzobisthiazole (BBT) containing analogues and their incorporation into functional electronic devices. Chapter 2 discusses the synthesis and functionalization of the unit BBT, and development of an orthogonal conjugation pathway. The effect of non-covalent heteroatom interactions - utilized to induce molecular planarity - are then discussed. Building on from Chapter 2, Chapter 3 discusses the synthesis, characterization and device applications of highly-planarised, 4,8-BBT containing polymeric materials. Furthermore, Chapter 4 discusses the synthesis, characterization and device applications of 4,8-BBT containing, donor-acceptor polymers synthesised analogously to that of literature 2,6-BBT polymers. Comparison of physical and electrochemical properties, as well as device performance has been conducted and utilised to confirm the beneficial characteristics of the 4,8-orientation *vs*. the traditional 2,6-substitution.

Abbreviations

°C	degrees celcius
2D	Two dimensional
3D	three dimensional
A	ampere
Å	angstrom
AFM	atomic force microscopy
a.u.	arbitrary units
BBT	benzobisthiazole
BDT	benzodithiophene
BHJ	bulk heterojunction
b.p.	boiling point
BT	benzothiadiazole
BTz	bisthiazole
Bu	butyl
C	capacitance
c	concentration
calc.	calculated
CB	chlorobenzene
conc.	concentrated
cm	centimetre
CT	charge transfer
CV	cyclic voltammetry
d	doublet
dd	doublet of doublets
o-DCB	1,2-dichlorobenzene
DCM	dichloromethane
DFT	density functional theory
DIO	1,8-diiodooctane
DMF	*N*,*N*-dimethylformamide
DMSO	dimethyl sulfoxide
DPP	diketopyrrolopyrrole
DTP	dithienopyrrole
DSC	differential scanning calorimetry
e	charge of an electron

e^-	electron
$E_{1/2}$	half-wave potential
e.g.	*exempli gratia*
E_d	energy of a dopant material
E_g	HOMO-LUMO energy gap
E_{ox}	oxidation potential
Et	ethyl
E_{red}	reduction potential
eV	electron volts
EQE	external quantum efficiency
F	furan
Fc	ferrocene
Fc^+	ferrocenium
FF	fill factor
g	gram
GPC	gel-permeation chromatography
h	hour
h	Planck's constant
HMDS	hexamethyldisilazane
HOMO	highest occupied molecular orbital
Hz	hertz
I	current
I_{DS}	drain-source current
iR	internal resistance
I_{SC}	short-circuit current
ITO	indium tin oxide
J	Joule
J	coupling constant
K	Kelvin
kJ	kilojoule
l	litre
L	channel length
LDA	lithium diisopropylamide
LUMO	lowest unoccupied molecular orbital
M	molarity
m	metre

MALDI-TOF	matrix-assisted laser desorption/ionization – time of flight
Me	methyl
MEH-PPV	poly[2-methoxy-5-(2-ethylhexyloxy)-1,4-phenylenevinylene]
mg	milligram
MHz	megahertz
min	minute
mL	millilitre
mM	millimolar
mmol	millimole
M_n	number-average molecular mass
mol	mole
mV	millivolt
M_w	weight-average molecular mass
NBS	*N*-bromosuccinimide
n-Bu	*n*-butyl
NIR	near infra-red
nm	nanometre
NMR	nuclear magnetic resonance
ODTS	octadecyltrichlorosilane
OFET	organic field-effect transistor
OLED	organic light-emitting diode
OTFT	organic thin film transistor
OPV	organic photovoltaic
p-	*para*-
P3HT	poly(3-hexylthiophene)
PAC	polyacetylene
C_{60}PCBM	[6,6]-phenyl-C_{61}-butyric acid methyl ester
C_{70}PCBM	[6,6]-phenyl-C_{71}-butyric acid methyl ester
PCE	power conversion efficiency
PDI	polydispersity index
PEDOT	poly(3,4-ethylenedioxythiophene)
PFO	poly(9,9-di-n-octylfluorenyl-2,7-diyl)
Ph	phenyl
P_{in}	incident light intensity
P_{out}	maximum output power
ppm	parts per million

PPSE	polyphosphoric acid trimethylsilyl ester
PPV	poly(*p*-phenylene vinylene)
PSS	polystyrene-sulfonate
PT	poly(thiophene)
q	quartet
rt	room temperature
s	second / singlet
SEC	spectroelectrochemistry
t	triplet
T	temperature
TBAF	tetra-*n*-butylammonium fluoride
$TBAPF_6$	tetra-*n*-butylammonium hexafluorophosphate
TGA	thermogravimetric analysis
Th	thiophene
THF	tetrahydrofuran
TIPS	triisopropylsilyl
TLC	thin-layer chromatography
TMS	trimethylsilyl
TOF	time of flight
UV	ultra-violet
V	Volt
V_G	gate voltage
Vis	visible
V_{mpp}	voltage at maximum power point
V_{OC}	open circuit voltage
Vs.	*versus*
V_{SD}	source-drain voltage
V_T	threshold voltage
W	Watt / channel width
X	halide substituent

Greek

α	1st position on heterocycle
β	2nd position on heterocycle
μ	charge-carrier mobility
μW	microwaves

δ	chemical shift
ε	dielectric constant
Φ	flux
π	pi bonding orbital
π^*	pi anti-bonding orbital
σ	sigma bonding orbital
σ^*	sigma anti-bonding orbital
θ	torsion angle
λ	wavelength
λ_{max}	absorption maximum
η	power conversion efficiency
ν	frequency

Table of Contents

1 Introduction

1.1 Band Theory

The ability of a solid material to conduct electricity is determined by its electronic structure using *band theory*. In single atoms, the electrons are split into atomic orbitals with relation to their energies. In molecules, the linear combination of N number of atomic orbitals leads to the formation of $\frac{N}{2}$ bonding and $\frac{N}{2}$ antibonding molecular orbitals (MOs). Electrons fill these orbitals in order of ascending energy, starting with the lowest energy bonding orbitals. The MO with the highest energy which is occupied in the ground state is known as the Highest Occupied Molecular Orbital (HOMO) and the lowest energy MO which is unoccupied in the ground state is known as the Lowest Unoccupied Molecular Orbital (LUMO).[1] In the solid state there are significantly more MOs that can interact with each other. With increasing overlap of these MOs, bands are eventually formed resulting in a smaller difference in energy between the occupied (valence) and unoccupied (conduction) bands (Figure 1).

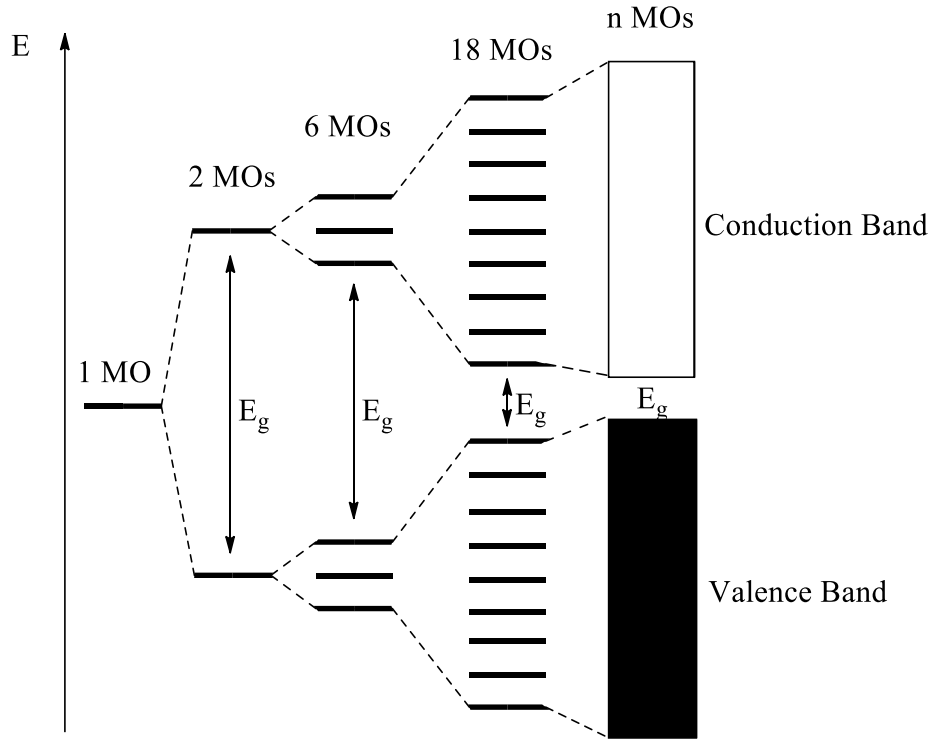

Figure 1 - Formation of bands from MOs

This energy difference is known as the band gap (E_g). The smaller the value of E_g, the easier it is to promote an electron from the valence to the conduction band and hence the greater the ability of the material to conduct electricity. In the case of polymeric species this energy gap is known

as the band gap due to the number of similar energy levels. However, monodisperse macromolecules can also possess small energy gaps and due to their well-defined structure, it is more accurate to refer to E_g, as the HOMO-LUMO gap.[2] Whilst many researchers report and compare E_g obtained *via* electrochemical and optical processes, despite these obtained values being incomparable. This is due to the different mechanisms required to generate a photo-excited state or an electrically excited state.[2]

If an electron resides in the conductance band it is considered as having the required energy to move from atom to atom in close proximity. Electrons within the valence band lack sufficient energy to do so, and are required to be excited to the conductance band before they can move. In insulating materials, the band gap tends to be very large; electrons require a great deal of energy to be excited to the conduction band. If the material contains enough MOs, the energy gap is small enough for excitation of an electron into the conduction band, leaving an unpaired electron and an electron "hole" in the valence band. The electron hole in the valence band can be filled by another electron, which in turn leaves another hole, and the material behaves as a conductor.[3]

A material is defined as being an insulator if E_g is too high to allow sufficient promotion of electrons to the conduction band, whilst metals are traditional conductors as they have no E_g in the solid state and hence electrons are readily promoted to the conduction band (Figure 2). Semiconducting materials can have band gaps which are too large for electrons to readily move to the conduction band and hence, without stimuli, they act as insulators. The E_g is however much smaller than traditional insulators (*ca* < 3 eV) and hence an electron can be excited by external stimuli such as absorption of a photon, electrical stimulation and, for very low E_g, by thermal excitation, resulting in the material behaving as a conductor.[3, 4]

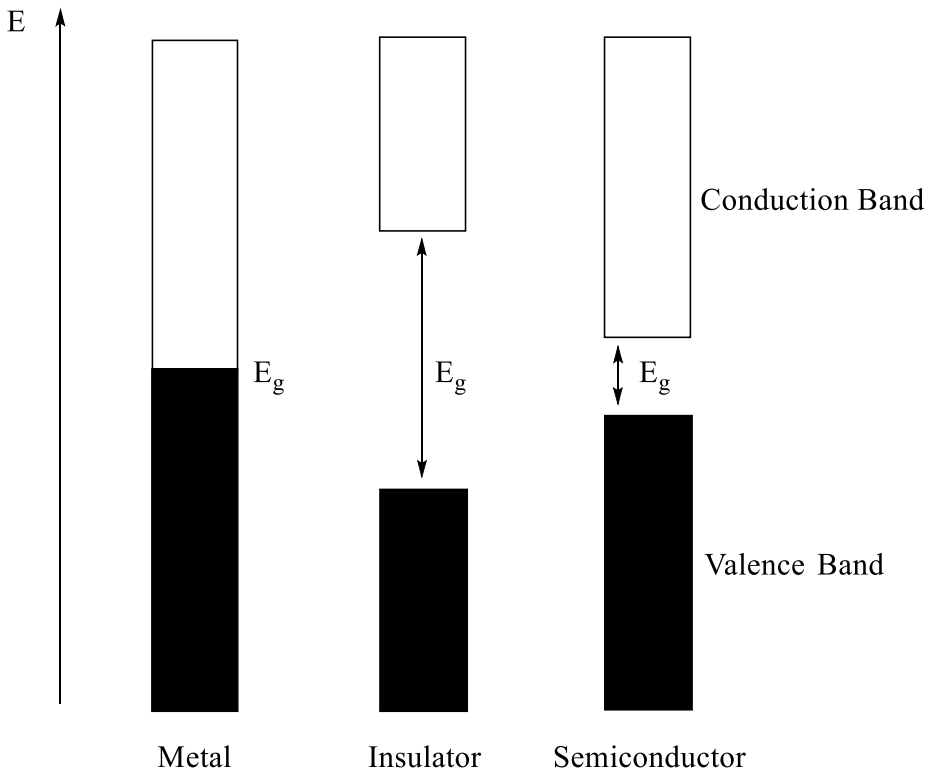

Figure 2 – Representation of bands in solids.

The MOs which are often used to describe the semiconductor properties are the HOMO and LUMO. Whilst these are useful for simplification of otherwise complicated processes, it is more accurate to describe additional MOs of similar energies. These are often represented using a Jablonski energy diagram.[5] The example below illustrates four possible absorption transitions. $\mathbf{S_n}$ describes singlet energy levels; $\mathbf{S_0}$ represents the ground state and $\mathbf{S_1}$, $\mathbf{S_2}$ and $\mathbf{S_3}$ represent the first, second and third singlet excited states respectively.

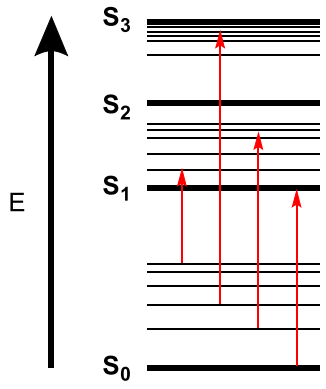

Figure 3 - Jablonski diagram illustrating excitation, via absorption of a photon[5]

At room temperature, the majority of electrons will be present in the $\mathbf{S_0}$ state and as a result, most optical transitions will occur from this energy level. The energy state to which an electron

is excited, is determined by the energy of the photon *e.g.* absorption of a low energy, long wavelength photon, will result in a low energy transition, whilst absorption of a high energy, short wavelength photon, can result in a transition of much higher energy.[5] Excitation can also occur from a singlet state to a triplet state, but due to this transition being spin forbidden (Pauli exclusion principle), these transitions are far less probable than singlet-singlet.[1]

The probability of a transition occurring (and subsequently, the intensity of the absorption) is explained using the Franck-Condon principle. This principle suggests that an electronic transition is most likely to occur without changes in the nuclei or its surrounding environment. The result of this is that any transition can be described as a vertical transition and therefore, the intensity of any absorption transition is proportional to the overlap of both transitional wavefunctions.[6]

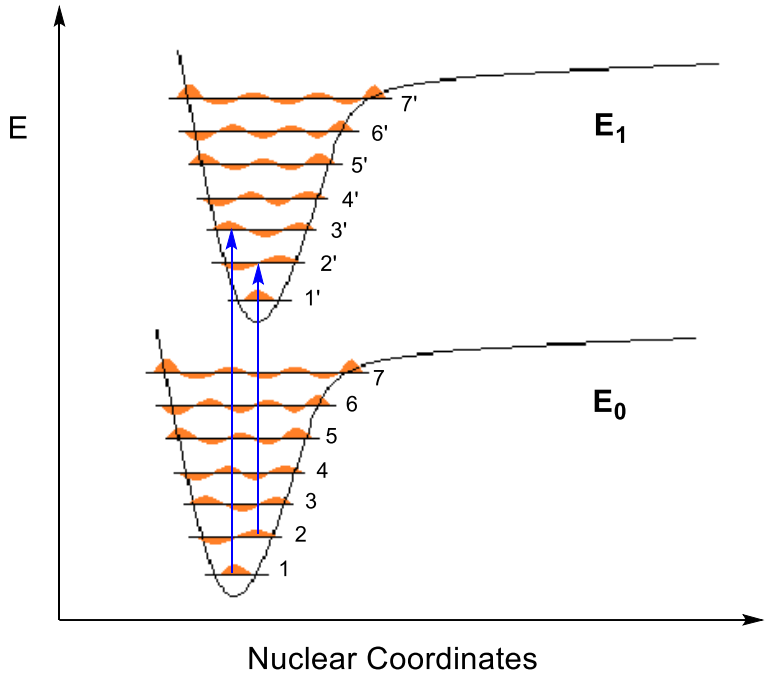

Figure 4 - Franck-Condon diagram. Wavefunctions are highlighted in orange and transitions depicted as blue arrows.

Figure 4 highlights two possible absorption transitions: 1-3' and 2-2'. The 1-3' occurs with excellent overlap of wavefunction, whilst 2-2' occurs with no overlap of wavefunction. From this, the absorption spectrum will display an intense peak for 1-3' but a weak signal for 2-2'.[7, 8]

1.2 Organic semiconductors

Conjugated organic small molecules and polymers have been shown to display semiconducting properties in the solid state.[4] These materials consist of alternating single and double/triple bonds along the backbone. This leads to effective overlap of the π orbitals and hence electrons within these orbitals can be considered as delocalized. The first organic semiconductor (OSC) to be discovered was polyacetylene, which can be considered the simplest form of a conjugated organic material. Since its discovery, most OSCs incorporate carbocyclic and/or heterocylic ring systems such as benzene, thiophene etc. Examples of some of the most common materials are shown in Figure 5.

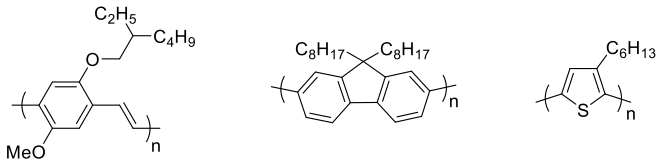

(1.1) **(1.2)** **(1.3)**

Figure 5 - Poly[2-methoxy-5-(2-ethylhexyloxy)-1,4-phenylenevinylene] ***(1.1),*** *poly(9,9-di-n-octylfluorenyl-2,7-diyl)* ***(1.2)*** *and poly(3-hexylthiophene-2,5-diyl)* ***(1.3)****.*

The control of E_g within these conjugated materials is critical for the material to find use in a specific application. For example, a material with a band gap of 3 eV would find little use as a donor in an organic photovoltaic (OPV) but may have applications in visible lighting. Likewise a material possessing a band gap of 1.3 eV would find little use in visible lighting applications but could potentially be a successful component in an OPV. Aside from just the band gap, the absolute energy for the HOMO and LUMO - relative to vacuum - are fundamental for many applications and can determine factors such as stability and type of charge transport.[9]

The band gap of conjugated materials can be engineered by considering five factors (Figure 6 and Equation 1).[10]

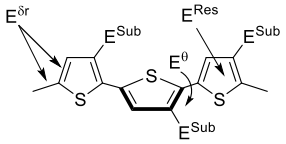

Figure 6 - Factors affecting band gap.

$$E_g = E^{\delta r} + E^{\theta} + E^{Res} + E^{Sub} + E^{Int}$$

Equation 1 - Factors affecting band gap.

$E^{\delta r}$ - Bond length alternation (BLA). BLA can be defined as the difference between the average length of a single and double bond. For example, in polyacetylene, if the C-C double bonds were perfectly delocalized, there would be no BLA and the material would possess metallic conductivity behaviour yielding an E_g of 0 eV. However, polyacetylene does not exist as a perfectly delocalised system, instead favouring the existence of alternating single and double bonds.[11] In aromatic systems it is possible to reduce the BLA by increasing the quinoidal behaviour of the material (*vide infra*).[12] However, quinoidal structures are energetically unfavourable in many cases, due to loss of aromatic stabilization energy.

E^{θ} – Dihedral angle between units. As conjugation requires overlap of the π orbitals, a dihedral angle of 0° would result in increased effective conjugation. Likewise, a larger dihedral angle between units will inhibit conjugation and widen the Eg. A common method for reducing dihedral angles between units is to synthesise fused ring systems, such as fluorene **(1.5)** compared to biphenyl **(1.4)** (Figure 7).[13] Favourable atomic interactions can also be used to planarise polymeric materials such as the non-covalent heteroatom close contacts seen in PEDOT **(1.6)** (Figure 8), which lead to high planarity, whilst PEDTT **(1.7)** exhibits an average dihedral angle of 45° in the solid state.[14]

(1.4) (1.5)

*Figure 7 – Dihedral angles of biphenyl **(1.4)** and fluorene **(1.5)**.*

(1.6) (1.7)

*Figure 8 – Structure of PEDOT **(1.6)** and PEDTT **(1.7)**.*

E^{Res} – Effects of resonance within each monomer unit. Aromatisation within each ring impedes the long-range delocalization of electrons along the polymer backbone and thus increases E_g. By reducing the aromatic stabilization energy for the monomer units, the energy required for the material to resonate to the quinoidal structure is lowered. One such way to achieve this was reported when Wudl and co-workers synthesized poly(isothianapthene) (PITN) (Figure 9).[15]

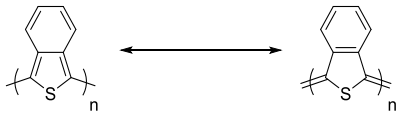

(1.8) (1.9)

*Figure 9 – Aromatic **(1.8)** and quinoidal **(1.9)** forms of PITN*

PITN is analogous to PT in that the conjugation flows through the polythiophene backbone. The key difference is that in PT the aromatic structure is favoured strongly, while in PITN the quinoidal form is in competition as the benzene ring must sacrifice some of its aromaticity, for the thiophene to be fully aromatic. Similarly, for the benzene to be aromatic, the thiophene must be in the quinoidal state and since the aromatic stabilization energy for benzene is larger than thiophene, PITN has a much larger contribution from its quinoidal character than PT resulting in an E_g of 1.1 eV for PITN compared with 2.0 eV for PT.[15]

E^{Sub} – Substitution effects. Substitution onto the conjugated backbone can have a notable effect on the electron density. For example, alkoxy groups can increase electron density within a ring system, thus raising the HOMO energy level of the material, whilst fluorination of cyclic units reduces electron density within the ring system, thus lowering the LUMO energy level.

E^{Int} – Effects of intermolecular interactions in the solid state. Molecules in the solid state can pack into tightly bound structures leading to orbital overlap between adjacent molecules. This can be in the form of π-π stacking interactions, non-covalent heteroatom interactions or dipole-dipole interactions.[16, 17] These interactions help to stabilise the material and, can have a significant impact on the E_g. The impact of these factors can clearly be seen by conducting absorption and emission spectroscopy in different phases.

Conjugated polymers, like their inorganic counterparts, require stimuli to allow electrical conductivity within the material. This is normally achieved through the use of "doping". In the case of inorganic materials, doping usually involves the addition of another semiconducting material to the solid sample. For instance silicon can be *p*- doped by the addition of a group 13 element such as boron which will allow the formation of a "hole" within the valence band and hence allow free flowing electrons within the solid. Similarly silicon can also be *n*- doped by addition of a group 15 element such as phosphorus, leading to a free electron within the conduction band and electrical conductivity (Figure 10).

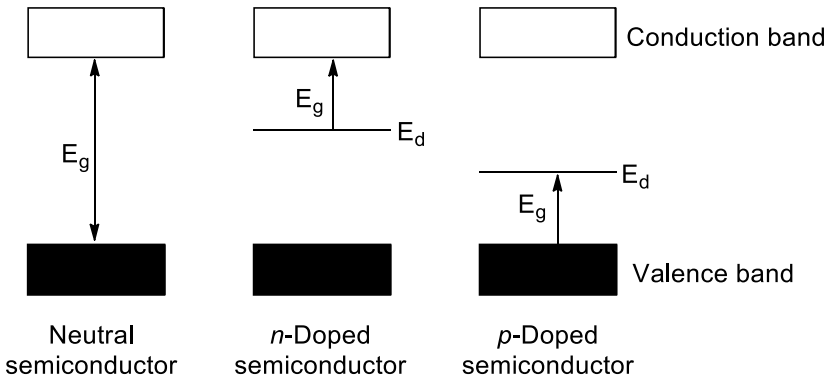

Figure 10 - Formation of new bands in doped semiconductors

Doping of organic materials can often be achieved by oxidation or reduction. This can be achieved by electrical or chemical methods and electrons can be injected or extracted from the material leading to *n*- and *p*-doping respectively. In the case of polyacetylene, removal of two electrons yields two radical cations which annihilate to form a bipolaron (Figure 11).

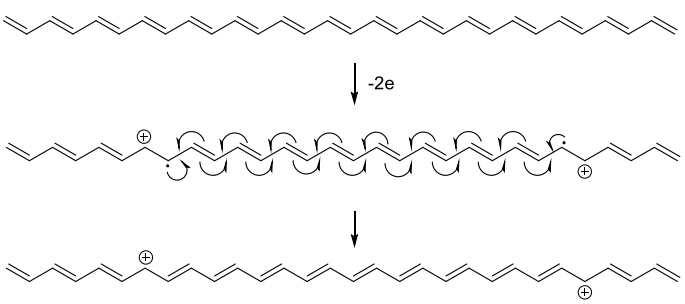

Figure 11 - p-Doping of polyacetylene

These charges are then free to dissociate along the polymer backbone which result in electrical conductivity.[11]

1.3 Synthesis of conjugated macromolecules and polymers

Conjugated organic materials have been synthesized by a variety of methods including chemical or electrochemical oxidative polymerization and transition metal catalysed cross-coupling reactions, such as Stille (organotin),[18] Suzuki (organoboron),[19] Kumada (organomagnesium),[20] Sonogashira (acetylene)[21] or Negishi (organozinc)[22] reactions. By far the most commonly utilized reactions are the Stille and Suzuki reactions due to their versatile reaction conditions and high functional group tolerance. More recently, direct arylation reactions have been shown to yield polymers of a moderate molecular weight in some cases and can eliminate synthetic steps and hazardous reagents in the Stille reaction.[23]

Selecting the correct synthetic procedure for synthesizing conjugated polymers can be of critical importance as defects, such as head-to-head coupling, can significantly alter the polymer properties. In 2010 Mauer and co-workers reported that P3HT with 98% regioregularity (rr) displays a hole mobility one order of magnitude higher than P3HT with 94% rr, indicating that effective coupling is required for a favourable morphology in the solid state. The high rr polymer exhibits a λ_{max} absorption that is red-shifted by 100 nm when compared to regiorandom (rra) P3HT.[24] This is a result of increased conjugation in the rr sample as steric hindrance from the neighbouring alkyl chains results in increased torsion angles for the rra polymer (Figure 12).[25]

The correlation between high molecular weight and high mobility has been thoroughly documented in the literature.[26] High molecular weight polymers tend to yield uniform films as a result of chain entanglement and their intrinsically high viscosity. Interchain "hopping" is considered to be the limiting factor for charge transport in organic semiconductors.[27] From this, a longer polymer chain reduces the number of required "hops", resulting in an increase in carrier mobility.[28, 29]

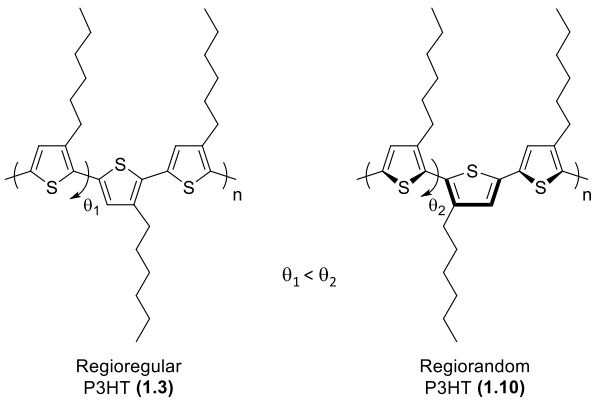

*Figure 12 – Regioregular **(1.3)** and regiorandom **(1.10)** P3HT.*

1.3.1 Stille coupling

The Stille reaction involves the cross-coupling of an organotin reagent with an organohalide (typically I, Br or OTf) in the presence of a catalytic amount of Pd(0).[30] The reaction mechanism is shown below in Figure 13. The first step of the mechanism – oxidative addition – is dependent on the ability of X to act as a leaving group. This results in the reactivity such that I > Br ≈ OTf > Cl. Organochlorides tend to react very slowly and often do not participate in the Stille reaction without modifying the reaction conditions. The next step is the transmetallation step which involves transmetallation of the organotin reagent forming the *trans*-palladium species above and elimination of $XSnR''_3$. Transmetallation is slow and generally the rate determining step. The final step involves *cis-trans* isomerization followed by reductive elimination of the new R-R' species and regeneration of the Pd(0) catalyst into the cycle.

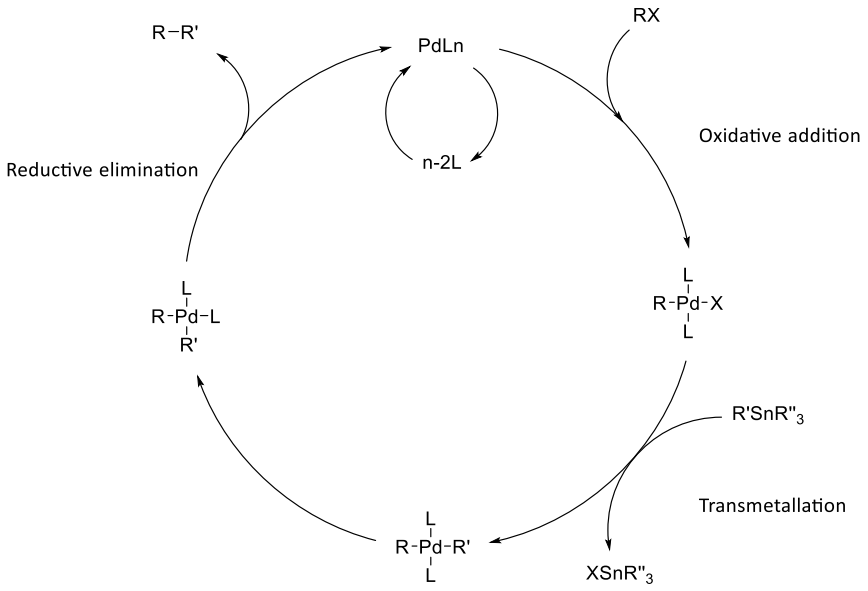

Figure 13 - Stille reaction mechanism

Despite the highly toxic nature of organotin reagents, the Stille reaction has found widespread use in many areas of organic synthesis. This is a result of it having excellent functional group tolerance, no requirement for base or water, very few homo-coupling side-reactions, the reagents are usually stable to purification (distillations, recrystallizations, workup and in some cases, chromatography) and it is applicable to a wide variety of R groups such as aryl, heteroaryl, benzyl, alkynyl and also alkenyl functionalities. The three ancillary R'' groups on the tin atom tend to be benign (methyl or butyl) groups as to minimize transfer from the tin to the palladium species. Several high performance conjugated polymers have been synthesized

using the Stille reaction as a result of the high-yielding reactions producing very high molecular weight polymeric materials.[31-33]

1.3.2 Suzuki coupling

Organoboron reagents offer many benefits over organotin reagents as they are environmentally benign, modern derivatives can be highly stable in ambient conditions and they have a very high rate of transmetallation.[34] Suzuki reactions involve the coupling of organoboron reagents with organohalides in the presence of base and catalytic Pd(0) species. The mechanism is shown below in Figure 14.

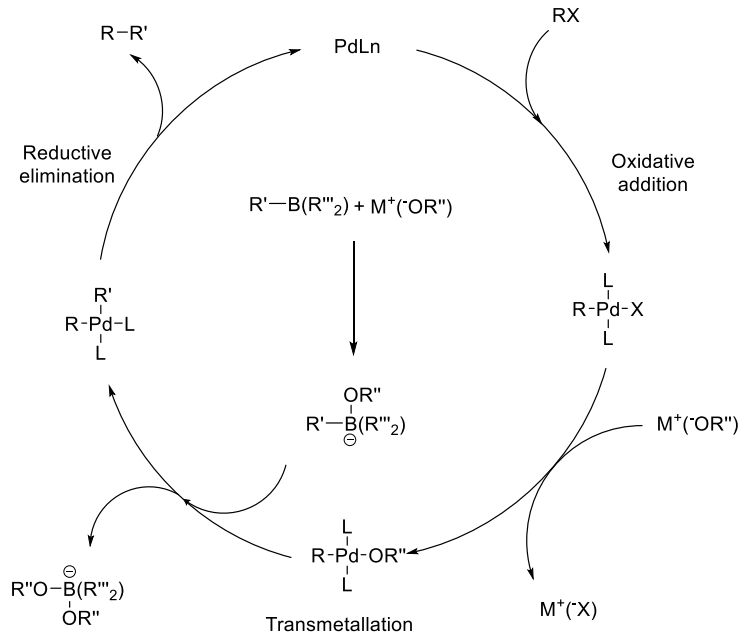

Figure 14 - Suzuki cross-coupling mechanism

Similar to the Stille reaction, the mechanism follows the same key steps: oxidative addition, transmetallation and reductive elimination. However, since a 4-coordinate boron species is required, the addition of base is critical to facilitate the reaction. Bases utilised in the Suzuki reaction are typically metal hydroxides, alkoxides, phosphates, carbonates or acetates. The ancillary R groups on the active boronate are commonly OH as the boronic acid derivatives have excellent reactivity and are easy to synthesise.

More recently, much work has been focussed on improving the stability of boronate esters due to the likelihood of boronic acids to undergo protodeboronation in the presence of moisture. Boronic acids can also convert to boroxines *via* condensation over time (Figure 15).[34]

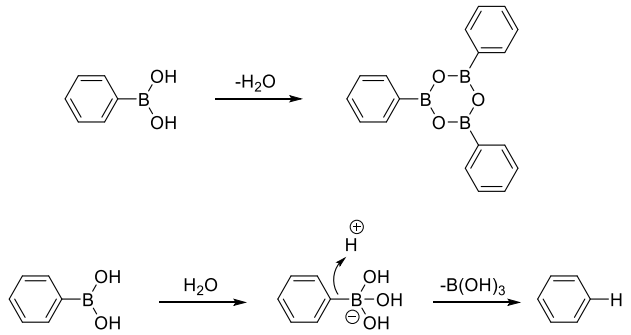

Figure 15 - Condensation (top) and protodeboronation (bottom) of boronic acids.

More stable organoboron reagents have been developed over the past decade and have resulted in significant increases in stability when compared to the standard boronic acid. Factors affecting the stability of the boron-carbon bond include, nucleophillicity of the boron centre, steric bulk and also coordination into the empty p orbital to name a few. A representation of some organoboron reagents is shown below (Figure 16). The MIDA ester is the most stable of these boronate reagents and can often be stored in air and atmospheric moisture for extended periods (>1 year) but consequently they suffer from slower reaction rates.[34] These issues explain why the Stille reaction is the most popular method for conjugated polymers.

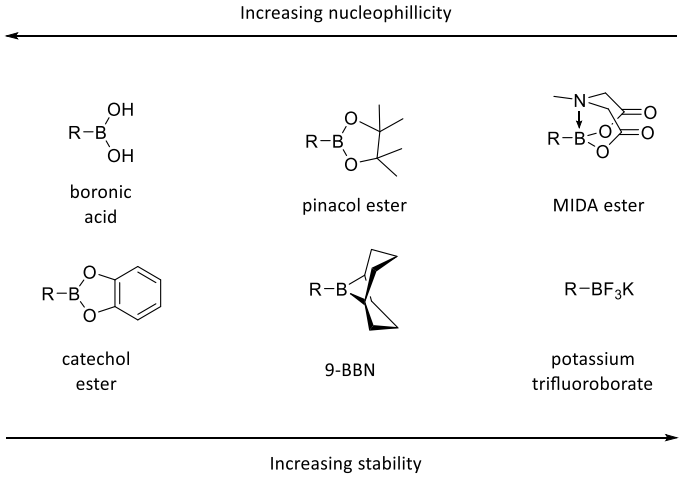

Figure 16 - Selected organoboron reagents

1.4 Direct C-H arylation reactions

In recent years direct C-H arylation reactions have gained significant interest for synthesis of aromatic macromolecules.[23] They are atom efficient due to no stoichiometric quantities of metal by-products, they require no toxic reagents and also they require less synthetic steps which can cut production costs significantly. However, there are drawbacks, as the reactions are typically less versatile than traditional cross-coupling reactions and support less functional groups. They generally work best when the Ar-H is acidic and can be easily abstracted. An example of a direct arylation reaction is shown below (Scheme 1).[35]

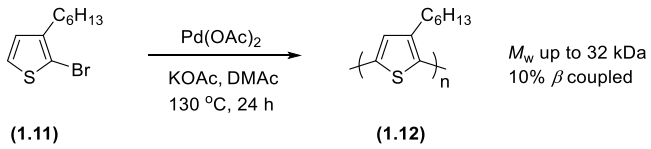

Scheme 1 - Direct arylation polymerisation of branched P3HT.

The branching arises from β hydrogen atom functionalization. Even though the α hydrogens are far more reactive, as the polymerization proceeds, the available number of α hydrogens when compared to β hydrogens available to react is infinitely smaller, hence increasing the likelihood for branching within the polymer backbone (Figure 17). By the time the degree of polymerisation has reached 180 thiophene rings (corresponding *M*w of ~30 kDa - commercial electronic grade P3HT is sold at ≥ 55 kDa[36]) along the backbone, the percentage of α hydrogen atoms is 0.0056% of the total available activation sites.

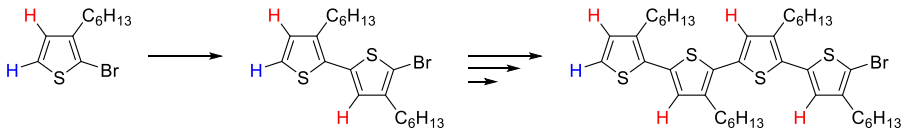

Figure 17 - Representation of available Ar-H bonds.

These defects have a profound effect on the morphology of the polymer in the solid state and hence in order for C-H arylation to find widespread use within the field of organic electronics, work needs to be done to improve reaction conditions to expand scope and further inhibit branched coupling.[23]

1.5 Non-covalent heteroatom interactions

Planarity within conjugated polymers is critical for ensuring efficient charge transport properties in devices by increasing the capacity for electrons to be free-flowing within the bulk solid.[37] In the early stages of the field, several groups attempted to synthesise ladder-type polymers as the fused nature of these materials could impart highly planar, well conjugated materials. However, there were issues with this as the materials were often highly insoluble and difficult to synthesise and purify.[38] More recently, many polymers have been synthesized with an optimal torsional angle between neighbouring ring systems close to 0° by engineering of the physical and atomic properties of the rings. This can be achieved by introducing favourable interactions between atoms that are likely to be otherwise sterically hindered. The most common example of this is PEDOT **(1.6)** where the thiophene backbone is completely planarised. In polythiophene or PEDTT **(1.7)** this is not the case with these systems having inter-ring torsional angles of 11° and 45° respectively (Figure 8).[14] Examples of some materials that have been planarised by non-covalent (S-O, S-N) interactions are shown below (Figure 18).[39-41]

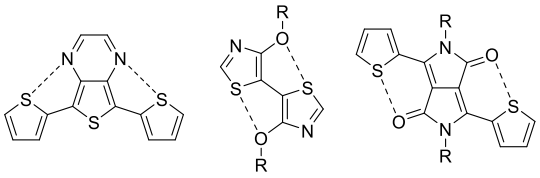

Figure 18 - Planarising non-covalent interactions

All of the above structures show very high degrees of planarity ($\theta < 2°$).[39, 41-43] These interactions can be identified when the atoms in the adjacent rings are closer than the combined sum of the Van der Waals radii. The interactions are prevalent in many modern conjugated polymers and play an important role in planarisation and hence facilitating improved interchain packing in the solid state.[44]

A recent theoretical study by Jackson and co-workers reports heteroatom non-bonding interactions as weak, attributing the planarity to weak hydrogen bonding effects (Figure 19).[45] Whilst these findings are undeniable in the molecules studied, hydrogen bonding cannot be used to explain the planarity observed in structures where no hydrogen bonding could possibly take place, such as in PEDOT **(1.6)** or **(1.15)**. It is entirely possible, that these effects are complimentary to each other (Figure 19).

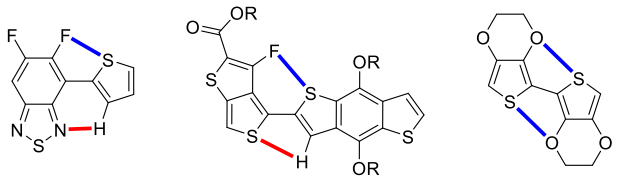

Figure 19 - Non-covalent (blue) and hydrogen bonding (red) interactions.

In some cases, where there are combined hydrogen bonding/heteroatom interactions, materials exhibit increased planarity. This is can be seen cases in such as Figure 20, where the thioalkyl derivative **(1.20)** has a significant dihedral angle of 46° compared to the relatively planar, 9° in the the alkoxy derivative **(1.19)** which includes hydrogen bonding, as well as S-O interactions.[46]

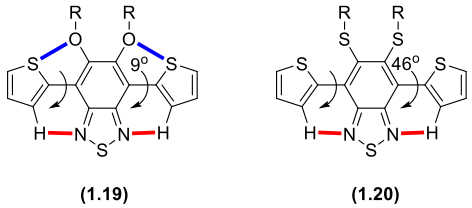

Figure 20 – Complimentary non-covalent interactions [blue] and hydrogen bonding [red] ***(1.19)****, and hydrogen bonding only* ***(1.20)****.*

1.6 Azole ring systems

Azoles are a class of aromatic five-membered heterocyclic ring systems containing at least one heteroatom and one C-N (imine) double bond (Figure 21). The C-N double bond is considered to be electron accepting and unlike in the case of pyrrole, the lone pair in the nitrogen is not located in the plane of the π system and hence is not involved in the aromaticity. Many azole-containing compounds have been shown to perform as highly efficient devices in the field of organic electronics with applications ranging from OTFT and OLED materials through to active layer components in OPVs.[47-49] They can offer several desirable properties when compared to other heteroles such as pyrrole, thiophene or furan.

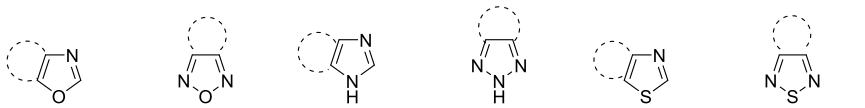

Figure 21 - Azoles commonly found in organic electronics.

Azoles typically exhibit lower lying HOMO and LUMO levels which aids air stability in devices.[50] They tend to have high thermal stability and structural rigidity derived from strong intra and interchain packing.[51] They appear to have a synergic effect when substituted such that when combined with electron rich moieties, they can behave as electron donors, but when combined with electron poor moieties they can behave as electron acceptors.[52, 53] These properties allow for azoles to be highly adaptable in terms of structure property engineering and, despite their complicated synthetic methodologies, research into these structures is growing at an unprecedented rate.[9]

Traditionally the azole ring structures are typically synthesised *via* condensation reactions promoted by strong acids or bases in the final stages of preparation. Whilst these reactions have been shown to work in a number of cases, they typically limit the available functional groups that are tolerated. They are also unsuitable for polymeric systems as incomplete condensation would result in broken conjugation, whilst purification of these systems would prove very challenging. An example synthesis of an azole compound is shown below (Scheme 2).[54]

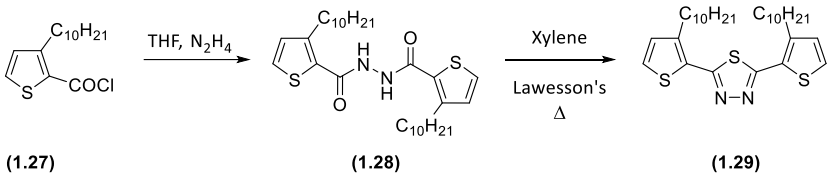

Scheme 2 - Synthesis of 1,3,4-thiadiazole.

The oxadiazole derivative of the above could also be synthesised by using catalytic polyphosphoric acid (PPA) in place Lawesson's reagent.

An important class of azoles which are currently utilised in some of the highest-performing devices in the field are the fused azoles. These possess similar electronic properties to the non-fused derivatives but benefit from increased structural rigidity and molecular packing.[55] Some of the most commonly studied materials are the benzochalcogenadiazoles (Figure 22). These materials have been incorporated into most areas of organic electronics and have shown promise in each of these fields.

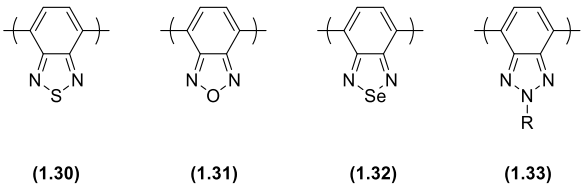

Figure 22 - Chalcogenadiazole compounds.

These acceptor units show relatively similar physical properties to each other but the choice of chalcogen atom can have a profound effect on the electrochemical properties of each unit. For example, three polymers were reported by Liu and co-workers, each containing a different chalcogenadiazole copolymerised with the same benzodifuran co-monomer (Figure 23).

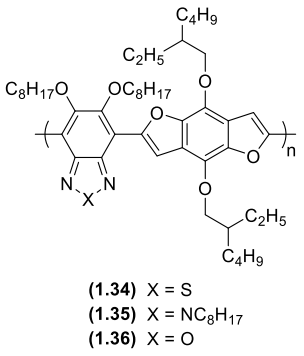

Figure 23 - Chalcogenadiazole containing polymers.

The three polymers exhibit significant variation of their electrochemical properties. For instance, **(1.36)** has a LUMO level 0.43 eV deeper than **(1.35)**. The absorption maxima for **(1.34)** and **(1.36)** are ~50 nm red-shifted when compared to **(1.35)** but at the same time, **(1.35)** exhibits the highest thermal stability with an onset of decomposition at 356 °C whilst **(1.34)** and **(1.36)** decompose at 318 and 319 °C respectively.[56] A summary of the polymer device performance is given below in Table 1.

Polymer	*M*w, PDI (kDa)	λ_{max} (nm)	E_g (eV)	HOMO (eV)	LUMO (eV)	PCE (%)	μ_h SCLC ($cm^2V^{-1}s^{-1}$)
(1.34)	14, 2.0	583	1.73	-5.11	-3.38	4.45	6.7×10^{-2}
(1.35)	18, 1.9	536	1.93	-4.99	-3.06	1.24	3.7×10^{-3}
(1.36)	34, 1.2	580	1.70	-5.19	-3.49	2.88	2.3×10^{-4}

Table 1 - Chalcogenadiazole polymer summary. SCLC – space-charge limited current model.

The authors credit the superior OPV performance of **(1.34)** to its significantly higher hole mobility in the blend film. They attribute this to increased aggregation of the thiadiazole containing derivative. This was further evidenced by AFM and TEM imaging which clearly shows formation of ~60 nm aggregates in the case of **(1.34)** and to a lesser extent also in **(1.36)**, whilst these aggregates were not visible at all in the case of **(1.35)**.[56]

Similarly, research published simultaneously by Jenekhe and co-workers and Jeffries-EL and co-workers have shown that by replacing the oxygen atoms in **(1.37)**, for the less electronegative sulphur atoms in **(1.38)**, materials show increased device performance as a result of increased delocalisation within the π system (Figure 24). Additionally it is also proposed that the empty d-orbitals of the sulphur atom can contribute to the MOs and hence lower the E_g for the π-π* transition.[57-60]

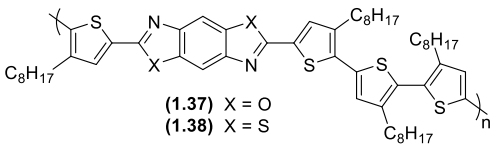

Figure 24 - Benzobisazole containing polymers.

1.6.1 Benzobisazoles

Another class of conjugated fused azole that has been relatively unexplored in the field of organic electronics are the benzobisazole compounds. Despite being first synthesised in the early 1960s, research into these as conjugated materials has been largely hindered by the

reaction conditions required to synthesise them.[61, 62] Typically, they are synthesised *via* acid catalysed condensation reactions with a carboxylic acid, starting from the corresponding dichalcogenol-diamine as shown in Figure 25.

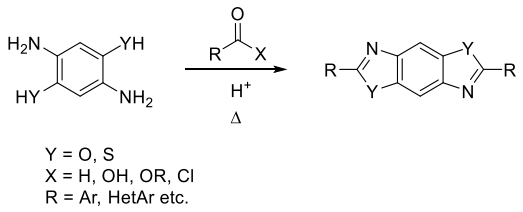

Figure 25 - Typical synthesis of benzobisazoles.

These reactions typically take place at reflux in a high boiling point solvent such as DMSO. Polyphosphoric acid (PPA) or methanesulfonic acid (MSA) are often used as the acid source in order to promote dehydration and rearomatisation. This reaction is however one of the simpler steps in the synthesis of these materials. Several groups have reported having issues regarding the stability of the intermediates, in that they are prone to rapid decomposition in ambient conditions and even - albeit slower - under an inert atmosphere.[57, 61, 63] An effective way to overcome the stability issue for the sulphur analogue is to isolate intermediate **(2.3)** as the hydrochloride salt which can be stored for a limited time (Scheme 3).

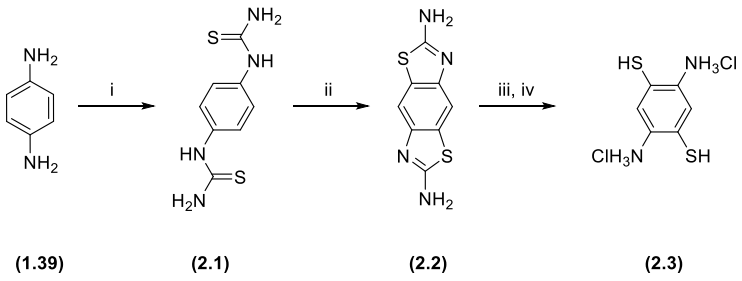

Scheme 3 – Reagents and conditions: i) NH_4SCN, $HCl_{(aq)}$ reflux (95 %); ii) Br_2, $CHCl_3$ 0 – 5 °C, then reflux (86 %); iii) $KOH_{(aq)}$ reflux, then rt; iv) $HCl_{(aq)}$

Compound **(2.3)** can then be used for the corresponding condensation reactions yielding 2,6-disubstituted benzobisthiazole (BBT) compounds. Jenekhe and co-workers synthesised **(1.41)** in 9% yield *via* condensation of **(2.3)** and **(1.40)** in the presence of diphenylphosphate (Scheme 4).

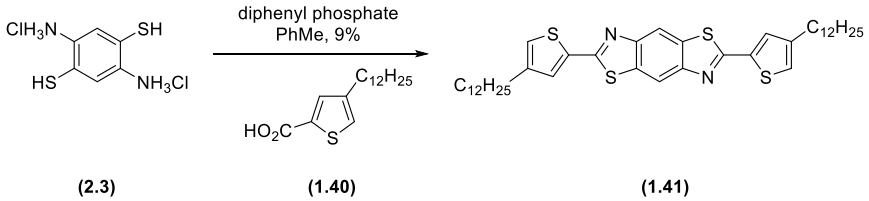

*Scheme 4 - Synthesis of 2,6-bis(4-dodecylthiophen-2-yl)benzobis(thiazole)**(1.41)**.*

The low yield can be attributed to a combination of the poor stability of **(2.3)** and the use of a carboxylic acid which is a poor electrophile and non-optimal for these reactions. Similarly when Ahmed and co-workers synthesised 2,6-bis(4-octylthiophen-2-yl)benzobis(thiazole) **(1.43)** *via* similar condensation reaction with **(2.3)** and 4-octylthiophene-2-carboxaldehyde **(1.42)**, they obtained the target material in only 12% yield.[58]

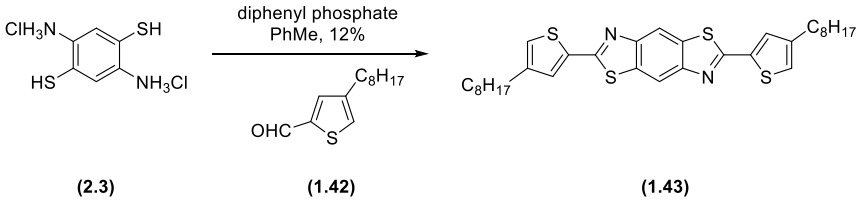

Scheme 5 - Synthesis of ***(1.43).***

Clearly, the low yields obtained highlight that an improved synthetic pathway is desirable for the synthesis of these derivatives and recently work within the Skabara research group demonstrated a synthetic pathway that does not involve intermediate **(2.3)** (Scheme 6).[17]

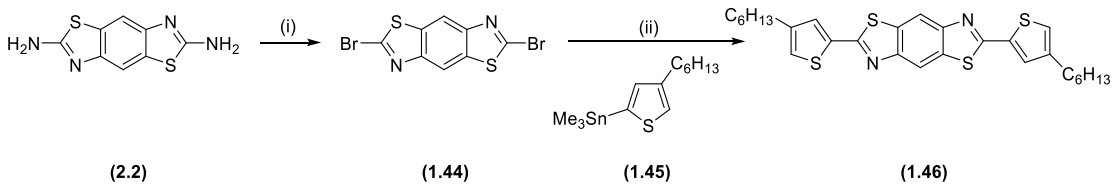

Scheme 6 - Reagents and conditions: (i) $CuBr_2$, t-BuONO, MeCN, 0–5 °C, then reflux (30 %); (ii) $Pd(PPh_3)_4$, μW, DMF, 300 W, 2 h (80 %).

Synthesis of the dibromo intermediate **(1.44)** *via* a Sandemeyer reaction allows for standard palladium catalysed cross-coupling reactions and hence synthesis of many derivatives can be realised. This synthetic pathway is however hindered as the dibromo intermediate suffers from very poor solubility and is hence difficult to isolate in high purity.[64]

In 2010, Mike and co-workers demonstrated the use of orthoesters, in the presence of catalytic lanthanide triflates, which are efficient in the ring closing reaction.[63] The reactions proceed in moderate to high yields (38 – 68%) and can be conducted at 50 °C, with short reaction times and in the absence of strong acid (Scheme 7).

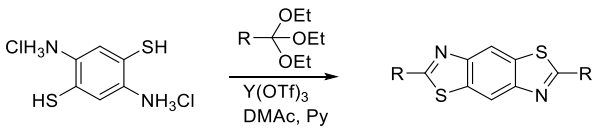

(2.3)

*Scheme 7 - Y(OTf)$_3$ catalysed 2,6- BBT synthesis. R = H **(1.47)**, Me **(1.48)**, CH_2Cl **(1.49)**, $C_2Si(Me)_3$ **(1.50)**, CO_2Et **(1.51)**.*[63]

The substrate tolerance for this reaction appears to be improved relative to the traditional method and the yields are significantly higher, but the authors note that the utility of the reaction is hindered due to the lack of an available synthetic protocol for many orthoesters.

1.7 Organic Field Effect Transistors

Transistors are a class of electrical switch that can be converted between the on and off states *via* an applied electrical potential. They are found in most modern electronics and to date, most of these rely on amorphous silicon (α-Si) as the semiconducting layer. In 1986 Tsumura and co-workers published the first OFET fabricated using polythiophene as the active semiconductor layer.[65] Whilst this device performed very poorly with a p-type mobility of 10^{-5} $cm^2V^{-1}s^{-1}$ compared to α-Si with a mobility of 0.1 – 1 $cm^2V^{-1}s^{-1}$, the discovery has stimulated growth of the field and mobility values for p-type materials have far exceeded the α-Si benchmark.[27]

OFETs are receiving significantly increased interest from industrial companies that recognise their potential as cost-effective replacements for α-Si. Organic materials can be solution processed through roll to roll fabrication methods, have the capability to perform on bendable and flexible substrates, show incredible stability over a period of several years and can display single-component ambipolarity without chemical doping.[66-70]

OFETs are commonly fabricated in three different configurations; bottom gate - bottom contact (BGBC), bottom gate - top contact (BGTC) and top gate - bottom contact (TGBC). A representative diagram of each of these can be seen in Figure 26.

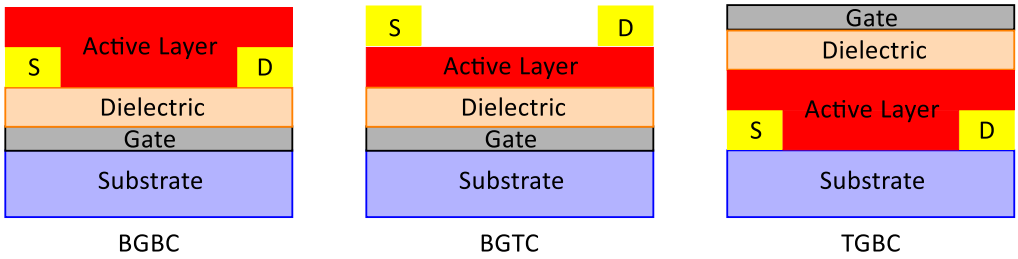

Figure 26 - OFET device structures; S – source, D – drain.

The easiest of these device architectures to build is undoubtedly the BGBC as the main structure including the dielectric and electrodes are fabricated before deposition of the organic material. In the BGTC devices, the active layer material is deposited onto the dielectric before thermal evaporation of the SD electrodes through a shadow mask. Finally, in the TGBC device, the active layer is deposited on top of the SD electrodes, before deposition of the dielectric (spin coating or thermal evaporation) and subsequent evaporation of metal gate electrodes again through a shadow mask. Typically, OFETs fabricated as TGBC are the most effective and many of the best performing devices utilise this architecture.[71] This is attributed to the semiconductor layer being encapsulated between two insulating layers, reducing the effect of atmospheric contaminants such as oxygen and also, due to reduced possibility of leakage or short circuiting between the gate and semiconductor. The increase in performance has been shown to be around one order of magnitude for mobility.[67, 72]

Typically these transistors are fabricated by using highly doped silicon as the gate electrode and thermally-grown SiO_2 as the dielectric as these relatively inexpensive, pre-fabricated chips can be bought commercially. There are however many dielectrics that have shown to be more effective in the literature such as PMMA, CYTOP, or aluminium oxide (Al_2O_3).[53, 73] In the case of p-type FETs, the electrodes are commonly fabricated from gold, silver or platinum that has been thermally evaporated through a shadow mask. These metals are effective as they have a high work function of φ= -5.1 eV, -4.9 eV and -4.7 eV, respectively, which enables an ohmic contact with the HOMO of the semiconducting material.[74] Alternatively, for n-type materials, electrodes consisting of calcium (φ= -2.87 eV) or aluminium (φ= -2.93 eV) are commonly used to provide an ohmic contact with the LUMO of the semiconductor.[27]

OFETs operate by application of a potential at the gate electrode (V_g) causing the generation of a large electric field at the insulator-semiconductor interface. Upon generation of this electric field it becomes possible to inject charge carriers into the semiconducting layer by application of a second potential across the source and drain electrodes (V_{ds}). When the gate voltage is negative ($V_g < 0$), the source electrode which is grounded (0 V) is more positive than V_g and

hence holes are injected from the source to the HOMO of the semiconductor (p-type). On the other hand, when the gate voltage is positive, ($V_g > 0$) resulting in the source electrode being more negative than V_g, electrons are injected into the LUMO of the semiconductor (n-type). An illustrative example of this effect can be seen in Figure 27.

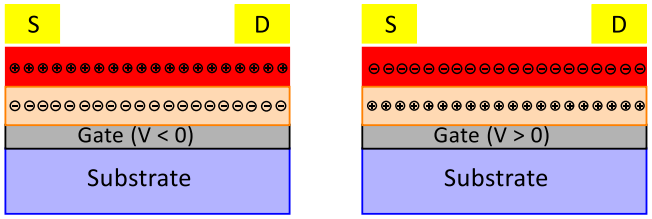

Figure 27 - Generation of charge carriers under an applied electric field in OFETs.

The performance capabilities for an OFET can be determined by three main parameters: the charge-carrier mobility (μ_h for holes, μ_e for electrons), current on-off ratio (I_{on}/I_{off}) and the threshold voltage (V_{th}). The mobility is dependent on effective overlap of the intra and intermolecular π orbitals within the bulk film and hence higher mobilities are often found in highly ordered structures. The mobility is of critical importance for high performance transistors as it is often the limiting factor when determining the switching speed of the device and a mobility of 0.1 $cm^2V^{-1}s^{-1}$ is required for enabling the replacement of α-Si in electronics.[27] The I_{on}/I_{off} ratio is the ratio of drain current in the on state ($V_g \neq 0$) when compared to the drain current in the off state ($V_g = 0$). High I_{on}/I_{off} ratios are desirable for highly efficient switching between the on and off state. Similarly, I_{off} should be as small as possible to prevent leakage and also reduce the possibility of short-circuits. Doping impurities in the semiconductor and also incomplete formation of the insulating dielectric can lead to high I_{off}. V_{th} is described as the V_g at which point charges are injected into the semiconductor layer. This arises due to the presence of charge traps which must be filled before effective conduction can be achieved and therefore the "effective V_g" can be described as (V_g - V_{th}). When $V_g < V_{th}$ there will be no conductivity.[75]

The current-voltage characteristics for an OFET can be analysed by checking the output and transfer characteristics. In the case of the output, the drain current (I_d) can be measured by keeping constant V_{ds} and sweeping V_g. On the other hand, by keeping V_g constant and sweeping V_{ds} the transfer characteristics can be assessed (Figure 28).

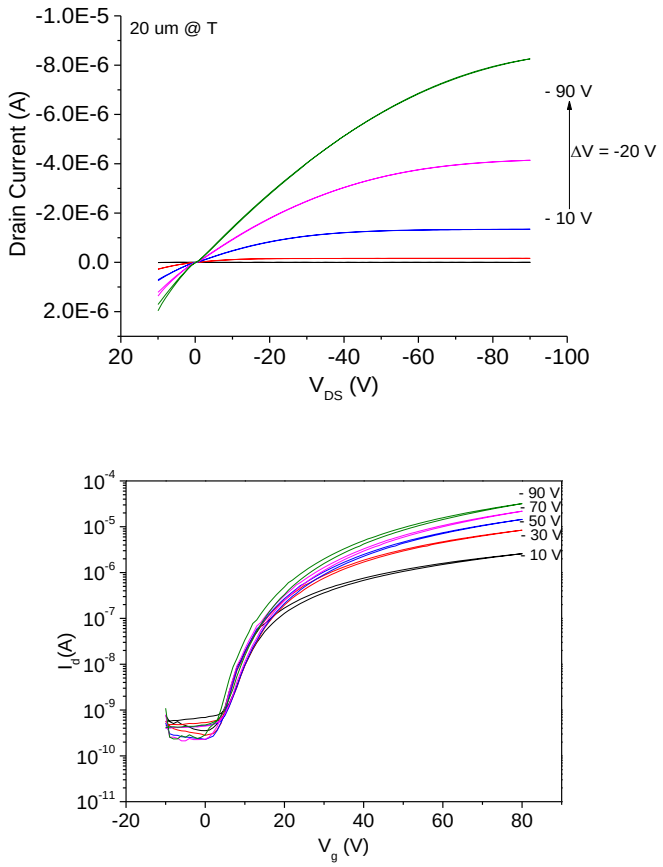

Figure 28 - Typical Output (top) and Transfer (bottom) characteristics.

I_d can be expressed as:[75]

$$I_d = \frac{W}{L}\mu C_i\left[(V_g - V_{Th})V_{ds} - \frac{1}{2}V_{ds}^2\right]$$

Equation 2

Where I_d is the drain current, μ is the carrier mobility, V_g is the gate voltage, L and W are the channel length and width respectively and C_i is the capacitance per unit area of the insulator material. Depending on the applied V_g, the drain current can be in either the linear regime (V_{ds} <<< V_g) or the saturation regime ($V_{ds} \geq V_g - V_{th}$).

In the linear regime, the current is linearly proportional to V_g and hence I_d can be expressed as:

$$I_d = \frac{W}{L}\mu_{lin}C_i(V_g - V_{Th})V_{ds}$$

Equation 3 – Linear regime

When $V_{ds} = V_g - V_{th}$, the current no longer increases substantially and the saturation region is reached where I_d can be expressed as:

$$I_d = \frac{W}{2L}\mu_{sat}C_i(V_g - V_{Th})^2$$

Equation 4 – Saturation regime

Calculating μ is usually achieved in the saturation region by plotting $\sqrt{I_d}$ versus V_g and extracting the slope of the curve which can be used in Equation 5 as follows:

$$\mu_{sat} = \frac{2L}{WC_i} \times \left(\frac{\partial\sqrt{I_d}}{\partial V_g}\right)^2$$

Equation 5 - Calculation of μ_{sat}.

1.8 Organic Solar Cells

1.8.1 Solar Energy

With year on year, global energy demand increasing by >2% from 2012 to 2013, and ever tightening legislation surrounding CO_2 emissions, the necessity for alternative, efficient, low carbon energy sources is clear. Current global energy demand is approximately 17 TW, or the equivalent of 13 billion tonnes of oil per year.[76] For reference, this is enough energy to continuously power 340 billion halogen, 50 W lamps.[77] In order to reduce dependence on fossil fuels and other environmentally impactful sources, a larger portion of energy demand must be satisfied by renewables.[76] Currently, 5.3% of global energy is currently generated by renewable sources and one third of growth in energy generation, is a result of renewables. Hydroelectric energy is currently responsible for generating the largest quantity of renewable energy and satisfies 2.5 % (0.43 TW) of global energy demand. However, a Department of Energy report in 2006 stated that based on current technologies, hydroelectric power was not a sustainable primary source of energy for the future, as if a dam was built across every single river, it would only supply 17.6% (3 TW) of current demand.[78] Wind energy is the second most prevalent source worldwide and accounts for 1.8 % of current demand (0.31 TW) but again the maximum obtainable energy from wind is estimated at 23.5 % (4 TW) of current demand. [79]

The sun is the earth's primary energy source and produces ~120,000 TW. While it is impossible to harness all of this energy, it is estimated that on average, around 1 $MWkm^{-2}$ reaches the surface and therefore by harnessing the energy reaching 1.7 million km^2 - 1.1% of the available land surface on earth – global energy demand would be met by solar energy alone.[78] The required area could also be reduced by creating solar farms in areas which receive more intense solar irradiance such as the Sahara desert. Recently, DESERTEC Foundation reported that the solar energy reaching 1% of desert land on earth, could satisfy current global energy consumption.[80] Obviously, the energy generated in such areas would have to be transported before use, but the appeal for creating solar farms in uninhabited areas is clear.

Solar radiance ranges from 300 – 4000 nm with the majority of the intensity ranged below 2000 nm (Figure 29) therefore, lower band gap materials are efficient for harvesting this energy.[81]

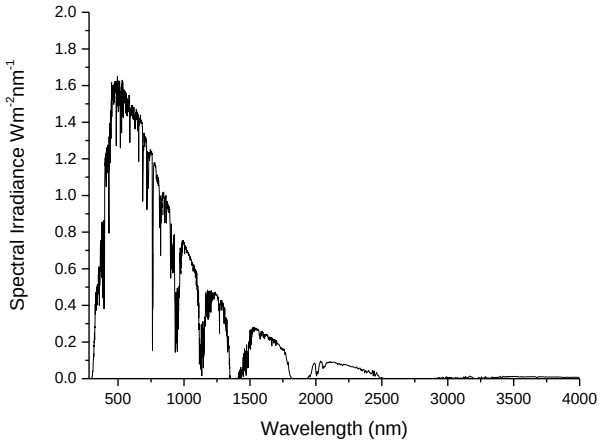

Figure 29 - Photons reaching earth from the sun.

1.8.2 Photovoltaic Technologies

The photovoltaic effect is the process in which a material absorbs a given wavelength of light and generates current. This effect was first reported in 1839 by Alexandre-Edmond Becquerel but was not utilised into a viable working solar cell until Bell Laboratories unveiled a Si cell in 1954 which provided a 6% power conversion efficiency (60 Wm^{-2}).[82] Since then PV technologies have grown at an unprecedented rate and solar energy can now be provided at \$0.11 kWh^{-1}, compared to \$0.09 kWh^{-1} for coal, making PV technology a very viable technology.[83] Some of the largest reductions in PV costs are derived from reduced cost of manufacture.[84] Currently Si-based PV technologies require high temperature and vacuum in order for them to be manufactured and due to their weight, they require sophisticated installation modules. These factors result in the manufacturing accounting for ~60% of the total cost (Figure 30).

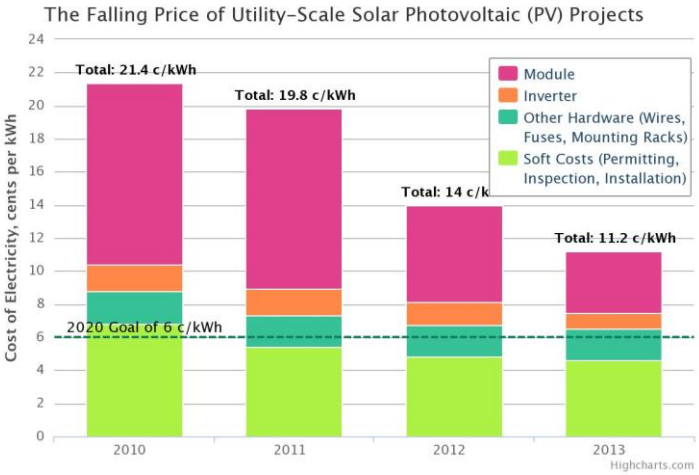

Figure 30 - Price per kWh for PV energy. [84]

Currently, there are several well established PV technologies with varying record power conversion efficiencies (η) including solar concentrators (44.7 %), crystalline GaAs (28.8 %), crystalline Si (25.6 %), inorganic thin-film technologies such as CdTe (21 %) and α-Si (13.4 %). More recently, there are the emerging PV technologies (sometimes referred to as Generation II or excitonic cells) which include dye-sensitised solar cells (11.9 %), perovskites (20.1 %) and tandem organic solar cells (11.1 %).[85]

The emerging PV technologies all benefit from being solution processable and hence the possibility for very low manufacture costs can be realised. Organic solar cells also benefit from the fact that they can have tuneable transmission[86], are applicable to flexible and bendable substrates[87] and can be produced in large scale due to their ease of synthesis and modification.

1.8.3 OPV device physics

Obviously, incident solar energy is variable due to a number of factors, therefore, it is essential to standardise lab conditions in order to compare devices fairly. The standardised test conditions for solar cells utilises the Air Mass 1.5 spectrum which corresponds to an incident power density of 1000 Wm^{-2} at 25 °C. This is often referred to as "one sun" incident power and should be calibrated by using a certified Si solar cell before use.[81] OPV device performance can be described by definition of the following terms:

V_{oc} – The potential of the cell during open-circuit (J = 0) whilst under illumination. V_{oc} is directly related to the difference between the HOMO of the donor material and LUMO of the acceptor material and losses are incurred due to poor morphology of the active layer and inefficient charge transport properties.[88] A Voc of greater than 1 V is considered a high voltage OPV.

J_{sc} – The current density at short-circuit (V = 0) whilst under illumination. J_{sc} is directly related to the generation of free charge carriers in the active layer due to incident photon absorption. Low J_{sc} can be a result of charge traps, inefficient charge-transfer from donor to acceptor and very short exciton diffusion length. Currently, record J_{sc} values for single junction OPVs are 15 to 18 mA cm^{-2}.[89]

P_{max} - OPVs cannot function under the above conditions and hence the maximum current (J_{max}) and voltage (V_{max}) are obtained from the maximum power ($P_{max} = J_{max} \times V_{max}$) that the device can exhibit.

FF – The fill factor can be described as the percentage of power generated, relative to the absolute maximum that could be generated and is defined in Equation 6.[88] In order to realise high efficiency OPVs, the FF should be as close as possible to the maximum value of 1.

$$FF = \frac{P_{max}}{J_{sc}V_{oc}} = \frac{J_{max}V_{max}}{J_{sc}V_{oc}}$$

Equation 6 - Determination of Fill Factor.

EQE – The external quantum efficiency (or incident photon-to-current efficiency [IPCE]) is the ratio of measured photocurrent at short-circuit conditions, to the possible current generation from incident photons (Equation 7). Similar to the FF, high efficiency cells require an EQE close to 1.

$$EQE = \frac{hcJ_{sc}}{\lambda P_{in}} = \frac{1241.5J_{sc}}{\lambda P_{in}}$$

Equation 7 - Calculation of EQE

Where *h*, *c*, λ and P_{in} are Planck's constant (6.626 x 10^{-34} Js), speed of light (2.997 x 10^{8} m s^{-1}), wavelength of incident photon and incident power respectively.

η - The photovoltaic power conversion efficiency (or PCE) of a solar cell is described by Equation 8.

$$\eta = \frac{V_{oc}J_{sc}FF}{P_{in}}$$

Equation 8 - Calculation of PCE

The process of converting light into electrical current in OPVs can be explained by the series of steps highlighted with blue arrows in Figure 31. The steps illustrated with red arrows are loss mechanisms that arise from recombination.

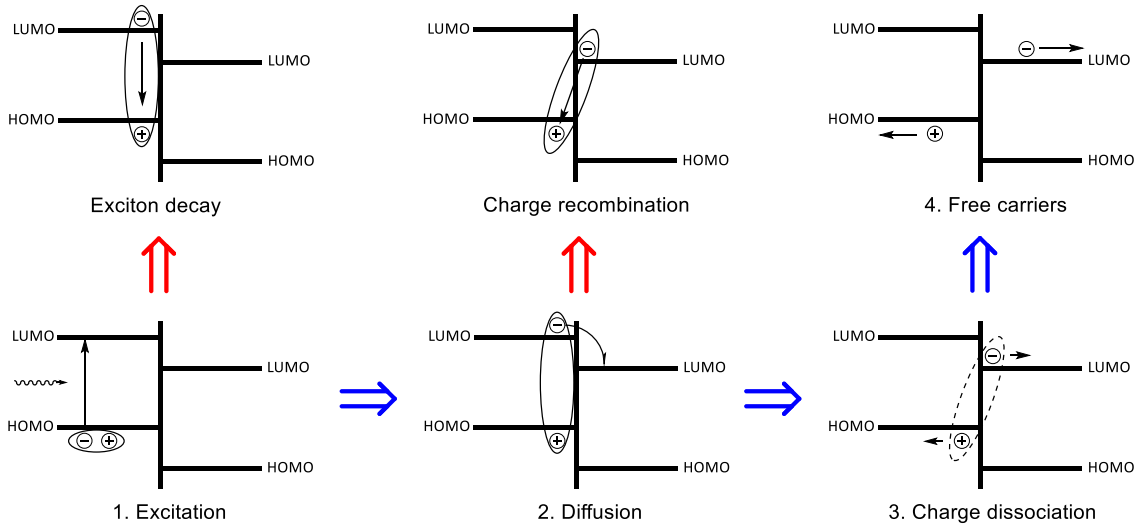

Figure 31 - Charge generation and losses in OPVs.

The first step involves photo-excitation of an electron from the HOMO of the donor to the LUMO of the donor generating a bound exciton. This exciton can then diffuse towards the D-A interface for ~10 nm. If the exciton does not reach the interface within the diffusion length it will decay back to the ground state. Any excitons which successfully decay to the interface can then dissociate and become free carriers if the exciton binding energy is smaller than the Δ_E between the LUMO of the donor and the acceptor (Δ_E typically $\geq$ 0.3 eV).[2, 90, 91] As explained earlier, the two main losses in OPVs are a result of exciton decay and charge recombination.[92] Charge recombination between the bound electron-hole pair is known as geminate recombination whilst recombination between free charge carriers is termed bimolecular recombination.

Assuming that all photons of energy larger than the material band-gap can be absorbed, it would be intuitive to assume that very low band-gap materials would be the best OPV materials. This is however not the case as when approaching very narrow gaps (<1.3 eV), the V_{oc} becomes the limiting factor in device efficiency. In 2006 Scharber and co-workers studied the correlation between V_{oc} and $HOMO_{donor}$ to $LUMO_{acceptor}$ energy levels and found that the V_{oc} could be estimated by:[93]

$$V_{oc} = \left[\frac{1}{e}\left(HOMO_{donor} - LUMO_{acceptor}\right) - 0.3\right]$$

Equation 9 - Estimation of V_{oc}

Where e is the elementary charge. The constant of 0.3 V is attributed to voltage loss at the electrode contacts. This equation shows that an ideal acceptor has a HOMO that is much deeper

than the LUMO of the acceptor but still remains low band gap (as to absorb the maximum number of photons) and retain a minimum of 0.3 eV offset between the LUMO of the donor to the LUMO of the acceptor to enable charge transfer.[93]

These variables led Scharber and co-workers to offer a set of "design rules" which would provide the optimal band gap and donor-acceptor offset, in order to achieve the maximum efficiencies.[93]

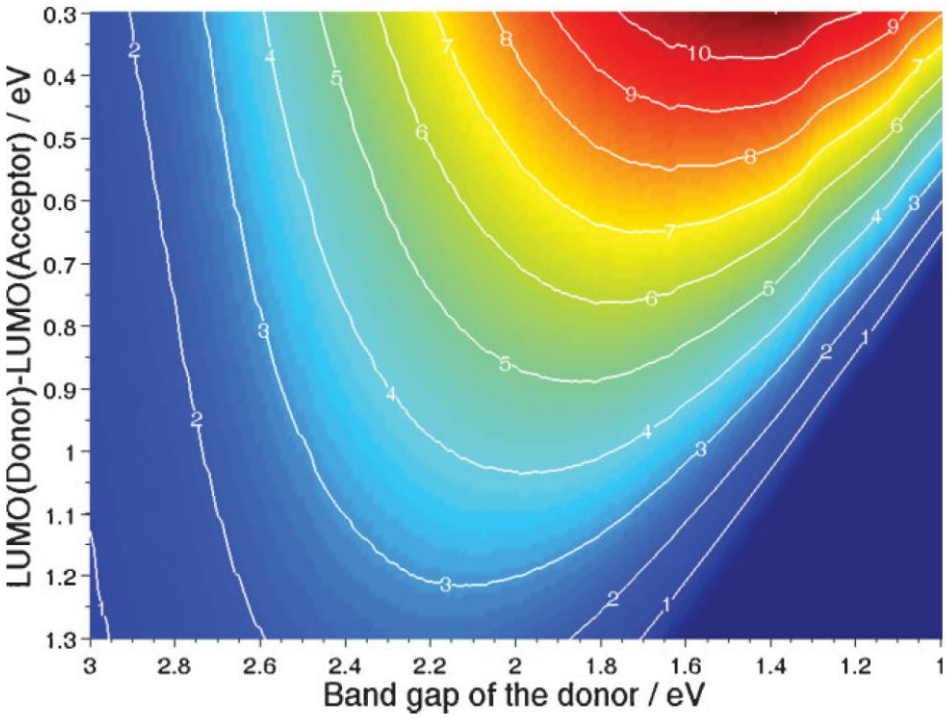

Figure 32 - Contour plot showing efficiency as a function of E_g and LUMO offset

From this, it is clear that an ideal donor will have 1.7 ≥ Eg ≥ 1.2 eV and a LUMO offset of as close to 0.3V as possible.

1.8.4 OPV device architectures

OPV devices require 4 basic components in order to function: a transparent electrode (typically ITO glass), two (or more) organic materials which are either deposited in discreet layers (bilayer device) or as a random blend within a single film (bulk heterojunction [BHJ] device) and finally, another electrode which is typically Ca/Al (Figure 33).

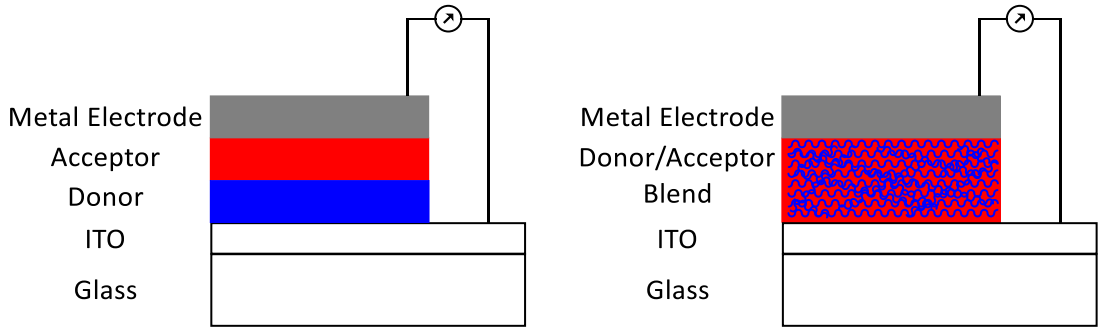

Figure 33 - Bilayer (left) and BHJ (right) solar cell

Bilayer devices were among the first OPVs to be fabricated in the literature and they are the most analogous to Si cells in that they have a discreet boundary between the donor and acceptor. Bilayer devices benefit from the fact that when free charges diffuse into the separate boundaries, the chance of recombination becomes low due to the lack of available opposite carriers. These devices do however perform quite poorly due to the fact that exciton diffusion length (how far the exciton can move before it will relax again) for organic materials is on the order of ~10 nm.[90, 94] This results in the majority of excitons, failing to become free carriers as they do not reach the interface.

As the lifetime of organic excitons tend to be much shorter than their inorganic counterpart, it is essential that nanoscale phase separation occurs.[91, 95] In BHJ cells this can be achieved in some cases and therefore it is possible for many of the generated excitons to reach the interface before the exciton decays. Controlling the morphology in BHJ cells can be extremely challenging and, as a result, BHJ cell performance is highly dependent on the processing parameters used to fabricate them.[96]

Almost all current research in OPVs is focussed on the BHJ architecture as they have the potential to be processed completely from solution. This would allow for significant reductions in manufacturing costs and ultimately, the production of low-cost, environmentally-friendly energy sources. Many factors affect the morphology of the active layer in the device including choice of donor (D) or acceptor (A), relative weight ratio of D:A, substrate wettability and roughness, solvent choice and post-fabrication treatment.[97, 98]

By far the most common acceptor units are fullerenes. Among these fullerenes, $PC_{61}BM$ and $PC_{71}BM$ are the most common due to a combination of their good electron mobilities (10^{-3} $cm^2V^{-1}s^{-1}$), deep LUMO (~3.7 - 3.9 eV) and three dimensional charge transport properties (Figure 34).[90, 99]

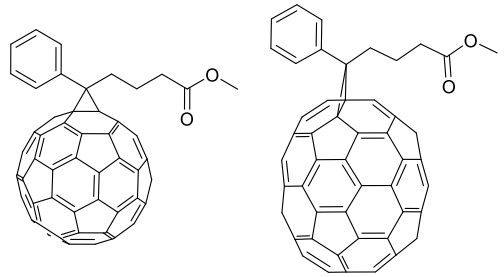

(1.52) (1.53)

*Figure 34 - $PC_{61}BM$ **(1.52)** and $PC_{71}BM$ **(1.53)**.*

Fullerenes (in particular $PC_{71}BM$) are the acceptor components in all of the current record devices, yielding PCEs above 9%.[87, 89, 100] Whilst the electrical characteristics of fullerenes are highly desirable as mentioned above, the optical properties of these materials can have a negative impact on device performance. They suffer from weak absorption in the visible region, very limited spectral breadth, phase segregation in the blend and their band-gaps are very difficult to tune.[101] Fullerenes are also limited by the complicated and often low yielding chemistry required to synthesise them which results in $PC_{71}BM$ having a retail price of $1000/g.

Inspired by the growing development of *n*-channel OFET materials, some research groups are now investigating the use of non-fullerene acceptor units for OPVs.[102-104] Azole containing polymers and small molecules have received interest for this application and have produced non-fullerene OPVs with efficiencies of up to 2.7% (Figure 35).[104]

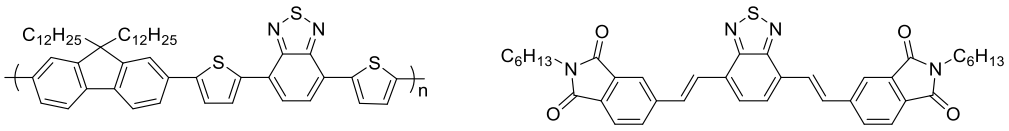

(1.54) (1.55)

*Figure 35 - Azole containing polymeric **(1.54)** and small molecule **(1.55)** acceptors.*

Whilst azole containing materials have shown promise as acceptor components, the most successful class of non-fullerene acceptors is undoubtedly the rylene diimide based materials such as naphthalene diimides (NDIs) and perylene diimides (PDIs) which have exhibited efficiencies of up to 5.9% (Figure 36).[90, 105]

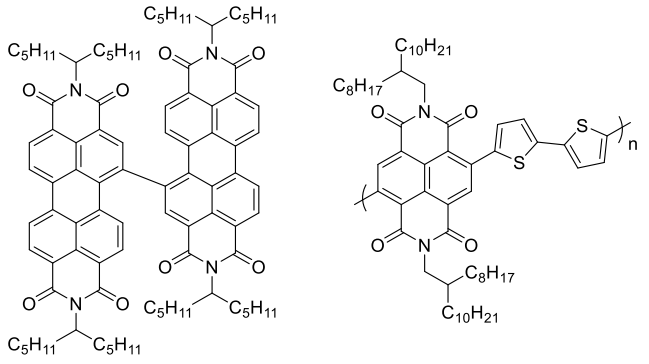

(1.56) (1.57)

*Figure 36 - PDI **(1.56)** and NDI **(1.57)** containing acceptors.*

These non-fullerene acceptors benefit from significantly increased molar absorption, the capability for complimentary donor-acceptor absorption properties, simplified synthetic protocol (enabling cheaper production costs) and fine tuning of material properties.[104]

There are many donor materials available in the literature that can produce a photovoltaic effect and most significant advancements in efficiency are a direct result of donor modification. P3HT **(1.3)** is currently the most widely known and studied donor material and routinely yields efficiencies of 3-5% in P3HT:fullerene cells.[24, 106] Whilst P3HT **(1.3)** has been shown to display reasonable OPV performance, its capabilities are limited by its non-optimal band gap (~ 2.0 eV), shallow HOMO level and limited hole mobility.[22] As a result, P3HT **(1.3)** is now being replaced with more sophisticated donor materials that have been synthesised to overcome these issues. Most recent donor polymers are copolymeric rather than homopolymeric as it enables the introduction of push-pull behaviour along the backbone which can lower E_g.[107]

Donor-acceptor (D-A) type materials work to lower the band gap *via* a similar method to doping. By incorporating electron rich units (such as thiophene) into the material backbone, the HOMO becomes localised mostly on these units and is destabilised. Simultaneously, incorporation of electron deficient units (such as azoles) causes the LUMO to become localised and is stabilised. The combination of these factors leads to a reduction in band gap for the material. Effective control of the band gap can be achieved by tailoring the electron density of each unit.

Examples of two of the more efficient commercial donor materials are shown in Figure 37. In the case of PCPDTBT **(1.59)**, the benzothiadiazole unit is the electron acceptor and the cyclopentadithiophene unit is the electron donor.

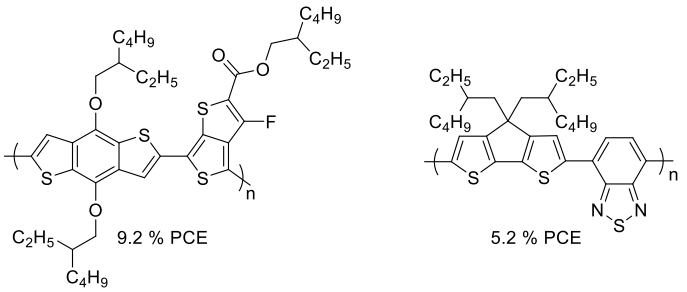

(1.58) **(1.59)**

*Figure 37 - Commercial polymers - PTB7[108] **(1.58)** and PCPDTBT[109] **(1.59)**.*

Even though PTB7 **(1.58)** displays the record efficiency in single junction OPVs, it is still limited by it's larger than ideal band gap (1.9 eV) and large offset (0.9 eV) between the LUMO of PTB7 and $PC_{71}BM$. Its high efficiency is due mostly to the excellent fill factor (72%) and EQE (up to 80%) so the efficiency is unlikely to be improved significantly for PTB7/$PC_{71}BM$ solar cells.

Most of the high efficiency OPV devices incorporate one or more additional layers than in the standard 4-component cells, by incorporation of hole or electron transport layers. These thin layers, deposited between the active layer (AL) and electrodes act to improve the diode behaviour of the cell by selectively allowing only one type of charge to diffuse through it, thus minimising bimolecular recombination. For example, PEDOT:PSS (Figure 38) is the most common hole transport layer (HTL) due to its solution processability (from H_2O), high conductivity and work function of ~5.0 eV which provides ohmic contacts to the HOMO of many donor molecules. Whilst electron transport layers (ETLs), such as PFN (Figure 38) are not as common as HTLs, they have been incorporated into many of the highest performing cells to date.[108, 110]

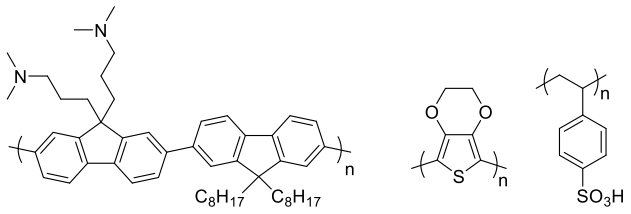

Figure 38 - PFN (left) and PEDOT:PSS (right)

2 Synthesis, characterisation and development of structure-property relationships for 4,8-diaryl-benzobisthiazole derivatives

2.1 Introduction

Whilst oligothiophenes and polythiophenes have been studied intensively due to their excellent semiconducting properties, thiazole containing materials have received far less interest due to their more complex synthesis and derivatisation.[111] This is despite significant evidence that thiazoles offer many more attractive physical properties than thiophenes, such as higher crystallinity and long-range order,[20] improved air stability[41] and larger V_{oc} in organic solar cells due to their deep HOMO level[52] and reduced steric hindrance between adjacent ring systems.[41]

A major contributing factor to the complexity of synthesising fused thiazole systems, such as benzobisthiazole (BBT), is derived from their poor solubility when compared with their thiophene analogues. This has resulted in all BBT based materials used in organic electronics thus far to incorporate solubilising spacers, *e.g.* 3-alkyl thiophenes. The spacer group can have a profound effect on the electronic and morphological properties of the material. In order to address this issue, the synthesis of a novel 2,6-dialkyl-4,8-diaryl BBT core has been achieved. By incorporation of alkyl chains into the thiazole rings, there is no longer the requirement for solubilising spacers. In order to assess the functionality of this interesting new moiety, a series of seven derivatives of the general structure heterocycle-BBT-heterocycle (Figure 39) have been synthesised and their physical properties investigated.

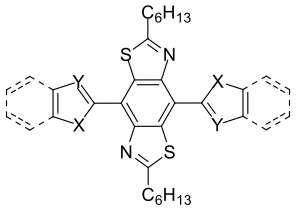

(2.7) X=S, Y=N
(2.8) X=O, Y=CH
(2.9) X=S, Y=CH

benzo derivatives
(2.10) X=O, Y=CH
(2.11) X=S, Y=CH
(2.13) X=S, Y=N
(2.15) X=O, Y=N

Figure 39 - Structure of new 4,8-BBT small molecules

These compounds are isostructural in that the first 3 compounds incorporate 5 member heterocyclic rings substituted to the BBT through the fully conjugated α position. In each of these small derivatives **(2.7-2.9)**, there is a chalcogen in position X and either CH or N in position Y. Compounds **(2.10)**, **(2.11)**, **(2.13)** and **(2.15)** were synthesised to probe the effect that increased conjugation length has on the HOMO and LUMO energy.

Non-covalent heteroatomic interactions within the molecules have also been studied to determine their strength and capability of planarising these otherwise quite sterically hindered materials. The strength of each individual interaction was determined using DFT calculations and the profound influence of molecular planarity on the electronic distribution of molecular orbitals, can be seen by the extensive delocalisation of π-electrons within these systems.

2.2 Synthesis

As the synthesis of 4,8-disubstituted BBT compounds has not been published to date, a method that involves the same synthetic intermediates as the previously published 2,6-BBT compounds was selected and modified accordingly. This involved the synthesis of 2,5-diaminobenzene-1,4-dithiol dihydrochloride **(2.3)** followed by acid catalysed ring closure with an alkanoyl chloride to yield the 2,6-dialkyl BBT **(2.4)**.

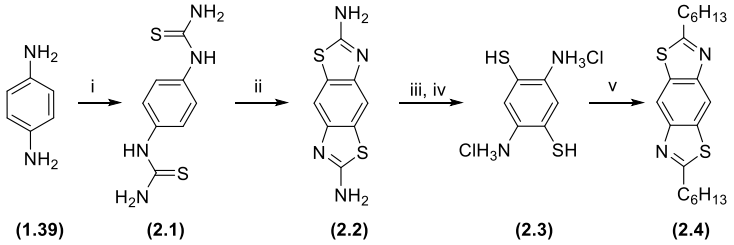

Scheme 8 - Reagents and conditions: i) NH_4SCN, $HCl_{(aq)}$ reflux (90 %); ii) Br_2, $CHCl_3$ 0 – 5 °C, then reflux (84 %); iii) $KOH_{(aq)}$ reflux, then rt; iv) $HCl_{(aq)}$; v) $C_6H_{13}COCl$, PPSE, o-DCB reflux (46 % over two steps)

Several variations of this method were attempted and proved largely unsuccessful. In most cases, a brown intractable gum was obtained and the product could not be identified by NMR spectroscopy. As the product yield of the reaction was increased, the quantity of the brown gum obtained was visibly reduced. Tabulated reactions conditions for these attempts can be seen below in Table 2.

Attempt	Solvent, temp (°C), time for (2.3) – (2.4)	Product yield (purity)	Notes
1	DMAc, 80 °C, 24 h	Brown gum	No product detected by NMR
2	DMSO, reflux, 48 h	Brown gum	No product detected by NMR
3	*o*-DCB, reflux, 48 h	1.4% (impure)	**(2.3)** turned purple before reaction, when drying under N_2. Brown gum formed after reaction and product isolated *via* chromatography but contained impurities.
4	*o*-DCB, reflux, 48 h	11% (pure)	**(2.3)** dried under vacuum overnight, Ar atmosphere used for reaction. Brown gum still obtained, but product could be isolated pure *via* chromatography.
5	*o*-DCB, reflux, 48 h	46% (pure)	**(2.3)** dried for 1 h under Ar then used immediately.

*Table 2 - Attempted synthesis of **(2.4)***

The limiting step for this reaction appears to be the inherent instability of **(2.3)**. Upon exposure to air the material turns dark purple in a matter of seconds and becomes completely insoluble in common organic solvents. In order to overcome this issue, this material was freshly prepared, dried for the minimum required time and used immediately without isolation. This requires strict Schlenk conditions including multiple inert filtrations. When done correctly, compound **(2.3)** can be crystallised as pristine white crystals from HCl and the overall yield for the cyclisation can be achieved in 46%. To simplify the synthetic procedure for this reaction, glassware was custom built to allow for this process to be conducted under inert atmosphere (Figure 40).

*Figure 40 - Reaction setup for conversion of **(2.2)** to **(2.4)**. [1] Reaction vessel; [2] Sintered filter; [3] Flask for filtrate collection; [4] Methanol degasification apparatus; [5] Water degasification apparatus; [6] Aqueous hydrochloric acid degasification apparatus.*

The successful synthesis of **(2.4)** can be seen above in Scheme 8. Freshly purified p-phenylene diamine **(1.39)** was treated with ammonium thiocyanate under acidic conditions to yield bisthiourea **(2.1)** of purity suitable for the next step. Oxidation of **(2.1)** with Br_2 in chloroform at rt, followed by cyclisation and rearomatisation yielded compound **(2.2)** which was purified *via* successive acid-base extractions. In order to ensure that sufficient material was available to develop the synthesis of **(2.4),** compound **(2.2)** was synthesised in >100g scale with no reduction in isolated yield or purity. Compound **(2.3)** was then generated *in-situ* under strict

inert conditions *via* nucleophilic ring opening with KOH followed by acidification with aqueous HCl. The crystalline product was filtered and dried briefly under an Ar gas flow. Polyphosphoric acid trimethylsilyl ester (PPSE) catalysed ring closing of **(2.3)** with an alkanoyl chloride yielded the fused dialkyl BBT compound **(2.4)** in 35 % yield over 5 steps. Currently, the yield for the ring closure represents the highest isolated for any acid catalysed condensation reaction with **(2.3)** reported in the literature to date,[59, 112] which is likely a result of the procedures taken to minimise degradation of the salt intermediate.

With compound **(2.4)** in hand, functionalisation of the central phenylene core with halogens was envisaged as this would allow transition metal cross-coupling reactions with a range of co-reactants to occur (Scheme 9). Several bromination procedures were attempted and these were mostly unsuccessful. These attempts are tabulated below (Table 3).

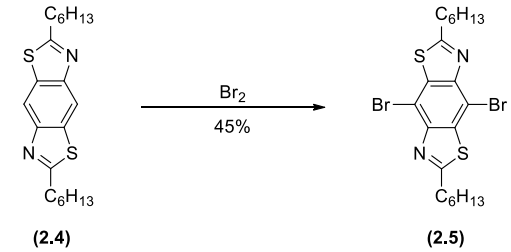

*Scheme 9 - Synthesis of **(2.5)**.*

With compound **(2.5)** in hand, utilisation of common palladium catalysed cross-coupling reactions was envisioned as in Scheme 10 below.

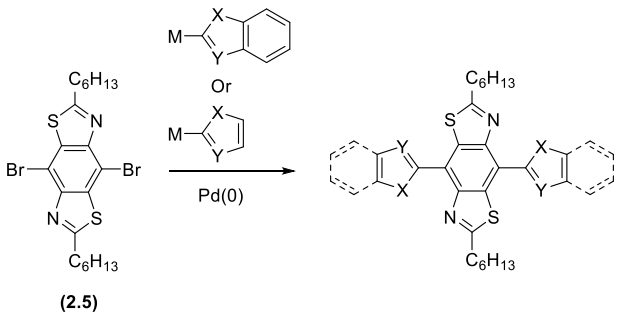

Scheme 10 - Proposed synthesis of BBT small molecule dyads.

Attempt	Halogen source	Solvent, temp (°C), time	Product yield, purity	Notes
1	NBS	$CHCl_3$, rt, 24 h	N/A	Several spots by TLC and ^{1}H NMR – not isolated
2	NBS	$CHCl_3$:AcOH various conditions	Black mixture	Large black baseline spot and insoluble precipitates
3	NBS	DMF, 80 °C, 24 h	Dark brown	Small black baseline and SM recovered
4	NIS	H_2SO_4, various conditions	Black mixture	Large black baseline spot and insoluble precipitates
5	Br_2	$CHCl_3$, rt - reflux, 24 h	Impure yellow solid	Crystallisation occurred during reaction. Product detected by NMR but too difficult to isolate pure.
6	Br_2	$CHCl_3$, $NaHCO_3$ (25 eq), rt-reflux, 24 h	Impure yellow solid	Crystallisation occurred during reaction. Product detected in very small quantities by NMR and difficult to isolate pure.
7	Br_2	$CHCl_3$, pyridine, rt, 24 h	Black mixture	Sticky brown/black gum formed with several spots by TLC. Product not detected by NMR.
8	Br_2	CH_2Cl_2, 0 ^{o}C to rt, overnight	White solid	Small quantity of crystallisation occurred after several hours of reaction. Product isolated in 45% yield pure after chromatography.

*Table 3 - Attempted syntheses of **(2.5)***

Attempts to use *N*-halogen succinimides as the halogen source in acid or halogenated solvent were unsuccessful under various temperatures, concentrations and reaction times. Whilst some halogenation was visible from ^{1}H NMR, significant quantities of insoluble by-products were produced and resulted in poor mass recovery. Whilst NMR studies were inconclusive due to solubility, it is assumed to be the result of ring opening of the thiazole. Use of NBS in DMF was also unsuccessful but did not result in the same production of black impurities which suggests that acidic conditions accelerate these processes. In acidic conditions, the thiazole can convert to thiazolium, creating increased electrophilicity at the 2-position, facilitating nucleophilic ring opening.[113]

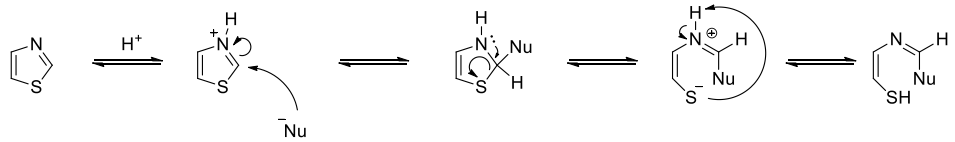

Scheme 11 – Example of nucleophillic ring opening of thiazole.[113]

Treatment of **(2.4)** with elemental bromine in chloroform results in partial halogenation of the SM but again, the degradation products are present and, due to the number of similar impurities, purification of this mixture was unsuccessful. It is also important to note that crystallisation occurred during the reaction after heating in the presence of Br_2. These crystals dissolved when quenched with aqueous base and as such they are presumed to be the hydrobromide salt of **(2.4)**. These hydrobromide salts are deactivated to electrophilic aromatic substitution and hence the reaction is inhibited.[114] In order to assess if the salt formation could be inhibited, solid $NaHCO_3$ or pyridine were added to quench the HBr formed. This was unsuccessful and the salt formation still occurred in the case of $NaHCO_3$, and decomposition in the case of pyridine.

Finally, treatment of **(2.4)** with elemental bromine in ice-salt cooled dichloromethane yielded **(2.5)** in 45% yield after purification by column chromatography and reprecipitation. Starting material **(2.4)** can also be recovered in up to 22% yield after chromatography.

As compounds **(2.6)**, **(2.12)** and **(2.14)** are not commercially available, they were synthesised *via* deprotonation of the unsubstituted heterocycles (with *n*-BuLi) then quenching of the anion with $SnBu_3Cl$ to yield the corresponding Stille reagent (Scheme 12).

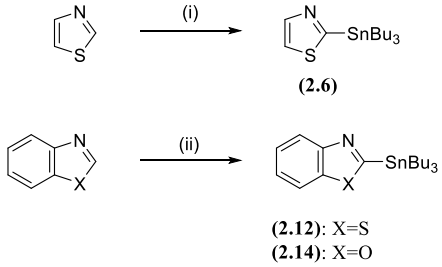

Scheme 12 - Synthesis of Stille reagents. Reagents and conditions: (i) n-BuLi, Et_2O, -50 °C 1h, then $SnBu_3Cl$, -50 °C to rt overnight (97%); (i) ***(2.12)*** *n-BuLi, THF, -78 °C 1h, then $SnBu_3Cl$, -78 °C to rt overnight (80%);* ***(2.14)*** *n-BuLi, THF, -110 °C 1h, then $SnBu_3Cl$, -110 °C to rt overnight (76%).*

Compound **(2.5)** was then subjected to transition metal catalysed cross coupling reactions with the corresponding metallated heterocycles (Scheme 13).

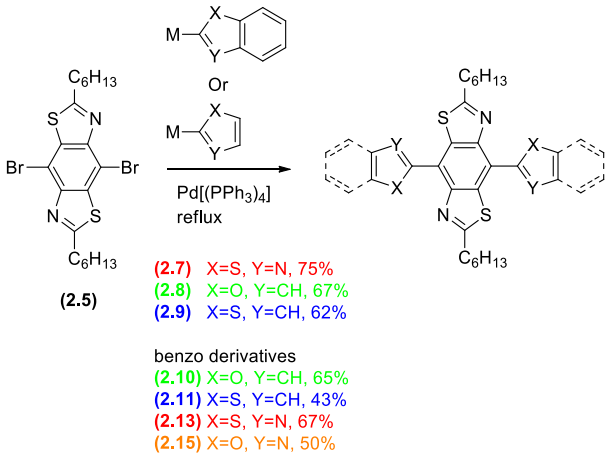

Scheme 13 - Synthesis of BBT small molecules; colour denotes heterocycle substitution - thiazole, furan, thiophene and oxazole are red, green, blue and orange respectively.

Compounds **(2.7)**, **(2.8)**, **(2.9)**, **(2.13)** and **(2.15)** were synthesised *via* a conventional Stille coupling procedure in anhydrous toluene with catalytic $Pd[(PPh_3)_4]$. Compounds **(2.10)** and **(2.11)** were synthesised *via* microwave-assisted Suzuki coupling reactions in a tetrahydrofuran:water mixture using $Ba(OH)_2.8H_2O$ as the base and $Pd[(PPh_3)_4]$ as the catalyst. The yields obtained for these reactions were moderate to high and the materials were purified *via* a combination of column chromatography and recrystallisations. Synthesis of the small oxazole derivative was also attempted but recrystallisation did not yield a product of satisfactory purity; this material appears to decompose on silica and could not be eluted, even with highly polar solvents.

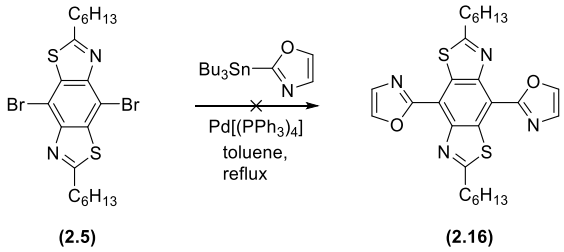

Scheme 14 - Attempted synthesis of bisoxazole BBT

2.3 Results and discussion

UV-Vis absorption and emission of each compound are shown below (Figure 41).

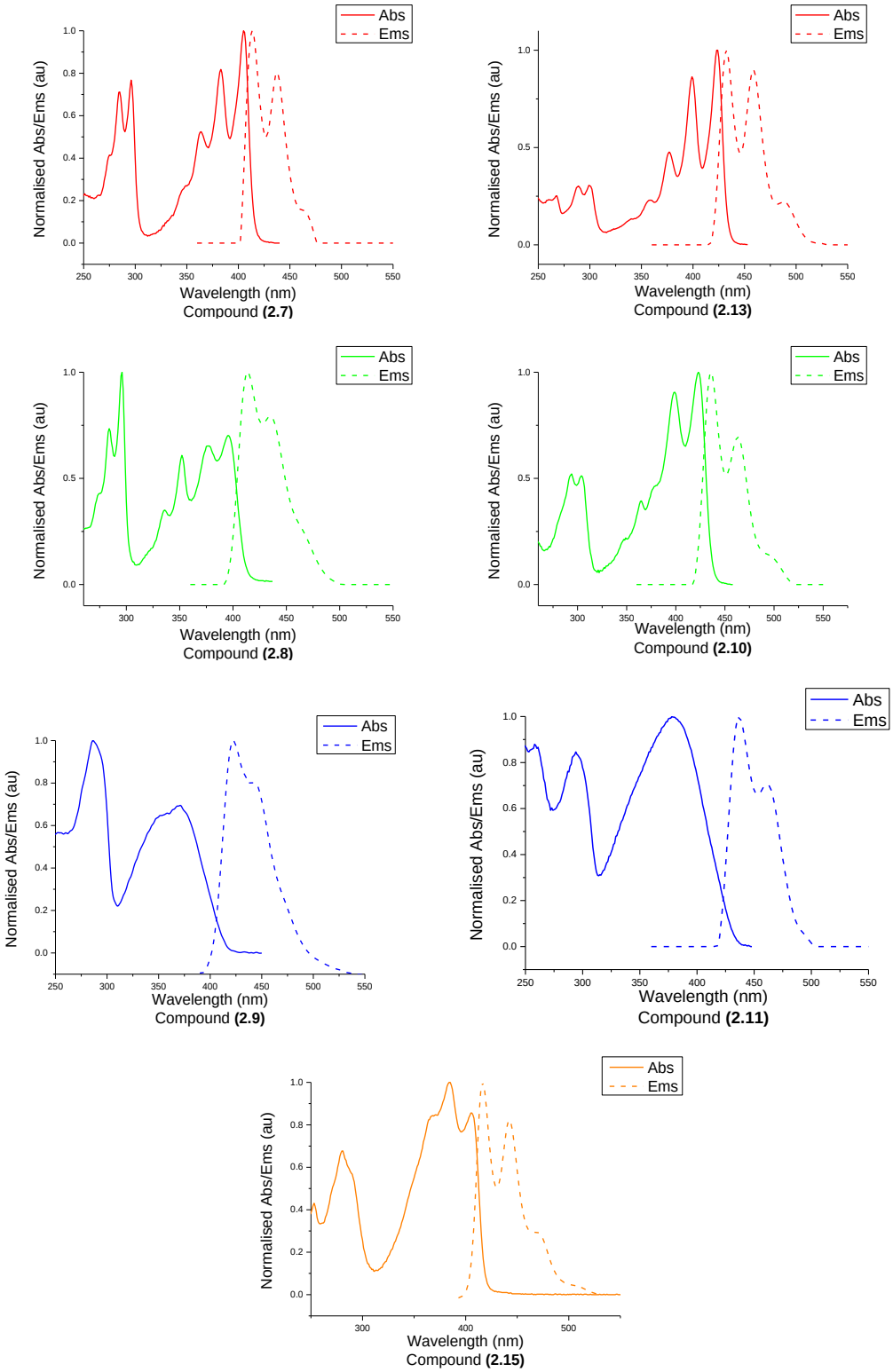

Figure 41 - Absorption (solid line) and emission (dashed line) of synthesised BBT materials (10^{-5}M in CH_2Cl_2). Colour coding is as seen in Scheme 13.

From the optical spectra it is clear that all of the small molecules exhibit very similar HOMO-LUMO gaps, with the benzo-derivatives exhibiting ~0.2 eV smaller gap due to the increased conjugation length. It is also very clear that each of the compounds – with the exception of **(2.9)** and **(2.11)** – exhibit very strong vibronic structure in solution. This is indicative of a rigid crystalline structure. The absorption spectra for **(2.7)**, **(2.8)**, **(2.10)**, **(2.13)** and **(2.15)** show very sharp, well defined peaks, indicating the rigid structure of these molecules even in solution.[115] Alternatively, the broad and undefined transitions exhibited by the thiophene derivatives **(2.9)** and **(2.11)** are clearly indicative of a disordered structure and low energy barrier for torsional rotation.

The BBT molecules **(2.7 - 2.15)** were also studied *via* cyclic voltammetry in order to determine the HOMO and LUMO energy of each material and the results are summarised below (Table 4).

Compound number	HOMO (eV)[a]	LUMO (eV)[a]	Electrochemical E_g (eV)[a]	Optical E_g (eV)[b]
(2.7)	-6.25	-3.04	3.21	2.99
(2.8)	-5.19	-2.38	2.81	3.01
(2.9)	-5.47	-2.76	2.71	3.02
(2.10)	-5.39	-2.71	2.68	2.83
(2.11)	-5.40	-2.69	2.71	2.84
(2.13)	-5.78	-3.02	2.76	2.84
(2.15)	-6.03	-3.12	2.91	2.96

Table 4 - [a] HOMO and LUMO found from onset of oxidation and reduction and referenced to Fc/Fc^+HOMO (-4.8 eV); [b] optical E_g calculated from onset of longest wavelength absorption. See appendices 1-7 for cyclic voltammograms of the synthesised dyads.

The electrochemistry of these materials highlights that by altering the peripheral heterocyclic ring, the absolute energy of the HOMO and LUMO can be variedly substantially. Within experimental error, the HOMO-LUMO E_g in each material is constant relative to conjugation length (2.8 or 3.0 eV), despite significant variation in the absolute HOMO or LUMO energies.

These BBT dyads can exhibit electron donating or electron accepting behaviour dependent on the heterocyclic substitution across the central ring. For example, when substituted with furan rings such as in **(2.8)**, the dyad has a shallow HOMO energy of -5.2 eV, similar to that of P3HT (5.1 eV) which is widely considered an electron rich polymer.[116] Furthermore, when the BBT is substituted with thiazole rings as in **(2.7)**, the HOMO energy is altered to -6.2 eV, identical to

that of 2-(4-Biphenylyl)-5-phenyl-1,3,4-oxadiazole (PBD), which is widely utilised as an electron transport, hole blocking layer in OLEDs.[117] These findings highlight the excellent versatility of 4,8-BBT based molecular materials, whilst the ability to manipulate the energy levels, without altering the gap, could be utilised to design materials possessing the optimum energy levels for a specific role.

Interestingly, the HOMO and LUMO are both altered similarly when the heteroatoms are changed. This, in combination with the optical data, suggests that in these materials, the HOMO and LUMO are delocalised across the entire molecule. This is unusual; in many other materials, the LUMO is localised on the electron deficient unit and the HOMO localised on the electron rich unit.[118] By having highly delocalised systems, it is possible to envisage that any generated charge carriers would be free to propagate indefinitely along the backbone of the material.

C_{60} exhibits similar delocalisation and it is often this which is used to explain its high performance in solar cells.[99, 104] It is believed that the acceptor (in this case $PC_{60}BM$) should overlap with the LUMO of the donor material. If this is the case, upon photo-excitation, the excited electron can transfer effectively to the acceptor. If the LUMO is highly localised, as in the example below by Graham and co-workers (Figure 42), then careful control of the donor-acceptor morphology is required in order to facilitate this overlap.[119]

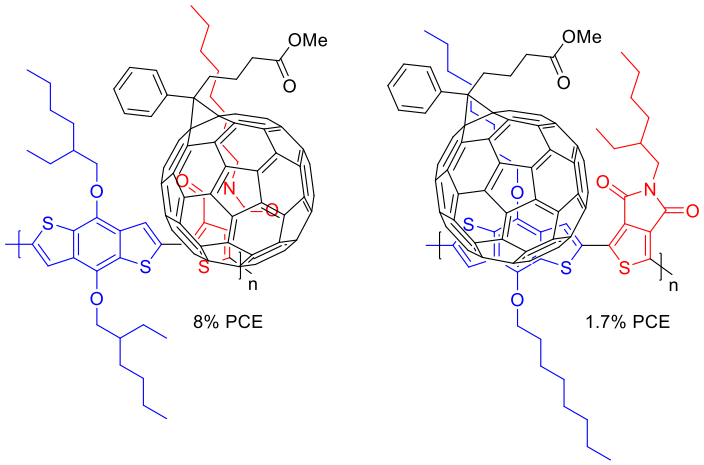

Figure 42 - LUMO-acceptor overlap and its impact on PCE. Donor and acceptor components highlighted in blue and red respectively.

In the above polymer, the LUMO is localised on the thienopyrrole (TPD) ring system. In the case of the example on the left, the branched alkyl chains on the benzodithiophene (BDT) ring force the PCBM to stack nearer the TPD unit and thus charge transfer is effective. On the other hand, when the TPD unit has the branched chains, PCBM stacks nearer the BDT unit and hence charge transfer is significantly less effective, resulting in a much lower PCE. In theory, if the

HOMO and LUMO are evenly delocalised across the molecule, then an effective donor-acceptor interface could be achieved at any point of the molecular backbone. This could prove critical for scale up processes as morphological control is difficult in large-area manufacture.[27, 120]

Single crystal X-ray diffraction was used to confirm the molecular geometry of these materials. Growing crystals of a suitable size and quality for these materials is challenging as they tend to crystallise quickly into very fine fibrous strands. It was however possible to grow suitable crystals of compounds **(2.7)**, **(2.10)**, **(2.11)** and **(2.15)**. It is reasonable to assume that the benzene ring is unlikely to affect torsional geometry or rigidity. As such, these four materials can be used to describe the BBT dyads, irrespective of the presence of the benzene ring.

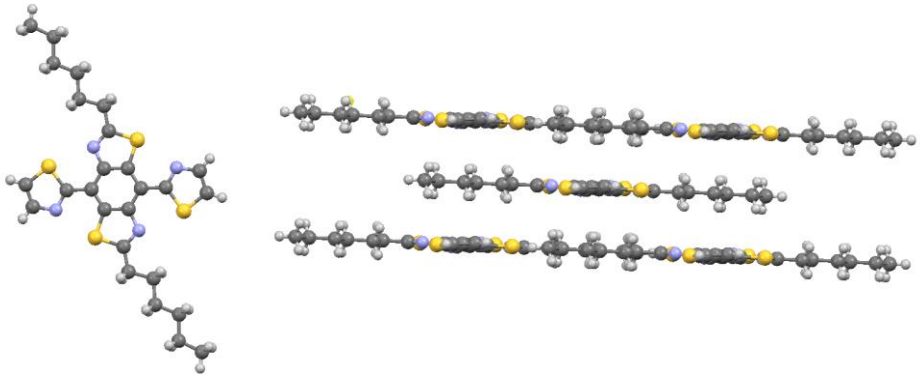

*Figure 43 - Crystal structure image of **(2.7)**. See Appendix 34 for full crystallographic details.*

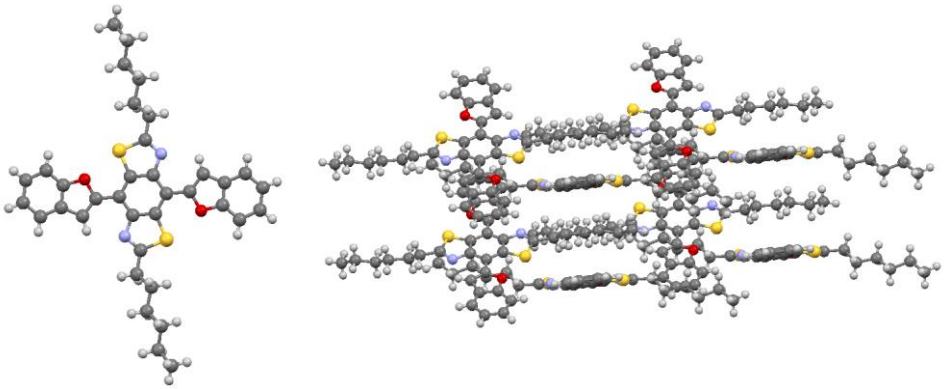

*Figure 44 - Crystal structure image of **(2.10)**. See Appendix 35 for full crystallographic details.*

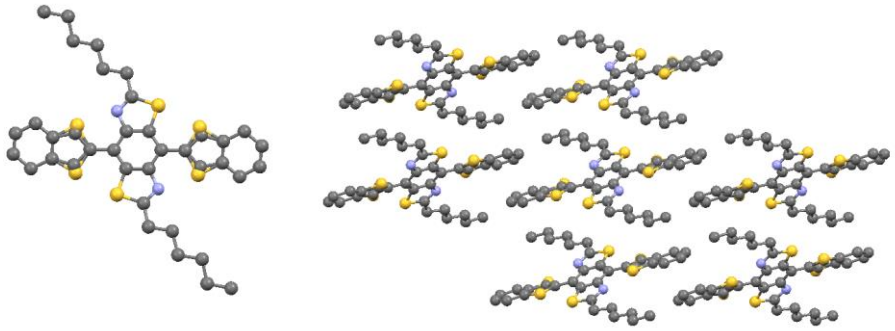

*Figure 45 - Crystal structure image of **(2.11)**. See Appendix 36 for full crystallographic details.*

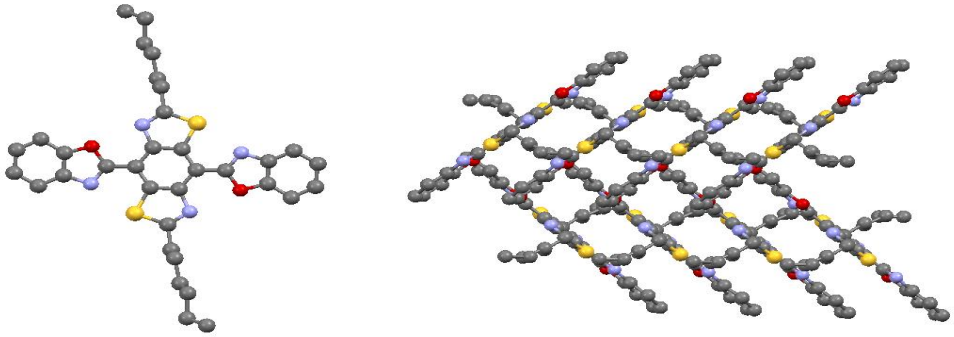

*Figure 46 - Crystal structure image of **(2.15)**. See Appendix 37 for full crystallographic details.*

The crystals structures confirm that compounds **(2.7)**, **(2.8)**, **(2.10)** **(2.13)** and **(2.15)** are highly planarised. Compound **(2.11)** displays a slight twist with a torsional angle of 18°, which is in good agreement with the torsional angle of 20° in the case of compound **(2.9)** reported by Kang and co-workers.[121] It is also worth noting that the disorder seen in the crystal structure of **(2.11)** suggests that the benzothiophene ring is free to rotate and that the energy barrier is small enough to allow rotation of up to 180°. This again is in agreement with the observed optical data.

Whilst the crystal structures show the molecular geometry of these materials, they do not provide information regarding the strength of the rigidity or the degree of delocalisation within these molecules. In order to do so, DFT calculations were performed on these molecules by Enrico Angioni (University of Strathclyde/Georgia Institute of Technology). To ensure the best method for calculating these parameters was selected, five functionals (B3LYP,[122] CAM-B3LYP,[123] M06-2X,[124] mPW1PW,[125] wB97xD[126]) and three basis sets (6-311G[127], 6-311G**, Ahlrichs pVDZ[128]) were tested for **(2.15)** and compared to the data obtained from its crystal structure. M06-2X/6-311G** yielded the results most in agreement with experimental and as such was selected for the ground state computations. All calculations unless otherwise stated were performed using Gaussian 09, revision D.01.[129] In order to simplify the calculations, the hexyl chains have been shortened to methyl chain groups.

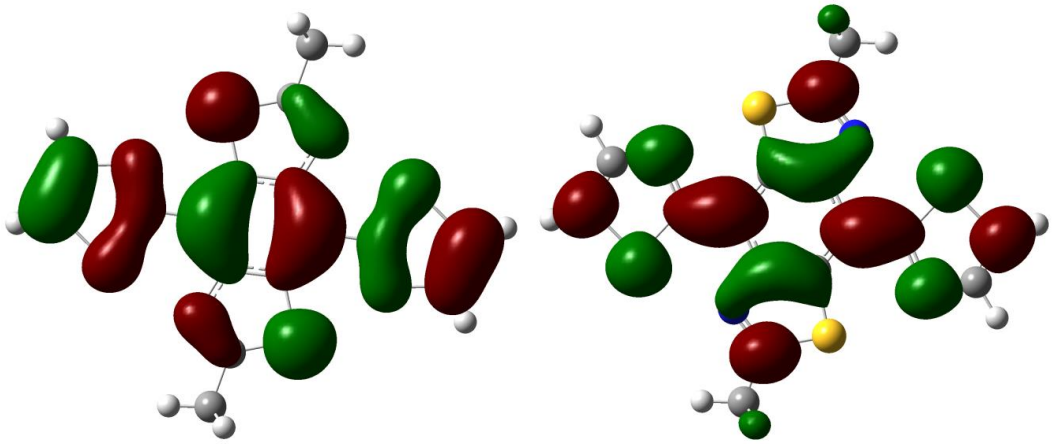

*Figure 47 - Kohn-Sham HOMO (left) and LUMO (right) graphical representation (isosurface 0.02) of **(2.7)** in the gas phase, calculated using M06-2X functional and 6-311G** basis set.*

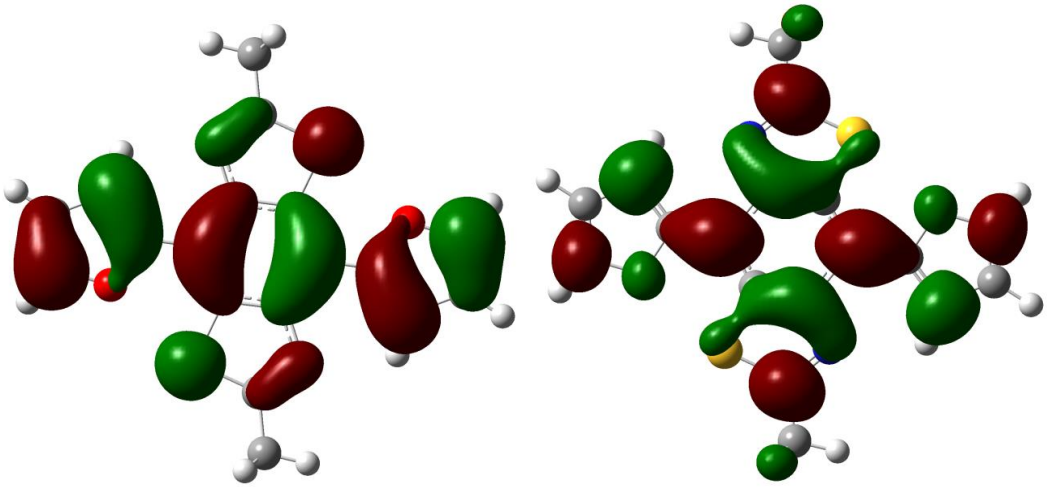

*Figure 48 - Kohn-Sham HOMO (left) and LUMO (right) graphical representation (isosurface 0.02) of **(2.8)** in the gas phase, calculated using M06-2X functional and 6-311G** basis set.*

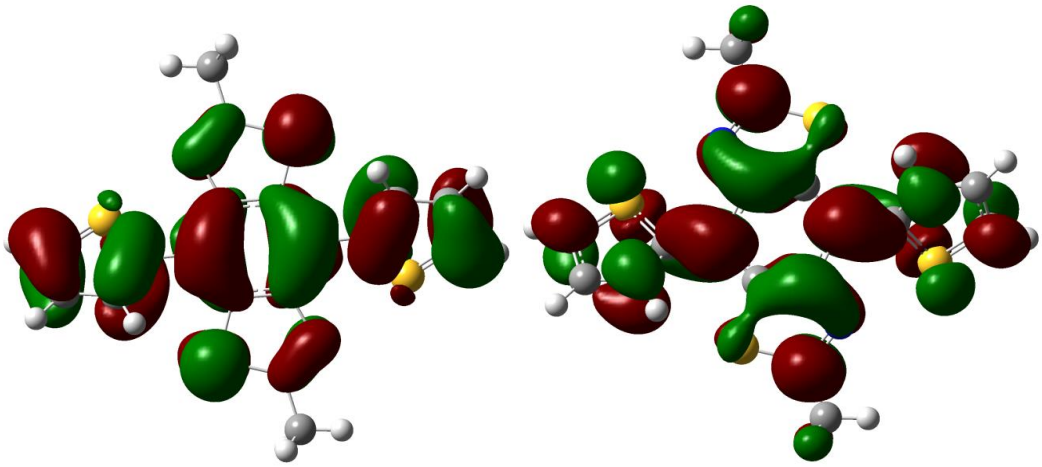

*Figure 49 - Kohn-Sham HOMO (left) and LUMO (right) graphical representation (isosurface 0.02) of **(2.9)** in the gas phase, calculated using M06-2X functional and 6-311G** basis set.*

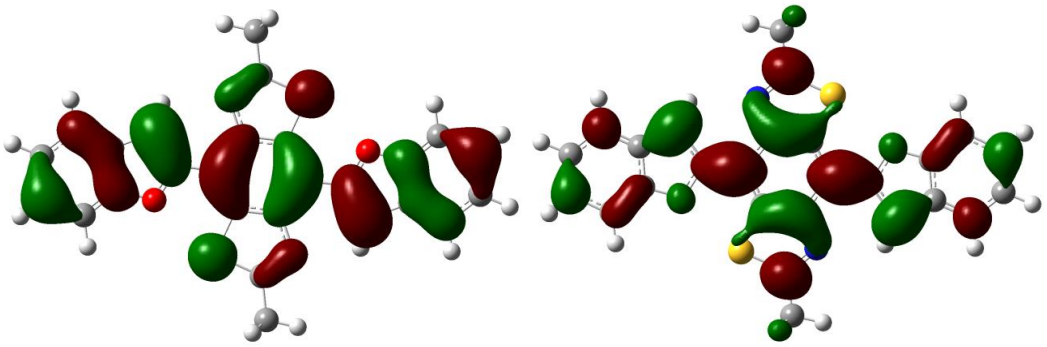

*Figure 50 - Kohn-Sham HOMO (left) and LUMO (right) graphical representation (isosurface 0.02) of **(2.10)** in the gas phase, calculated using M06-2X functional and 6-311G** basis set.*

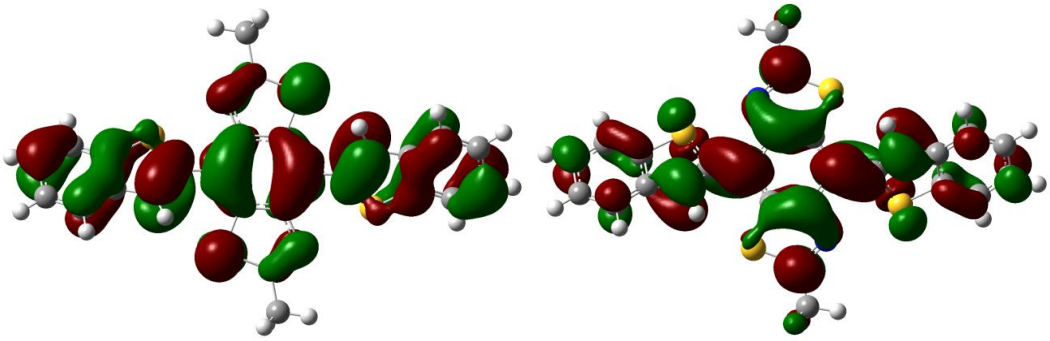

*Figure 51 - Kohn-Sham HOMO (left) and LUMO (right) graphical representation (isosurface 0.02) of **(2.11)** in the gas phase, calculated using M06-2X functional and 6-311G** basis set.*

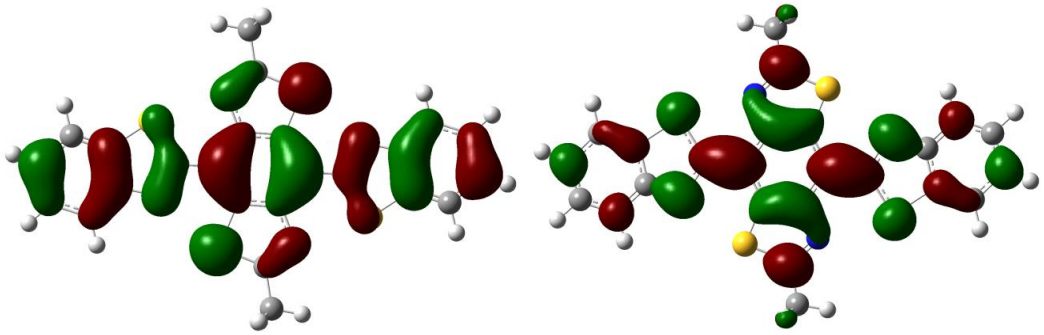

*Figure 52 - Kohn-Sham HOMO (left) and LUMO (right) graphical representation (isosurface 0.02) of **(2.13)** in the gas phase, calculated using M06-2X functional and 6-311G** basis set.*

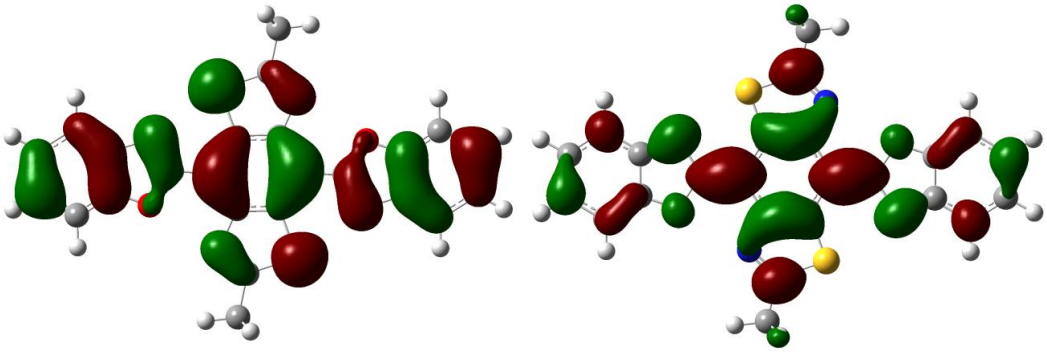

*Figure 53 - Kohn-Sham HOMO (left) and LUMO (right) graphical representation (isosurface 0.02) of **(2.15)** in the gas phase, calculated using M06-2X functional and 6-311G** basis set.*

The calculations are in agreement with the observed experimental data and show that in the ground state, only compounds **(2.9)** and **(2.11)** are non-planar. They also show that in each of

the molecules, the HOMO and LUMO are delocalised across the entire molecule with significant contributions from the BBT core as well as the peripheral heterocyclic units. Surprisingly, despite the torsional twist exhibited in **(2.9)** and **(2.11)**, they still exhibit the same highly delocalised nature as the planar materials. In the literature, materials with a twisted backbone, containing electron rich and poor units, tend to exhibit donor-acceptor behaviour. The lack of donor-acceptor charge transfer character may explain the relatively large band gap of these molecules.[130, 131]

In order to calculate the torsional potentials, shortened versions of the oligomers are used in which one of the heterocyclic substituents is replaced with a hydrogen atom and the hexyl chains are shortened to methyl. The dihedral angle between the BBT and the heterocycle is then fixed (from 0° to 180° at 10° intervals) and the geometry optimised on all remaining degrees of freedom at the M06-2X/6-311G** level of theory. These geometries are then used as inputs for RI-MP2[132]/cc-pVTZ[133] single-point energy calculations (QCHEM 4.1.2).[134] The results of this study can be seen below in Figure 54.

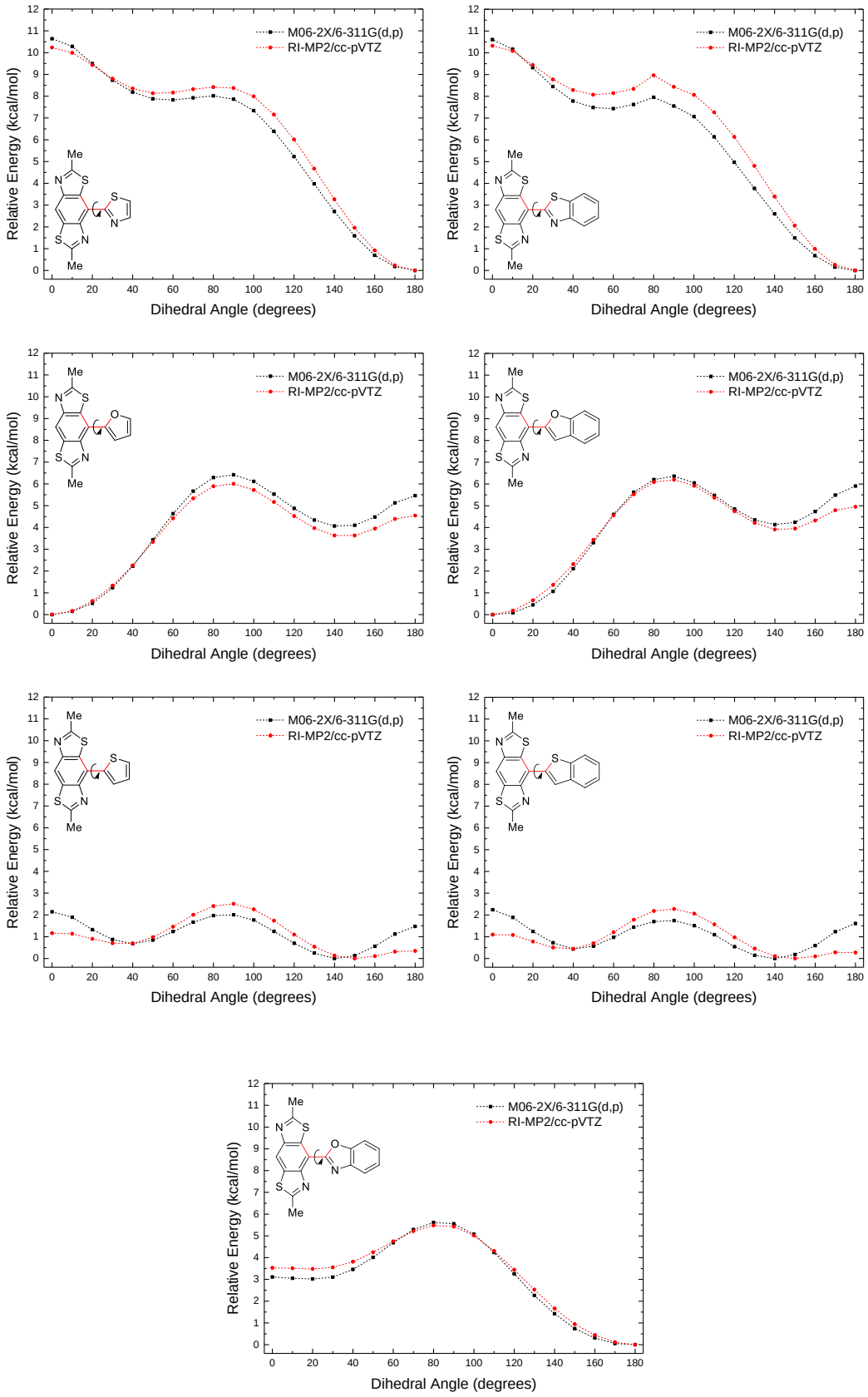

*Figure 54 - Torsional energy plots of BBT analogues. Compounds **(2.7)**, **(2.13)**, **(2.8)**, **(2.10)**, **(2.9)**, **(2.11)** and **(2.15)** from left to right in order.*

A summary of the barrier angle and energies can be seen below in Table 5 below.

Torsion	Analogue synthesised	Torsion barrier [a] (kcal/mol)	Torsion barrier [b] (kcal/mol)
BBT-Tz	**2.7**	10.64 (0°)	10.23 (0°)
BBT-F	**2.8**	6.42 (90°)	6.00 (90°)
BBT-T	**2.9**	2.14 (0°)	2.51 (0°)
BBT-BF	**2.10**	6.36 (90°)	6.20 (90°)
BBT-BT	**2.11**	2.24 (0°)	2.28 (90°)
BBT-BTz	**2.13**	10.61 (0°)	10.32 (0°)
BBT-BO	**2.15**	5.61 (80°)	5.47 (80°)

*Table 5 - Torsional energy barrier calculated for BBT analogues. Calculated at the [a]M06-2X/6-311G** and [b]RI-MP2/cc-pVTZ level of theory.*

These calculations support the observation that these materials – again, with the exception of **(2.9)** and **(2.11)** – are rigidly planar. The torsional energy barrier of 10.6 kcal/mol is very high for a non-bonding interaction and whilst not comparable to formal bonds, they are still highly significant. It is important to consider steric effects in these systems as most of the heteroatom contacts in these molecules are closer than the sum of the van der Waals radii. As a result of this, absolute interactions strength cannot be obtained. The interactions can instead be considered based on how favourable they are in comparison to each other.

These results can also confirm that non-covalent heteroatomic interactions (S-O and S-N) are present and have a significant effect on the geometry of the molecule. For example, if these interactions were unfavourable, then it would be fair to assume that **(2.15)** should have a similar (if not more) rigidly planar structure to that of **(2.13)** due to its reduced steric hindrance when comparing S-N to O-N contacts. This however is not the case, as **(2.13)** exhibits a significantly larger torsional barrier, suggesting that S-N interactions are favourable enough to overcome the steric hindrance. In **(2.7)** and **(2.13)**, there are two S-N contacts and no other possible interactions, leading to a torsional barrier of ~5.3 kcal/mol per S-N interaction.

Similar interactions are observed in each of the materials and where possible, S-O and S-N close contacts prevail. In **(2.8)** and **(2.10)** the S-O interactions are visible and the material is planar. Weak hydrogen bonding CH-N/CH-S should also be considered in these materials and is likely to play an important role in determining the energy barrier. Contrary to findings by Jackson and co-workers, in the case of **(2.9)** and **(2.11)**, CH-S interactions appear to be unfavourable in these systems, resulting in a low energy barrier of 2.2 kcal/mol.[45] In these systems it appears the strength of the S-N interaction is not sufficient to completely overcome the S-H steric hindrance.

From the torsional plot of **(2.15)**, the configuration with a S-N contact exhibits a binding energy ~3 kcal/mol stronger the S-O configuration, suggesting that S-N is more favourable. As the strength of S-O is estimated at being ~3 kcal/mol weaker than S-N, the data suggests that CH-N interactions possess a strength of ~4 kcal/mol. This value, which is ~1 kcal/mol weaker than an S-N contact, is in good agreement with the data obtained for **(2.9)** and **(2.11)**, where the configuration which favours the S-N contact, is ~1.1 kcal/mol more favourable than the configuration facilitating CH-N contacts.

Furthermore, the order of binding strength for the interactions can be assigned in the order as follows:

S-N > CH-N > S-O

As mentioned above, CH-S and S-S interactions appear unfavourable in these systems, perhaps due to steric hindrance. In this study there are no possible CH-O contacts and as a result, the strength of this interaction cannot be deduced. It is likely that CH-O hydrogen bonds would have a higher binding affinity than CH-S but a weaker affinity then CH-N, similar to traditional hydrogen bonds. It is also important to note, that the strength of interactions discussed here are specific to 4,8-BBT-heterocycle type molecules.

These interactions can be utilised to impart very specific properties into materials. For example, by varying the rigidity of a polymer backbone, it is possible to increase or decrease the conjugation length. This variation of conjugation length can be controlled to tailor the band-gap to the desired level. For low band-gap applications, incorporation of many S-N or CH-N contacts would impart excellent long-range order of the polymer backbone. Similarly, for applications in areas such as OLEDs, where a wider band-gap is desirable, by avoiding these favourable interactions, it is possible to reduce backbone rigidity and hence increase the band-gap.

When designing materials for application as Thermally Activated Delayed Fluorescence (TADF) emitters, it is beneficial to have the donor and acceptor components spacially separated, but to also maintain highly delocalised character within both the donor and acceptor arms.[135, 136] By utilising these interactions, this situation can be realised (Figure 55).

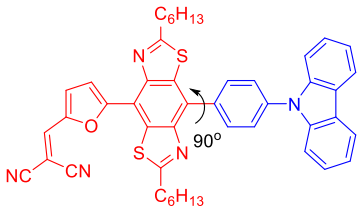

Figure 55 - Use of non-covalent interactions for proposed TADF emitter. Blue and red colours represent donor and acceptor components respectively.

With the generalised structure seen in Figure 55, the donor and acceptor units could be altered to afford the desired band-gap, energy levels and emission colour without compromising on the twisted configuration of the molecule. Furthermore, utilisation of various heterocyclic ring systems can facilitate alteration of the donating and accepting strength of these materials, and ultimately, fine-tuning of their electronic properties.

Investigation of these materials as active layer components in OFET devices was attempted by solution and vacuum deposition methods. In both cases, non-uniform films were obtained due to excessive crystallisation of the materials. As a result of the poor active layer morphology, these materials did not yield working devices. In order to inhibit over-crystallisation, incorporation of these moieties into polymeric systems was proposed and is discussed in Chapter 3.

2.4 Conclusions and future work

A novel synthetic protocol for the synthesis of 2,6-dialkyl-4,8-dibromobenzobisthiazole has been developed. The synthesis of this interesting core material has been achieved in moderate yield and has shown to be easily scaled to multigram synthesis.

Seven BBT containing small molecule dyads have been synthesised from this core material and their physical properties fully characterised by UV-visible absorption and emission spectroscopy, cyclic voltammetry, single crystal X-ray crystallography and DFT calculations.

The effect of non-covalent heteroatomic interactions on molecular geometry and orbital overlap has been investigated. These materials exhibit exceptional delocalisation of the HOMO and LUMO levels and, as a result, the absolute HOMO and LUMO energies, have been altered by over 1 eV, whilst maintaining a constant band-gap relative to molecular conjugation length. Furthermore, by switching a single atom within the peripheral heterocyclic rings, it is possible to achieve electron rich or electron poor materials from this versatile core. This degree of fine-tuning is expected to have significant implications in the design of custom materials that require specific orbital energies such as in OPV donor materials.

Growing crystals of compounds **(2.8)** and **(2.13)** of a suitable size for single crystal X-ray diffraction was unsuccessful when attempted *via* solution thermal crystallisation, slow evaporation, thermal sublimation and solvent diffusion techniques. It may be possible to sublime these with a very strong vacuum, but efforts thus far have proven unsuccessful.

It would also be of interest to synthesise similar materials in which the BBT core is substituted for a benzobisoxazole (Figure 56).

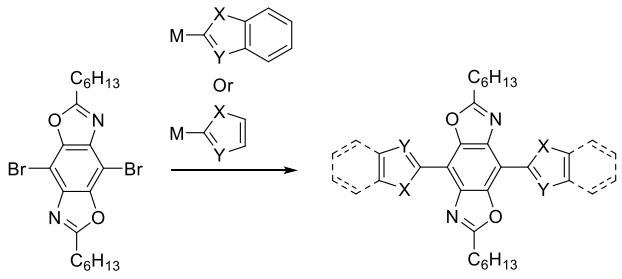

(2.17)

Figure 56 - Proposed BBO small molecule.

The dibrominated core **(2.17)** has been previously published by Tlach and co-workers and thus these materials could be synthesised by cross-coupling procedures analogous to the BBT derivatives.[137] These new materials could provide further support to the findings in this research and help to develop further understanding of non-covalent heteroatomic interactions.

3 Highly planarised 4,8-benzobisthiazole-containing conjugated polymers for organic field-effect transistors

3.1 Introduction

In previous work (see Chapter 2), rigidly planar and highly delocalised BBT-containing small molecules were synthesised and used to investigate intramolecular heteroatomic interactions. From this, it was concluded that, due to the extensive delocalisation and increased molecular planarity, macromolecular materials based on this design principle would exhibit promising charge transport properties.

Firstly, increased molecular planarity should allow for closer bulk packing as a direct result of reduced intermolecular steric hindrance in the thin film (Figure 57).

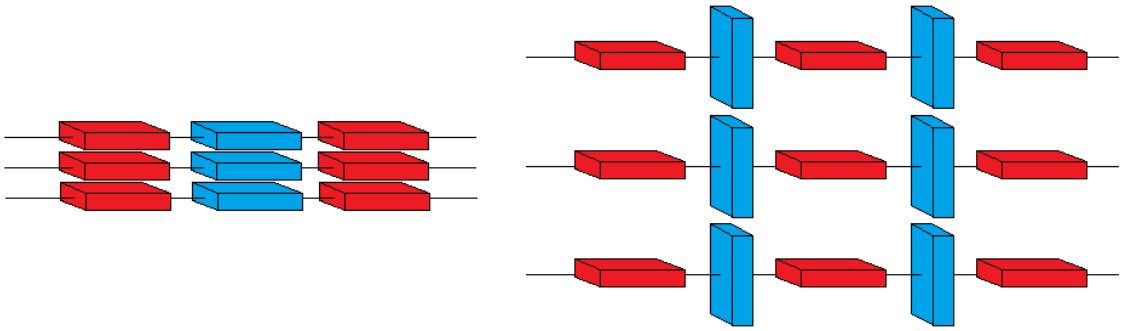

Figure 57 – Representation of tighter bulk packing in planar materials

Tighter packing in the solid state is known to increase efficiency of charge transport. This is due to a combination of increased bulk π orbital overlap and reduced grain boundaries.[72] Furthermore, the BBT polymers synthesised in this work exhibit highly delocalised molecular orbitals and, as a result, intramolecular charge transport is likely to be very efficient along each polymer chain.[138]

In order to correlate structural rigidity with OFET device performance, a series of four polymers were synthesised, with the degree of planarity altered between each material. The materials range from highly rigid and planar in the case of **p(BTzBBT)** to the least rigidly planar in the case of **p(DPP2ThBBT)**. The polymers have been characterised using UV-vis absorption, CV, GPC, AFM and as the active layer in OFETs and OPVs.

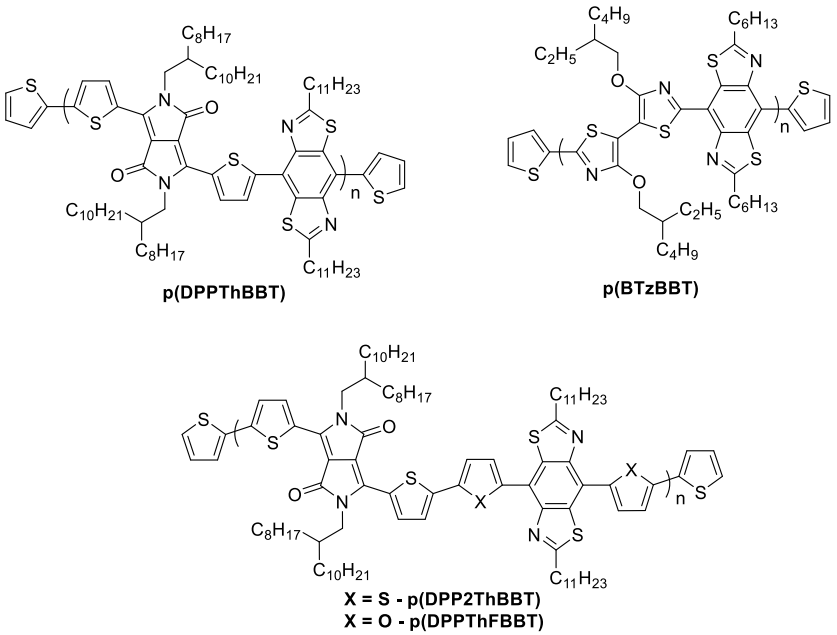

Figure 58 - BBT copolymers synthesised for OFET applications

Bisthienyl-diketopyrrolopyrrole (DPP) and 4,4'-dialkoxybithiazole (BTz) were selected as suitable co-monomer units as these have shown promise in OFET applications[40, 41] and the synthesis of these co-monomers could be adapted in order to modify the torsional geometry of the polymer backbone. DPP has gained significant attention in recent years, with very high efficiency OFETs and OPVs.[40] It is attractive due to its low band-gap, low lying LUMO level, high solubility when substituted with branched alkyl chains, strong aggregation in the solid state and its ambipolar transport characteristics.[16, 33, 40] It is also known to exhibit long-range order and extended delocalisation of the HOMO and LUMO.[9]

In 2010, Li and co-workers reported a DPP-thienothiophene copolymer (PDBT-co-TT) that exhibited a p-type field-effect mobility of 0.94 $cm^2V^{-1}s^{-1}$ in OFET devices (Figure 59).[33] The excellent mobility is attributed to the strong π-stacking interactions of the DPP core in the solid state.

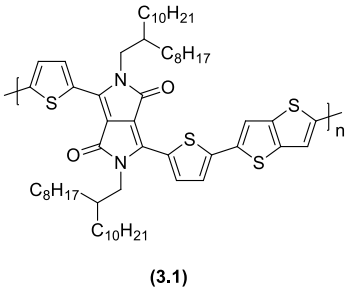

*Figure 59 - PDBT-co-TT **(3.1)***

In 2014, Marks and co-workers reported two dicyanovinyl substituted DPP small molecules (Figure 60) that exhibit balanced, high mobility ambipolarity in OFET devices. The materials yield slightly enhanced n-type performance (up to 0.16 $cm^2V^{-1}s^{-1}$) compared to p-type (up to 0.02 $cm^2V^{-1}s^{-1}$) due to the addition of the strongly electron withdrawing dicyanovinyl groups.[139]

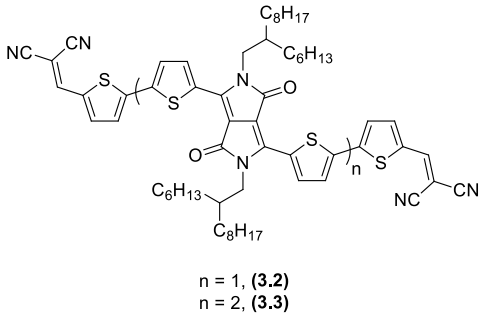

*Figure 60 - Dicyanovinyl DPP derivatives **(3.2)** and **(3.3)***

Recently, the Skabara group incorporated tetrathiafulvalene into a DPP copolymer (Figure 61) **(3.4)** and the material displayed excellent device stability in ambient conditions, with negligible loss of performance over a period of 15 days. Furthermore, the material exhibited this performance despite having a non-optimal morphology of the active layer, which resulted in grain boundaries visible by AFM spectroscopy.[68]

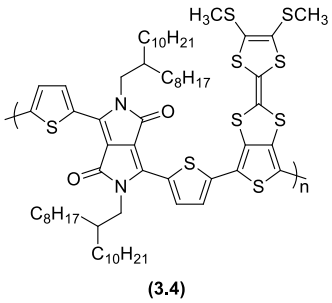

*Figure 61 - p(DPP-TTF) **(3.4)***

In 2013, Facchetti and co-workers reported the OFET properties of four BTz polymers (Figure 62). These polymers all possess low band-gaps as a direct result of the highly planarised polymer backbone. The polymers exhibit reasonable solubility in common organic solvents as well as high mobilities (up to 0.025 $cm^2V^{-1}s^{-1}$), ambient stability for over 6 weeks and substantial I_{on}/I_{off} ratios (10^5).[41]

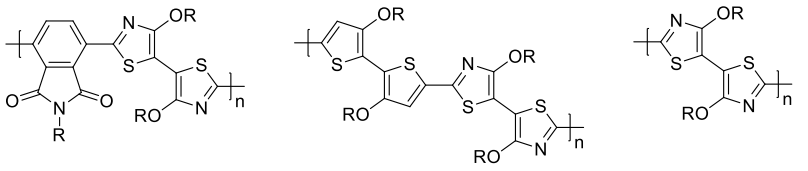

(3.5), R = n-dodecyl
(3.6), R = 2-ethylhexyl

(3.7), R = n-dodecyl

(3.8), R = n-dodecyl

*Figure 62 - BTz containing polymers **(3.5-8)***

To date, these materials are the only examples present in the literature which feature the 4,4'-dialkoxybithiazole (BTz) moiety.

3.2 Synthesis

Synthesis of the BTz building block was conducted *via* modification of the literature procedure starting from the commercially available material, 2,4-thiazolidinedione **(3.9)** as shown below (Scheme 15).[41]

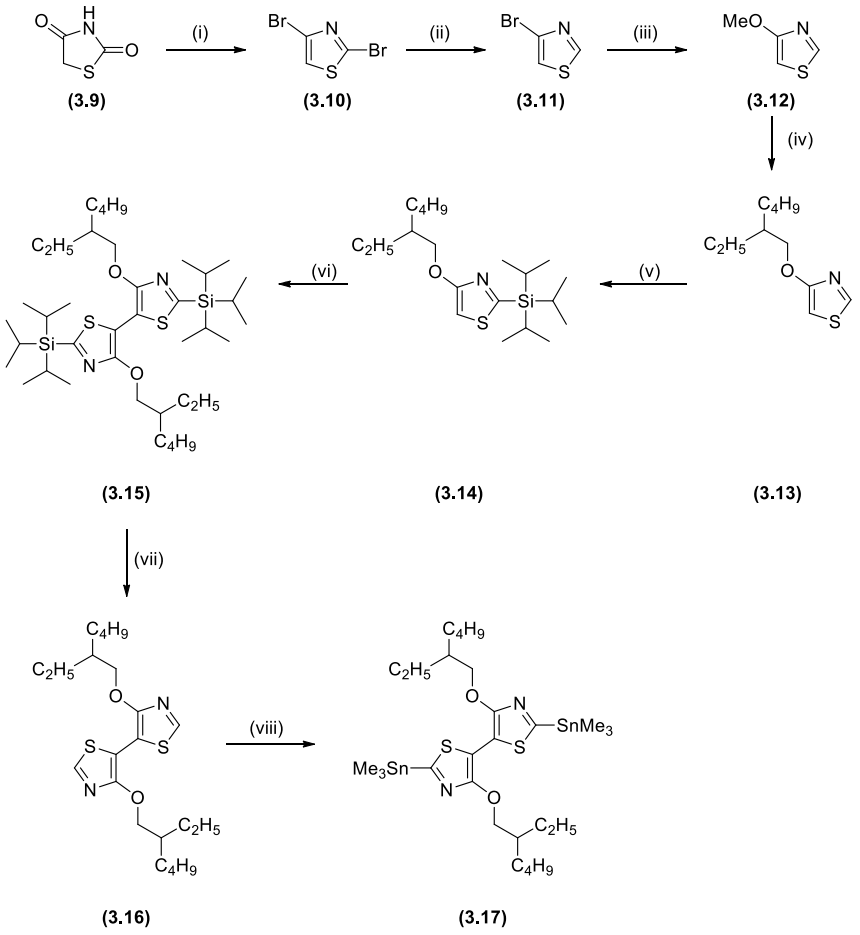

*Scheme 15 - Synthesis of BTz distannane **(3.17)**. Reagents and conditions: (i) P_2O_5, nBu_4NBr, PhMe, reflux 20 h (80%); (ii) nBuLi, Et_2O, -78 °C 30 min then MeOH -78 °C to rt (96%); (iii) NaOMe, reflux 24 h (70%); (iv) 2-ethylhexanol, TsOH (cat.), PhMe, reflux 24 h (71%); (v) nBuLi, THF, -78 °C 2 h then TIPSCl -78 °C to rt (89%); (vi) nBuLi, THF, -78 °C to rt 1 h then $Fe(acac)_3$, 0 °C to reflux 2 h (88%); (vii) TBAF, THF, 0 °C to rt 1.5 h (59%); (vii) nBuLi, THF, -78 °C to rt 30 min then $SnMe_3Cl$, 0 °C to 60 °C 1 h (98%).*

In the original procedure, 2,4-thiazolidinedione **(3.9)** was converted to 2,4-dichlorothiazole in 53% yield *via* treatment with phosphorus oxychloride at reflux. 2,4-Dichlorothiazole was then subjected to dehalogenative reduction with zinc metal in acetic acid to afford 4-chlorothiazole in 73% yield. Due to the modest yields, hazardous nature of phosphorus oxychloride and the advantage of a bromide leaving group for step (iii), synthesis of **(3.13)** *via* 2,4-dibromothiazole **(3.10)** was selected as an alternative route.

2,4-Dibromothiazole **(3.10)** was synthesised in high yield *via* the procedure reported by Grubb and co-workers which utilised nBu$_4$NBr as the halogen source in the presence of P_2O_5.[140] Lithium-halogen exchange of **(3.10)** using *n*BuLi, followed by quenching of the lithium salt with methanol, provided 4-bromothiazole **(3.11)** in near-quantitative yield. 4-Methoxythiazole **(3.12)** was obtained in 70% yield after nucleophilic aromatic substitution with sodium methoxide. Transetherification with 2-ethylhexan-1-ol and catalytic *p*-toluenesulfonic acid, afforded **(3.13)** in moderate yield after purification. As the 2-position is the most acidic, in order to achieve the 5-lithiated species, the 2-position was triisopropylsilyl protected, prior to deprotonation with *n*BuLi, followed by addition of chlorotriisopropylsilane, providing **(3.14)** in excellent yield. Further treatment with *n*BuLi, followed by Fe(acac)$_3$ mediated coupling yielded bisthiazole compound **(3.15)** in very high yield. Silyl deprotection was achieved by treatment with nBu$_4$NF to yield the BTz unit **(3.16)** in modest yield after purification. Finally, lithiation *via* *n*BuLi, followed by quenching with trimethyltin chloride afforded the distannyl BTz monomer **(3.17)** quantitatively. Synthesis of **(3.17)** was obtained in 17% overall yield over 8 steps.

Ths BTz monomer was then copolymerised with the previously synthesised 4,8-dibromo-2,6-dihexyl BBT **(2.4)** *via* microwave-assisted Stille polymerisation (Scheme 16). The resulting dark blue mixture was purified *via* Soxhlet extraction with methanol, hexane, acetone and chloroform, and then collected in chlorobenzene and precipitated into acetone to yield **p(BTzBBT)** as a dark blue solid which has limited solubility in common organic solvents. The polymer is insoluble in chloroform, exhibits limited solubility in hot chlorobenzene and moderate solubility in hot *o*-dichlorobenzene.

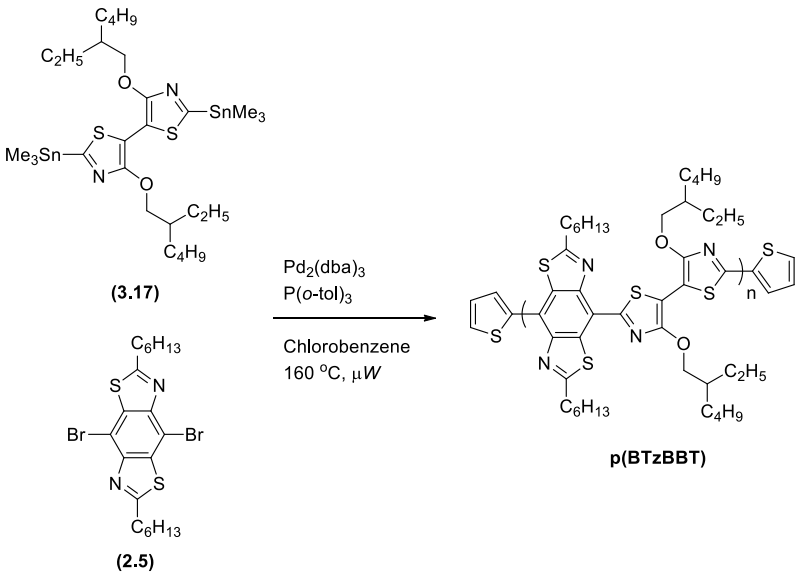

*Scheme 16 - Synthesis of **p(BTzBBT)***

Synthesis of the DPP boronate ester unit **(3.20)** was conducted starting from 3,6-di(thiophen-2-yl)pyrrolo[3,4-c]pyrrole-1,4(2H,5H)-dione **(3.18)**, which was kindly provided by Dr Diego Cortizo-Lacalle (Scheme 17).

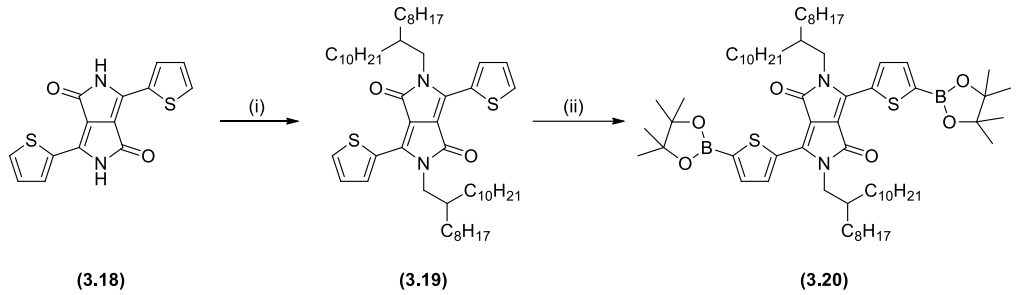

Scheme 17 - Reagents and conditions: (i) K_2CO_3, DMF, 120 °C 1 h then 9-(bromomethyl)nonadecane, 130 °C overnight (43%); (ii) 2-isopropoxy-4,4,5,5-tetramethyl-1,3,2-dioxaborolane, LDA, THF, -25 °C 1 h (68%).

Alkylation of the **(3.18)** unit yielded a mixture of products, which were purified *via* silica gel column chromatography to afford the dialkylated derivative **(3.19)**. Compound **(3.19)** was subjected to anion trapping by treatment with lithium diisopropylamide in the presence of 2-isopropoxy-4,4,5,5-tetramethyl-1,3,2-dioxaborolane, affording **(3.20)** in 68% yield after precipitation, of a purity suitable for polymerisation.

As **p(BTzBBT)** showed very poor solubility in common organic solvents, a BBT derivative incorporating undecyl alkyl chains **(3.22)** was synthesised following the procedure developed previously for the dihexyl derivative (Scheme 18).

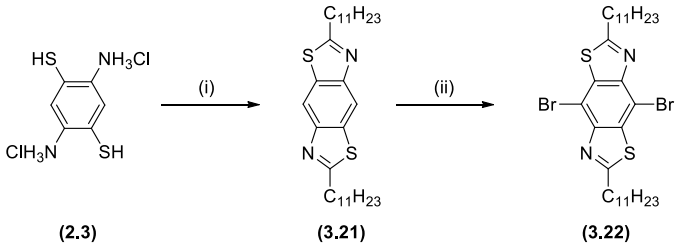

Scheme 18 - Reagents and conditions: (i) $C_{11}H_{23}COCl$, PPSE, o-DCB, reflux 24h (67% over two steps); (ii) Br_2, $CHCl_3$, rt overnight (9%).

PPSE assisted condensation of freshly prepared **(2.3)** proceeded in moderate yield to afford compound **(3.21)**. Unexpectedly, after precipitation compound **(3.21)** exhibited microcrystallinity and has poorer solubility in chlorinated solvents than the hexyl variant **(2.5)**. Unfortunately, due to the poor solubility of this material in dichloromethane, chloroform was selected as the solvent for the bromination step and the temperature adjusted to room temperature. Treatment of **(3.21)** with elemental bromine in $CHCl_3$ provided compound **(3.22)**

in 9% yield as well as residual starting material **(3.21)** in 53% yield after purification *via* silica gel chromatography.

Dibromo BBT monomer **(3.22)** was then subjected to Suzuki polymerisation with **(3.20)** to yield **p(DPPThBBT)** as shown below in Scheme 19.

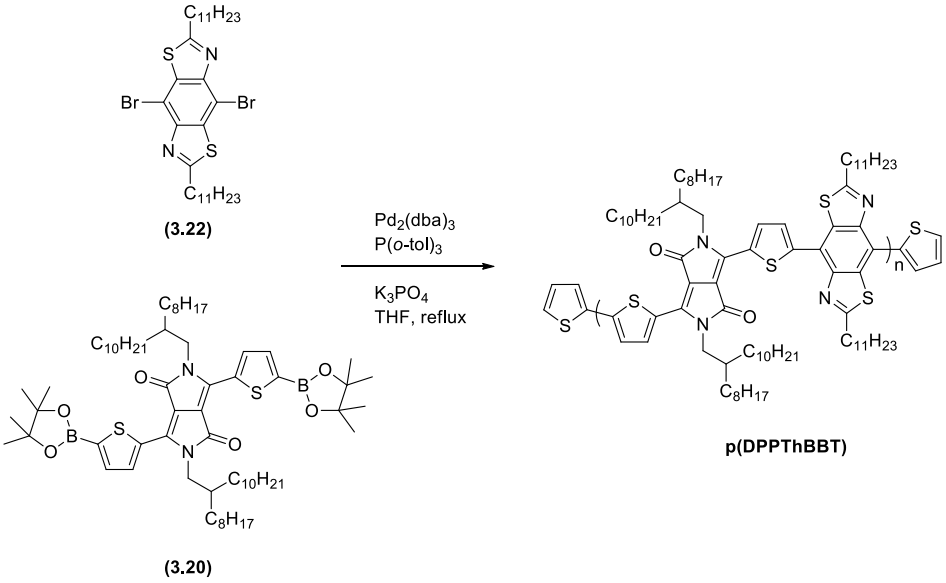

*Scheme 19 - Synthesis of **p(DPPThBBT)***

The polymer was purified *via* successive Soxhlet extractions with methanol, acetone and hexane, before collection of the polymer in chloroform and precipitation into acetone to yield a dark green-black sticky solid which displays excellent solubility in $CHCl_3$, toluene, chlorobenzene and dichlorobenzene.

In order to synthesise **p(DPP2ThBBT)** and **p(DPPThFBBT)** *via* random stille polymerisation, the dibromo DPP monomer unit **(3.23)**, was first synthesised by treatment of **(3.19)** with elemental bromine, to afford (**3.23)** in excellent yield. 2,5-Bistrimethylstannyl thiophene **(3.26)** and 2,5-bistrimethylstannyl furan **(3.27)** were synthesised *via* lithiation with *n*BuLi [*sec*-BuLi for **(3.27)**] and TMEDA, followed by anion quenching with trimethyltin chloride in moderate to high yields (Scheme 20).

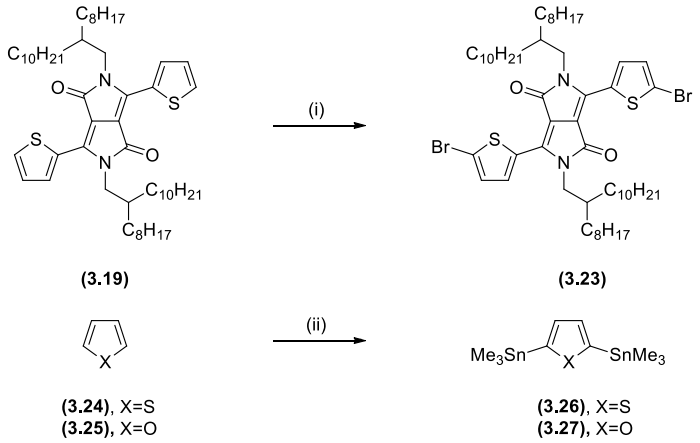

Scheme 20 - Reagents and conditions: (i) Br_2, $CHCl_3$, rt overnight (90%); (ii) ***(3.26)*** *nBuLi, TMEDA, hexane, rt to reflux 1 h then $SnMe_3Cl$, 0 °C to rt overnight (79%);* ***(3.27)*** *sBuLi, TMEDA, hexane, 0 °C to rt 4 h then $SnMe_3Cl$, 0 °C to rt overnight (69%).*

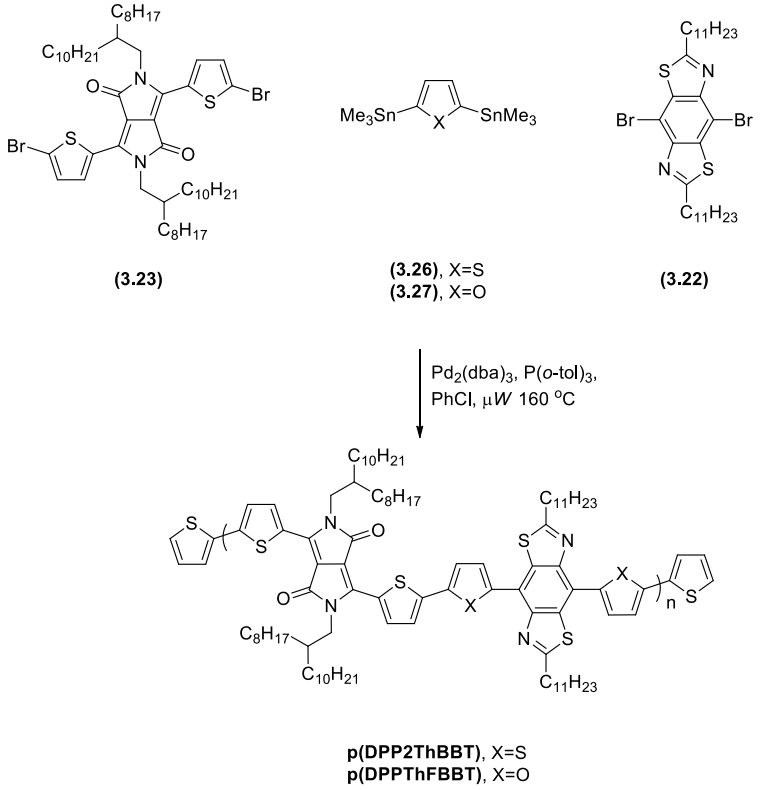

Scheme 21 - Synthesis of p(DPP2ThDPP) and ***p(DPPThFBBT)***

Polymers **p(DPP2ThBBT)** and **p(DPPThFBBT)** were then synthesised *via* microwave-assisted random Stille polymerisation in chlorobenzene using a 1:1:2 ratio of **(3.22)**:**(3.23)**:**(3.26/3.27)** in the presence of catalytic $Pd_2(dba)_3$ and P(*o*-tol)$_3$ as in Scheme 21 above. Both polymers were purified *via* Soxhlet extraction with methanol, acetone and hexane, before collection of the polymers in chloroform and precipitation into acetone to afford dark green-black solids. These polymers exhibit moderate solubility in $CHCl_3$ and toluene, and excellent solubility in chlorobenzene and dichlorobenzene.

3.3 Results and discussion

The absorption spectra of the synthesised polymers were characterised as a solution in dichlorobenzene and as a thin film for comparison.

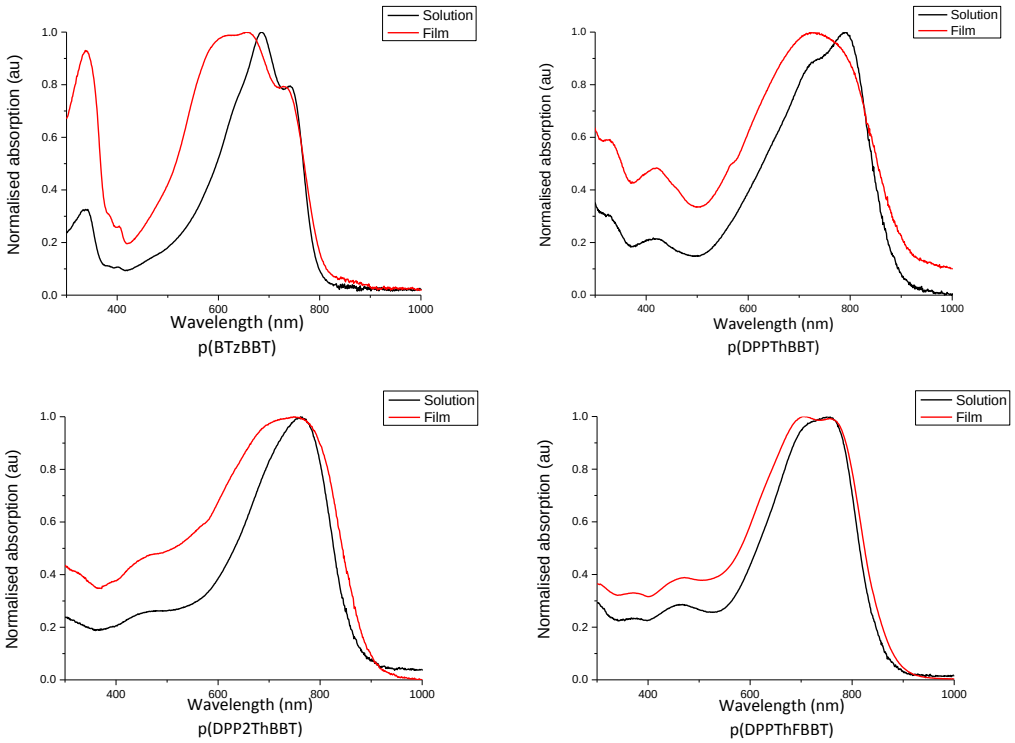

Figure 63 - Absorption spectra of synthesised BBT containing copolymers

From the absorption spectra it is clear that these polymers are very narrow band gap materials with optical band gaps ranging from 1.36 to 1.52 eV. It is also very clear that there is negligible difference between the energetics of the polymers in the solution state and in the thin film. This is not a common phenomenon in conjugated polymers. In most cases, intermolecular interactions are facilitated more substantially in the thin film, compared to the solution state, resulting in a red shift in the absorption spectra.[46, 70, 141, 142] As the absorption spectra for these polymers are so similar in either medium, this would suggest that these materials possess a rigid, aggregated structure, even in solution.

Also as expected, the polymers exhibit some vibronic structure in the absorption spectrum which is indicative of the structural rigidity. Compared to the monodisperse small molecules (Chapter 2), the polymers exhibit less well-defined vibronic structure and this can be attributed to the inherent disorder of polymeric systems, which arise from issues such as chain entanglement and backbone curvature.[25] However, when compared to many polymers described as crystalline in the literature, these polymers exhibit highly defined absorption peaks.[143-145]

The polymers were then studied *via* cyclic voltammetry in order to determine their electrochemical HOMO and LUMO energy levels, then by GPC to determine the molecular weight and polydispersity. A summary of the polymer properties is given below in Table 6.

Polymer	M_w (kg mol^{-1})[a]	PDI	Optical E_g (eV)[b]	Electrochemical E_g (eV)[c]	HOMO (eV)[c]	LUMO (eV)[c]
p(BTzBBT)	N/A	N/A	1.52	1.69[α]	-4.69	-3.00
p(DPPThBBT)	14.4	1.70	1.36	1.39[β]	-4.90	-3.51
p(DPP2ThBBT)	96.0	2.75	1.40	1.43[γ]	-5.10	-3.67
p(DPPThFBBT)	18.0	2.04	1.41	1.26[δ]	-4.86	-3.60

*Table 6 - BBT copolymer properties. [a]Calculated from GPC using 0.5 mgml^{-1} solutions in chlorobenzene at 80 °C. GPC data not obtained for **p(BTzBBT)** due to incomplete polymer solubility in chlorobenzene. [b]Calculated from the onset of the longest wavelength absorption peak. [c]Found from CV, using the onset of redox activity and referenced to Fc/Fc$^+$ (-4.8 eV). [α]Appendix 18. [β]Appendix 19. [γ]Appendix 21. [δ]Appendix 23.*

Unfortunately due to the very poor solubility of **p(BTzBBT)**, GPC analysis could not be performed. The remaining three polymers show moderate to high molecular weight and relatively low polydispersity for conjugated polymers. It is possible that they polymerise until reaching the solubility threshold in such a concentrated solution, at which point the polymer chain precipitates and the reaction is inhibited. This is supported by visual observations. In each case, the polymers precipitate at the end of the reaction and do not redissolve, even at very elevated temperature.

This theory can also explain the difference in molecular weight between **p(DPP2ThBBT)** and **p(DPPThFBBT)**. For a similar molecular weight it would be reasonable to assume very similar solubility of these two polymers. However, this is not the case, as both polymers display very similar solubility, despite **p(DPP2ThBBT)** having a molecular weight over five times larger than **p(DPPThFBBT)** and material solubility exhibiting inverse proportionality to molecular weight.[29] The reduced solubility of **p(DPPThFBBT)** is attributed to the reduced rotational freedom as a result of the intramolecular S-O and CH-N interactions discussed in Chapter 2.

It is highly likely that the polymerisation of **p(DPPThBBT)** was not limited by polymer solubility but instead limited by non-optimal reaction conditions required to make it. DPP has a well-documented base sensitive nature. For this reason, a weak base was selected to prevent decomposition, and this may have led to inefficient polymerisation. This is again further supported by the excellent solubility of this polymer, compared to the other two DPP containing polymers.

Increased planarity has previously been linked to increased semiconductor mobility.[42, 72, 146] As such, **p(BTzBBT)** was expected to exhibit the best transistor behaviour, followed by **p(DPPThFBBT)**, **p(DPP2ThBBT)** and **p(DPPThFBBT)** respectively. In order to support this theory, bottom-gate, bottom-contact field effect transistors (BGBC FETs) were fabricated and tested in dry-glovebox conditions under N_2 atmosphere (see chapter 5 – General experimental for detailed fabrication).

In order to determine the ideal processing conditions, the device fabrication procedure was optimised using **p(DPP2ThBBT)**. To facilitate accurate assessment of the intrinsic semiconducting properties of the material, additional processing steps, such as self-assembled monolayers (SAMs) or processing additives were avoided. These processing parameters can have major impact on factors such as charge injection, surface wettability and morphology of the organic semiconductor.[33, 147, 148] Once suitable processing conditions had been determined, each of the polymers were fabricated and tested identically.

Field-effect transistors were fabricated on untreated SiO_2, and the processing conditions varied, to determine the optimal solvent and temperature. In order to avoid issues with device variation, one chip (16 devices per chip) was fabricated from each solvent. Devices were then tested "as-cast" before annealing to 60, 100, 150 and 200 °C respectively, with the same devices tested at each temperature increment. The solvents tested were chloroform (CF), chlorobenzene (CB) and *o*-dichlorobenzene (DCB). 10 mg ml^{-1} solutions were stirred at 50 °C before cast at 2000 rpm (whilst hot) onto commercially available substrates and the films dried under high vacuum before testing. Annealing of the active layer was achieved by heating on a hot-plate under N_2. The output and transfer characteristics for each device are shown below.

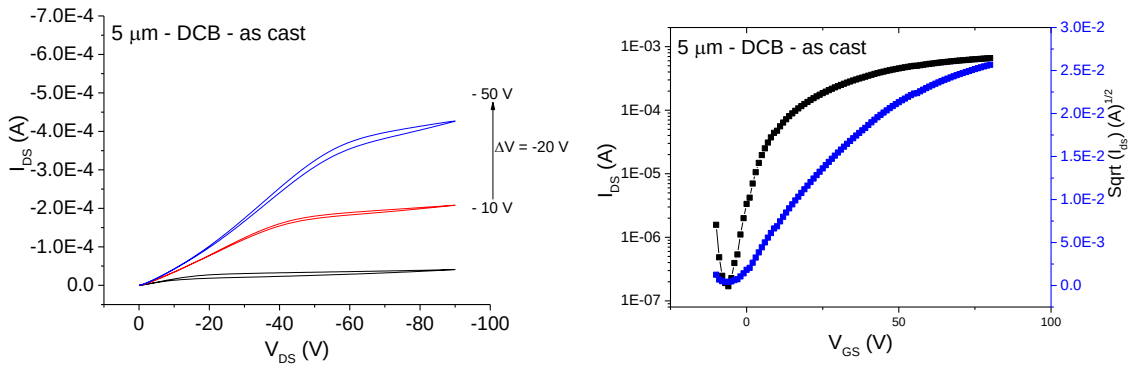

Figure 64 - Output (left) and Transfer (right) characteristics (5 μm/DCB/as cast).

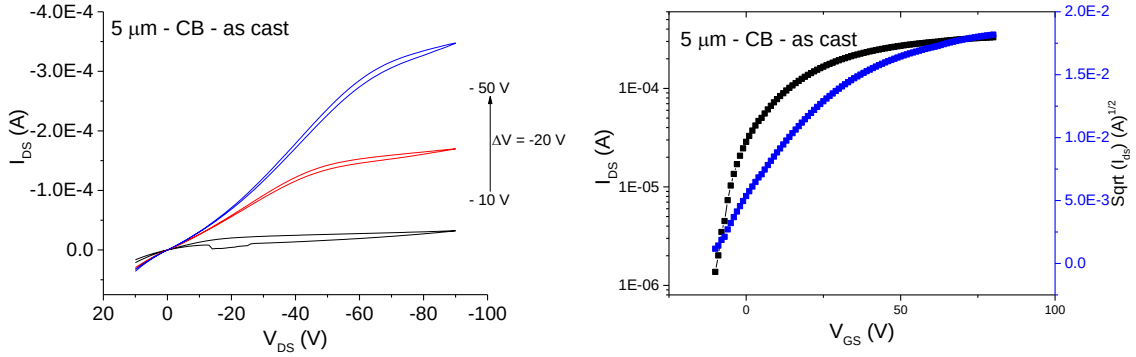

Figure 65 - Output (left) and Transfer (right) characteristics (5µm/CB/as cast).

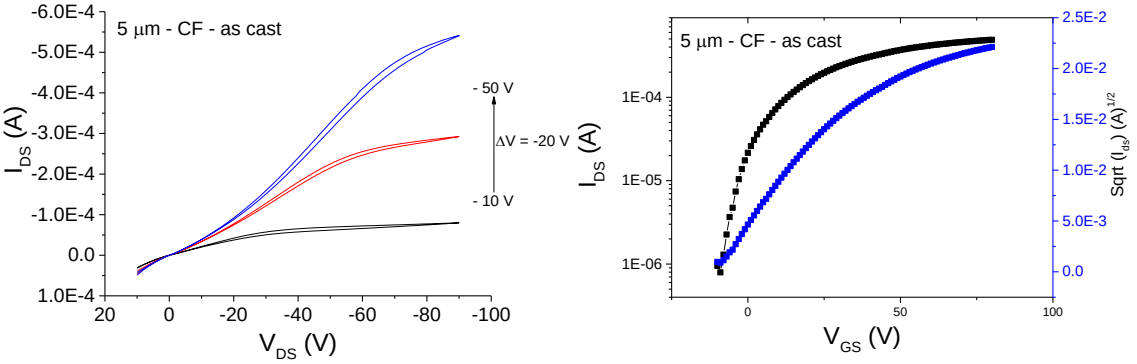

Figure 66 - Output (left) and Transfer (right) characteristics (5µm/CF/as cast).

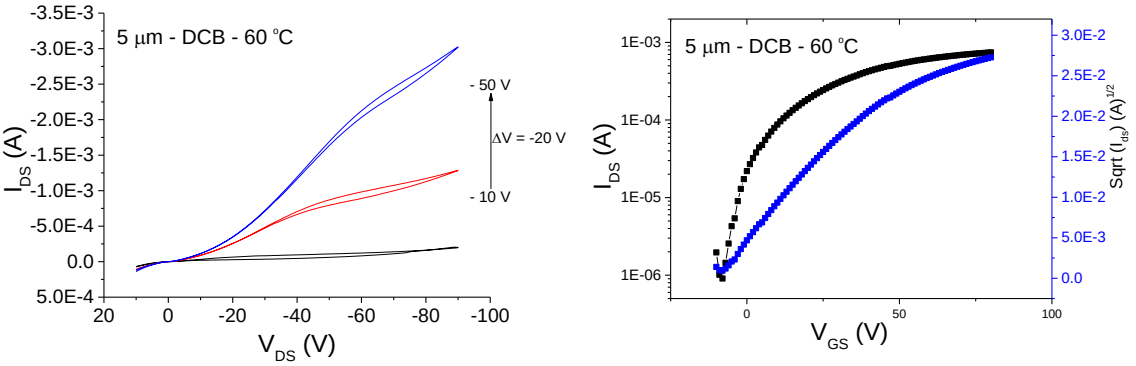

Figure 67 - Output (left) and Transfer (right) characteristics (5µm/DCB/60 °C).

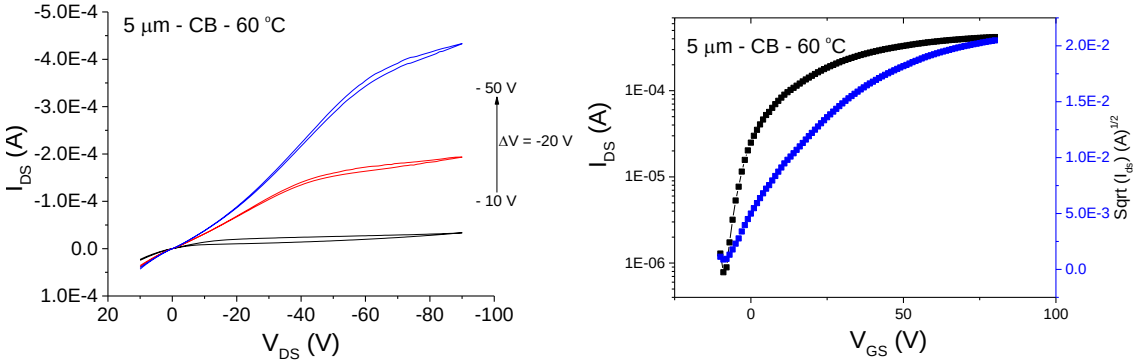

Figure 68 - Output (left) and Transfer (right) characteristics (5µm/CB/60 °C).

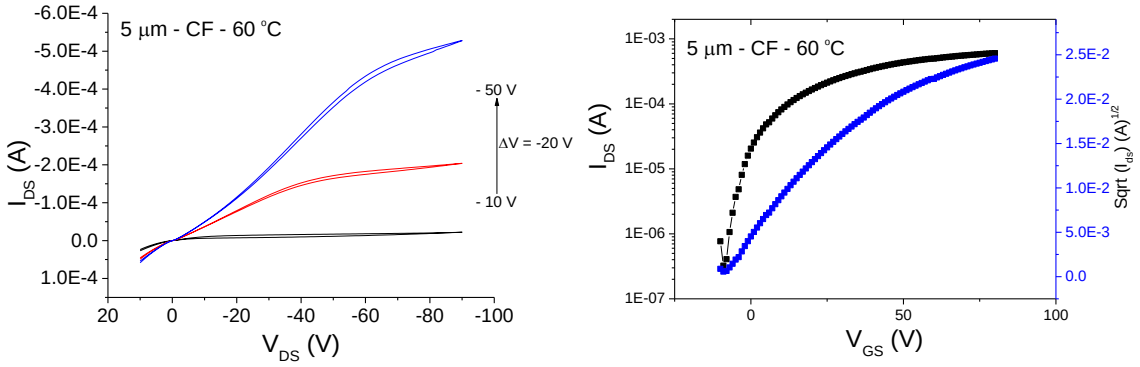

Figure 69 - Output (left) and Transfer (right) characteristics (5µm/CF/60 °C).

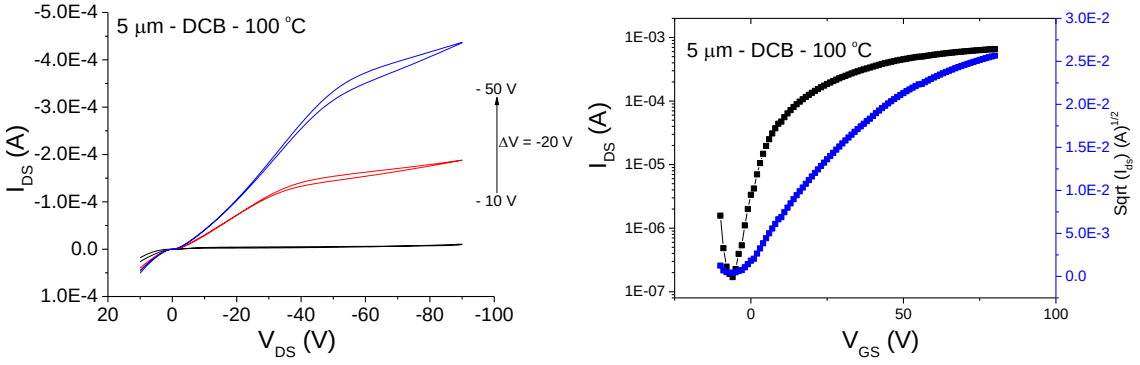

Figure 70 - Output (left) and Transfer (right) characteristics (5µm/DCB/100 °C).

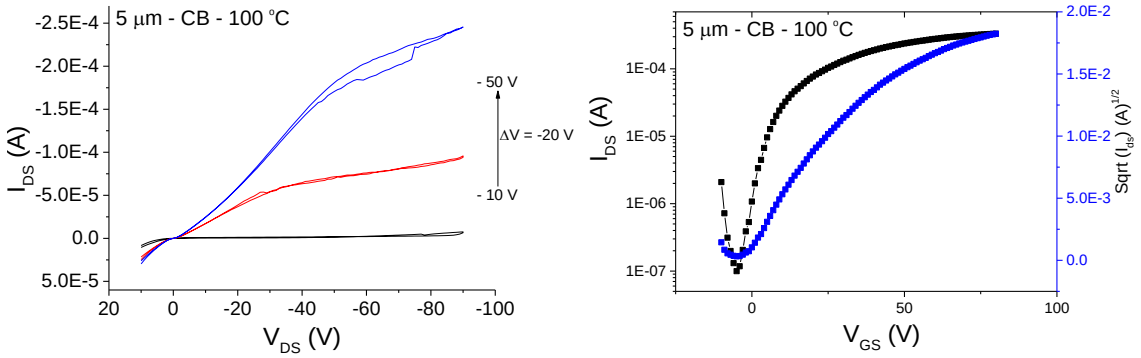

Figure 71 - Output (left) and Transfer (right) characteristics (5µm/CB/100 °C).

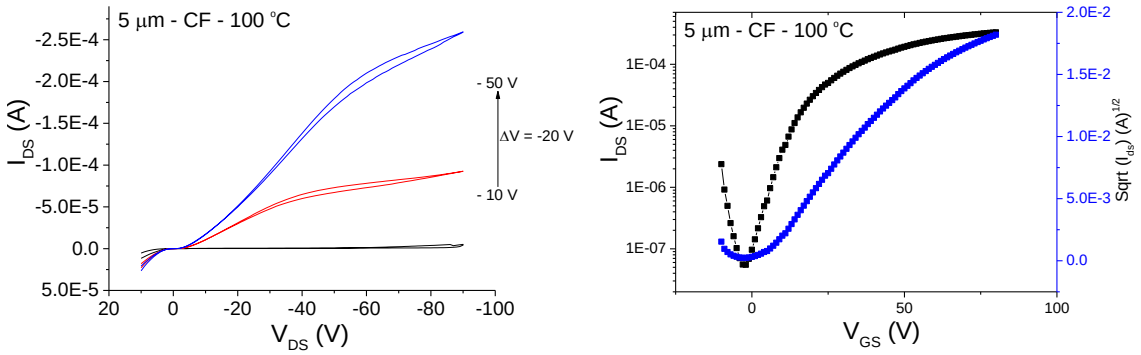

Figure 72 - Output (left) and Transfer (right) characteristics (5µm/CF/100 °C).

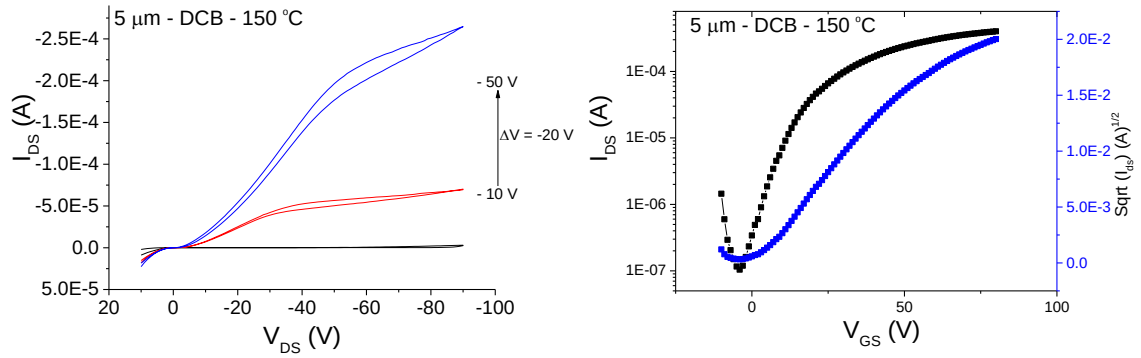

Figure 73 - Output (left) and Transfer (right) characteristics (5µm/DCB/150 °C).

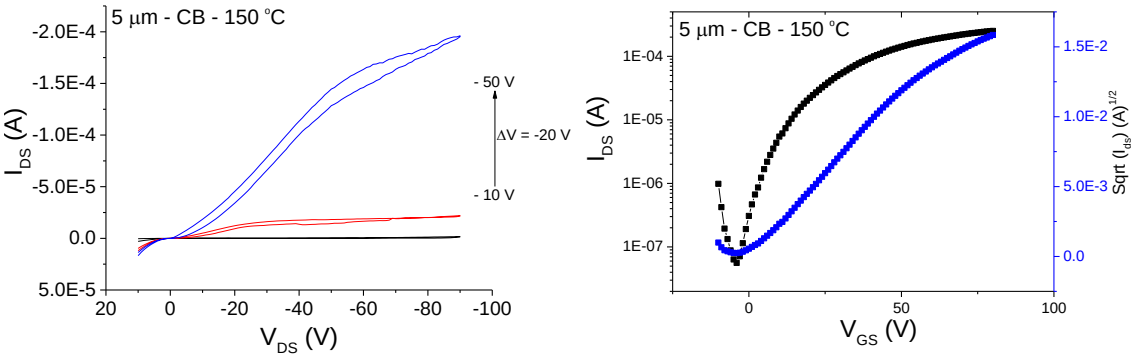

Figure 74 - Output (left) and Transfer (right) characteristics (5µm/CB/150 °C).

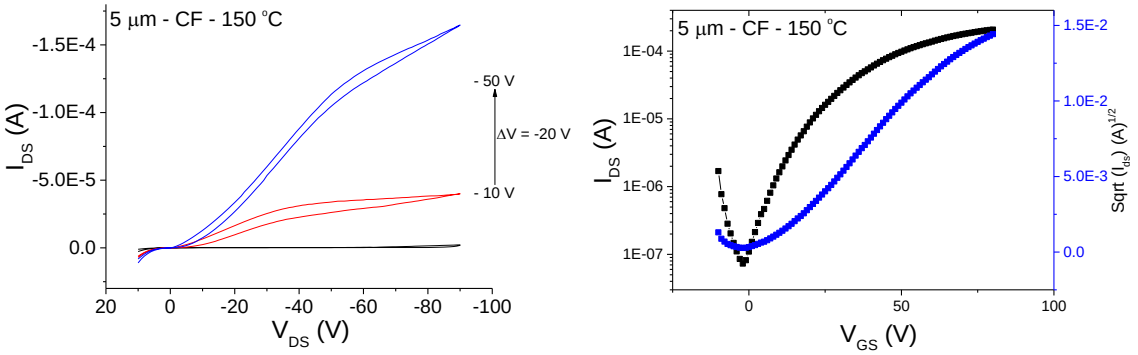

Figure 75 - Output (left) and Transfer (right) characteristics (5µm/CF/150 °C).

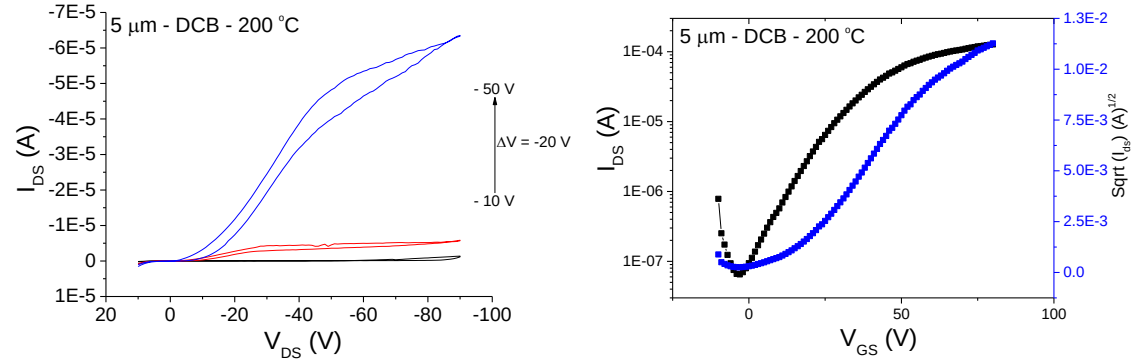

Figure 76 - Output (left) and Transfer (right) characteristics (5µm/DCB/200 °C).

The devices processed from chlorobenzene and chloroform failed to exhibit semiconducting behaviour when annealed at 200 °C. Whilst the device fabricated from dichlorobenzene functions, it exhibits significantly increased hysteresis, reduced mobility and increased threshold voltage, indicating that the devices become over-annealed at this temperature. As the TGA data showed excellent thermal stability of this polymer, it is unlikely to be a result of chemical degradation and more likely to be related to overcrystallisation leading to grain boundaries. This

effect has been well documented in the literature and is common among many crystalline conjugated polymers.[149]

It is clear from the output and transfer graphs that dichlorobenzene is the best performing solvent for this material and this is in agreement with many other polymeric transistors in the literature. It is likely that with use of a high boiling point solvent, residual solvent remains in the active layer after spin coating which, due to its slow evaporation, allows the material to rearrange to an optimal morphology.[31, 96]

Solvent	Annealing temperature (°C)	μ_h ($cm^2V^{-1}s^{-1}$)	I_{on}/I_{off}	V_{th} (V)
***o*-dichlorobenzene**	As cast	1.69×10^{-2}	10^3	-5
	60	2.49×10^{-2}	10^3	-8
	100	3.06×10^{-2}	10^4	-6
	150	2.07×10^{-2}	10^4	-4
	200	7.27×10^{-3}	10^4	-3
chlorobenzene	As cast	3.89×10^{-3}	10^2	-10
	60	6.11×10^{-3}	10^3	-9
	100	6.64×10^{-3}	10^3	-5
	150	8.23×10^{-3}	10^2	-4
	200	N/A	N/A	N/A
chloroform	As cast	1.14×10^{-2}	10^3	-9
	60	1.17×10^{-2}	10^3	-9
	100	1.06×10^{-2}	10^4	-2
	150	8.69×10^{-3}	10^3	-2
	200	N/A	N/A	N/A

Table 7 – Effect of solvent and annealing temperature on hole mobility.

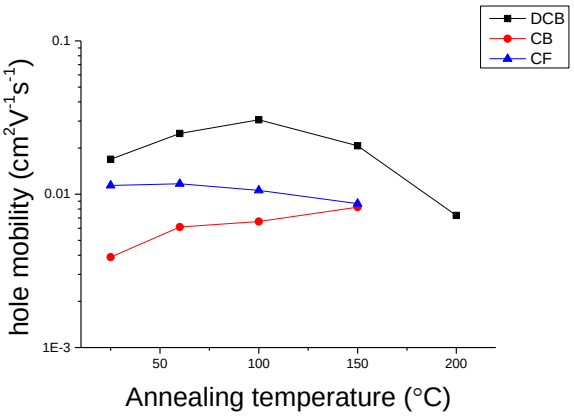

Figure 77 - Hole mobility as a function of annealing temperature

Figure 77 shows that the ideal annealing temperature for these materials is between 100 °C and 150 °C. The dichlorobenzene processed device increases in performance up to this temperature before rolling off, whilst the chloroform device steadily decreases as a function of temperature. The chlorobenzene device steadily increases with increasing temperature until 200 °C, at which point the device no longer functions.

In order to compare the four synthesised polymers, the remaining materials were fabricated using *o*-dichlorobenzene and annealed at 100 °C. The device performance characteristics for each can be seen below.

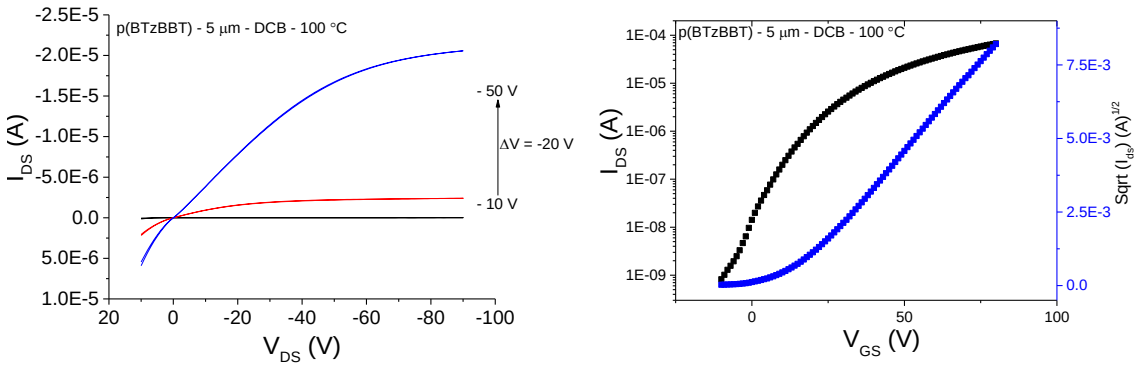

Figure 78 - Output (left) and Transfer (right) characteristics of ***p(BTzBBT)*** *[5µm/DCB/100 °C].*

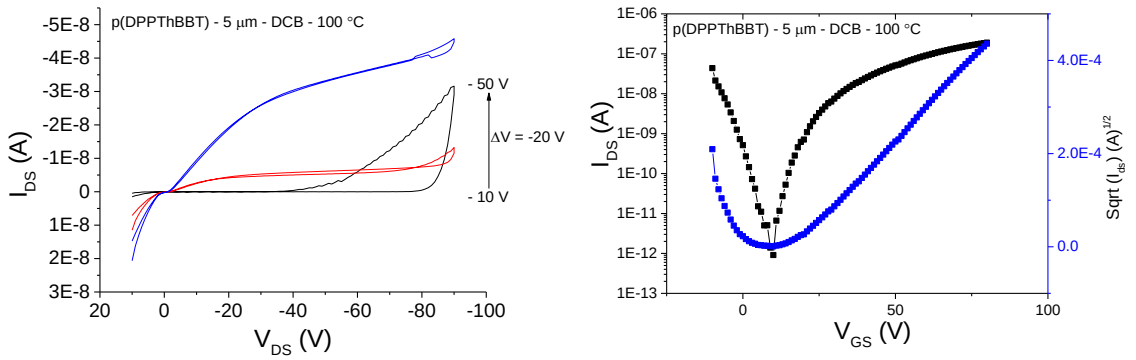

Figure 79 - Output (left) and Transfer (right) characteristics of ***p(DPPThBBT)*** *[5µm/DCB/100 °C].*

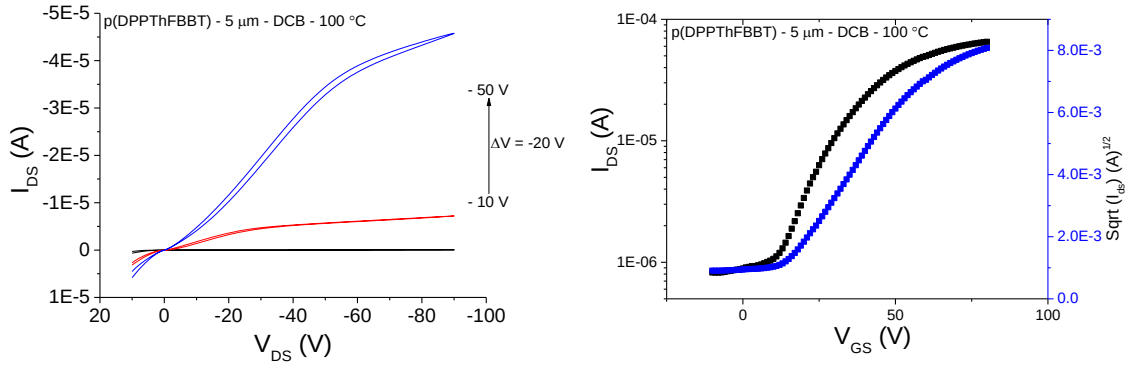

Figure 80 - Output (left) and Transfer (right) characteristics of ***p(DPPThFBBT)*** *[5µm/DCB/100 °C].*

Material	**μ_h ($cm^2V^{-1}s^{-1}$)**	**I_{on}/I_{off}**	**V_{th} (V)**
p(DPP2ThBBT)	3.06×10^{-2}	10^4	-6
p(BTzBBT)	2.23×10^{-3}	10^5	-10
p(DPPThBBT)	5.43×10^{-6}	10^6	10
p(DPPThFBBT)	2.83×10^{-3}	10^2	10

Table 8 – Hole mobility of the synthesised BBT copolymers

Due to the limited solubility of **p(BTzBBT)**, the solution was heated to 100 °C for 3 hours and spin coated whilst hot to prevent precipitation of the material. The film obtained from this procedure had complete coverage of the substrate but still suffered from significant roughness and poor uniformity (Figure 81). Despite this, the device exhibited the most "ideal" output and transfer characteristics of the four materials. Whilst it does not possess the highest mobility, the hysteresis observed is negligeable, with a high $\frac{I_{on}}{I_{off}}$ ratio and the required driving voltage is very low. These characteristics indicate the excellent capability for this material to perform in low-cost, solution processed OFETs.

Alternatively, **p(DPP2ThBBT)** exhibits the highest mobility of these polymers, as well as moderate $\frac{I_{on}}{I_{off}}$ ratio and threshold voltage, but suffers from increased hysteresis in both the output and transfer modes. This is indicative of charge trapping sites within the bulk film, which may arise from chemical impurities or an unfavourable molecular orientation. The hysteresis could also be a result of device structure and could possibly be overcome with selecting different electrodes or dielectric layers, or by changing from BGBC to other configurations such as top-gate bottom-contact (TGBC).[150] Unfortunately, due to a lack of available instrumentation with which to deposit the electrodes, this was not investigated.

While **p(DPPThFBBT)** exhibits moderately high mobility of 2.83 x 10^{-3} $cm^2V^{-1}s^{-1}$, it has a very low $\frac{I_{on}}{I_{off}}$ ratio and also has a high threshold voltage of 10 V. This suggests a non-ohmic contact between the gold electrodes (work function of 5.1 - 5.5) and the shallow HOMO of the polymer (4.86). This non-ohmic contact can lead to poor injection into the active layer and as a result, increases device leakage and the likelihood of device short-circuit. It is possible to alter the work function of gold by addition of thiol SAMs. One common monolayer is pentafluorothiophenol (PFBT).[151] In an attempt to improve charge injection, the pre-fabricated devices were treated with PFBT using the method previously published.[152] Unfortunately, the devices fabricated onto the treated Au surface exhibited no field effect mobility. This is likely due to the SAM altering the active layer morphology within the device. This effect has been previously documented and because of this, use of thiol SAMs is still an area of intensive research.[151]

Finally, **p(DPPThBBT)** exhibits poor mobility and threshold voltage. The very low mobility suggests a non-optimal active layer morphology and significant grain boundaries.

In order to probe active layer morphology, the devices were analysed using tapping mode atomic force microscopy (AFM). Due to the roughness of **p(BTzBBT)** films, accurate AFM analysis of the devices fabricated from this material was impossible.

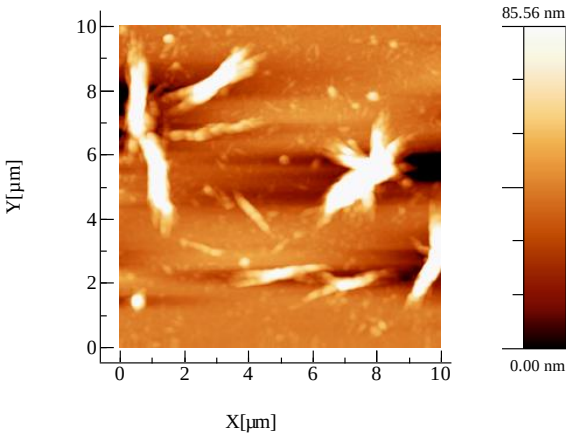

*Figure 81 - AFM height image of **p(BTzBBT)** OFET device.*

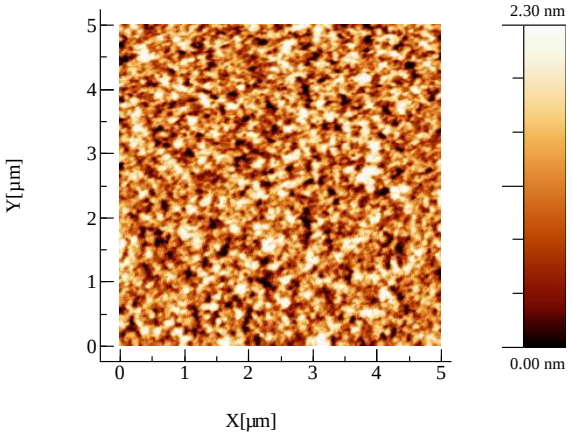

*Figure 82 - AFM height image of **p(DPP2ThBBT)** OFET device.*

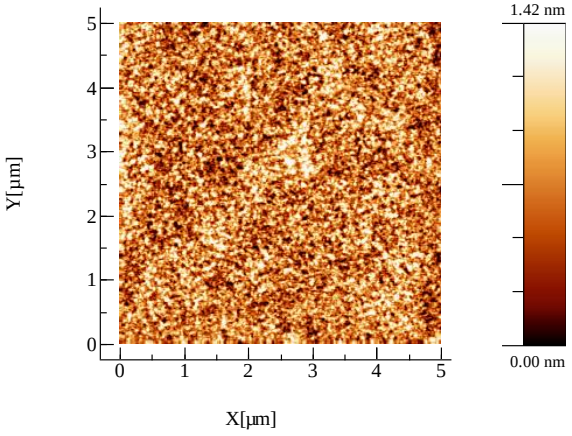

Figure 83 - AFM height image of p(DDPThFBBT) OFET device.

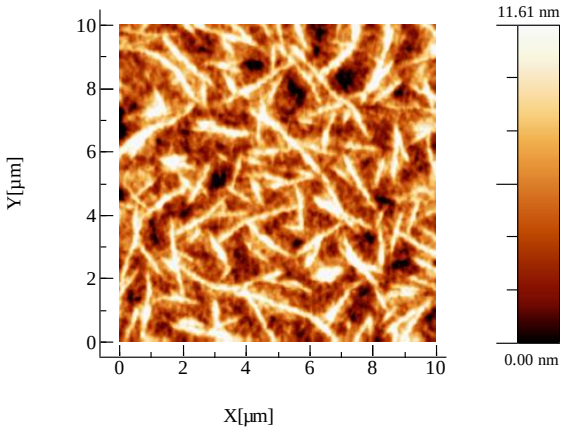

*Figure 84 - AFM height image of **p(DPPThBBT)** OFET device.*

The AFM image for **p(BTzBBT)** displays the very rough surface of the device with particles several microns wide and ~100 nm tall (Figure 81). It is surprising that the device exhibits near ideal FET behaviour with this morphology as crystallites of this size are responsible for forming grain boundaries. It is expected that with an optimised, uniform film formation, this material could exhibit significantly improved FET performance. One possible method to improve film forming properties could be to utilise an amorphous polymer matrix such as polystyrene as a host material. Previous studies have shown that introduction of crystalline semiconducting materials into an amorphous host can offer the flexible, uniform film properties of the amorphous host, whilst retaining the charge transfer characteristics of the semiconductor.[153] Furthermore, due to reduced crystallisation, phase-segregation is inhibited, improving transistor stability and lifetime.[53]

Both **p(DPP2ThBBT)** (Figure 82) and **p(DPPThFBBT)** (Figure 83) exhibit smooth, uniform films with grain boundaries that are on the order of 0.1 µm or less. This morphology is expected to contribute significantly to the high mobility found in these devices. The difference in mobility between these polymers is attributed to the difference in polymer molecular weight. It has been previously shown that higher molecular weight conjugated polymers exhibit higher field-effect mobilities.[29] Charge carrier mobility is at its peak within a single polymer chain, and at its lowest at grain boundaries. For this reason, longer polymer chains can result in the carrier encountering fewer boundaries between the source and drain electrodes.[29, 138]

The same phenomenon as above can justify the very poor mobility exhibited for **p(DPPThBBT)** (Figure 84) as the single crystallites extend up to 5 µm, and grain boundaries greater than 1 µm wide. The significant crystallinity exhibited by this material compared to the

other DPP containing polymers, is likely to be a result of the relatively low molecular weight. The molecular weight is also expected to be detrimental to the FET performance. The combination of these factors results in devices that are comparatively, very inferior.

Due to the strong optical absorption, narrow band-gap and efficient charge carrier properties of these materials, they were investigated for use as components in OPVs. Unfortunately, due to the very poor solubility of **p(BTzBBT)**, a blend solution with $PC_{71}BM$ of concentration suitable for OPVs, could not be obtained. The remaining materials were fabricated into OPV devices using the conventional architecture of ITO/PEDOT:PSS/Active Layer/Ca/Al by collaborators at the University of St Andrews (Mr Bernd Ebenhoch and Dr. Gopala K. Thalluri).

In the first instance, **p(DPPThBBT)** was investigated. The LUMO energy of the synthesised DPP-BBT copolymers are significantly deeper than traditional high efficiency donor materials *e.g.* P3HT has a LUMO level of -3.0 eV (measured in-house). Further to this, $PC_{61}BM$ and $PC_{71}BM$ have LUMO energies of -3.7 and -3.75 eV respectively. As the deep LUMO of the synthesised copolymer is between that of common donor and acceptor components, this material was investigated as both a donor and acceptor in OPV devices.

As a donor, **p(DPPThBBT)** was incorporated in conventional and inverted bulk-heterojunction solar cells with $PC_{71}BM$. For full fabrication details see Chapter 5 – Experimental.

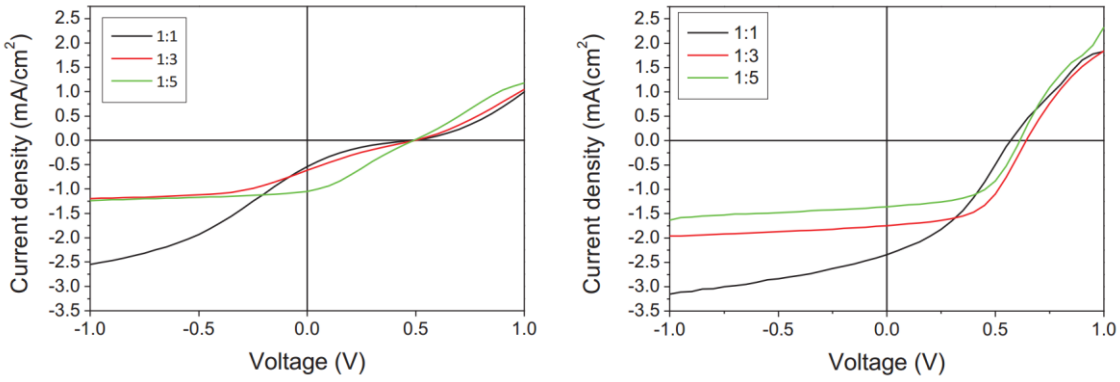

Figure 85 - Conventional (left) and Inverted (right) solar cell parameters as a function of D:A ratio. Conventional architecture: ITO/MoO_3/active layer/Ca/Al). Inverted architecture: ITO/Cs_2CO_3/active layer/MoO_3/Ag.(Adapted with permission from B. Ebenhoch).

Blend ratio	**1:1**		**1:3**		**1:5**	
Concentration (mg/ml)	69		75		74	
Thickness (nm)	91±10		110±15		132±14	
Architecture	Inverted	Conventional	Inverted	Conventional	Inverted	Conventional
Ƞ (%)	0.48 ± 0.02	0.04 ± 0.00	0.5 ± 0.03	0.06 ± 0.01	0.41 ± 0.02	0.14 ± 0.01
J_{sc} (mA/cm^2)	2.28 ± 0.05	0.52 ± 0.03	1.60 ± 0.05	0.61 ± 0.02	1.28 ± 0.02	1.03 ± 0.02
V_{oc} (mV)	557 ± 18	495 ± 2	622 ± 27	478 ± 14	588 ± 23	498 ± 4
FF (%)	37.9 ± 0.4	15.2 ± 0.2	50.2 ± 1	19.2 ± 0.8	54.9 ± 2.0	27.3 ± 0.9

*Table 9 - **p(DPPThBBT)** device parameters as a function of blend ratio.Device averages were obtained over 6 devices. (Adapted with permission from B. Ebenhoch).*

In each of the OPV devices fabricated, it is clear that the limiting factor is the very low J_{sc}. This is indicative of very poor charge separation in the bulk heterojunction. The performance is improved in the inverted architecture and is attributed to improved charge extraction, resulting from the addition of the Cs_2CO_3 electron transport layer. The low J_{sc} is attributed to the very low LUMO offset between **p(DPPThBBT)** and $PC_{71}BM$. Generally, an energy offset of > 0.3 eV between the donor and acceptor components is required to overcome the coloumbic binding energy of an exciton.[93]

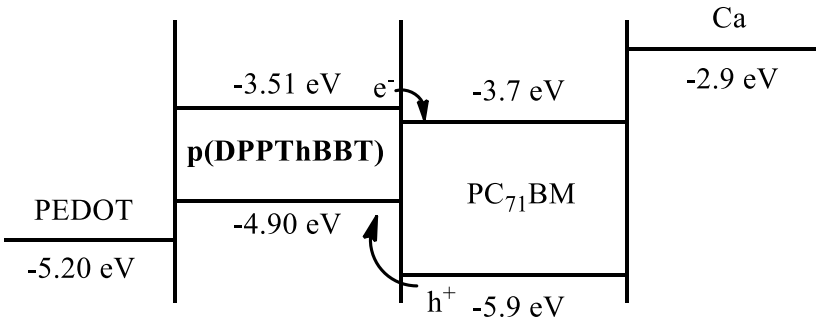

Figure 86 - Representation of OPV energy levels.

While the HOMO offset is more than sufficient, the LUMO offset is ~ 0.2 eV. To confirm that energy transfer from **p(DPPThBBT)** to PCBM was not occurring, the EQE of the blend film was measured.

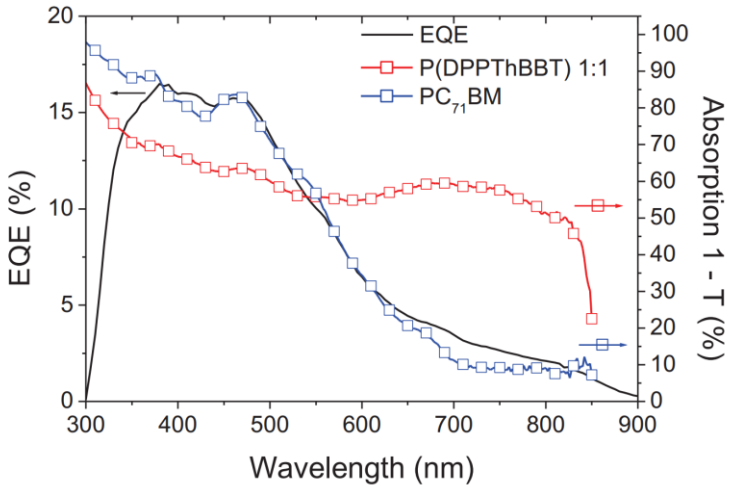

*Figure 87 - EQE spectrum of **p(DPPThBBT)**:$PC_{71}BM$ (black), absorption spectra of blend film (red) and absorption spectra of $PC_{71}BM$ film (blue). (Adapted with permission from B Ebenhoch).*

As expected, the major absorption peak of **p(DPPThBBT)** at ~700-900 nm is not represented on the EQE. This indicates that excitons generated in **p(DPPThBBT)** are not effectively transferred to $PC_{71}BM$ and, as a result, only excitons generated in $PC_{71}BM$ contribute to the solar cell photocurrent. These factors significantly limit the functionality of **p(DPPThBBT)** as a donor material in conjunction with $PC_{71}BM$, however, this material is promising for use in conjunction with acceptors exhibiting a deeper LUMO level such as PNDIS-HD synthesised by Jenekhe and co-workers which has a deep LUMO of -4.0 eV.[154]

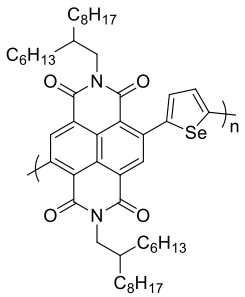

Figure 88 - PNDIS-HD acceptor polymer.[154]

The energy offset for polymer solar cells with this material is expected to be sufficient to facilitate charge transfer and hence improve PCE. Furthermore, by removing $PC_{71}BM$ from the OPV architecture, stability can be significantly improved.[104]

Further to this, **p(DPPThBBT)** was incorporated as an acceptor, in conjunction with P3HT. Unfortunately, due to a combination of poor electron transport and unfavourable HOMO energy offset, these devices showed no photovoltaic effect.

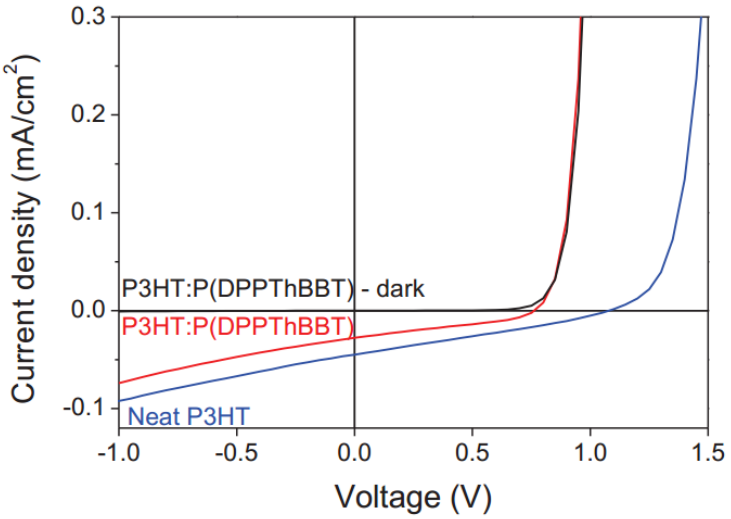

*Figure 89 – JV curve for P3HT:**p(DPPThBBT)** solar cells. For comparison, a neat P3HT device is shown. (Adapted with permission from B. Ebenhoch).*

Figure 89 clearly highlights that there is no photocurrent from this device. This is attributed to the inefficient energy offset for solar cells utilising **p(DPPThBBT)** as an acceptor. Due to the lack of available donor materials with optimal energy offset, further investigation of **p(DPPThBBT)** as an acceptor was not pursued.

Similar results were obtained for **p(DPP2ThBBT)** and **p(DPPThFBBT)** with efficiencies up to 0.89 % achieved (Figure 90). The increased PCE for these materials is attributed to the high FF of 60% and 55% respectively. The FF obtained for each of the DPP-BBT copolymers increases proportionally with increasing μ_h, which is in good agreement with previously published data.[93] The J_{sc} values obtained for these materials are comparable with that of **p(DPPThBBT)** at 2.51 and 2.43 mA/cm^2, respectively. Whilst **p(DPPThFBBT)** and **p(DPP2ThBBT)** exhibit superior polymer:fullerene OPV performance compared to **p(DPPThBBT)**, they still exhibit poor performance as a result of low J_{sc} generation and thus were not investigated further.

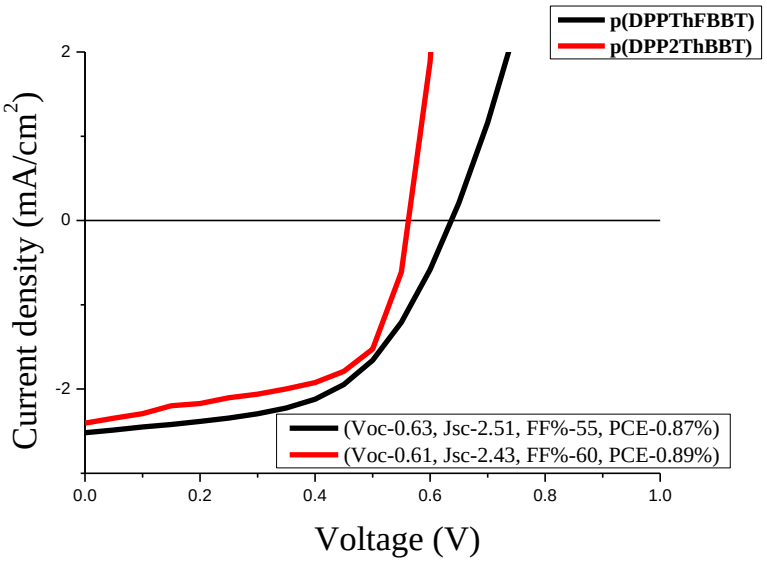

*Figure 90 - JV curve for **p(DPPThFBBT)** [black] and **p(DPP2ThBBT)** [red] solar cells. Device architecture – ITO/PEDOT:PSS/Active layer/Ca/Al. (Adapted with permission from G. K. Thalluri).*

3.4 Conclusions

Four novel, low band-gap, highly planarised conjugated copolymers have been synthesised in high yield and characterised using UV-Visible absorption, cyclic voltammetry and gel-permeation chromatography.

Whilst GPC analysis of **p(BTzBBT)** was unsuccessful due to poor solubility in chlorobenzene, it may be possible to obtain reasonable data using higher boiling point solvents, such as 1,2,4-trichlorobenzene, for high-temperature analysis. Unfortunately, access to instrumentation with such capabilities was not available during this research.

The polymers were then further characterised as the active layer materials in organic field-effect transistors and donor (and acceptor) components in organic photovoltaics.

Each of the materials exhibit moderate to high performance in OFETs, with mobilities reaching up to 3.06 x 10^{-2} $cm^2V^{-1}s^{-1}$ for **p(DPP2ThBBT)**. Futhermore, three of these polymers exhibit I_{on}/I_{off} ratios above 10^3, the requirement for mainstream logic applications.[155] Interestingly, despite the poor active layer morphology of **p(BTzBBT)**, OFET devices based on these materials still exhibit near-perfect transistor profiles and negligible hysteresis. The excellent performance of this material in such an unoptimised morphology highlights the potential of rigid, highly planarised polymers. Whilst optimisation of the active layer in this material was unsuccessful, incorporation of longer alkyl substituents (*e.g.* butyl-octyl or hexyl-decyl) could improve solution processability, allowing for easier morphological optimisation and ultimately, improved device performance could be realised. Furthermore, incorporation of **p(BTzBBT)** and **p(DPPThBBT)** into polymer:insulator matrices could improve device morphology, leading to enhanced device performance.

Further optimisation of OFET device performance could be achieved by altering the device architecture. In this study, BGBC devices were fabricated and tested, to reduce complexity of fabrication. Alternatively, TGBC devices have been shown to yield improved transistor properties due to reduced leakage,[156] increased stability resulting from insulator encapsulation[53] and improved carrier injection.[71] These improvements have previously been shown to result in up to two orders of magnitude increase in μ_h.[157, 158]

Time-resolved microwave conductivity could be used to accurately determine the intrinsic charge carrier mobility of each polymer. This technique is particularly interesting as it is

conducted in the solution state and therefore, bulk packing effects do not contribute to the mobility.[138] This would offer quantitive information, correlating backbone rigidity with charge carrier mobility.

When incorporated as donor materials in OPV devices, efficiencies of up to 0.9 % PCE were achieved. Despite achieving high FF and reasonable V_{oc}, these materials suffered from very poor photocurrent generation, as a result of non-optimal LUMO offset. Further investigation as donor materials in conjunction with acceptors exhibiting deep LUMO levels is on-going at the University of St Andrews. Furthermore, in order to realise high efficiency donor materials for use in polymer/fullerene BHJ cells, the LUMO energy level must be raised closer to vacuum with an optimal energy of -3.1 to -3.4 eV, whilst retaining a narrow band-gap for effective photon harvesting. To achieve this, three polymers have been synthesised and are discussed in Chapter 4.

4 Low band-gap, donor-acceptor copolymers containing 4,8-benzobisthiazole for organic photovoltaics.

4.1 Introduction

In recent years, many research groups have focussed intensive research into developing electron-deficient monomer units for conjugated polymers. When copolymerised with electron-rich units, a narrower band-gap can be achieved. Many accepting units have found success in OPVs such as imides,[159] quinoxalines[160] and chalcogenadiazoles.[161] Each of these have seen significant increase in research activity in the past decade and, resulting from this, dramatic increases in photovoltaic performance.

Despite the electron-deficient nature of BBT, it has thus far had comparatively poor results as an accepting unit when incorporated into donor polymers for OPVs, with PCEs reaching up to 3.8%.[59, 131] To investigate BBT based donor materials, three copolymers were synthesised. Building on previous work within this thesis (See Chapter 3), the polymers were designed to retain a similar narrow band-gap and charge carrier properties to the materials previously synthesised, as well as ensuring significantly increased solubility and ideal energy level offset for charge separation. The three polymers were designed as D-A [**p(BDTBBT)**], A_1-D-A_2-D [**p(BBT2ThBT)**] and also D-A with a strong donor monomer [**p(DTPBBT)**]. The structure of each polymer can be seen in Figure 91 below.

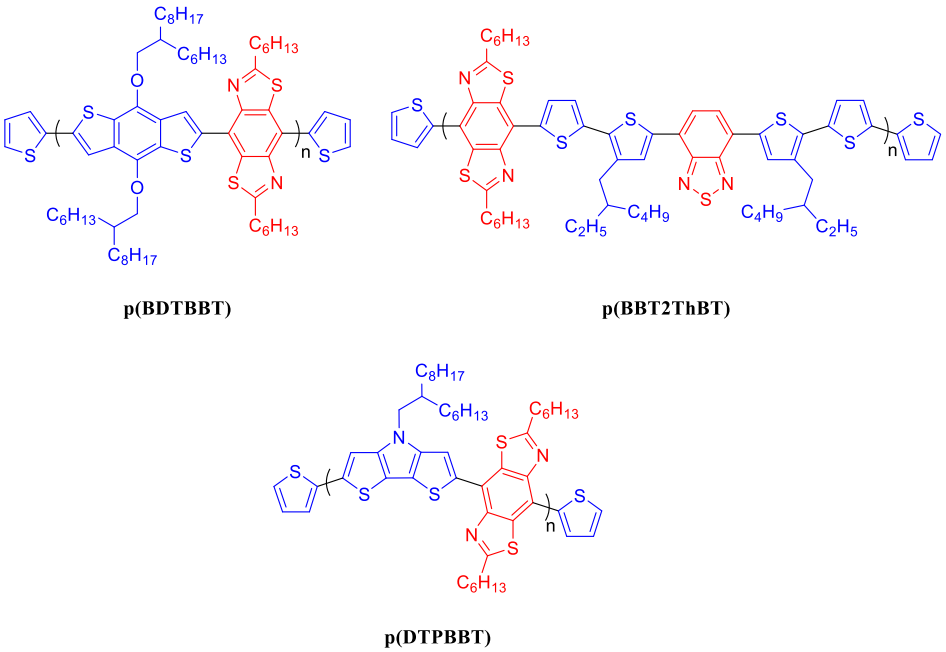

Figure 91 - Synthesised BBT donor polymers (donating and accepting units are highlighted in blue and red respectively).

The first polymer, **p(BDTBBT)** incorporates BBT with the moderate strength donor unit benzodithiophene **(4.1)**. In **p(DTPBBT)**, the strong donor unit dithienopyrrole **(4.2)** is used to encourage a narrowing of the polymer band-gap and tuning of the HOMO and LUMO energy levels. Finally, in **p(BBT2ThBT)**, the benzothiadiazole **(1.30)** unit is added into the polymer chain to generate an A_1-D-A_2-D system (analogous to those in Chapter 3) which reduces the HOMO and LUMO respectively. As benzothiadiazole **(1.30)** is a weaker acceptor than DPP **(4.3)**,[162] the LUMO was predicted to be shallower than that seen in **p(DPP2ThBBT)**, whilst retaining a relatively deep HOMO.

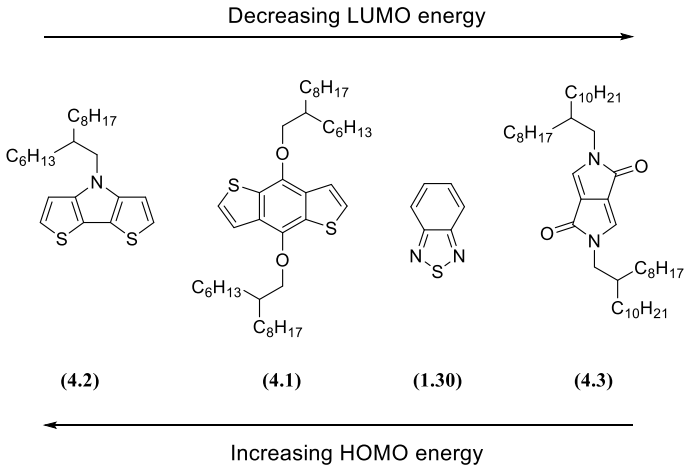

Figure 92 - Graphical representation of HOMO and LUMO energy levels.

Previously, 2,6-disubstituted BBT has been utilised as an acceptor unit in D-A copolymers synthesised by Jenekhe and co-workers **(4.4** and **4.5)**.[59] These polymers exhibit efficient charge transport and excellent absorption characteristics, yielding OPV efficiencies of up to 3% with $PC_{71}BM$.

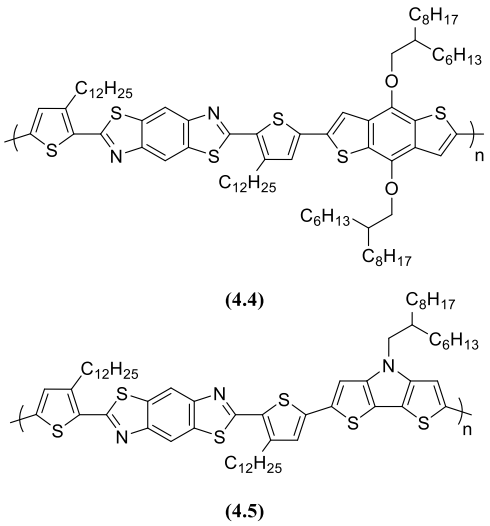

Figure 93 - 2,6-BBT copolymers synthesised by Jenekhe and co-workers.[59]

Polymer	HOMO (eV)	LUMO (eV)	μ_h ($cm^2V^{-1}s^{-1}$)	η_{avg} (η_{max}) (%)
(4.4)	5.71	3.33	9.3×10^{-3}	2.94 (3.00)
(4.5)	4.79	3.30	5.5×10^{-4}	0.30 (0.31)

Table 10 - 2,6-BBT copolymer properties.[59]

Whilst these polymers exhibit reasonable device performance, BBT containing donor polymers still perform very poorly compared to many other azole-containing donor polymers.[49] Recently, Seki and co-workers incorporated 2,6-BBT into a random copolymer with benzothiadiazole (Figure 94).[131] This material yielded conventional OPV devices with a PCE of up to 2.37%, increasing to 3.84% in the inverted architecture. This efficiency represents the highest PCE published for any BBT containing polymer to date.

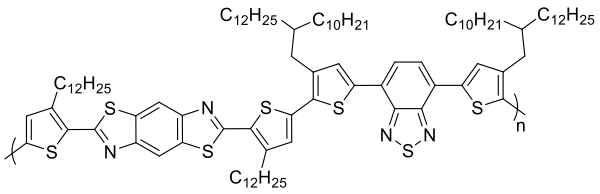

(4.6)

Figure 94 - 2,6-BBT copolymer synthesised by Seki and co-workers.[131]

Inspired by these results, synthesis of structurally similar 4,8-BBT copolymers was envisioned to compare functionalisation at the 2- and 6-, or the 4- and 8- positions. Furthermore, the implications of extensive π-delocalisation found in 4,8-BBT derivatives can be investigated (See Chapter 2).

4.2 Synthesis

Synthesis of monomer **(4.11)** was conducted starting from 3-bromothiophene **(4.7)** in 65% overall yield across four steps (Scheme 22).

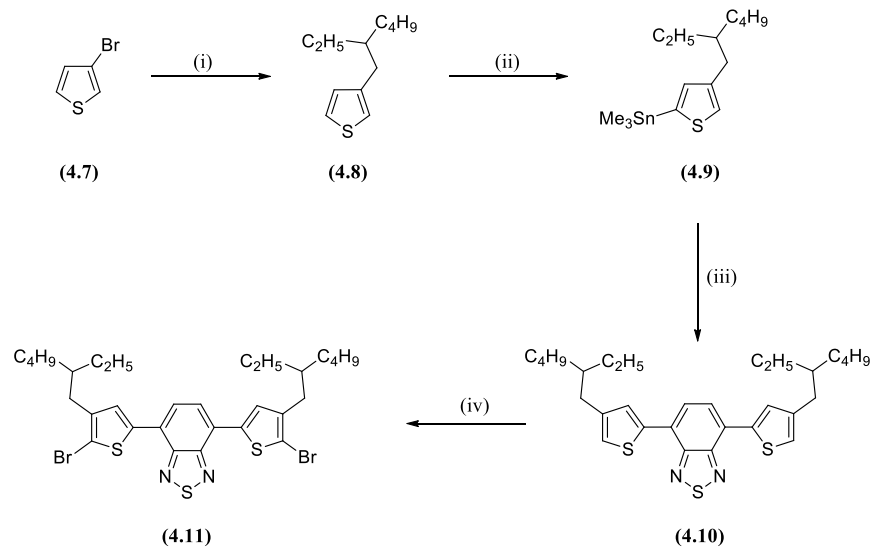

Scheme 22 – Reagents and conditions: (i) Mg, 2-ethylhexyl bromide, THF reflux 2 h then 3-bromothiophene, Ni(dppp)Cl_2, THF reflux overnight (80%); (ii) N,N,N',N'-TMEDA, n-BuLi, Et_2O rt to reflux 1 h then $SnMe_3Cl$, THF 0 °C to rt overnight (98%); (iii) 4,7-dibromobenzo[c][1,2,5]thiadiazole, Pd[(PPh_3)$_4$], PhMe reflux 24 h (85%); (iv) NBS, THF 0 °C to rt overnight (98%).

Commercially available 2-ethylhexyl bromide was converted to the corresponding Grignard reagent *via* treatment with magnesium turnings in anhydrous tetrahydrofuran, followed by Kumada coupling with commercially available 3-bromothiophene **(4.7)** in the presence of catalytic Ni(dppp)Cl_2 to afford **(4.8)** in 80% yield after distillation. Lithiation of **(4.8)** with *n*-BuLi/TMEDA in anhydrous Et_2O, followed by anion quenching with $SnMe_3Cl$ afforded the stannylated derivative **(4.9)** in near-quantitative yield with no further purification required. Conventional Stille cross-coupling of **(4.9)** with 4,7-dibromobenzo[c][1,2,5]thiadiazole in anhydrous PhMe and Pd[(PPh_3)$_4$] as catalyst, provided **(4.10)** in high yield after purification. Bromination of **(4.10)** *via* N-bromosuccinimide, in tetrahydrofuran and the absence of light, afforded compound **(4.11)** in near-quantitative yield after purification *via* chromatography.

p(BBT2ThBT) was synthesised *via* microwave-assisted random Stille polymerisation with **(4.11)**, **(2.5)** and **(3.26)** in a 1:1:2 ratio respectively. End capping was achieved by Stille cross-coupling with commercially available tributyl(thiophen-2-yl)stannane and 2-bromothiophene.

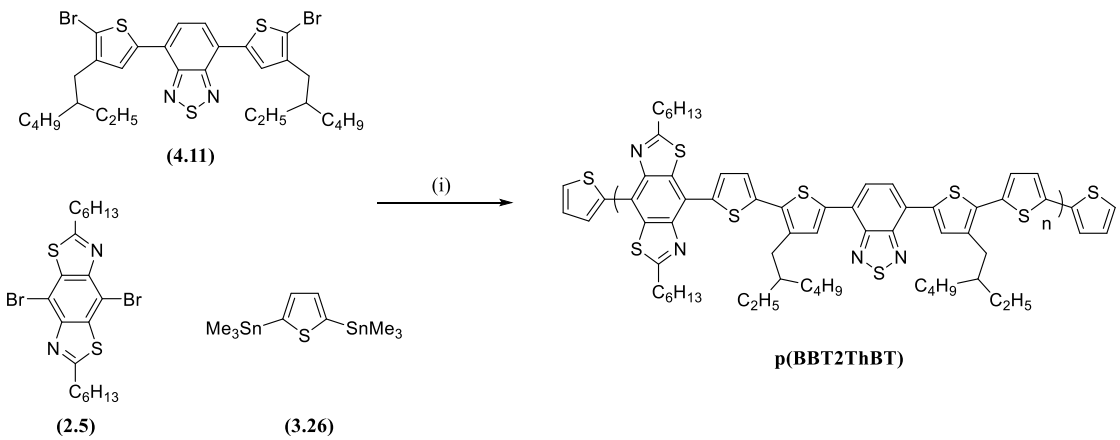

*Scheme 23 - Synthesis of **p(BBT2ThBT)**. Reagents and conditions: (i) $Pd_2(dba)_3$, P(o-tol)$_3$,PhCl 160 °C μW 50 min, then tributyl(thiophen-2-yl)stannane, 160 °C μW 10 min, then 2-bromothiophene, 160 °C μW 10 min.*

$Pd_2(dba)_3$, P(*o*-tol)$_3$ and PhCl were selected as the catalyst, ligand and solvent respectively. Microwave-assisted polymerisation was used to ensure a high molecular weight sample was obtained from the polymerisation. The resulting crude mixture was precipitated into methanol, filtered into a Soxhlet thimble and purified *via* Soxhlet extraction with methanol, acetone and chloroform to remove residual catalyst, oligomers and low molecular weight polymer. The pure polymer was then collected in chlorobenzene and precipitated into acetone, affording **p(BBT2ThBT)** as a dark purple solid.

Synthesis of the distannylated BDT monomer **(4.14)** was achieved in 36% yield over three steps as seen in Scheme 24.

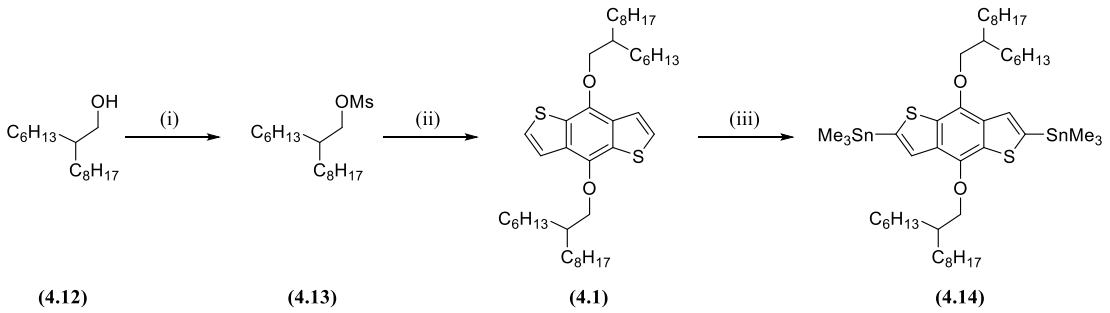

*Scheme 24 - Synthesis of **(4.14)**. Reagents and conditions: (i) MsCl, Et_3N, CH_2Cl_2 rt 1 h (70%); (ii) n-Bu_4NBr, benzo[1,2-b:4,5-b']dithiophene-4,8-dione, Zn powder, NaOH, H_2O reflux 1 h then **(4.13)**, reflux 2 h then Zn powder, reflux overnight (84%); (iii) n-BuLi, THF -78 °C to rt 1.5 h then $SnMe_3Cl$, THF 0 °C to rt overnight (61%).*

Commercially available 2-hexyldecanol **(4.12)** was converted to the corresponding mesylate, *via* treatment with MsCl and Et_3N. Commercially available benzo[1,2-b:4,5-b']dithiophene-4,8-dione was reduced with NaOH and Zinc metal, followed by treatment with **(4.13)** to afford the dialkoxy-BDT unit **(4.1)** in 84% yield. Lithiation of **(4.1)** with *n*-BuLi in anhydrous

tetrahydrofuran, at -78 °C, followed by anion quenching with $SnMe_3Cl$ provided the stannylated BDT **(4.14)** as a pure monomer after recrystallization (61% yield).

Attempts to polymerise this monomer with **(2.5)** *via* the same microwave-assisted Stille cross-coupling method as **p(BBT2ThBT)** were unsuccessful, yielding a black reaction mixture that was composed of mostly starting monomers. Consequently, conventional Stille polymerisation of this monomer was used as an alternative (Scheme 25). As conventional cross-couplings are traditionally slower than microwave-assisted, the reaction time was increased to 48 h before end capping with tributyl(thiophen-2-yl)stannane for 8 h, then 2-bromothiophene for 8 h.

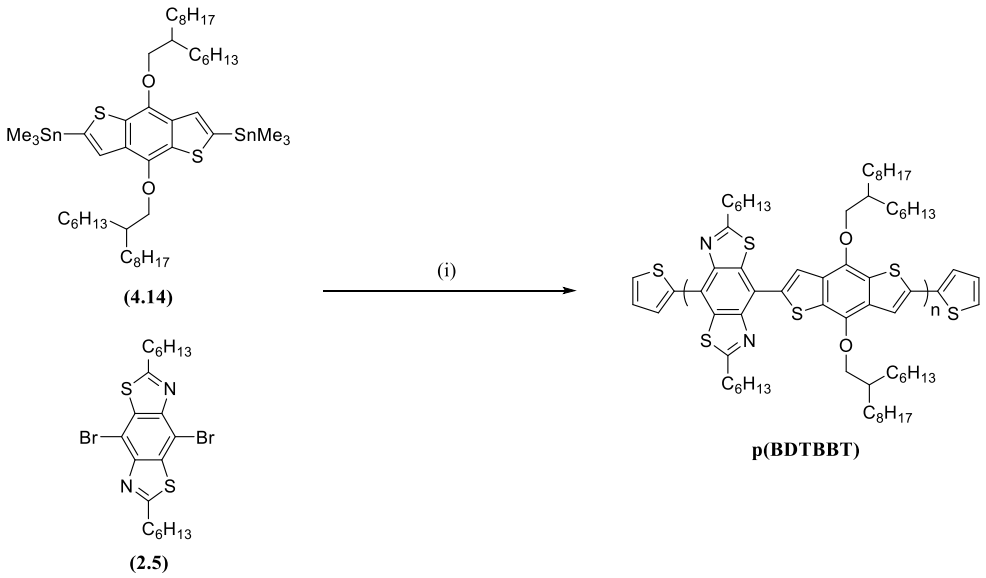

*Scheme 25 - Synthesis of **p(BDTBBT)**. Reagents and conditions: (i) $Pd_2(dba)_3$, $P(o\text{-}tol)_3$, PhMe reflux 48 h then tributyl(thiophen-2-yl)stannane, reflux 8 h then 2-bromothiophene, reflux overnight.*

The dark mixture was precipitated into methanol, filtered into a Soxhlet thimble and purified *via* Soxhlet extractions with methanol, acetone and hexane. The resulting red polymer was collected in chloroform, passed through a short silica gel plug eluting with chloroform, then concentrated and precipitated into acetone to yield **p(BDTBBT)** as a dark red solid.

Synthesis of the distannyl DTP monomer **(4.19)** was achieved in 6 steps from commercially available precursors (Scheme 26). Initially, synthesis of the trimethylstannyl derivative of **(4.19)** was achieved in moderate yield and purification of the monomer *via* silica gel chromatography results in cleavage of the C-Sn bond. Distillation of the trimethylstannyl derivative was also attempted but the material again decomposes. Therefore, the tributylstannyl derivative was synthesised. The longer butyl chains afford increased stability of the C-Sn bond and hence **(4.19)** could be purified by chromatography on Et_3N treated silica gel in excellent yield.

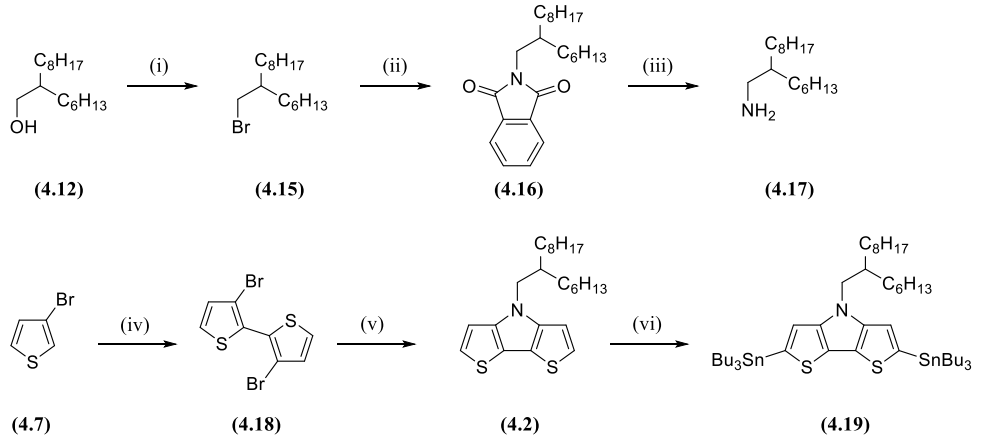

*Scheme 26 - Synthesis of **(4.19)**. Reagents and conditions: (i) PPh_3,Br_2, CH_2Cl_2 rt overnight (97%); (ii) potassium pthalimide, DMF 90 °C 18 h (94%); (iii) $N_2H_4.H_2O$, MeOH reflux 6 h (89%); (iv) n-BuLi, N,N'-diisopropylamine, THF -78 °C to rt 15 min, then **(4.7)**, -78 °C 1 h, then $CuCl_2$, -78 °C to rt (46%); (v) $Pd_2(dba)_3$, BINAP, t-BuONa, **(4.17)**, PhMe reflux 12 h (69%); (vi) LiTMP, THF 1 h -78 °C to rt 1 h, then $SnBu_3Cl$, THF -78 °C to rt overnight (95%).*

As before, (Scheme 23) microwave-assisted Stille polymerisation was chosen for the synthesis of **p(DTPBBT)**. The detailed reaction conditions can be seen below (Scheme 27).

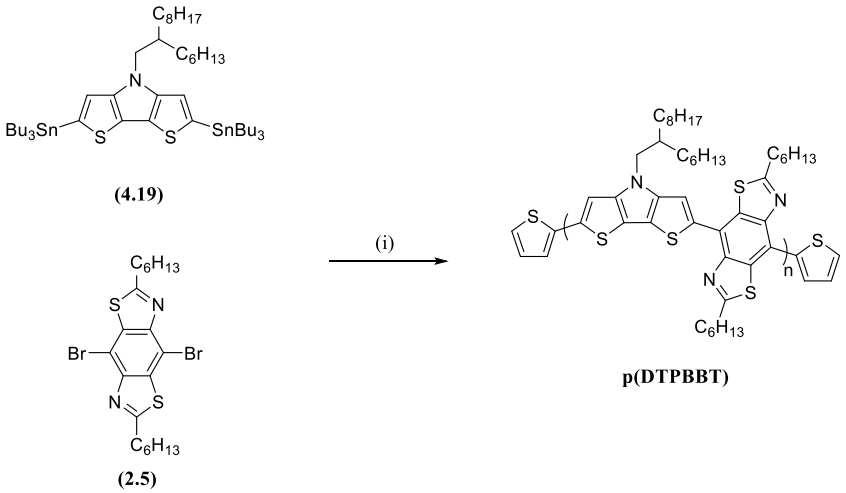

*Scheme 27 - Synthesis of **p(DTPBBT)**. Reagents and conditions: (i) $Pd_2(dba)_3$, $P(o\text{-}tol)_3$,PhCl 160 °C μW 50 min, then tributyl(thiophen-2-yl)stannane, 160 °C μW 10 min, then 2-bromothiophene, 160 °C μW 10 min.*

The crude mixture was precipitated into methanol, filtered into a Soxhlet thimble and purified *via* Soxhlet extraction with methanol, acetone and hexane. The polymer was then collected in chloroform, concentrated and precipitated into acetone to yield the pure polymer as a dark purple solid.

Both **p(DTPBBT)** and **p(BDTBBT)** exhibit moderate solubility in toluene and tetrahydrofuran, as well as excellent solubility in chloroform, chlorobenzene and *o*-dichlorobenzene at room temperature. Whilst **p(BBT2ThBT)** exhibits no solubility in chloroform, it is highly soluble in chlorobenzene and *o*-dichlorobenzene at 50 °C.

4.3 Results and Discussion

The absorption spectra of the synthesised polymers were characterised as a solution in dichlorobenzene and as a thin film for comparison.

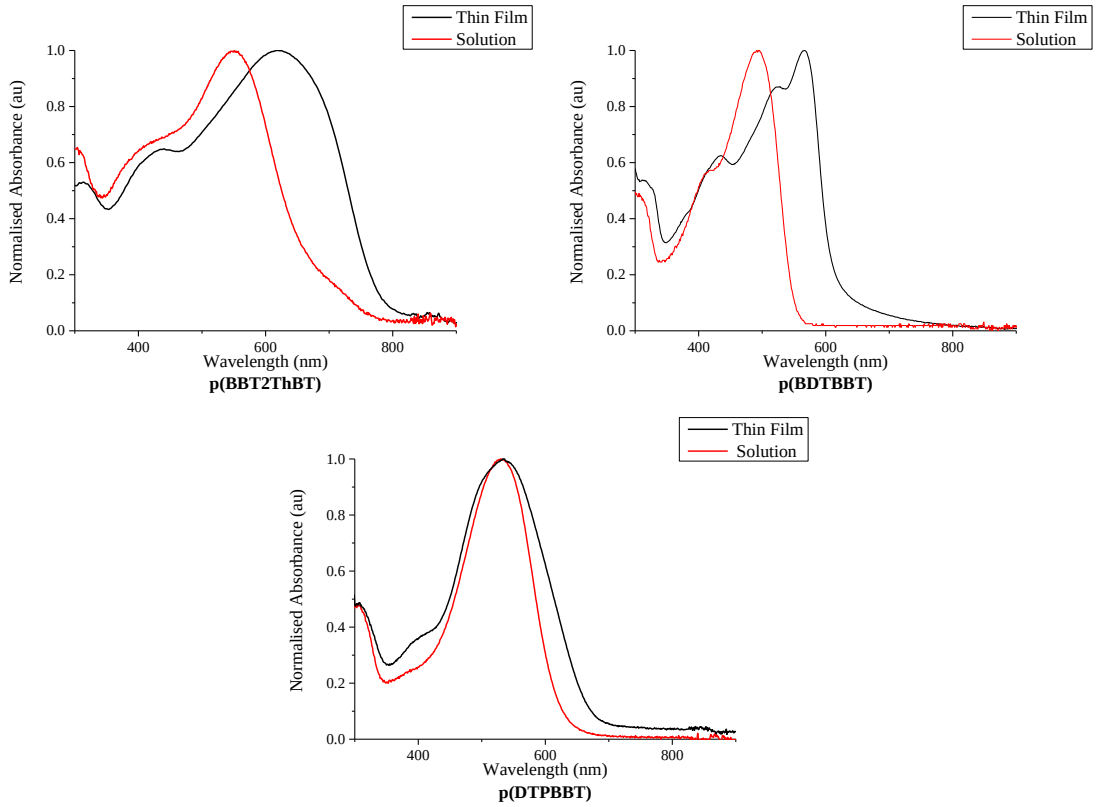

Figure 95 - Absorption spectra of BBT containing donor polymers.

From the absorption spectra, the optical band-gap of the polymers range from 1.8 to 2.2 eV in the solution state [excluding the shoulder of **p(BBT2ThBT)**], narrowing to between 1.6 and 2.0 eV in the thin film. This red shift of the absorption between solution and solid state is attributed to enhanced molecular packing and order in the solid state. This is further supported by the increased definition of the low energy maxima for **p(BDTBBT)**. In the solution spectra for **p(BBT2ThBT)**, a small shoulder is partially visible at ~ 700 nm wavelength. This shoulder has an onset wavelength close to that of the onset of solid state absorption, indicative of a partially ordered structure in solution, facilitating intermolecular interactions in this material. **p(DTPBBT)** does not exhibit a significant bathochromic shift in the solid state, suggesting that intermolecular interactions (if any) are similar in the solution and solid state.

The UV-Visible absorption data for the 4,8-BBT polymers was then compared with the literature 2,6-BBT polymers. When excluding the shoulder visible in the solution spectra for **p(BBT2ThBT)**, this polymer exhibits a ~30nm hypsochromic shift relative to the 2,6-derivative **(4.6)** synthesised by Seki and coworkers.[131] More interestingly, in the solid state,

p(BBT2ThBT) exhibits a 95 nm bathochromic shift, giving an onset of absorption at ~785 nm. On the other hand, **(4.6)** has a much smaller ~20 nm bathochromic shift in the thin film giving an onset of absorption at ~720 nm. This data is indicative of significantly increased intermolecular interactions in the 4,8-derivative in the solid state. Moreover, the absorption window of **p(BBT2ThBT)** is significantly broader than that of **(4.6)** allowing for increased photon absorption.

Similar results are obtained for **p(BDTBBT)**, which has solution and solid state onsets at 555 nm and 620 nm respectively, representing a bathochromic shift of 65 nm. The 2,6-derivative **(4.4)** synthesised by Jenekhe and coworkers, displays no significant bathochromic shift between the solution and solid state spectra with an onset of ~ 600nm for both.[59] Therefore, in the case of **p(BDTBBT)**, the solution state absorption is hypsochromically shifted, while the thin film absorption bathochromically shifted relative to the 2,6-derivative. Once again, this highlights the improved intermolecular solid state packing in the 4,8-BBT derivative. Finally, **p(DTPBBT)** displays a solution state onset that is hypsochromically shifted by 50 nm relative to that of the 2,6-derivative **(4.5)** synthesised by Jenekhe and co-workers.[59] Furthermore, the solid state onset of **p(DTPBBT)** is almost identical to that of **(4.5)** which further supports an increase in intermolecular interactions in the solid state. A summary of this data can be seen below in Table 11.

	2ThBT	**(4.6)**	**BDT**	**(4.4)**	**DTP**	**(4.5)**
Solution λ_{onset} (nm)	690, *775$_{sh}$*	700	555	600	620	670
Solid λ_{onset} (nm)	785	720	620	600	675	675
Shift (nm)	**95, *10$_{sh}$***	**20**	**65**	**0**	**55**	**5**

*Table 11 - Comparison of 2,6- (red) and 4,8- (black) BBT copolymer optical characteristics. Shoulder observed for **p(BBT2ThBT)** highlighted in italics for clarity.*

The combined data shows that in solution, the 4,8-derivatives have slightly larger band-gaps than the 2,6-derivatives. This is most prominent in **p(BDTBBT)** and **p(DTPBBT)** possibly due to increased steric hinderance caused by bulky alkyl chains on the donor monomer, which are absent in the 2,6-derivatives. The solid state energy gaps in the 4,8-polymers are narrowed substantially compared to that of the 2,6-polymers, likely due to the strong intermolecular interactions discussed in Chapter 2. The interactions in thin film, are strong enough to overcome

steric effects, affording a band gap which is narrower than, or equal to, the 2,6-polymers. For reference, a summary of the 2,6-polymer physical properties can be seen below in Table 12.

Polymer	M_w (kg mol^{-1})	PDI	Optical E_g (eV)	HOMO (eV)	LUMO (eV)
(4.6)	35[a]	1.2[a]	1.7	-5.5[b]	-3.8[c]
(4.4)	57[d]	2.9[d]	2.1	-5.7[e]	-3.3[e]
(4.5)	148[d]	2.8[d]	1.8	-4.8[e]	-3.3[e]

Table 12 – Literature 2,6-BBT polymer physical properties. [a]Calculated from GPC using polymer solution in THF at 40 °C.[b]Calculated from photoelectron spectroscopy. [c]Calculated using (E_g + E_{HOMO}).[d]Calculated from GPC using polymer solution in chlorobenzene at 60 °C. [e]Found from CV using the onset of redox activity and referenced to Fc/Fc^+. (Adapted from publications by Seki[131] and Jenekhe[59]).

The synthesised 4,8-polymers were then studied *via* cyclic voltammetry to determine the HOMO and LUMO energy levels, followed by GPC analysis to determine the molecular weight and polydispersity index. A summary of physical properties can be seen below in Table 13.

Polymer	M_w (kg mol^{-1})	PDI	Optical E_g (eV)[c]	Electrochemical E_g (eV)[d]	HOMO (eV)[d]	LUMO (eV)[d]
p(BBT2ThBT) $^{\alpha}$	17[a]	1.8	1.60	–	-5.20	-3.60[e]
p(BDTBBT) $^{\beta}$	61[b]	1.9	2.02	2.24	-5.29	-3.05
p(DTPBBT) $^{\gamma}$	N/A	N/A	1.84	2.11	-4.80	-2.69

Table 13 – 4,8-BBT donor polymer physical properties. . [a]Calculated from GPC using 0.5 mgml^{-1} solutions in chlorobenzene at 80 °C.[b]Calculated from GPC using 1 mgml^{-1} solutions in chloroform at 22 °C [c]Calculated from the onset of the longest wavelength absorption peak. [d]Found from CV, using the onset of redox activity and referenced to Fc/Fc^+ (-4.8 eV). [e]Calculated from Eg = (E_{HOMO} + Eg_{opt}). $^{\alpha}$Appendix 28. $^{\beta}$Appendix 30. $^{\gamma}$Appendix 32.

Interestingly, each of the 2,6-polymers possess HOMO and LUMO energies that are significantly different to that of the 4,8-polymers. Whilst **p(BBT2ThBT)** has a deeper HOMO and LUMO than that of **(4.6)**, **p(BDTBBT)** has a much shallower HOMO and LUMO than that of **(4.4)**. Futhermore, **p(DTPBBT)** possesses the same HOMO energy, but a much shallower LUMO than that of **(4.5)**. [*N.B. The absolute energy of **(4.6)** is adjusted by +0.5 eV to allow for comparison between the $PC_{71}BM$ LUMO of -3.7 eV (found from CV in-house) and the value determined by Seki at -4.2 eV. Variation in the determination of absolute energies can occur, depending on the method used and as such, $PC_{71}BM$ was used as a reference standard]*. Significantly, **(4.4)** and **(4.5)** both exhibit the same LUMO energy at -3.3 eV, whilst the LUMO of the 4,8-polymers varies substantially relative to the comonomer utilised. This further supports

the extensive delocalisation seen in the 4,8-polymers and highlights the excellent fine-tuning capabilities of the 4,8-BBT monomer.

Unexpectedly, the reduction CV for **p(BBT2ThBT)** as a thin film, showed no redox activity, even at potentials 1.5 V beyond the potential expected from the band-gap. This is surprising as, of the three polymers, **p(BBT2ThBT)** should possess the most n-type character, arising from its A_1-D-A_2-D structure. When conducted in solution, a reduction wave is visible (Appendix 29). The solution state HOMO and LUMO are determined as 4.96 and -3.34 eV respectively, suggesting that in the solid state, **p(BBT2ThBT)** exhibits a more electron-deficient nature than in solution. Due to the significant variation in energetics between solution and solid state observed from UV-Vis, it was determined more accurate to calculate the solid state LUMO from the electrochemical solid state HOMO, and the solid state optical E_g. For **p(BDTBBT)** and **p(DTPBBT)** both reduction and oxidation waves were clearly visible in the solid state and used to determine energy levels.

GPC analysis of **p(BBT2ThBT)** shows a moderately low molecular weight of 17 kg mol^{-1} and low polydispersity index of 1.8. The low molecular weight of this material can be attributed to the poor solubility afforded by the short hexyl and 2-ethylhexyl alkyl chains, compared to the significantly longer hexyl-decyl chains in **p(BDTBBT)** which has a molecular weight of 61 kg mol^{-1} and PDI of 1.9. Unfortunately, after **p(BBT2ThBT)** was analysed in chlorobenzene at 80 °C, access to this instrumentation was no longer posssible and, as a result, GPC analysis for **p(BDTBBT)** and **p(DTPBBT)** was conducted by Dr. Mariolino Carta in the group of Prof. Neil McKeown. Due to different instrument capabilities, analysis could therefore only be conducted in chloroform at 22 °C and, since **p(DTPBBT)** exhibits poor solubility in chloroform at rt, accurate determination of molecular weight could not be achieved. Furthermore, **p(BBT2ThBT)** and **p(BDTBBT)** have M_w and PDI values similar enough to **(4.6)** and **(4.4)** to allow for accurate comparison of physical properties.

As previously discussed, in order to achieved high efficiency OPV devices, balanced charge carrier mobilities should be obtained for both the donor and acceptor components. Therefore, to determine the hole mobility of these polymers, they were incorporated into bottom-gate, bottom-contact (BGBC) field-effect transistor devices using the same conditions as in Chapter 3. As before, the polymers were tested in the absence of self-assembled monolayers (SAM) or other chemical modification to better emulate the conditions during OPV fabrication. Solutions (10 mg/ml in *o*-DCB) were spin-coated at 2000 rpm onto commercially available pre-patterned SiO_2 substrates and annealed at 100 °C prior to testing in an N_2 filled dry-glovebox.

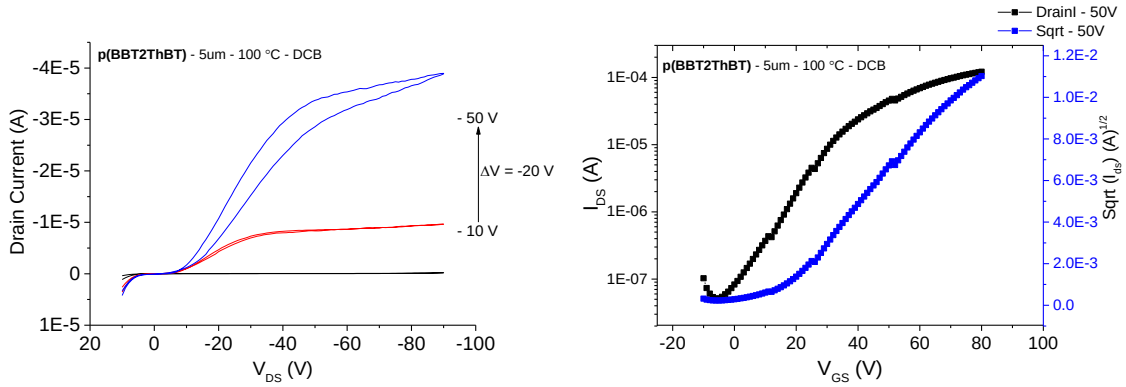

*Figure 96 - Output (left) and transfer (right) characteristics of **p(BBT2ThBT)** [5μm/DCB/100 °C].*

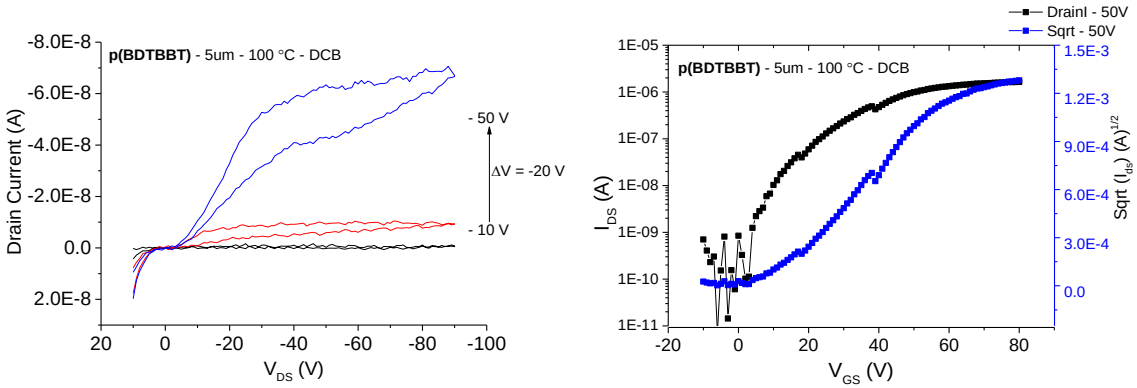

*Figure 97 - Output (left) and transfer (right) characteristics of **p(BDTBBT)** [5μm/DCB/100 °C].*

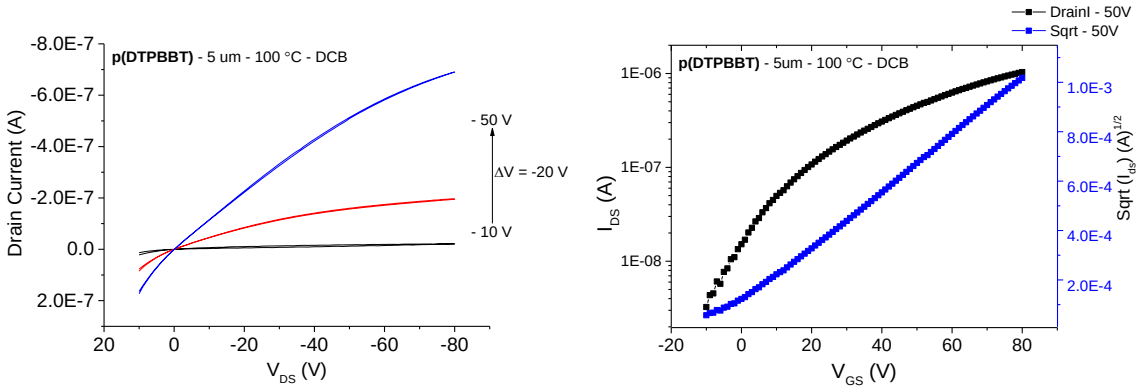

*Figure 98 - Output (left) and transfer (right) characteristics of **p(DTPBBT)** [5mm/DCB/100 °C].*

The output and transfer characteristics of these polymers all show typical p-type behaviour. **p(BDTBBT)** exhibits significant hysteresis in both the output and transfer characteristics. This is attributed to contact resistance between the gold electrode (work function of -5.0 – -5.1 eV) and the HOMO of the polymer at -5.3 eV. This hysteresis is reduced in the case of **p(BBT2ThBT)** due to the shallower HOMO at -5.2 eV and further reduced to an insiginificant

amount in **p(DTPBBT)** with the HOMO at -4.80 eV. A summary of the device performance for these materials is given in Table 14).

Material	μ_h ($cm^2V^{-1}s^{-1}$)	I_{on}/I_{off}	V_{th} (V)
p(BBT2ThBT)	4.97×10^{-3}	10^4	5
p(BDTBBT)	1.36×10^{-4}	10^4	-2
p(DTPBBT)	3.14×10^{-5}	10^3	-10

Table 14 - OFET device parameters of BBT copolymers

Whilst these devices were fabricated to probe charge carrier properties, the hole mobility of **p(BBT2ThBT)** is over two orders of magnitude higher than all-BT analogue **PT3B1**, (Figure 99) which exhibits a hole mobility of 3.0×10^{-5} $cm^2V^{-1}s^{-1}$ under similar fabrication conditions.[163] This result highlights the increased crystallinity afforded by incorporation of BBT into the polymer backbone.

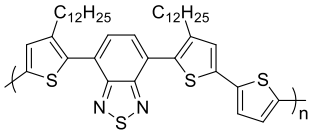

*Figure 99 – Structure of polymer **PT3B1**.* [163]

The hole mobility of each of these materials is expected to be sufficient to allow for effective charge dissociation in OPV devices, with **p(BBT2ThBT)** expected to exhibit a high FF as a result of balanced polymer/fullerene charge carrier mobilities.

At the University of St Andrews, **p(BBT2ThBT)** was investigated as a donor for BHJ solar cells with $PC_{71}BM$ (see Chapter 5 – Experimental for full fabrication details). First, the absorption spectra of blend films, fabricated using various D:A ratios were measured.

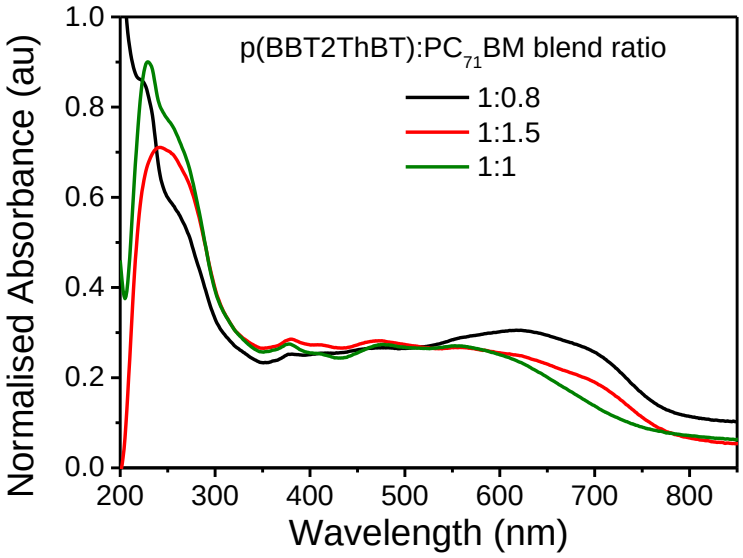

*Figure 100 - UV-Visible absorption of **p(BBT2ThBT)**:PC71BM blend films. (Adapted with permission from S. Ghosh).*

The UV-Vis absorption of the blend films, exhibit excellent coverage of the visible spectrum, from 800-200 nm. The long wavelength absorption band is increased in intensity when the D:A ratio is reduced from 1:1 to 1:1.5. This is indicative of increased intermolecular charge transfer band in the 1:1.5 blend. This band is further increased when the blend ratio is set at 1:0.8, suggesting an optimum ratio for formation of charge transfer states. To confirm this, OPV devices were fabricated and tested with D:A ratios of 1:0.8, 1:1 and 1:1.5 (Figure 101).

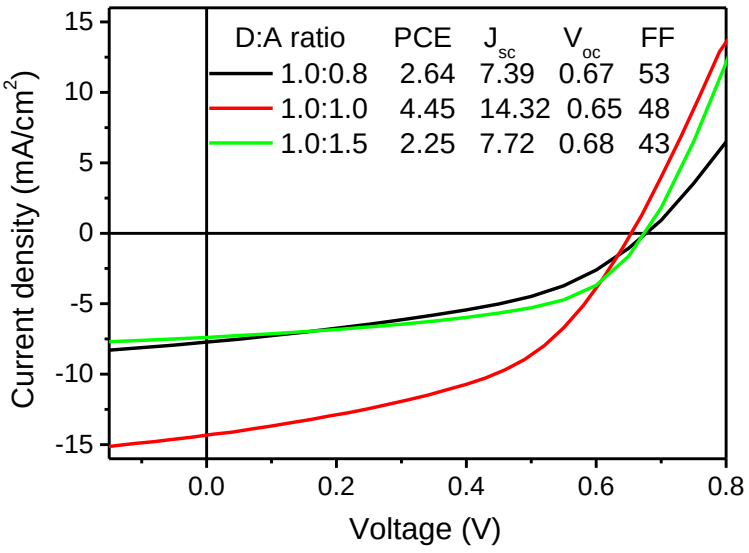

Figure 101 - JV parameters for various blend ratios. Device architecture – ITO/PEDOT:PSS/Active layer/Ca/Al. (Adapted with permission from S. Ghosh).

Contrary to the absorption data, the blend ratio of 1:1 yields the best device efficiency, as a result of significantly increased J_{sc} generation, as well as moderate FF. This increase in J_{sc} is attributed to improved charge extraction from the 1:1 blend film. The increased exciton generation expected from the 1:0.8 blend is offset by a reduction in charge separation.

Further to this, the device thickness was varied to determine the optimal active layer thickness. The results of this study can be seen in Figure 102 below.

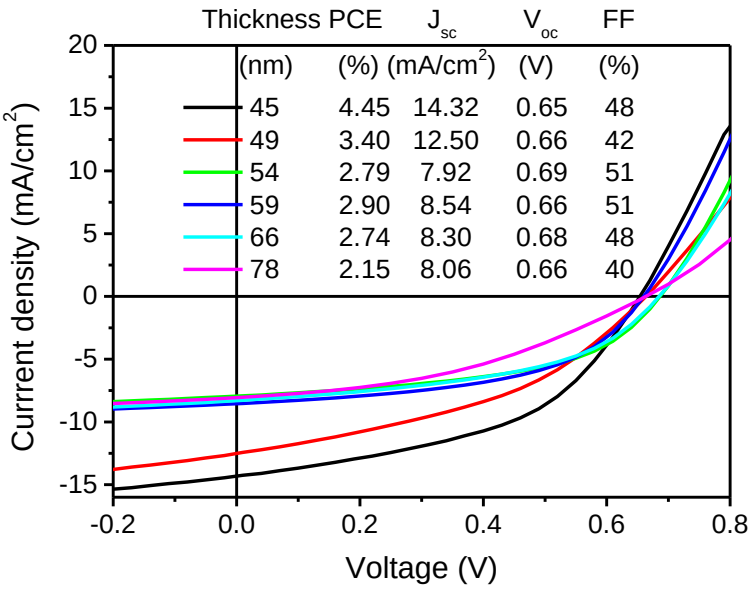

Figure 102 - JV parameters for varying active layer thickness. Device architecture – ITO/PEDOT:PSS/Active layer/Ca/Al. (Adapted with permission from S. Ghosh).

Figure 102 shows that of the thicknesses tested, 45 nm results in devices of the highest efficiency. This suggests that the increased optical absorption density of the thicker films, is offset by increased exciton recombination. This is common in organic solar cells and is often attributed to the very short exciton diffusion length, typically around 10nm.[90]

Surprisingly, for all of the devices fabricated thus far, the V_{oc} is significantly lower than expected from the material energy levels. V_{oc} is directly proportional to the offset between the LUMO of the acceptor and the HOMO of the donor.[164] In this case, the V_{oc} is expected to be on the order of 1 V as a result of the deep lying HOMO of **p(BBT2ThBT)**. However, this is not the case and can be explained due to loss of potential at the contact due to non-ohmic interfaces.[165]

The very high J_{sc} generated from this device indicates that this material is a promising candidate for high-efficiency OPV devices. A similar J_{sc} of 15.4 mA/cm^2 is obtained using the record single junction solar cell material PTB7 in the conventional architecture. Combined with a FF of

70.6 % and V_{oc} of 0.759, this material yields a certified efficiency of 8.24% in PTB7:$PC_{71}BM$ solar cells.[108] The deeper HOMO and LUMO of **p(BBT2ThBT)** relative to PTB7, is expected to lead to an increase in V_{oc} for this material leading to increased efficiency.[88]

Both V_{oc} and FF are commonly improved as a result of improved fabrication procedures. A common method involves the use of solvent additives, such as chloronaphthalene (CN), which is added as a slow evaporating solvent to reduce polymer:fullerene phase segregation.[166] Whilst 3% diiodooctane (DIO) v/v was used in this study, variation of additive % v/v can have substantial impact on device performance and therefore further optimisation is likely to yield improved PCE. Furthermore, by fabrication of inverted solar cells, electron transport layers can be incorporated. As a result, ohmic contacts are achieved at both the anode and cathode of the OPV devices often resulting in significant improvement in V_{oc}, FF and J_{sc}.[108, 110, 144]

Comparison of the performance capabilities of 2,6- and 4,8-BBT copolymers can be achieved by comparing the OPV device performance of **(4.6)** and **p(BBT2ThBT)**. A summary of both polymers performance is given in Table 15 below.

Polymer	μ_{hole} ($cm^2V^{-1}s^{-1}$)	η (%)	J_{sc} (mA/cm^2)	V_{oc} (V)	FF (%)
p(BBT2ThBT)	$^{\alpha}4.97 \times 10^{-3}$	4.45^{γ}	14.32^{γ}	0.65^{γ}	48^{γ}
(4.6)	$^{\beta}5 \times 10^{-4}$	2.37^{γ}	5.74^{γ}	0.83^{γ}	50^{γ}
		3.84^{δ}	8.01^{δ}	0.84^{δ}	57^{δ}

Table 15 – Device performance of similar 2,6- and 4,8-BBT copolymer donors. $^{\alpha}$Calculated from BGBC FET devices. $^{\beta}$Calculated from time-resolved microwave conductivity. $^{\gamma}$Conventional device – ITO/PEDOT:PSS/Active layer/Ca/Al. Inverted device – ITO/TiO_x/Active layer/MoO_x/Au. Adapted from work published by Seki and co-workers.[131]

Interestingly, despite **(4.6)** having a higher molecular weight, **p(BBT2ThBT)** exhibits an order of magnitude higher hole mobility. This is made more significant when it is considered that the mobility of **(4.6)** was measured using time-resolved microwave conductivity (TRMC) which has been previously shown to yield significantly higher mobility values than bulk methods.[138] TMRC measures intrinsic (intrachain) mobility and as a result, is unaffected by bulk disorder or grain boundaries.[138]

When comparing the performance in conventional solar cells of the same architecture, **p(BBT2ThBT)** yields a power conversion efficiency 88% greater than that of **(4.6)** as a result of notably higher J_{sc}. When **(4.6)** is fabricated into inverted solar cells, both the FF and J_{sc} are significantly improved, a result akin to that of other research groups, affording an overall PCE

increase of 62%.[108, 110, 167] Therefore, it is reasonable to assume that by incorporating **p(BBT2ThBT)** into inverted solar cells, an increase in PCE could be realised. Further investigations of this material, as well as **p(BDTBBT)** and **p(DTPBBT)** are on-going.

4.4 Conclusions and Future work

Three 4,8-BBT containing conjugated polymers - of which there are analogous 2,6-derivatives in the literature - were synthesised as donor materials for bulk heterojunction solar cells. The polymers were synthesised *via* Stille polymerisation and their physical properties characterised by NMR, elemental analysis, DSC, UV-Visible spectroscopy, cyclic voltammetry, and GPC analysis. Comparison of polymer physical properties indicates that 4,8-BBT derivatives benefit from increased backbone delocalisation, allowing for fine-tuning of the HOMO and LUMO energies (See Chapter 2 for more details).

Furthermore, the charge carrier properties of the synthesised polymers were investigated by fabricating bottom-gate, bottom-contact organic field effect transistors. The polymers were all found to be p-type conducting, with hole mobilities of up to 5 x 10^{-3} $cm^2V^{-1}s^{-1}$ achieved for **p(BBT2ThBT)**, which is at least 1 order of magnitude higher than that of the corresponding 2,6-derivative.

Of the three synthesised polymers, **p(BBT2ThBT)** indicated the most "ideal" properties for polymer:fullerene solar cells and yielded 4.45% efficiency, compared with 2.37% for the 2,6-polymer, in the conventional architecture. The remarkable J_{sc} of 14.32 mA cm^{-2} for this material highlights the excellent light-harvesting capabilities of 4,8-BBT polymers. Further optimisation of device architecture is on-going and is expected to improve overall PCE, paralleling that of other reports. OPV device performance of **p(BDTBBT)** and **p(DTPBBT)** is currently being investigated at the University of St Andrews.

Recently, fluorination of the backbone in conjugated polymers has been shown to improve device performance as a result of increased crystallinity, deeper HOMO energy and enhanced intermolecular packing.[168, 169] This is particularly evident when the acceptor unit benzothiadiazole is replaced with difluorobenzothiadiazole as in the polymers synthesised by Li and co-workers (Figure 103).

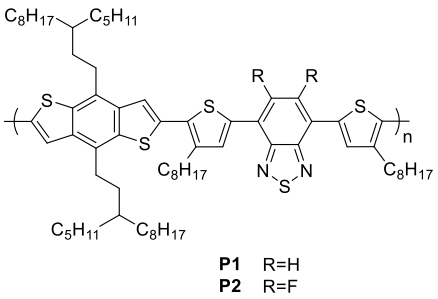

Figure 103 - Benzothiadiazole (left) and difluorobenzothiadiazole (right) containing donor polymers.[170]

P2 yields OPV devices with 3.40% efficiency compared to 1.88% for **P1** due to improved intermolecular packing and deeper HOMO energy. Therefore, *via* incorporation of difluorobenzothiadiazole into **p(BBT2ThBT)**, further improvements in OPV performance could be realised (Figure 104).

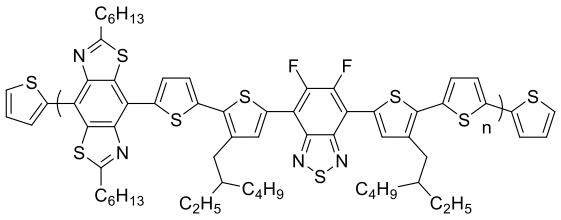

*Figure 104 - Proposed fluoro-**p(BBT2ThBT)** polymer.*

5 Experimental

General Experimental

LDA was purchased from Sigma Aldrich and titrated against (+)-menthol with 2,2-bipyridyl as an indicator before use. *n*-BuLi was purchased from Sigma Aldrich and titrated against diphenylacetic acid before use. TMP was purchased from alfa aesar and freshly distilled from CaH before use. NBS was purchased from Sigma Aldrich and recrystallized from water, dried under vacuum and stored under Ar. $Pd(PPh_3)_4$ was synthesised prior to use and stored under Ar. Unless otherwise stated all other reagents were sourced commercially and used without further purification. Microwave syntheses were conducted using Biotage Initiator Classic microwave heating apparatus. Commercial TLC plates (Silica gel 60 F254) were used for thin-layer chromatography and column chromatography was performed on silica gel Zeoprep 60 Hyd (40-63 µm mesh). Solvents were removed using a rotary evaporator (vacuum supplied by low vacuum pump) and, when necessary, a high vacuum pump was used to remove residual volatiles. Distillation of high boiling liquids was performed on a Kugelrohr Z24 with a high vacuum pump. Dry solvents were obtained from a solvent purification system using alumina as drying agent (SPS 400 from Innovative Technologies).

^{1}H and ^{13}C NMR spectra were recorded on either a Bruker AVIII 400 or Bruker AV400 at 400MHz and 100MHz, or a Bruker DRX500 apparatus at 500MHz and 125MHz. Chemical shifts are given in ppm; all *J* values are in Hz and samples are referenced to residual solvent peaks. Elemental analyses were obtained on a Perkin-Elmer 2400 analyser and MALDI-TOF spectra were run on a Shimadzu Axima-CFR spectrometer (mass range 1-150000 Da).

Differential Scanning Calorimetry was conducted on a TA Instruments Q1000 with a RC-90 refrigerated cooling unit attached. The calibration was conducted using Indium (melt temperature 156.42°C, ΔH_f 28.42 J/g). The test procedure used was a standard Heat-Cool-Reheat, which allows the removal of thermal history on the first heat allowing examination of any thermal processes on the cooling and second heat scan. The temperature range was from -50 °C to 300 °C at 10 °C/min unless otherwise stated. For thermogravimetric analysis, the sample (approx. 5 mg) was placed on a standard platinum pan and loaded at 35 °C to be analysed with a Perkin Elmer. Thermogravimetric Analyser (TGA7) under a constant flow of Ar (20 mL/min). The temperature was raised to 50 °C followed by an isothermal period of 5 minutes. The temperature was raised again at a rate of 10 °C/min until the desired temperature, at which point, the material was left for an isothermal period of 30 minutes. The percentage weight loss

over time was recorded at this temperature and the data was processed using the Pyris Series Software.

UV-Vis-NIR spectroscopy was conducted on a Shimadzu 2600 spectrophotometer fitted with an integrating sphere and results normalised to λ_{max}. Fluorescence spectroscopy measurements were conducted on Perkin Elmer LS45 or Jasco FP-6500 fluorescence spectrometers. CV measurements were performed on a CH Instruments 660A electrochemical workstation with *iR* compensation using anhydrous solvents (dichloromethane or acetonitrile). The electrodes were 8mm platinum disk, platinum wire, and silver wire as the working, counter, and reference electrodes, respectively. All solutions were degassed (Ar) and contained monomer substrates in concentrations *ca.* 10^{-4} M, together with $TBAPF_6$ (0.1 M) as the supporting electrolyte. All measurements are displayed relative to the $E_{1/2}$ of the Fc/Fc^+ redox couple. Thin-film CV measurements were conducted using material drop-cast from an appropriate solvent ($CHCl_3$ or chlorobenzene) onto the disk electrode and dried under low vacuum before use.

Analysis of polymer molecular weight and distribution was performed on an Agilent 1200 series GPC system using chlorobenzene as eluent with a column temperature of 80 °C.

Atomic force microscopy (AFM) experiments were performed on a Nanoscope III AFM (Digital Instruments) under ambient conditions. The charge carrier properties of polymers were investigated by fabricating bottom gate/bottom contact (BGBC) TFTs. The polymers were dissolved in chloroform, chlorobenzene or *o*-dichlorobenzene (10 $mgmL^{-1}$) at 50 °C on a hot plate for at least 3 h, then deposited by spin-coating the polymer at 2000 rpm in a nitrogen filled glovebox whilst hot. The films were annealed at elevated temperature under N_2. Commercially available (Fraunhofer institute) n-doped silicon chips with 200 nm of thermally grown SiO_2 with prefabricated interdigitated Au fingers (50 nm S/D electrodes) were used as substrates. Channel lengths were 2.5, 5, 10 and 20 μm, and the channel width was 1 μm. The semiconductor performance was measured on a Keithley 4200 semiconductor characterisation system. Mobilities were calculated in the saturation region *via* the standard method using Equation 10 as follows:

$$\mu_{sat} = \frac{2L}{WC_i} \times \left(\frac{\partial\sqrt{I_d}}{\partial V_g}\right)^2$$

Equation 10 - Calculation of saturation mobility

Where I_d is the source drain current, μ is the carrier mobility, V_g is the gate voltage, L is the channel length, W is the channel width and C is the capacitance per unit area of the insulator material.

Solar cells were fabricated on patterned ITO coated glass substrates (Xinyan Technology Ltd.) having sheet resistance of 10-13 ohm/cm^2. The substrates were cleaned by ultra-sonication in acetone and isopropyl alcohol successively for 10 mins each before drying in an oven at 100 °C. The dried substrates were then treated with oxygen plasma for 3 mins before being coated with poly(3,4-ethylenedioxythiophene)-poly(styrenesulfonate) (PEDOT-PSS) (CLEVIOS™ P VP AI 4083) *via* spin-coating at 4000 rpm to obtain films of ~30 nm thickness. The films were then annealed on a hot plate at 140 ^{o}C for 10 mins to remove the residual moisture. The dried substrates were then transferred into a nitrogen glove box to deposit the active layer blend. The blend solution (in *o*-dichlorobenzene) was stirred at 40 °C for at least 24h prior to being spin coated at 800. 3% (v/v) Diiodooctane (DIO) was added into the solution before spin coating as a solvent additive. The solution concentration and rpm were varied to provide films of different thicknesses. Calcium layer of thickness of 15 nm followed by a 100 nm aluminium layer were evaporated at a pressure of 2 x 10^{-6} mbar. Active areas of devices (2 x 4 mm^2) were defined by a shadow mask. The devices were then encapsulated by using UV-curable epoxy to glue a glass slide over the device. The current-voltage (*J*-*V*) characteristics were measured using a Keithley 2400 source measure unit and a Science-Tech, SS150 solar simulator under illumination at 100 mW/cm^2 intensity. The light intensity at the test surface was calibrated using a Newport Oriel reference cell. For *J*-*V* measurement of the solar cells a shadow mask equal to the size of the test pixel was used.

Tetrakis(triphenylphosphine) palladium(0)

$Pd[(PPh_3)_4]$

Palladium (II) chloride (0.5 g, 2.82 mmol) and triphenylphosphine (3.7 g, 14.11 mmol), suspended in dry DMSO (40 mL) and under Ar, were heated with rapid stirring to 140 °C, where complete dissolution occurred. Hydrazine monohydrate (0.35 mL, 11.28 mmol) was then added rapidly *via* syringe (vigorous reaction) to produce a dark solution. The solution was cooled with the aid of a water bath until crystallisation began to occur (ca. 125 °C). The water bath was removed and the solution was then allowed to cool to room temperature without external cooling. The mixture was filtered under Ar and the precipitate washed with anhydrous MeOH (3 x 15 mL) and Et_2O (3 x 15 mL) to give the product as a bright yellow solid. (3.1 g, 96 %).

1,1'-(1,4-Phenylene)bis(thiourea) ***(2.1)***[112]

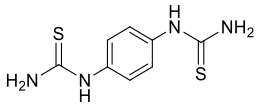

Benzene-1,4-diamine (17.0 g, 157 mmol), hydrochloric acid (30.7 mL, 125 mmol) and activated charcoal (1.1 g, 157 mmol) were added to a 500 mL round bottom flask then heated to 50 °C. The mixture was then filtered through a pad of celite, directly into another 500 mL flask. Ammonium thiocyanate (48.4 g, 636 mmol) was then added and the reaction heated at 95 °C for 24 h with stirring. A yellow granular product precipitated during the reaction. The mixture was allowed to cool and the product was filtered and washed with hot water (2 x 40 mL). The yellow granular product was dried in a vacuum desiccator for 48 h and used without further purification (31.9 g, 90 %); m.p.: 280 °C (dec); ^{1}H NMR; δ_H (400 MHz DMSO-d^6): 10.08 (4H, s, NH_2), 7.80-8.04 (4H, m, Ar-H). The analysis was comparable with previously published data.[112]

Large scale synthesis of ***(2.1)***

Benzene-1,4-diamine (53.3 g, 493 mmol), degassed water (330 mL), hydrochloric acid (97 mL, 3.9 mol) and activated charcoal (3.5 g) were added to a 1 L round bottom flask then heated to 50 °C under Ar. The mixture was then filtered through a pad of celite, directly into another 1 L flask. Ammonium thiocyanate (150 g, 1.97 mol) was then added and the reaction heated at 95 °C for 24 h with stirring. A yellow granular product precipitated during the reaction. The

mixture was allowed to cool and the product was filtered and washed with hot water (2 x 400 mL). The yellow granular product was dried in a vacuum desiccator for 48 h and used without further purification (106.3 g, 95 %); m.p.: 280 °C (dec); ^{1}H NMR; δ_H (400 MHz DMSO-d^6): 10.08 (4H, s, NH_2), 7.80-8.04 (4H, m, Ar-H). The analysis was comparable with previously published data.[112]

*Benzo[1,2-d:4,5-d']bis(thiazole)-2,6-diamine **(2.2)**[61]*

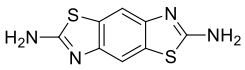

To a stirred suspension of 1,1'-(1,4-phenylene)bis(thiourea) **(2.1)** (30 g, 133 mmol) in chloroform (80 mL) was added a solution of bromine (15.8 mL, 307 mmol) in chloroform (100 mL) slowly, as to prevent the reaction exceeding 50 °C. The orange slurry was stirred at rt. overnight. The reaction was then heated to reflux for 24 h. The reaction was allowed to cool before being filtered and washed with chloroform (4 x 300 mL). The product was then stirred with 20% sodium bisulfite solution at 90 °C until the orange colour subsided. The solid was filtered off when cold before being dissolved in boiling dilute HCl (1500 mL) and stirred with activated carbon for 3 h before being filtered through celite. Basification with ammonia precipitated a white amorphous solid. The solid was filtered, washed (3 x 100 mL methanol then 100 mL diethyl ether) and then dried in a vacuum desiccator (24.8 g, 84 %); m.p: >350 °C (>350 °C lit.); ^{1}H NMR; δ_H (400 MHz DMSO-d^6): 7.74 (2H, s, Ar-H), 7.43 (4H, s, NH_2). This was consistent with previously published data.[61]

*Large scale synthesis of **(2.2)***

To a stirred suspension of 1,1'-(1,4-phenylene)bis(thiourea) **(2.1)** (120 g, 530 mmol) in chloroform (320 mL) was added a solution of bromine (63 mL, 1.2 mol) in chloroform (400 mL) slowly, as to prevent the reaction exceeding 50 °C. The orange slurry was stirred at rt. overnight. The reaction was then heated to reflux for 24 h. The reaction was allowed to cool before being filtered and washed with chloroform (4 x 500 mL). The product was then stirred with 20% sodium bisulfite solution at 90 °C until the orange colour subsided. The solid was filtered off when cold before being split into 4 equal batches and each dissolved in boiling dilute HCl (1500 mL), stirred with activated carbon for 3 h and filtered through celite. Basification with ammonia precipitated a white amorphous solid. The solid was filtered, washed (3 x 100 mL methanol then 100 mL diethyl ether) before being combined and then dried in a vacuum

desiccator (101.4 g, 86 %); m.p: >350 °C (>350 °C lit.); ^{1}H NMR; δ_H (400 MHz DMSO-d^6): 7.74 (2H, s, Ar-H), 7.43 (4H, s, NH_2). This was consistent with previously published data.[61]

2,5-Diaminobenzene-1,4-dithiol dihydrochloride ***(2.3)***[112]

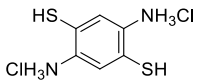

Benzo[1,2-d:4,5-d']bis(thiazole)-2,6-diamine (12.0 g, 54.0 mmol) **(2.2)** was added to a 250 mL round bottomed flask and the flask degassed several times. Potassium hydroxide (48.5 g, 864 mmol) was dissolved in another round bottom flask in degassed water (60 mL) then transferred via syringe to the reaction flask. The mixture was stirred for 5 h under reflux then cooled overnight with stirring. The resulting mixture was filtered under Ar. The yellow precipitate was then dissolved in deaerated water (60 mL) and filtered directly into a flask containing deaerated water (120 mL) and concentrated hydrochloric acid (120 mL). The resulting white crystals were filtered, washed with degassed methanol and dried under Ar for 1 h before being used immediately in the next step without purification or exposure to air.

2,6-Dihexylbenzo[1,2-d:4,5-d']bis(thiazole) ***(2.4)***

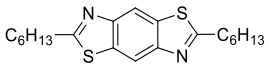

To an evacuated 250 mL 2-neck flask containing freshly synthesized **(2.3)** under Ar was added 1,2-dichlorobenzene (100 mL), heptanoyl chloride (18.9 mL, 122 mmol) and trimethylsilyl polyphosphate (33.7 mL, 294 mmol). The flask was heated to reflux for 48 h under Ar. Upon cooling, the solution was quenched with sat. $NaHCO_3$ solution and then extracted with dichloromethane (3 x 100 mL). The solution was then washed with sat. $NaHCO_3$ (3 x 200 mL) and brine (200 mL). The combined organics were then dried ($MgSO_4$) and the dichloromethane removed by rotary evaporation. The dichlorobenzene was distilled via Kughelrohr distillation and the resulting dark brown residue purified by silica gel column chromatography eluting with dichloromethane. The off-white solid was reprecipitated from dichloromethane/methanol and dried under vacuum to yield the *title compound* as a white solid (8.9 g, 46% over two steps); m.p.: 102 – 104 °C; ^{1}H NMR; δ_H (400 MHz $CDCl_3$): 8.38 (2H, s, Ar-H), 3.13 (4H, t, *J* 7.8 Hz, CH_2), 1.90 (4H, quint, *J* 7.7 Hz CH_2), 1.50-1.26 (12H, m, CH_2), 0.90 (6H, t, *J* 7.0 Hz, CH_3); ^{13}C NMR; δ_C (125 MHz, $CDCl_3$): 173.7, 151.3, 134.4, 114.9, 35.0, 31.8, 29.9, 29.2, 22.8, 14.3; *m/z* (MALDI-TOF): 361; HRMS calculated for $C_{20}H_{28}N_2S_2$: 361.1761. Found 361.1767.

4,8-Dibromo-2,6-dihexylbenzo[1,2-d:4,5-d']bis(thiazole) **(2.5)**

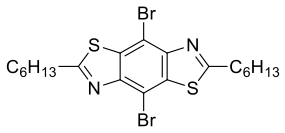

2,6-Dihexylbenzo[1,2-d:4,5-d']bis(thiazole) (8.0 g, 22.19 mmol) **(2.4)** was added to a 250 mL two neck flask under Ar. Dichloromethane (80 mL) was then added and the flask cooled to 0 °C. Bromine (2.8 mL, 55.5 mmol) in dichloromethane (80 mL) was then added dropwise while at 0 °C. The reaction was then stirred at 0 °C for 6 h and then allowed to stir at r.t. overnight. The mixture was then diluted with dichloromethane (250 mL), quenched with sat. sodium sulphite (50 mL) and washed with water (2 x 100 mL), before being dried ($MgSO_4$) and concentrated to dryness. Purification by silica gel column chromatography eluting with 3:2 hexane:dichloromethane yielded a white solid, which was recrystallized with hexane:methanol to yield the *title compound* as a white crystalline solid (5.1 g, 45%); m.p.: 114 – 117 °C; ^{1}H NMR; δ_H (400 MHz $CDCl_3$): 3.17 (4H, t, *J* 7.8 Hz, CH_2), 1.90 (4H, quint, *J* 7.7 Hz CH_2), 1.50-1.26 (12H, m, CH_2), 0.92 (6H, t, *J* 7.0 Hz, CH_3); ^{13}C NMR; δ_C (125 MHz, $CDCl_3$): 174.8, 148.1, 137.4, 106.2, 35.3, 31.8, 30.1, 29.2, 22.8, 14.4; *m/z* (MALDI-TOF): 519; Anal. Calculated for $C_{20}H_{26}Br_2N_2S_2$: C, 46.34; H, 5.06; N, 5.40. Found C, 46.46; H, 5.01; N, 5.28.

2-(Tributylstannyl)thiazole ***(2.6)***[171]

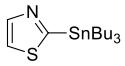

To a stirred solution of thiazole (1.0 g, 11.75 mmol) in dry diethyl ether (45 mL) under Ar, was added n-butyllithium (5.38 mL, 12.92 mmol, 2.38M in hexane) dropwise at −50 °C. The mixture was stirred at −50 °C for 1 h and then tributylstannyl chloride (3.66 mL, 13.51 mmol) was added dropwise. After one additional hour at low temperature, the resulting mixture was warmed to r.t. and stirred overnight. The reaction mixture was washed with saturated aqueous $NaHCO_3$ (50 mL) and brine (50 mL) before being dried ($MgSO_4$) and the solvent removed in vacuo to yield the title compound as a yellow oil which was used without further purification (4.26 g, 97%). ^{1}H NMR; δ_H (400 MHz $CDCl_3$): 8.16 (1H, d, *J* 3.0 Hz, Ar-H), 7.54 (1H, d, *J* 3.0 Hz, Ar-H), 1.65-1.55 (6H, m, CH_2), 1.40-1.20 (12H, m, CH_2), 0.89 (9H, s, CH_3). This was consistent with previously published data.[171]

2,6-Dihexyl-4,8-di(thiazol-2-yl)benzo[1,2-d:4,5-d']bis(thiazole) ***(2.7)***

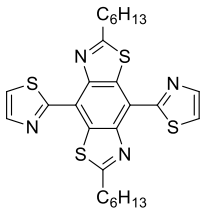

4,8-Dibromo-2,6-dihexylbenzo[1,2-d:4,5-d']bis(thiazole) **(2.5)** (100 mg, 0.193 mmol), and tetrakis(triphenylphosphine) palladium(0) (44.6 mg, 0.039 mmol) were added to a 50 mL round bottom flask under Ar. 2-(Tributylstannyl)thiazole **(2.6)** (180 mg, 0.482 mmol) was added and the flask purged further with Ar. Dry toluene (20 mL) was then added and reaction was heated to 100 °C for 24 h then cooled. The solution was diluted with dichloromethane (100 mL) and washed with water (100 mL) and brine (100 mL) before being dried ($MgSO_4$) and concentrated to dryness. The crude residue was purified by silica gel column chromatography eluting with 1:1 dichloromethane:hexane to yield a yellow powder which was recrystallized from ethanol to yield the *title compound* as fine yellow needles (76 mg, 75% yield). ^{1}H NMR; δ_H (400 MHz $CDCl_3$): 8.14 (2H, d, *J* 3.3 Hz, Ar-H), 7.58 (2H, d, *J* 3.3 Hz, Ar-H), 3.27 (4H, t, *J* 7.6 Hz, CH_2) 2.07 (4H, quint, *J* 7.5 Hz CH_2), 1.60-1.50 (4H, m, CH_2), 1.47-1.30 (8H, m, CH_2), 0.92 (6H, t, *J* 7.0 Hz, CH_3); ^{13}C NMR; δ_C (125 MHz, $CDCl_3$): 177.1, 161.9, 147.1, 141.7, 131.0, 122.0, 120.5, 33.74, 31.09, 28.64, 28.41, 22.06, 13.62; *m/z* (MALDI-TOF): 527; HRMS calculated for $C_{26}H_{30}N_4S_4$: 527.1426. Found: 527.1418. *See Appendix 1 for DSC analysis.*

4,8-Di(furan-2-yl)-2,6-dihexylbenzo[1,2-d:4,5-d']bis(thiazole) ***(2.8)***

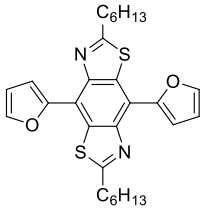

To a 50 mL round bottom flask under Ar was added tributyl(furan-2-yl)stannane (0.23 mL, 0.723 mmol), 4,8-dibromo-2,6-dihexylbenzo[1,2-d:4,5-d']bis(thiazole) **(2.5)** (150 mg, 0.289 mmol) and tetrakis(triphenylphosphine) palladium(0) (67 mg, 0.058 mmol), and the flask then evacuated again with Ar. Dry toluene (15 mL) was then added *via* syringe and the flask heated to reflux for 24 h before being cooled and poured into water. The solution was then extracted with dichloromethane (3 x 50 mL) and the combined organic layers washed with water (2 x 50

mL), dried ($MgSO_4$) and concentrated to dryness. Silica gel column chromatography eluting with 1:2 dichloromethane:hexane yielded the product as an off-white solid which was further purified by recrystallisation from hexane to yield the *title compound* as fine, off-white needles (95 mg, 67%). ^{1}H NMR; δ_H (400 MHz $CDCl_3$): 7.90 (2H, d, *J* 3.4 Hz, Ar-H), 7.72 (2H, d, *J* 1.4 Hz, Ar-H), 6.68 (2H, dd, ^4J 1.7, ^3J 3.4 Hz, Ar-H), 3.23 (4H, t, *J* 7.6 Hz, CH_2) 2.00 (4H, quint, *J* 7.5 Hz CH_2), 1.57-1.48 (4H, m, CH_2), 1.45-1.30 (8H, m, CH_2), 0.92 (6H, t, J 7.0 Hz, CH_3); ^{13}C NMR; δ_C (125 MHz, $CDCl_3$): 174.5, 150.6, 146.8, 142.4, 130.6, 117.1, 113.6, 112.9, 34.8, 31.9, 29.7, 29.3, 22.9, 14.4; m/z (MALDI-TOF): 492; Anal. Calculated for $C_{28}H_{32}N_2O_2S_2$: C, 68.26; H, 6.55; N, 5.69. Found C, 68.11; H, 6.49; N, 5.72. *See Appendix 2 for DSC analysis.*

2,6-Dihexyl-4,8-di(thiophen-2-yl)benzo[1,2-d:4,5-d']bis(thiazole) ***(2.9)***[121]

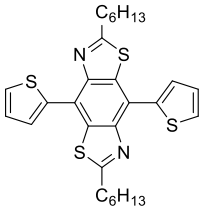

To a 25 mL round bottom flask under Ar was added 4,8-dibromo-2,6-dihexylbenzo[1,2-d:4,5-d']bis(thiazole) **(2.5)** (100 mg, 0.193 mmol), tributyl(thiophen-2-yl)stannane (216 mg, 0.579 mmol) and tetrakis(triphenylphosphine) palladium(0) (45 mg, 0.039 mmol). Anhydrous toluene (10 mL) was then added *via* syringe and the reaction heated to reflux for 24 h. Once cool, the reaction was passed through a short silica gel plug eluting with dichloromethane before being concentrated *via* rotary evaporation. The resulting off-yellow solid was recrystallised from hexane to yield the title compound as bright yellow crystals (62 mg, 62 %); ^{1}H NMR; δ_H (400 MHz $CDCl_3$): 7.93 (2H, dd, *J* 3.7, 1.0 Hz, Ar-H), 7.54 (2H, dd, *J* 5.1, 1.0 Hz, Ar-H), 7.24 (2H, dd, *J* 5.1, 3.7 Hz, Ar-H), 3.18 (4H, t, *J* 7.5 Hz, CH_2), 1.96 (4H, m, CH_2), 1.59-1.29 (12H, m, CH_2), 0.86 (6H, m, CH_3). This was consistent with previously published data.[121]

4,8-Di(benzofuran-2-yl)-2,6-dihexylbenzo[1,2-d:4,5-d']bis(thiazole) ***(2.10)***

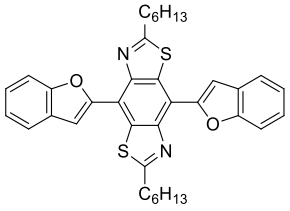

To a 5 mL microwave vial under Ar was added 4,8-dibromo-2,6-dihexylbenzo[1,2-d:4,5-d']bis(thiazole) **(2.5)** (100 mg, 0.193 mmol), 2-benzofuranylboronic acid MIDA ester (93 mg, 0.579 mmol), tetrakis(triphenylphosphine) palladium(0) (45 mg, 0.039 mmol) and barium hydroxide octahydrate (262 mg, 0.830 mmol), and the flask evacuated several times with Ar. Dry tetrahydrofuran (4 mL) and degassed water (1 mL) were then added and the flask fitted with a cap. The vial was then heated to 120 °C for 2 h in the microwave. The reaction was then cooled before being poured into water (50 mL) and extracted with dichloromethane (3 x 50 mL). The combined organic layers were then washed with (50 mL) water before being dried ($MgSO_4$) and concentrated to dryness. The crude residue was purified by silica gel column chromatography eluting with 20% dichloromethane in hexane. The yellow powder was recrystallised from hexane to yield the *title compound* as fibrous crystals (74 mg, 65%). ^{1}H NMR; δ_H (400 MHz CD_2Cl_2): 8.38 (2H, s, Ar-H), 7.74 (2H, d, *J* 7.5 Hz, Ar-H), 7.68 (2H, d, *J* 8.0 Hz, Ar-H), 7.42-7.35 (2H, m, Ar-H), 7.34-7.28 (2H, m, Ar-H), 3.30 (4H, t, *J* 7.6 Hz, CH_2), 2.06 (4H, quint, *J* 7.0 Hz CH_2), 1.61-1.51 (4H, m, CH_2), 1.49-1.32 (8H, m, CH_2), 0.93 (6H, t, *J* 7.1 Hz, CH_3); ^{13}C NMR; δ_C (125 MHz, $CDCl_3$): 175.3, 154.7, 152.1, 147.8, 131.8, 129.8, 125.1, 123.5, 122.1, 117.6, 111.6, 110.3, 34.8, 32.0, 29.8, 29.4, 23.0, 14.5; m/z (MALDI-TOF): 592; HRMS calculated for $C_{36}H_{36}N_2O_2S_2$: 593.2291. Found 593.2286. *See Appendix 3 for DSC analysis.*

4,8-Bis(benzo[b]thiophen-2-yl)-2,6-dihexylbenzo[1,2-d:4,5-d']bis(thiazole) ***(2.11)***

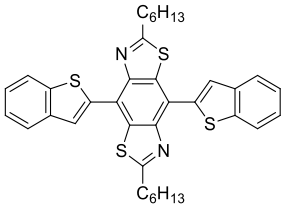

To a 5 mL microwave vial under Ar was added 4,8-dibromo-2,6-dihexylbenzo[1,2-d:4,5-d']bis(thiazole) **(2.5)** (100 mg, 0.193 mmol), benzothiophene-2-boronic acid MIDA ester (102 mg, 0.579 mmol), tetrakis(triphenylphosphine) palladium(0) (45 mg, 0.039 mmol) and barium hydroxide octahydrate (262 mg, 0.830 mmol), and the flask evacuated several times with Ar. Dry tetrahydrofuran (4 mL) and degassed water (1 mL) were then added and the flask fitted with a cap. The vial was then heated to 120 °C for 2 h in the microwave. The reaction was then cooled before being poured into water (50 mL) and extracted with dichloromethane (3 x 50 mL). The combined organic layers were then washed with water (50 mL) before being dried ($MgSO_4$) and concentrated to dryness. The crude residue was purified by silica gel column chromatography eluting with 30% dichloromethane in hexane. The resulting yellow powder was

recrystallised from hot ethanol with small additions of tetrahydrofuran to yield the *title compound* as yellow crystals (52 mg, 43%). ^{1}H NMR; δ_H (400 MHz CD_2Cl_2): 8.11 (2H, s, Ar-H), 7.95-7.9 (4H, m, Ar-H), 7.45-7.37 (4H, m, Ar-H), 3.20 (4H, t, *J* 7.6 Hz, CH_2), 1.96 (4H, quint, *J* 7.5 Hz CH_2), 1.50 (4H, q, *J* 6.9 Hz, CH_2), 1.43-1.28 (8H, m, CH_2), 0.89 (6H, t, *J* 7.0 Hz, CH_3); ^{13}C NMR; δ_C (125 MHz, $CDCl_3$): 173.4, 148.7, 141.4, 139.9, 139.8, 135.2, 125.8, 125.2, 124.7, 124.4, 122.4; m/z (MALDI-TOF): 624; HRMS calculated for $C_{36}H_{36}N_2S_4$: 625.1834. Found 625.1829. *See Appendix 4 for DSC analysis.*

2-(Tributylstannyl)benzo[d]thiazole ***(2.12)***[171]

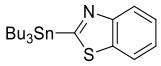

To a solution of benzo[d]thiazole (4.0 mL, 37.0 mmol) in dry tetrahydrofuran (50 mL) under Ar at -78 °C was added dropwise n-butyllithium (14.8 mL, 37.0 mmol, 2.5M in hexane) over a period of 1 h. The resulting suspension was stirred at -78 °C for a further 1 h before addition of chlorotributylstannane (10.5 mL, 38.8 mmol) dropwise. The reaction was then allowed to warm to r.t. overnight with stirring. The reaction was then poured into water (50 mL) and extracted with dichloromethane (3 x 50 mL). The combined organic layers were washed with water (2 x 50 mL), dried ($MgSO_4$) and concentrated to a brown oil which was then purified by Kugelrhor distillation (b.p. 165°C/0.15mm Hg) to yield the title compound as a pale yellow oil (12.5g, 80%). ^{1}H NMR; δ_H (400 MHz $CDCl_3$): 8.17 (1H, d, *J* 8.0 Hz, Ar-H), 7.96 (1H, d, *J* 7.4 Hz, Ar-H), 7.46 (1H, ddd, ^{4}J = 1.2, ^{3}J = 7.1, ^{3}J = 8.2 Hz, Ar-H), 7.36 (1H, ddd, ^{4}J = 1.1, ^{3}J = 7.2, ^{3}J = 8.2 Hz, Ar-H), 1.68-1.59 (6H, m, CH_2), 1.43-1.21 (12H, m, CH_2), 0.90 (9H, s, CH_3). This was consistent with previously published data.[171]

4,8-Bis(benzo[d]thiazol-2-yl)-2,6-dihexylbenzo[1,2-d:4,5-d']bis(thiazole) ***(2.13)***

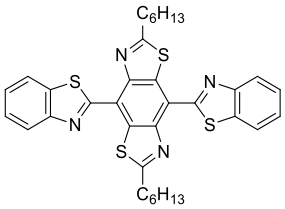

To a 50 mL oven dried flask under Ar was added 4,8-dibromo-2,6-dihexylbenzo[1,2-d:4,5-d']bis(thiazole) **(2.5)** (150 mg, 0.289 mmol), 2-(tributylstannyl)benzo[d]thiazole **(2.12)** (307 mg, 0.723 mmol) and tetrakis(triphenylphosphine) palladium(0) (67 mg, 0.058 mmol), and the

flask purged with Ar several times. Dry toluene (20 mL) was then added and the flask heated to reflux for 48 h under Ar. The reaction was then poured into water (100 mL) and extracted with dichloromethane (3 x 50 mL) before being washed with water (2 x 50 mL), dried ($MgSO_4$) and concentrated to a deep red residue. The crude residue was then purified *via* silica gel column chromatography eluting with 40% dichloromethane in hexane to yield a bright yellow powder which was then recrystallised from toluene:ethanol to yield the *title compound* as yellow fibrous crystals (122 mg, 67%). ^{1}H NMR; δ_H (400 MHz CD_2Cl_2): 8.27 (2H, d, *J* 8.1 Hz, Ar-H), 8.11 (2H, d, *J* 7.9 Hz, Ar-H), 7.62 (2H, ddd, ^4J = 1.2, ^3J = 7.2, ^3J = 8.1 Hz, Ar-H), 7.52 (2H, ddd, ^4J = 1.2, ^3J = 7.2, ^3J = 8.1, Hz, Ar-H), 3.39 (4H, t, *J* 7.6 Hz, CH_2) 2.18 (4H, quint, *J* 7.5 Hz CH_2), 1.66 (4H, q, *J* 6.9 Hz, CH_2), 1.52-1.4 (8H, m, CH_2), 0.99 (6H, t, *J* 7.0 Hz, CH_3); ^{13}C NMR; δ_C (125 MHz, $CDCl_3$): 178.2, 162.7, 152.5, 148.8, 137.9, 132.9, 126.4, 125.7, 123.7, 122.1, 121.9, 34.6, 32.0, 29.5, 29.4, 23.0, 14.5; m/z (MALDI-TOF): 627; HRMS calculated for $C_{34}H_{34}N_4S_4$: 627.1739. Found 627.1735. *See Appendix 5 for DSC analysis.*

2-(Tributylstannyl)benzo[d]oxazole ***(2.14)***[171]

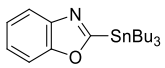

To a solution of benzo[d]oxazole (5.0 g, 42.0 mmol) in dry tetrahydrofuran (50 mL) under Ar at -110 °C was added dropwise n-butyllithium (16.8 mL, 42.0 mmol, 2.5M in hexane) over a period of 1 h. The solution was stirred at -110 °C for a further 1 h before addition of chlorotributylstannane (11.95 mL, 44.1 mmol) dropwise. The reaction was then allowed to warm to r.t. overnight with stirring. The reaction was then poured into water (100 mL) and extracted with dichloromethane (3 x 50 mL). The combined organic layers were washed with water (2 x 50 mL), dried ($MgSO_4$) and concentrated to a deep red oil which was purified by Kugelrhor distillation (bp 170 °C/0.2 mmHg) to yield the title compound as a pale yellow oil (13.0 g, 76%). ^{1}H NMR; δ_H (400 MHz $CDCl_3$): 7.80-7.72 (1H, m, Ar-H), 7.58-7.53 (1H, m, Ar-H), 7.33-7.27 (2H, m, Ar-H), 1.67-1.57 (6H, m, CH_2), 1.42-1.25 (12H, m, CH_2), 0.90 (9H, s, CH_3). This was consistent with previously published data.[171]

2,2'-(2,6-Dihexylbenzo[1,2-d:4,5-d']bis(thiazole)-4,8-diyl)bis(benzo[d]oxazole) ***(2.15)***

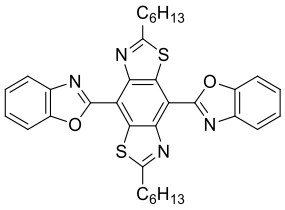

To a 50 mL oven dried flask under Ar was added 4,8-dibromo-2,6-dihexylbenzo[1,2-d:4,5-d']bis(thiazole) **(2.5)** (150 mg, 0.289 mmol), 2-(tributylstannyl)benzo[d]oxazole **(2.14)** (295 mg, 0.723 mmol) and tetrakis(triphenylphosphine) palladium(0) (67 mg, 0.058 mmol) and the flask purged with Ar several times. Dry toluene (20 mL) was then added and the flask heated to reflux for 24 h under Ar. Once cool, the reaction mixture was poured into water (100 mL) and extracted with dichloromethane (3 x 50 mL) before being dried ($MgSO_4$) and concentrated to a deep orange residue. The crude product was purified by silica gel column chromatography eluting with dichloromethane to remove the impurities then tetrahydrofuran to elute the product. Evaporation of solvent afforded the *title compound* as a bright yellow crystalline solid (86 mg, 50%). ^{1}H NMR; δ_H (400 MHz $CDCl_3$): 8.02-7.98 (2H, m, Ar-H), 7.92-7.88 (2H, m, Ar-H), 7.61-7.50 (4H, m, Ar-H), 3.46 (4H, t, *J* 8.0 Hz, CH_2), 2.11 (4H, quint, *J* 7.9 Hz CH_2), 1.68-1.58 (4H, m, CH_2), 1.52-1.38 (8H, m, CH_2), 0.97 (6H, t, *J* 7.0 Hz, CH_3); ^{13}C NMR; δ_C (125 MHz, $CDCl_3$): 178.6, 161.2, 151.6, 148.9, 141.8, 136.7, 126.3, 125.2, 120.9, 116.7, 111.8; m/z (MALDI-TOF): 595; HRMS calculated for $C_{34}H_{34}N_4O_2S_2$: 594.2196. Found 595.2191. *See Appendix 6 for DSC analysis.*

2,4-Dibromothiazole ***(3.10)***[140]

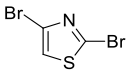

To a 100 mL round bottom flask under Ar was added thiazolidine-2,4-dione **(3.9)** (25.0 g, 0.213 mol), phosphorus pentoxide (142.0 g, 1.003 mol) and tetrabutylammonium bromide (158.0 g, 0.491 mol) and the flask evacuated several times. Anhydrous toluene (480 mL) was then added *via* syringe and the reaction heated to reflux for 20 h under Ar. The solution was concentrated and the resulting residue partitioned between Et_2O (150 mL) and H_2O (450 mL). The aqueous layer was adjusted to pH 9 with solid Na_2CO_3. The organic layer was separated and the aqueous layer was extracted with Et_2O (3 x 75 mL). The combined organic extracts were washed with brine (200 mL), dried ($MgSO_4$) and concentrated to give a dark brown solid. Recrystalization from hexane yielded the product as off-white crystals (41.3g, 80%); m.p.: 80 – 81 °C (81 – 82

°C lit.); ^{1}H NMR; δ_H (400 MHz $CDCl_3$): 7.22 (1H, s, Ar-H). This was consistent with previously published data.[140]

*4-Bromothiazole **(3.11)**[172]*

To a stirred solution of 2,4-dibromothiazole **(3.10)** (10.0 g, 41.2 mmol) in anhydrous diethyl ether (200 mL) under Ar at -78 °C was added a solution of *n*-butyllithium (18.5 mL, 45.3 mmol, 2.45M in hexane) dropwise. The reaction was then allowed to stir for 30 min at -78 °C before addition of methanol (3.3 g, 103 mmol) dropwise. The reaction was then slowly allowed to increase to rt overnight with stirring. The reaction mixture was filtered through a plug of silica and washed with a 1:2 mixture of ethyl acetate:hexane. The solvent was removed in *vacuo* to yield the title compound as a clear oil, which was used without further purification (6.5 g, 96%); ^{1}H NMR; δ_H (400 MHz $CDCl_3$): 8.75 (1H, d, *J* 2.2 Hz, Ar-H), 7.31 (1H, d, *J* 2.2 Hz, Ar-H). This was consistent with previously published data.[172]

*4-Methoxythiazole **(3.12)**[41]*

A mixture of sodium methoxide - prepared by treating anhydrous methanol (54.7 mL, 1.35 mol) with sodium (2.6 g, 114 mmol) - and 4-bromothiazole **(3.11)** (5.0 g, 30.5 mmol) was refluxed for 24 h. The mixture was then cooled to room temperature. The solution was then dissolved in water (100 mL) and extracted with diethyl ether (3 x 50 mL). The combined organics were washed with brine (50 mL) before being dried ($MgSO_4$) and concentrated to a deep red oil which was purified by silica gel column chromatography eluting with 1:1 hexane:chloroform to yield the title compound as a colourless oil (2.5 g, 70%); ^{1}H NMR; δ_H (400 MHz $CDCl_3$): 8.55 (1H, d, *J* 2.3 Hz, Ar-H), 6.13 (1H, d, *J* 2.4 Hz, Ar-H), 3.93 (3H, s, CH_3). This was consistent with previously published data.[41]

4-((2-Ethylhexyl)oxy)thiazole ***(3.13)***[41]

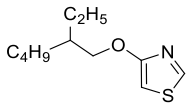

A mixture of 2-ethylhexan-1-ol (23.1 mL, 148 mmol), 4-methoxythiazole **(3.12)** (8.5 g, 73.8 mmol) and p-toluenesulfonic acid monohydrate (1.53 g, 8.05 mmol) in toluene (200 mL) was heated to 130 °C for 24 h. The mixture was cooled to room temperature and passed through a short plug of silica eluting with dichloromethane. Further purification *via* silica gel column chromatography eluting with 1:1 dichloromethane:hexane yielded the title compound as a pale yellow oil (11.2 g, 71%). ^{1}H NMR; δ_{H} (400 MHz $CDCl_3$): 8.57 (1H, d, *J* 2.3 Hz, Ar-H), 6.12 (1H, d, *J* 2.4 Hz, Ar-H), 4.01 (2H, m, CH_2), 1.80-1.70 (1H, m, CH), 1.58-1.25 (8H, m, CH_2), 0.93 (6H, m, CH_3); This was consistent with previously published data.[41]

4-((2-Ethylhexyl)oxy)-2-(triisopropylsilyl)thiazole ***(3.14)***[41]

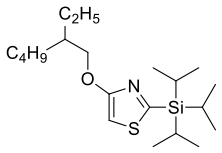

To a stirred solution of 4-((2-ethylhexyl)oxy)thiazole **(3.13)** (2.0 g, 9.37 mmol) in anhydrous tetrahydrofuran (80 mL) at -78 °C under Ar was added a solution of n-BuLi (3.75 mL, 9.37 mmol) in hexane dropwise over 30 min. The resulting suspension was stirred at -78 °C for 2 h before addition of chlorotriisopropylsilane (2.41 mL, 11.25 mmol). The mixture was allowed to stir and warm to rt overnight before being concentrated in vacuo and purified *via* silica gel column chromatography eluting with 6:1 hexane:dichloromethane to yield the title compound as a pale yellow oil (3.1 g, 89%). ^{1}H NMR; δ_{H} (400 MHz $CDCl_3$): 6.62 (1H, s, Ar-H), 4.04 (2H, m, CH_2), 1.85-1.74 (1H, m, CH), 1.60-1.23 (11H, m, CH/CH_2), 1.14 (18H, d, *J* 7.4 Hz, CH_3), 0.95-0.85 (6H, m, CH_3); This was consistent with previously published data.[41]

4,4'-Bis((2-ethylhexyl)oxy)-2,2'-bis(triisopropylsilyl)-5,5'-bithiazole ***(3.15)***[41]

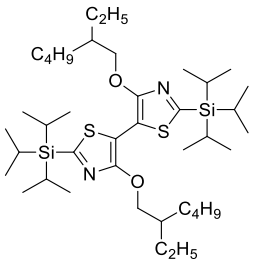

A solution of 4-((2-ethylhexyl)oxy)-2-(triisopropylsilyl)thiazole **(3.14)** (2.5 g, 6.76 mmol) in anhydrous tetrahydrofuran (70 mL) was cooled to -78 °C under Ar. A solution of *n*-BuLi in hexanes (2.98 mL, 7.44 mmol) was then added dropwise over 30 mins. After addition the mixture was stirred for 45 min at -78 °C then a further 1 h at rt. The solution was then cooled to 0 °C before addition of ferric acetylacetonate (2.63 g, 7.44 mmol). The reaction was then heated to 80 °C for 2 h, filtered, and the filter cake washed with THF (3 x 25 mL). The filtrate was concentrated in *vacuo* and purified by column chromatography eluting with hexane to 9:1 hexane:dichloromethane which yielded a pale yellow oil which was recrystallized from hexane/ethanol to yield the title compound as white prisms (2.2 g, 88%); m.p.: 58 °C; ^{1}H NMR; δ_H (400 MHz $CDCl_3$): 4.59-4.38 (4H, m, CH_2), 1.81-1.72 (2H, m, CH), 1.65-1.30 (22H, m, CH/CH_2), 1.18 (36H, d, *J* 7.4 Hz, CH_3), 1.02-0.88 (12H, m, CH_3); This was consistent with previously published data.[41]

4,4'-Bis((2-ethylhexyl)oxy)-5,5'-bithiazole ***(3.16)***[41]

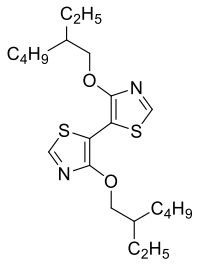

To a solution of 4,4'-bis((2-ethylhexyl)oxy)-2,2'-bis(triisopropylsilyl)-5,5'-bithiazole **(3.15)** (2.0 g, 2.71 mmol) in anhydrous tetrahydrofuran (25 mL) under Ar at 0 °C was added a solution of tetra-n-butylammonium fluoride (8.14 mL, 8.14 mmol) in tetrahydrofuran dropwise over 5 min. The solution was stirred at 0 °C for 30 min before being allowed to warm to rt and stirred for 90 min. Water (1 mL) was then added to the reaction and the solvent concentrated in *vacuo* before being purified by column chromatography eluting with dichloromethane:hexane 1:1 to yield the

title compound as a pale yellow oil (680 mg, 59%); ^{1}H NMR; δ_H (400 MHz $CDCl_3$): 8.40 (2H, s, Ar-H), 4.38 (4H, m, CH_2), 1.87-1.69 (2H, m, CH), 1.69-1.24 (16H, m, CH_2), 0.96 (12H, m, CH_3). This was consistent with previously published data.[41]

*4,4'-Bis((2-ethylhexyl)oxy)-2,2'-bis(trimethylstannyl)-5,5'-bithiazole **(3.17)**[41]*

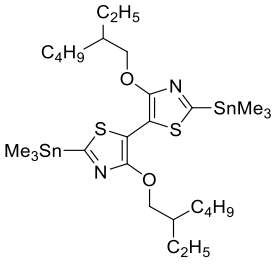

To a stirred solution of 4,4'-bis((2-ethylhexyl)oxy)-5,5'-bithiazole **(3.16)** (380 mg, 0.895 mmol) in anhydrous tetrahydrofuran (30 mL) under Ar at -78°C was added a solution of n-butyllithium (0.92 mL, 2.237 mmol) in hexane dropwise. The reaction was then stirred for 30 min before being allowed to warm to rt and stirred for a further 30 min. Trimethyltin chloride (3.13 mL, 3.13 mmol) (1M in THF) was then added in a single portion to the reaction and the reaction heated to 60 °C for 1 h before being carefully quenched with water (2 mL). The resulting mixture was then poured into water (100 mL) and extracted with hexane (3 x 50 mL). The combined organic layers were then washed with water (2 x 100 mL) and brine (100 mL) before being dried ($MgSO_4$) and concentrated to a red oil which was used without further purification (660 mg, 98%); ^{1}H NMR; δ_H (400 MHz $CDCl_3$): 4.48-4.29 (4H, m, CH_2), 1.83-1.67 (2H, m, CH), 1.62-1.23 (16H, m, CH_2), 1.04-0.81 (12H, m, CH_3), 0.43 (18H, s, CH_3). This was consistent with previously published data.[41]

p(BTzBBT)

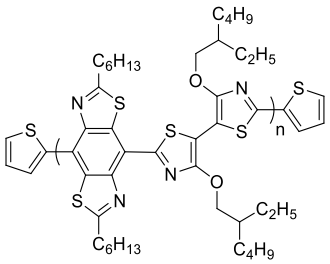

To a 5 mL microwave vial under Ar was added 4,4'-bis((2-ethylhexyl)oxy)-2,2'-bis(trimethylstannyl)-5,5'-bithiazole **(3.17)** (301 mg, 0.401 mmol) and 4,8-dibromo-2,6-

dihexylbenzo[1,2-d:4,5-d']bis(thiazole) **(2.5)** (208 mg, 0.401 mmol) and the vial purged several times with Ar. Anhydrous chlorobenzene (2 mL), $Pd_2(dba)_3$ (18 mg, 0.020 mmol) and $P(o\text{-}tol)_3$ (24 mg, 0.080 mmol) were then added and the vial purged for a further 10 min before being heated to 160 °C for 1 h under microwave irradiation. Once cool, tributyl(thiophen-2-yl)stannane (0.1 mL, 0.315 mmol) was then added and the flask heated to 160 °C for 10 min. 2-Bromothiophene (0.5 mL, 2.066 mmol) was then added and the flask heated to 160 °C for a further 10 min before being cooled to rt and precipitated into methanol (150 mL). The precipitated polymer was then purified via Soxhlet extraction with methanol, acetone, hexane and chloroform to remove low molecular weight impurities. The product was then collected in chlorobenzene and concentrated. The resulting blue residue was dissolved in the minimum volume of o-dichlorobenzene and precipitated into acetone to yield the title compound as a dark blue solid (201 mg); Anal. Calculated for $C_{42}H_{62}N_4O_2S_4$: C, 64.41; H, 7.98; N, 7.15. Found: C, 64.57; H, 7.73; N, 7.03; *GPC data not obtained due to incomplete polymer solubility.* See Appendix 14 for ^{1}H NMR spectra.

2,5-Bis(2-octyldodecyl)-3,6-di(thiophen-2-yl)pyrrolo[3,4-c]pyrrole-1,4(2H,5H)-dione ***(3.19)***[33]

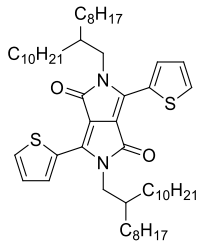

To a 250 mL oven-dried flask under Ar was added 3,6-di(thiophen-2-yl)pyrrolo[3,4-c]pyrrole-1,4(2H,5H)-dione **(3.18)** (3.0 g, 9.99 mmol) and anhydrous potassium carbonate (4.1 g, 30.0 mmol) and the flask evacuated several times with Ar. Anhydrous dimethylformamide (85 mL) was then added and the reaction heated to 120 °C for 1 h, at which point 9-(bromomethyl)nonadecane (10.8 g, 30.0 mmol) was added dropwise. After addition the reaction was heated to 130 °C overnight. After cooling to room temperature, diethyl ether (250 mL) was added and the organic layer extracted with water (3 x 200 mL) and brine (200 mL) before being dried ($MgSO_4$) and concentrated in *vacuo*. Silica gel column chromatography eluting with hexane:ethyl acetate 20:1 yielded the title compound as a dark purple solid which was reprecipitated from dichloromethane/methanol to yield the title compound as a purple solid (3.7 g, 43%); m.p.: 70 – 74 °C; ^{1}H NMR; δ_H (400 MHz $CDCl_3$): 8.86 (2H, dd, ^4J = 1.1, ^3J = 7.7 Hz, Ar-H), 7.61 (2H, dd, ^4J = 1.1, ^3J = 5.0 Hz, Ar-H), 7.26 (2H, m, Ar-H), 4.02 (4H, d, *J* 7.7 Hz, Ar-

H), 1.89 (2H, br, CH), 1.45-1.13 (64H, m, CH_2), 0.87 (12H, m, CH_3). This was consistent with previously published data.[33]

2,5-Bis(2-octyldodecyl)-3,6-bis(5-(4,4,5,5-tetramethyl-1,3,2-dioxaborolan-2-yl)thiophen-2-yl)pyrrolo[3,4-c]pyrrole-1,4(2H,5H)-dione ***(3.20)***[68]

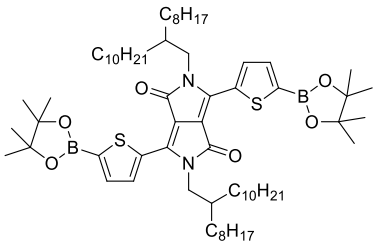

To a stirred solution of 2,5-bis(2-octyldodecyl)-3,6-di(thiophen-2-yl)pyrrolo[3,4-c]pyrrole-1,4(2H,5H)-dione **(3.19)** (1.1 g, 1.277 mmol) and 2-isopropoxy-4,4,5,5-tetramethyl-1,3,2-dioxaborolane (0.78 mL, 3.83 mmol) in anhydrous tetrahydrofuran (12 mL) at -25 °C under Ar was added a solution of lithium diisopropylamide (1.63 mL, 2.94 mmol) in tetrahydrofuran dropwise. The solution was stirred at 0 °C for 1 h before addition of a 0.1M solution of HCl (12 mL) and the product extracted with dichloromethane (3 x 25 mL). The combined organic layers were washed with water (25 mL), dried ($MgSO_4$) and concentrated to dryness. The crude mixture was dissolved in a minimal amount of dichloromethane and precipitated into cold acetone and filtered. The filtered solid was washed with cold acetone and dried in *vacuo* to yield a dark pink-red solid (0.97 g, 68%); m.p.: 165 – 168 °C (166 – 168 °C lit.); ^{1}H NMR; δ_H (400 MHz $CDCl_3$): 8.91 (2H, d, *J* 3.9 Hz, Ar-H), 7.71 (2H, d, *J* 3.9 Hz, Ar-H), 4.05 (4H, d, *J* 7.7 Hz, CH_2), 1.89 (2H, br, CH), 1.37 (24H, s, CH_3), 1.30-1.17 (64H, m, CH_2), 0.86 (12H, m, CH_3). This was consistent with previously published data.[68]

2,6-Diundecylbenzo[1,2-d:4,5-d']bis(thiazole) ***(3.21)***

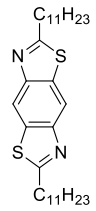

To a flask containing compound **(2.3)**, freshly prepared from 6 g of compound **(2.2)** was added a solution of trimethylsilyl polyphosphate (19.91 g, 147 mmol) in anhydrous 1,2-dichlorobenzene (50 mL) under Ar. Dodecanoyl chloride (14.15 mL, 61.2 mmol) was then

added *via* syringe and the flask heated to reflux for 48 h under Ar. Once cool the solution was diluted with dichloromethane (250 mL) and carefully washed several times with sat. $NaHCO_3$ solution. The solution was then washed with brine (2 x 200 mL) and water (2 x 200 mL) before being dried ($MgSO_4$) and the dichloromethane removed by rotary evaporation. The residual volatiles were distilled *via* vacuum distillation and the resulting dark brown residue purified *via* silica gel column chromatography eluting with dichloromethane. Reprecipitation from dichloromethane/methanol yielded the *title compound* as a crystalline white solid (8.24 g, 67 % over 2 steps); m.p.: 83 – 88 °C; ^{1}H NMR; δ_H (400 MHz $CDCl_3$): 8.38 (2H, s, Ar-H), 3.17 (4H, t, *J* 7.8 Hz CH_2), 1.91 (4H, quint, *J* 7.7 Hz CH_2), 1.51-1.20 (32H, m, CH_2), 0.88 (6H, t, *J* 6.8 Hz CH_3); ^{13}C NMR; δ_C (125 MHz, $CDCl_3$): 173.4, 151.0, 134.1, 114.6, 34.6, 31.9, 29.6, 29.5, 29.32, 29.28, 29.17, 22.7, 14.1; *m/z* (MALDI-TOF): 501; Anal. Calculated for $C_{30}H_{48}N_2S_2$: C, 71.94; H, 9.66; N, 5.59. Found: C, 72.00; H, 9.57; N, 5.84.

4,8-Dibromo-2,6-diundecylbenzo[1,2-d:4,5-d']bis(thiazole) ***(3.22)***

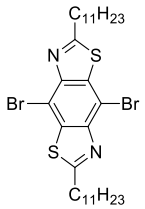

2,6-Diundecylbenzo[1,2-d:4,5-d']bis(thiazole) **(3.21)** (4.5 g, 8.98 mmol) was added to a 250 mL two neck flask under Ar. Chloroform (100 mL) was then added and allowed to stir until complete dissolution. Bromine (1.2 mL, 22.46 mmol) was then added dropwise and the reaction then stirred at rt for 24 h. The reaction was then diluted with chloroform (100 mL), quenched with sat. Na_2SO_3 (50 mL) and washed with sat. $NaHCO_3$ (150 mL) and water (150 mL) before being dried ($MgSO_4$) and concentrated in *vacuo* to an off-white solid. Silica gel column chromatography eluting with 1:4 dichloromethane:hexane yielded the *title compound* as a white solid. (550 mg, 9%); m.p.: 96 – 99 °C; ^{1}H NMR; δ_H (400 MHz $CDCl_3$): 3.17 (4H, t, *J* 7.8 Hz, CH_2), 1.91 (4H, quint, *J* 7.7 Hz, CH_2), 1.51-1.20 (32H, m, CH_2), 0.88 (6H, t, *J* 6.8 Hz, CH_3); ^{13}C NMR; δ_C (125 MHz, $CDCl_3$): 174.5, 147.8, 137.1, 105.9, 34.9, 31.9, 29.8, 29.6, 29.4, 29.3, 29.25, 29.2, 22.7; *m/z* (MALDI-TOF): 657 (^{79}Br, 100), 659 (^{81}Br, 100); Anal. Calculated for $C_{30}H_{46}Br_2N_2S_2$: C, 54.71; H, 7.04; N, 4.25. Found: C, 54.95; H, 7.01; N, 4.14. *N.B. compound* ***(3.21)*** *recovered in 54% yield after chromatography.*

p(DPPThBBT)

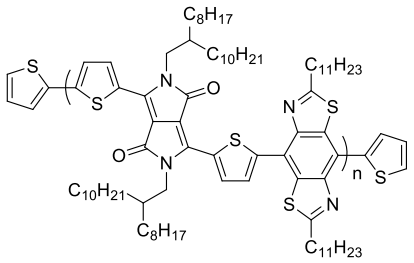

To a 25 mL two neck flask under Ar was added 2,5-bis(2-octyldodecyl)-3,6-bis(5-(4,4,5,5-tetramethyl-1,3,2-dioxaborolan-2-yl)thiophen-2-yl)pyrrolo[3,4-c]pyrrole-1,4(2H,5H)-dione **(3.20)** (290 mg, 0.260 mmol), 4,8-dibromo-2,6-diundecylbenzo[1,2-d:4,5-d']bis(thiazole) **(3.22)** (172 mg, 0.260 mmol), P(*o*-tol)$_3$ (24 mg, 0.078 mmol) and $Pd_2(dba)_3$ (17 mg, 0.018 mmol). The flask was evacuated several times with Ar and to the flask was added anhydrous THF (10 mL). A solution of potassium phosphate (79 mg, 0.372 mmol) in degassed water (1.5 mL) was added to this solution and the mixture stirred at reflux under Ar for 24 h. To the reaction was then added thiophen-2-ylboronic acid (17mg, 0.130 mmol), P(o-tol)$_3$ (12 mg, 0.039 mmol) and $Pd_2(dba)_3$ (8 mg, 7.81 µmol) and the flask stirred at reflux for a further 2 h before addition of 2-bromothiophene (0.5 mL) and the reaction stirred for a further 2 h at reflux. The mixture was then cooled to rt, poured into cold methanol (400 mL) and filtered. The crude product was then subjected to Soxhlet extraction with methanol, acetone and chloroform respectively. The chloroform fraction was concentrated in *vacuo* then dissolved in the minimum volume of chloroform, precipitated into acetone and filtered yielding the *title compound* as a dark green-black solid (292mg); ^{1}H NMR; δ_H (400 MHz $CDCl_3$): 9.4-8.8 (2H, br, Ar-H), 8.4-7.6 (2H br, Ar-H), 4.5-3.8 (4H, br, CH_2), 3.6-3.1 (4H, br, CH_2), 2.4-2.2 (2H, br, CH), 2.15-1.85 (4H, br, CH_2), 1.85-0.65 (96H, br, CH_2), 1.0-0.7 (18H, br, CH_3); Anal. Calculated for $C_{84}H_{134}N_4O_2S_4$: C, 74.17; H, 9.93; N, 4.12. Found: C, 72.33; H, 9.59; N, 4.09; GPC: M_n = 9 kDa, M_w = 14 kDa, PDI = 1.68. See Appendix 15 for ^{1}H NMR spectra.

3,6-Bis(5-bromothiophen-2-yl)-2,5-bis(2-octyldodecyl)pyrrolo[3,4-c]pyrrole-1,4(2H,5H)-dione ***(3.23)***[33]

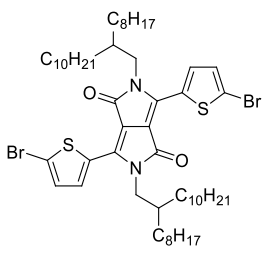

To a stirred solution of 2,5-bis(2-octyldodecyl)-3,6-di(thiophen-2-yl)pyrrolo[3,4-c]pyrrole-1,4(2H,5H)-dione **(3.19)** (2.0 g, 2.322 mmol) in chloroform (15 mL) in the absence of light was added a solution of bromine (0.25 mL, 4.76 mmol) in chloroform (5 mL) dropwise at rt. The solution was then allowed to stir at rt overnight before being poured into sat. aqueous sodium sulfite (20 mL) and stirred. The product was extracted with chloroform (3 x 50 mL) and washed with water (2 x 50 mL) before being dried ($MgSO_4$) and concentrated to dryness. Silica gel column chromatography eluting with 3:7 dichloromethane:hexane yielded the title compound as a purple solid which was reprecipitated from dichloromethane/methanol (2.1 g, 90%); m.p.: 88 – 90 °C; ^{1}H NMR; δ_H (400 MHz $CDCl_3$): 8.62 (2H, d, *J* 4.2 Hz, Ar-H), 7.22 (2H, d, *J* 4.2 Hz, Ar-H), 3.92 (4H, d, *J* 7.7 Hz, CH_2), 1.88 (2H, br, CH), 1.47-1.10 (64H, m, CH_2), 0.86 (12H, m, CH_3). This was consistent with previously published data.[33]

*2,5-Bis(trimethylstannyl)thiophene **(3.26)**[173]*

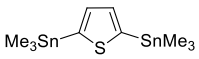

To a stirred solution of thiophene (0.46 mL, 5.94 mmol) and *N,N,N',N'*-tetramethylethylene-1,2-diamine (1.82 mL, 12.18 mmol) in anhydrous hexane (15 mL) was added a solution of *n*-butyllithium (4.99 mL, 12.18 mmol, 2.44M in hexane) dropwise over 10 min. The reaction was then heated to reflux for 45 min before being cooled to 0 °C. A solution of chlorotrimethylstannane (17.83 mL, 17.83 mmol) (1M in THF) was then added over 10 min and the reaction stirred at rt overnight before being quenched with sat. ammonium chloride solution (100 mL). The aqueous layer was then extracted with diethyl ether (3 x 50 mL) and washed with brine (2 x 50 mL) before being dried ($MgSO_4$) and concentrated to a yellow solid which was further purified by recrystallization from hexane to yield the title compound as white needles (1.93 g, 79%); ^{1}H NMR; δ_H (400 MHz $CDCl_3$): 7.40 (2H, s, Ar-H), 0.39, (18H, s, CH_3). This was consistent with previously published data.[173]

p(DPP2ThBBT)

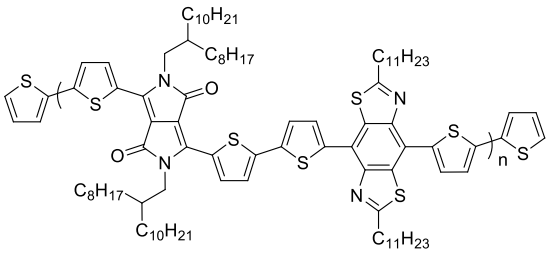

To a 5 mL microwave vial under Ar was added 2,5-bis(trimethylstannyl)thiophene **(3.22)** (195 mg, 0.477 mmol), 4,8-dibromo-2,6-diundecylbenzo[1,2-d:4,5-d']bis(thiazole) **(3.22)** (157 mg, 0.238 mmol) and 3,6-bis(5-bromothiophen-2-yl)-2,5-bis(2-octyldodecyl)pyrrolo[3,4-c]pyrrole-1,4(2H,5H)-dione **(3.23)** (243mg, 0.238 mmol) and the flask purged with Ar for 10 min. Anhydrous chlorobenzene (2 mL) was then added *via* syringe and the vial purged for a further 15 min with Ar. $Pd_2(dba)_3$ (11 mg, 0.012 mmol) and $P(o\text{-}tol)_3$ (15 mg, 0.048 mmol) were then added and the vial purged for a final 5 min. The reaction was then heated to 160 °C for 1 h before being cooled to rt and tributyl(thiophen-2-yl)stannane (0.1 mL) added. The flask was then heated to 160 °C for 10 min before addition of 2-bromothiophene (0.5 mL) and heated to 160 °C for a further 10 min. The crude solution was then precipitated into methanol (400 mL) and filtered. The crude product was then subjected to Soxhlet extraction with methanol, acetone and chloroform respectively. The chloroform fraction was concentrated in *vacuo* then dissolved in the minimum volume of chloroform, precipitated into acetone and filtered yielding the *title compound* as a dark green-black solid (351 mg); Anal. Calculated for $C_{92}H_{138}N_4O_2S_6$: C, 72.48; H, 9.12; N, 3.68. Found: C, 72.37; H, 9.06; N, 3.55; GPC: M_n = 35 kDa, M_w = 96 kDa, PDI = 2.75. See Appendix 16 for ^{1}H NMR spectra.

*2,5-Bis(trimethylstannyl)furan **(3.27)**[173]*

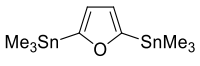

To a stirred solution of furan (0.53 mL, 7.34 mmol) and *N,N,N',N'*-tetramethylethylene-1,2-diamine (2.75 mL, 18.36 mmol) in anhydrous hexane (15 mL) at 0 °C was added a solution of sec-butyllithium in hexane (15.05 mL, 18.36 mmol) dropwise over 10 min. The reaction was stirred for 1 h at 0 °C followed by rt for 4 h after which the solution was cooled to 0 °C again. A solution of chlorotrimethylstannane (22.03 mL, 22.03 mmol) in THF was then added over 10 min and the reaction stirred at rt overnight before being quenched with sat. ammonium chloride solution (100 mL). The aqueous layer was then extracted with diethyl ether (3 x 50 mL) and washed with brine (2 x 50 mL) before being dried ($MgSO_4$) and concentrated to a yellow oil which was purified by Kugelrohr distillation (bp 140 °C, low vacuum) to yield the title compound as a pale yellow oil (1.98 g, 69%); ^{1}H NMR; δ_H (400 MHz $CDCl_3$): 6.63 (2H, s, Ar-H), 0.32 (18H, s, CH_3). This was consistent with previously published data.[173]

p(DPPThFBBT)

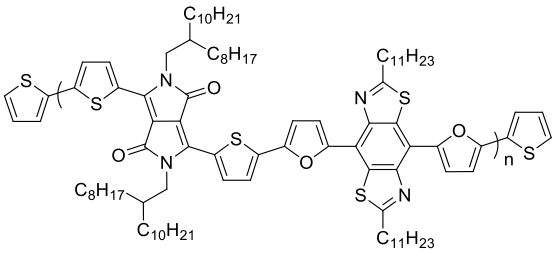

To a 5 mL microwave vial under Ar was added 2,5-bis(trimethylstannyl)furan **(3.27)** (161mg, 0.409 mmol), 4,8-dibromo-2,6-diundecylbenzo[1,2-d:4,5-d']bis(thiazole) **(3.22)** (135 mg, 0.204 mmol) and 3,6-bis(5-bromothiophen-2-yl)-2,5-bis(2-octyldodecyl)pyrrolo[3,4-c]pyrrole-1,4(2H,5H)-dione **(3.23)** (208 mg, 0.204 mmol) and the flask purged with Ar for 10 min. Anhydrous chlorobenzene (2 mL) was then added *via* syringe and the vial purged for a further 15 min with Ar. $Pd_2(dba)_3$ (9 mg, 10.22 μmol) and $P(o\text{-}tol)_3$ (12 mg, 0.041 mmol) were then added and the vial purged for a final 5 minutes. The reaction was then heated to 160 °C for 1 h before being cooled to rt and tributyl(thiophen-2-yl)stannane (0.1 mL) added. The flask was then heated to 160 °C for 10 mins before addition of 2-bromothiophene (0.5 mL) and heated to 160 °C for a further 10 mins. The crude solution was then precipitated into methanol (400 mL) and filtered. Soxhlet extraction with methanol, hexane and acetone removed low molecular weight impurities and the product was collected *via* Soxhlet extraction using chloroform and precipitated into acetone to yield the product as a dark green solid (195 mg); Anal. Calculated for $C_{92}H_{138}N_4O_4S_4$: C, 74.04; H, 9.32; N, 3.75. Found: C, 73.63; H, 8.85; N, 3.77; GPC: M_n = 9 kDa, M_w = 18 kDa, PDI = 2.04. See Appendix 17 for ^{1}H NMR spectra.

*3-(2-Ethylhexyl)thiophene **(4.8)**[174]*

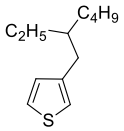

To a suspension of magnesium turnings (1.61 g, 66.2 mmol) in anhydrous tetrahydrofuran (5 mL) was added a solution of 2-ethylhexyl bromide (10.93 mL, 61.1 mmol) in anhydrous tetrahydrofuran (15 mL) at a rate sufficient to maintain gentle reflux. After addition, reflux was maintained for 2 h before being cooled to rt and transferred dropwise *via* syringe into a flask containing a solution of 3-bromothiophene **(4.7)** (4.77 mL, 50.9 mmol) and dichloro(1,3-bis(diphenylphosphino)propane)nickel (0.276 g, 0.509 mmol) in anhydrous tetrahydrofuran (30

mL). The resulting solution was stirred at reflux under Ar overnight. After cooling to rt the reaction was quenched with water (10 mL) followed by conc. HCl (2 mL) and extracted with dichloromethane (3 x 50 mL). The combined organic phase was washed with brine (100 mL) and water (100 mL) before being dried ($MgSO_4$) and concentrated to a yellow oil, which was purified by Kughelrohr distillation (b.p, 110 °C, low vacuum) to yield the title compound as a colourless oil (8.0 g, 80%); ^{1}H NMR; δ_H (400 MHz $CDCl_3$): 7.22 (1H, dd, ^4J = 3.0 ^4J = 4.9 Hz, Ar-H), 6.93-6.87 (2H, m, Ar-H), 2.57 (2H, d, J 6.9 Hz, CH_2), 1.68-1.48 (1H, m, CH), 1.36-1.17 (8H, m, CH_2), 0.99-0.80 (6H, m, CH_3). This was consistent with previously published data.[174]

(4-(2-Ethylhexyl)thiophen-2-yl)trimethylstannane ***(4.9)***[174]

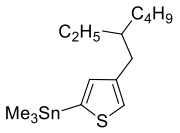

A solution of n-butyllithium (2.31 mL, 5.63 mmol) in hexane was added to a flask containing 3-(2-ethylhexyl)thiophene **(4.8)** (1.1 g, 5.60 mmol) in diethyl ether (25 ml) and N,N,N',N' -tetramethylethylenediamine (0.93 mL, 6.16 mmol) under Ar at room temperature. The mixture was then allowed to reflux for 1 hr before being cooled to 0 °C using an ice bath. A solution of trimethyltinchloride (8.40 mL, 8.40 mmol) (1M in THF) was then added and allowed to stir overnight. The mixture was quenched using sat. ammonium chloride solution (20 mL) before being washed with brine (50 mL), dried ($MgSO_4$) and concentrated to a pale yellow oil which was used without further purification (2.0 g, 98%); ^{1}H NMR; δ_H (400 MHz $CDCl_3$): 7.19 (1H, s, Ar-H), 6.99 (1H, s, Ar-H), 2.61 (2H, d, J 6.8 Hz), 1.59 (1H, m, CH), 1.30 (8H, m, CH_2), 0.90 (6H, m, CH_3), 0.38 (9H, s, CH_3). This was consistent with previously published data.[174]

4,7-Bis(4-(2-ethylhexyl)thiophen-2-yl)benzo[c][1,2,5]thiadiazole ***(4.10)***[174]

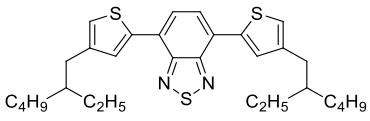

To a 25 mL flask under Ar was added 4,7-dibromobenzo[c][1,2,5]thiadiazole (200 mg, 0.68 mmol), (4-(2-ethylhexyl)thiophen-2-yl)trimethylstannane **(4.9)** (733 mg, 2.041 mmol) and tetrakis(triphenylphosphine) palladium(0) (157 mg, 0.136 mmol), and the flask purged several times with Ar. Anhydrous toluene (10 mL) was then added and the flask heated to reflux for 24 h. Once cool the solution was poured into water (20 mL) and extracted with dichloromethane (3

x 50 mL). The combined organic layers were washed with water (2 x 50 mL) and brine (50 mL) before being dried ($MgSO_4$) and concentrated to dryness. The crude product was purified by silica gel column chromatography eluting with 20:1 hexane:dichloromethane to yield the product as an orange solid which was further recrystallised from ethanol to yield the title compound as a bright orange solid (302 mg, 85%); m.p.: 49 – 50 °C; ^{1}H NMR; δ_H (400 MHz $CDCl_3$): 7.97 (2H, s, Ar-H), 7.86 (2H, s, Ar-H), 7.04 (2H, s, Ar-H), 2.66 (4H, d, *J* 6.9 Hz, CH_2), 1.68 (2H, m, CH), 1.35 (16H, m, CH_2), 0.92 (12H, t, *J* 7.4 Hz, CH_3). This was consistent with previously published data.[174]

4,7-Bis(5-bromo-4-(2-ethylhexyl)thiophen-2-yl)benzo[c][1,2,5]thiadiazole ***(4.11)***[174]

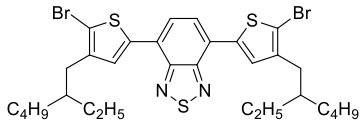

To a stirred solution of 4,7-bis(4-(2-ethylhexyl)thiophen-2-yl)benzo[c][1,2,5]thiadiazole **(4.10)** (240 mg, 0.457 mmol) in anhydrous tetrahydrofuran (20 mL) under Ar and in the absence of light was added *N*-bromosuccinimide (203 mg, 1.143 mmol) in several portions at 0 °C. After addition, the reaction was stirred for a further 30 min before being warmed to rt and stirred overnight. The reaction was then quenched with sat. NH_4Cl solution, extracted with dichloromethane (3 x 50 mL) and the combined organic layers washed with water (2 x 50mL) before being dried ($MgSO_4$) and concentrated to dryness. The pure product was obtained *via* silica gel column chromatography eluting with hexane to yield the product as a dark red oil (305 mg, 98%); ^{1}H NMR; δ_H (400 MHz $CDCl_3$): 7.75 (4H, m, Ar-H), 2.58 (4H, d, *J* 7.2 Hz, CH_2), 1.77-1.62 (2H, m, CH), 1.45-1.25 (16H, m, CH_2), 0.97-0.85 (12H, m, CH_3). This was consistent with previously published data.[174]

p(BBT2ThBT)

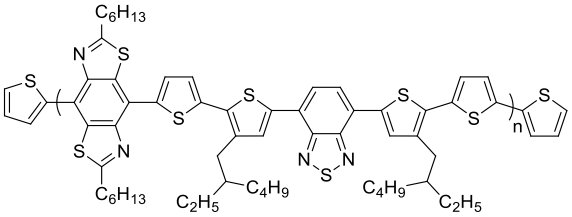

To a 20 mL microwave vial under Ar was added 2,5-bis(trimethylstannyl)thiophene **(3.26)** (420 mg, 1.025 mmol), 4,8-dibromo-2,6-dihexylbenzo[1,2-d:4,5-d']bis(thiazole) **(2.5)** (266 mg, 0.513

mmol) and 4,7-bis(5-bromo-4-(2-ethylhexyl)thiophen-2-yl)benzo[c][1,2,5]thiadiazole **(4.11)** (350 mg, 0.513 mmol) and the flask purged several times with Ar. P(*o*-tol)$_3$ (31 mg, 0.103 mmol) and $Pd_2(dba)_3$ (23 mg, 0.026 mmol) were then added followed by anhydrous chlorobenzene (5 mL) and the solution purged with Ar for 15 min. The vial was then heated to 160 °C in the microwave for 50 min. Once cool, tributyl(thiophen-2-yl)stannane (0.1 mL) was then added and the flask heated to 160 °C for 10 min followed by addition of 2-bromothiophene (0.5 mL) and heating for a final 10 min. The crude reaction mixture was precipitated into methanol (400 mL) and the resulting precipitate was purified *via* Soxhlet extraction with methanol, acetone and chloroform, followed by collection of the product with chlorobenzene which was then concentrated in *vacuo* and precipitated into acetone to yield the product as a dark purple-blue solid (512 mg); Anal. Calculated for $C_{58}H_{70}N_4S_7$: C, 66.50; H, 6.74; N, 5.35. Found: C, 66.29; H, 6.47; N, 5.41; GPC: M_n = 9 kDa, M_w = 17 kDa, PDI = 1.8. See Appendix 25 for ^{1}H NMR spectrum.

*2-Hexyldecyl methanesulfonate **(4.13)**[175]*

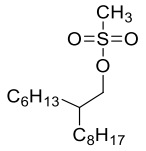

To a 250 mL round bottom flask under Ar was added 2-hexyldecan-1-ol **(4.12)** (4.78 mL, 16.50 mmol), methanesulfonyl chloride (1.41 mL, 18.15 mmol) and anhydrous dichloromethane (80 mL). Triethylamine (2.53 mL, 18.15 mmol) was then added dropwise *via* syringe. After stirring for 1 h at rt the solvent was removed in *vacuo* and the oily residue was extracted with diethyl ether (150 mL) and washed with water (3 x 100 mL) before being dried ($MgSO_4$) and concentrated to a yellow oil, which was purified by column chromatography (9:1 hexane:dichloromethane) to yield the title compound as a colourless oil (3.7 g, 70%); ^{1}H NMR; δ_H (400 MHz $CDCl_3$): 4.09 (2H, d, *J* 5.5 Hz, CH_2), 2.96 (3H, s, CH_3), 1.68 - 1.66 (1H, m, CH), 1.42-1.25 (22H, m, CH_2), 0.86 ppm (6H, m, CH_3). This was consistent with previously published data.[175]

4,8-Bis((2-hexyldecyl)oxy)benzo[1,2-b:4,5-b']dithiophene ***(4.1)***[175]

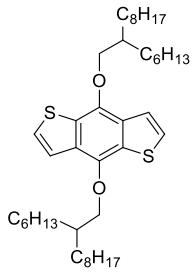

To a 50 mL round bottom flask under Ar was added tetrabutylammonium bromide (220 mg, 0.681 mmol), benzo[1,2-b:4,5-b']dithiophene-4,8-dione (500 mg, 2.270 mmol), zinc powder (386 mg, 5.90 mmol), sodium hydroxide pellets (1.362 g, 34.0 mmol) and degassed water (7 mL), and the flask heated to reflux for 1 h, then 2-hexyldecyl methanesulfonate **(4.13)** (2.183 g, 6.81 mmol) was added and the reaction heated to reflux for a further 2 h yielding an orange suspension. An additional portion of zinc powder (148 mg, 2.270 mmol) was added and then the reaction heated to reflux overnight. The reaction was then poured into water and extracted with diethyl ether (3 x 50 mL) and the combined organic layer washed with water (2 x 50 mL) before being dried ($MgSO_4$) and concentrated to an orange oil. The crude product was purified by silica gel column chromatography eluting with hexane to yield the title compound as a pale yellow oil (1.28 g, 84%); ^{1}H NMR; δ_H (400 MHz $CDCl_3$): 7.47 (2H, d, *J* 5.5 Hz, Ar-H), 7.36 (2H, d, *J* 5.5 Hz, Ar-H), 4.20 (4H, d, *J* 5.4 Hz, CH_2), 1.89 (2H, m, CH), 1.65 (8H, m, CH_2), 1.45-1.35 (40H, m, CH_2), 0.93 (12H, m, CH_3). This was consistent with previously published data.[175]

(4,8-Bis((2-hexyldecyl)oxy)benzo[1,2-b:4,5-b']dithiophene-2,6-diyl)bis(trimethylstannane) ***(4.14)***[175]

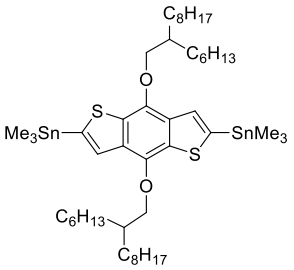

To a solution of 4,8-bis((2-hexyldecyl)oxy)benzo[1,2-b:4,5-b']dithiophene **(4.1)** (800 mg, 1.192 mmol) in anhydrous tetrahydrofuran (15 mL) at -78 °C was added a solution of *n*-butyllithium (1.19 mL, 2.86 mmol, 2.4M in hexane) dropwise under Ar. This mixture was stirred at -78 °C for 15 mins before being warmed to rt and stirred for 1.5 h. The solution was subsequently

cooled to 0 °C and trimethyltin chloride (3.58 mL, 3.58 mmol, 1M in tetrahydrofuran) added. The solution was allowed to warm to rt and stirred overnight. After this time the reaction was quenched with water (100 mL) and extracted with diethyl ether (3 x 100 mL). The combined organic layers were washed with water (3 x 50 mL) before being dried ($MgSO_4$) and concentrated to dryness. The resulting pale yellow oil was recrystallized from isopropanol to yield the title compound as a white solid (725 mg, 61%); ^{1}H NMR; δ_H (400 MHz $CDCl_3$): 7.51 (2H, s, Ar-H), 4.18 (4H, d, *J* 5.3 Hz, CH_2), 1.96-1.80 (2H, m, CH), 1.73-1.58 (4H, m, CH_2), 1.52-1.15 (44H, m, CH_2), 1.0-0.77 (12H, m, CH_3), 0.44 (18H, s, CH_3). This was consistent with previously published data.[175]

p(BDTBBT)

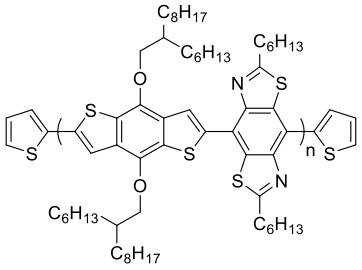

To a 25 mL round bottom flask under Ar was added (4,8-bis((2-hexyldecyl)oxy)benzo[1,2-b:4,5-b']dithiophene-2,6-diyl)bis(trimethylstannane) **(4.14)** (299 mg, 0.3 mmol) and 4,8-dibromo-2,6-dihexylbenzo[1,2-d:4,5-d']bis(thiazole) **(2.5)** (156 mg, 0.300 mmol) and the flask purged with Ar several times before addition of anhydrous toluene (10 mL) *via* syringe. The solution was then bubbled with Ar for 5 min and then $Pd_2(dba)_3$ (13 mg, 0.015 mmol) and P(*o*-tol)$_3$ (18 mg, 0.060 mmol) added. The solution was then heated to reflux for 48 h under Ar. 2-Tributylstannyl thiophene (0.1 mL) was then added *via* syringe and the reaction heated to reflux for a further 8 h before addition of 2-bromothiophene (0.5 mL) and heating overnight. The reaction mixture was cooled to rt and precipitated into methanol (100 mL). The precipitate was filtered into a Soxhlet thimble and extracted with methanol, acetone and hexane before being collected in chloroform. The chloroform fraction was then passed through a short silica gel plug to remove inorganic impurities before being concentrated and precipitated into acetone to yield the title compound as a red solid (284 mg); Anal. Calculated for $C_{62}H_{96}N_2O_2S_4$: C, 72.32; H, 9.40; N, 2.72. Found: C, 72.26; H, 9.13; N, 2.69; GPC: M_n = 31.5 kDa, M_w = 60.7 kDa, PDI = 1.93. See Appendix 26 for ^{1}H NMR spectrum.

*7-(Bromomethyl)pentadecane **(4.15)**[176]*

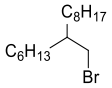

A solution of triphenylphosphine (10.82 g, 41.2 mmol) in dichloromethane (60 mL) was purged with Ar for 15 min before addition of Br_2 (2.13 mL, 41.2 mmol). 2-Hexyldecan-1-ol **(4.12)** (11.96 mL, 41.2 mmol) was then added dropwise over 30 mins and the reaction left to stir at rt overnight. The solvent was removed in *vacuo* and the resulting residue washed with hexane (100 mL) and filtered. The filtrate was concentrated under reduced pressure and purified *via* silica gel column chromatography eluting with 20% dichloromethane in hexanes to yield the title compound as a colourless oil (12.3 g, 97%); ^{1}H NMR; δ_H (400 MHz $CDCl_3$): 3.45 (2H, d, *J* 4.8 Hz, CH_2), 1.68-1.51 (1H, m, CH), 1.46-1.15 (24H, m, CH_2), 1.02-0.80 (6H, m, CH_3). This was consistent with previously published data.[176]

*2-(2-Hexyldecyl)isoindoline-1,3-dione **(4.16)**[176]*

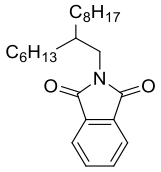

To a stirred solution of 7-(bromomethyl)pentadecane **(4.15)** (3.0 g, 9.83 mmol) in anhydrous DMF (10 mL) was added potassium phthalimide (1.911 g, 10.32 mmol) under Ar. The reaction was then heated to 90 °C for 18 h before being cooled to rt, poured into water (50 mL) and extracted with diethyl ether (3 x 30 mL). The combined organic layers were then washed with 0.2 M KOH (50 mL), water (50 mL) and sat NH_4Cl (50 mL) before being dried ($MgSO_4$) and concentrated to a crude yellow oil. The crude oil was purified *via* silica gel column chromatography eluting with dichloromethane to yield the title compound as a colourless oil (3.43 g, 94%); ^{1}H NMR; δ_H (400 MHz $CDCl_3$): 7.9-7.84 (2H, m, Ar-H), 7.76-7.70 (2H, m, Ar-H), 3.57 (2H, d, *J* 7.3 Hz, CH_2), 1.93-1.82 (1H, m, CH), 1.45-1.15 (24H, m, CH_2), 0.96-0.78 (6H, m, CH_3). This was consistent with previously published data.[176]

*2-Hexyldecan-1-amine **(4.17)**[176]*

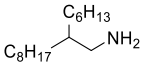

2-(2-Hexyldecyl)isoindoline-1,3-dione **(4.16)** (3.4 g, 9.15 mmol), hydrazine hydrate (0.852 mL, 27.5 mmol) and methanol (40 mL) were stirred at 95 °C until complete consumption of the starting material was observed (6 h). The residual solvent was removed in *vacuo* and the resulting residue diluted with dichloromethane (100 mL) and washed with 10% KOH solution (2 x 50 mL). The combined aqueous layers were extracted with dichloromethane (3 x 30 mL). The combined organic layers were then washed with brine (2 x 50 mL) before being dried ($MgSO_4$) and concentrated to a yellow oil which was passed through a short silica plug eluting with ethyl acetate to yield the title compound as a colourless oil (1.96 g, 89%); ^{1}H NMR; δ_H (400 MHz $CDCl_3$): 2.60 (2H, d, J = 5.0 Hz, CH_2), 1.39 (1H, m, CH), 1.45-1.15 (24H, m, CH_2), 0.96-0.78 (6H, m, CH_3). This was consistent with previously published data.[176]

*3,3'-Dibromo-2,2'-bithiophene **(4.18)***[177]

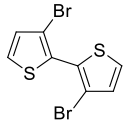

To a stirred solution of diisopropylamine (9.52 mL, 67.5 mmol) in anhydrous tetrahydrofuran (60 mL) was added a solution of *n*-butyllithium (25.6 mL, 61.3 mmol, 2.39M in hexane) dropwise at -78 °C under Ar. The solution was then allowed to warm to rt and stirred for 15 min before being cooled to -78 °C and 3-bromothiophene **(4.7)** (5.75 mL, 61.3 mmol) added dropwise. The suspension was then stirred for 1 h at low temperature before careful addition of copper (II) chloride (8.66 g, 64.4 mmol) in one portion. The mixture was then allowed to warm to rt and treated with aqueous HCl (10 mL) and extracted with diethyl ether (3 x 150 mL) before being washed with water (2 x 100 mL), dried ($MgSO_4$) and concentrated to dryness. The crude product was purified *via* silica gel column chromatography eluting with hexane and further purified *via* recrystallization from hexane to yield the title compound as a pale yellow solid (4.54 g, 46% yield); m.p.: 101 – 102 °C (98 – 99 °C lit.); ^{1}H NMR; δ_H (400 MHz $CDCl_3$): 7.41 (2H, d, J 5.4 Hz, Ar-H), 7.08 (2H, d, J 5.4 Hz, Ar-H). This was consistent with previously published data.[177]

*4-(2-Hexyldecyl)-4H-dithieno[3,2-b:2',3'-d]pyrrole **(4.2)***

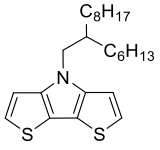

A solution of sodium tert-butoxide (741 mg, 7.71 mmol), $Pd_2(dba)_3$ (141 mg, 0.154 mmol), 2,2'-bis(diphenylphosphenyl)-1,1'-binaphthalene (384 mg, 0.617 mmol) and 3,3'-dibromo-2,2'-bithiophene **(4.18)** (1.0g, 3.09 mmol) in anhydrous toluene (10 mL) was purged with Ar for 20 min before addition of 2-hexyldecan-1-amine **(4.17)** (820 mg, 3.39 mmol) *via* syringe and the reaction heated to 110 °C for 12 h under Ar. Once cool, the reaction was poured into water (100 mL) and extracted with ethyl acetate (3 x 50 mL). The combined organic layers were washed with water (50 mL) before being dried ($MgSO_4$) and concentrated to a pale yellow oil. The crude product was purified via silica gel column chromatography eluting with hexane to yield the *title compound* as a colourless oil (854 mg, 69%); ^{1}H NMR; δ_H (400 MHz $CDCl_3$): δ 7.12 (2H, d, J = 5.3 Hz, Ar-H), 6.98 (2H, d, J = 5.3 Hz, Ar-H), 4.05 (2H, d, J = 7.3 Hz, CH_2), 2.00 (1H, br, CH), 1.41 – 1.12 (24H, m, CH_2), 0.97 – 0.79 (6H, m, CH_3); ^{13}C NMR; δ_c (125 MHz $CDCl_3$): 145.3, 122.7, 114.6, 111.1, 51.7, 39.1, 31.9, 31.8, 31.6, 29.9, 29.6, 29.5, 29.2, 26.4, 22.7, 22.6, 14.10, 14.06; *m/z* (MALDI-TOF): 403.

*4-(2-Hexyldecyl)-2,6-bis(tributylstannyl)-4H-dithieno[3,2-b:2',3'-d]pyrrole **(4.19)***

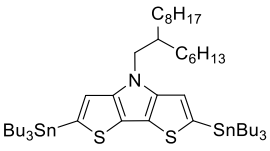

To a stirred solution of 2,2,6,6-tetramethylpiperidine (0.41 mL, 2.477 mmol) in anhydrous tetrahydrofuran (10 mL) under Ar at -78 °C was added a solution of *n*-butyllithium (0.95 mL, 2.378 mmol, 2.5M in hexane) dropwise *via* syringe. The reaction was then stirred for 1 h at -78 °C before addition of 4-(2-Hexyldecyl)-4H-dithieno[3,2-b:2',3'-d]pyrrole **(4.2)** (400 mg, 0.991 mmol) in anhydrous tetrahydrofuran (10 mL). The reaction was stirred for 10 min at -78 °C before being warmed to rt and stirred for 1 h. The reaction was then cooled to -78 °C and tributyltin chloride (0.59 mL, 2.180 mmol) added in one portion and the reaction allowed to warm to rt and stirred overnight. The reaction was then quenched with sat. ammonium chloride solution (50 mL) and extracted with diethyl ether (3 x 20 mL). The combined organic layers were then washed with brine (20 mL) and water (20 mL) before being dried ($MgSO_4$) and concentrated in *vacuo*. The resulting oil was purified *via* silica gel column chromatography (pre-treated with triethylamine) eluting with hexane to yield the title compound as a pale yellow oil (921 mg, 95%); ^{1}H NMR; δ_H (400 MHz $CDCl_3$): 6.92 (2H, s, Ar-H), 4.05 (2H, d, J = 7.1 Hz, CH_2), 1.99 (1H, br, CH), 1.69 - 1.55 (12H, m, CH_2), 1.45 - 1.05 (48H, m, CH_2), 0.95 – 0.80 (24H, m, CH_3); ^{13}C NMR; δ_c (125 MHz $CDCl_3$): 148.3, 134.6, 120.1, 118.2, 51.6, 39.2, 31.2,

31.8, 31.7, 30.0, 29.6, 29.3, 29.1, 29.0, 28.9, 27.3, 26.5, 26.4, 22.7, 22.6, 14.1, 13.7, 12.6, 10.9; *m/z* (MALDI-TOF): 982.

p(DTPBBT)

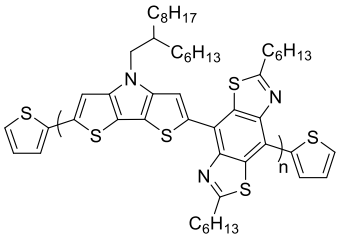

To a 5 mL microwave vial under Ar was added 4,8-Dibromo-2,6-dihexylbenzo[1,2-d:4,5-d']bis(thiazole) **(2.5)** (306 mg, 0.590 mmol), 4-(2-Hexyldecyl)-2,6-bis(tributylstannyl)-4H-dithieno[3,2-b:2',3'-d]pyrrole **(4.19)** (430 mg, 0.590 mmol) and anhydrous chlorobenzene (2 mL) and the vial purged with Ar for 20 min. $Pd_2(dba)_3$ (27 mg, 0.029 mmol) and P(*o*-tol)$_3$ (36 mg, 0.118 mmol) were then added and the vial purged for a further 10 min. The vial was then heated to 160 °C for 50 min under Ar before addition of tributyl(thiophen-2-yl)stannane (0.1 mL) and heating for a further 10 min. 2-Bromothiophene (0.5 mL) was then added and the reaction heated for a final 10 min before being cooled to rt and precipitated into methanol (300 mL). The crude polymer was then purified via Soxhlet extraction with methanol, acetone, hexane and finally collection of the product with chloroform. The chloroform extract was concentrated and reprecipitated into acetone to yield the title compound as a dark purple solid (264 mg); Anal. Calculated for $C_{44}H_{63}N_3S_4$: C, 69.52; H, 8.09; N, 5.53. Found: C, 68.30; H, 7.84; N, 5.19; Awaiting GPC analysis. See Appendix 27 for ^{1}H NMR spectrum.

6 References

1. P. Atkins and J. de Paula, *Atkins' Physical Chemistry*, 8th edn., 2006.
2. J.-L. Bredas, *Mater. Horiz.*, 2014, **1**, 17-19.
3. P. Atkins and J. de Paula, *Atkins' Physical Chemistry*, 9 edn., 2009.
4. A. Kraft, A. C. Grimsdale and A. B. Holmes, *Angew. Chem. Int. Ed.*, 1998, **37**, 402-428.
5. H. H. Jaffe and A. L. Miller, *J. Chem. Educ.*, 1966, **43**, 469.
6. IUPAC, *Compendium of Chemical Technology*, 2 edn., Blackwell Scientific Publications, Oxford, 1997.
7. E. Condon, *Phys. Rev.*, 1926, **28**, 1182-1201.
8. J. Franck and E. G. Dymond, *Trans. Faraday Soc.*, 1926, **21**, 536-542.
9. S. Holliday, J. E. Donaghey and I. McCulloch, *Chem. Mater.*, 2014, **26**, 647-663.
10. J. Roncali, *Chem. Rev.*, 1997, **97**, 173-206.
11. J. L. Brédas, *J. Chem. Phys.*, 1985, **82**, 3808-3811.
12. M. Kertesz and Y. S. Lee, *J. Phys. Chem.*, 1987, **91**, 2690-2692.
13. F. Grein, *J. Mol. Struct. - Theochem.*, 2003, **624**, 23-28.
14. Y. H. Wijsboom, Y. Sheynin, A. Patra, N. Zamoshchik, R. Vardimon, G. Leitus and M. Bendikov, *J. Mater. Chem.*, 2011, **21**, 1368-1372.
15. F. Wudl, M. Kobayashi and A. J. Heeger, *J. Org. Chem.*, 1984, **49**, 3382-3384.
16. A. L. Kanibolotsky, F. Vilela, J. C. Forgie, S. E. Elmasly, P. J. Skabara, K. Zhang, B. Tieke, J. McGurk, C. R. Belton, P. N. Stavrinou and D. D. Bradley, *Adv. Mater,*, 2011, **23**, 2093-2097.
17. H. Pang, F. Vilela, P. J. Skabara, J. J. W. McDouall, D. J. Crouch, T. D. Anthopoulos, D. D. C. Bradley, D. M. de Leeuw, P. N. Horton and M. B. Hursthouse, *Adv. Mater.*, 2007, **19**, 4438-4442.
18. Z. Xiao, J. Subbiah, K. Sun, S. Ji, D. J. Jones, A. B. Holmes and W. W. H. Wong, *J. Mater. Chem. C*, 2014, **2**, 1306-1313.
19. A. P. Zoombelt, S. G. J. Mathijssen, M. G. R. Turbiez, M. M. Wienk and R. A. J. Janssen, *J. Mater. Chem.*, 2010, **20**, 2240-2246.
20. F. Pammer, J. Jager, B. Rudolf and Y. Sun, *Macromolecules*, 2014, **47**, 5904-5912.
21. S. Zhu, N. Dorh, J. Zhang, G. Vegesna, H. Li, F.-T. Luo, A. Tiwari and H. Liu, *J. Mater. Chem.*, 2012, **22**, 2781-2790.
22. T. Erdmann, J. Back, R. Tkachov, A. Ruff, B. Voit, S. Ludwigs and A. Kiriy, *Poly. Chem.*, 2014, **5**, 5383-5390.
23. K. Okamoto, J. Zhang, J. B. Housekeeper, S. R. Marder and C. K. Luscombe, *Macromolecules*, 2013, **46**, 8059-8078.

24. R. Mauer, M. Kastler and F. Laquai, *Adv. Funct. Mater.*, 2010, **20**, 2085-2092.

25. R. S. Bhatta, Y. Y. Yimer, M. Tsige and D. S. Perry, *Comp. Theor. Chem*, 2012, **995**, 36-42.

26. D. S. Pearson, P. A. Pincus, G. W. Heffner and S. J. Dahman, *Macromolecules*, 1993, **26**, 1570-1575.

27. Y. Zhao, Y. Guo and Y. Liu, *Adv. Mater.*, 2013, **25**, 5372-5391.

28. S. Himmelberger, K. Vandewal, Z. P. Fei, M. Heeney and A. Salleo, *Macromolecules*, 2014, **47**, 7151-7157.

29. J. J. Intemann, K. Yao, H.-L. Yip, Y.-X. Xu, Y.-X. Li, P.-W. Liang, F.-Z. Ding, X. Li and A. K. Y. Jen, *Chem. Mater.*, 2013, **25**, 3188-3195.

30. J. K. Stille, *Angew. Chem. Int. Ed.*, 1986, **25**, 508-524.

31. S. Subramaniyan, T. Earmme, N. M. Murari and S. A. Jenekhe, *Poly. Chem.*, 2014, **5**, 5707.

32. I. Kang, H. J. Yun, D. S. Chung, S. K. Kwon and Y. H. Kim, *J. Am. Chem. Soc.*, 2013, **135**, 14896-14899.

33. Y. Li, S. P. Singh and P. Sonar, *Adv. Mater.*, 2010, **22**, 4862-4866.

34. A. J. J. Lennox and G. C. Lloyd-Jones, *Chem. Soc. Rev.*, 2014, **43**, 412-443.

35. K. Okamoto, J. B. Housekeeper, F. E. Michael and C. K. Luscombe, *Poly. Chem.*, 2013, **4**, 3499-3506.

36. Plextronics, *Plexcore OS 2100*, www.sigmaaldrich.com.

37. P. Zhou, Z.-G. Zhang, Y. Li, X. Chen and J. Qin, *Chem. Mater.*, 2014, **26**, 3495-3501.

38. K. Oyaizu, T. Iwasaki, Y. Tsukahara and E. Tsuchida, *Macromolecules*, 2004, **37**, 1257-1270.

39. L. Pandey, C. Risko, J. E. Norton and J.-L. Brédas, *Macromolecules*, 2012, **45**, 6405-6414.

40. Y. Li, P. Sonar, L. Murphy and W. Hong, *Energy Environ. Sci.*, 2013, **6**, 1684-1710.

41. X. Guo, J. Quinn, Z. Chen, H. Usta, Y. Zheng, Y. Xia, J. W. Hennek, R. P. Ortiz, T. J. Marks and A. Facchetti, *J. Am. Chem. Soc.*, 2013, **135**, 1986-1996.

42. S. Yum, T. K. An, X. Wang, W. Lee, M. A. Uddin, Y. J. Kim, T. L. Nguyen, S. Xu, S. Hwang, C. E. Park and H. Y. Woo, *Chem. Mater.*, 2014, **26**, 2147-2154.

43. L. Fu, W. Fu, P. Cheng, Z. Xie, C. Fan, M. Shi, J. Ling, J. Hou, X. Zhan and H. Chen, *J. Mater. Chem. A.*, 2014, **2**, 6589-6597.

44. M. Jeffries-El, B. M. Kobilka and B. J. Hale, *Macromolecules*, 2014, **47**, 7253-7271.

45. N. E. Jackson, B. M. Savoie, K. L. Kohlstedt, M. Olvera de la Cruz, G. C. Schatz, L. X. Chen and M. A. Ratner, *J. Am. Chem. Soc.*, 2013, **135**, 10475-10483.

46. A. Casey, R. S. Ashraf, Z. Fei and M. Heeney, *Macromolecules*, 2014, **47**, 2279-2288.

47. Y. He, W. Hong and Y. Li, *J. Mater. Chem. C*, 2014, **2**, 8651-8661.

48. E. S. Hellerich, J. J. Intemann, M. Cai, R. Liu, M. D. Ewan, B. C. Tlach, M. Jeffries-El, R. Shinar and J. Shinar, *J. Mater. Chem. C*, 2013, **1**, 5191-5199.

49. T. C. Parker, D. G. Patel, K. Moudgil, S. Barlow, C. Risko, J.-L. Brédas, J. R. Reynolds and S. R. Marder, *Mater. Horiz.*, 2014, **2**, 22-36.

50. T. C. Parker, D. G. Patel, K. Moudgil, S. Barlow, C. Risko, J.-L. Bredas, J. R. Reynolds and S. R. Marder, *Materials Horizons*, 2015, **2**, 22-36.

51. J. F. W. B. H. Loo, *Macromolecules*, 1981, **14**, 915-920.

52. E. Zaborova, P. Chavez, R. Bechara, P. Leveque, T. Heiser, S. Mery and N. Leclerc, *Chem. Commun.*, 2013, **49**, 9938-9940.

53. Y. A. Getmanenko, S. Singh, B. Sandhu, C.-Y. Wang, T. Timofeeva, B. Kippelen and S. R. Marder, *J. Mater. Chem. C*, 2014, **2**, 124-131.

54. H. Pang, P. J. Skabara, D. J. Crouch, W. Duffy, M. Heeney, I. McCulloch, S. J. Coles, P. N. Horton and M. B. Hursthouse, *Macromolecules*, 2007, **40**, 6585-6593.

55. B. C. Schroeder, S. Rossbauer, R. J. Kline, L. Biniek, S. E. Watkins, T. D. Anthopoulos, I. McCulloch and C. B. Nielsen, *Macromolecules*, 2014, **47**, 2883-2890.

56. B. Liu, X. Chen, Y. Zou, L. Xiao, X. Xu, Y. He, L. Li and Y. Li, *Macromolecules*, 2012, **45**, 6898-6905.

57. A. Bhuwalka, J. F. Mike, M. He, J. J. Intemann, T. Nelson, M. D. Ewan, R. A. Roggers, Z. Lin and M. Jeffries-El, *Macromolecules*, 2011, **44**, 9611-9617.

58. E. Ahmed, F. S. Kim, H. Xin and S. A. Jenekhe, *Macromolecules*, 2009, **42**, 8615-8618.

59. E. Ahmed, S. Subramaniyan, F. S. Kim, H. Xin and S. A. Jenekhe, *Macromolecules*, 2011, **44**, 7207-7219.

60. J. F. Mike, J. J. Intemann, M. Cai, T. Xiao, R. Shinar, J. Shinar and M. Jeffries-El, *Poly. Chem.*, 2011, **2**, 2299.

61. J. K. Landquist, *J. Chem. Soc. C*, 1967, **1**, 2212-2220.

62. R. C. Evers, F. E. Arnold and T. E. Helminiak, *Macromolecules*, 1981, **14**, 925-930.

63. J. F. Mike, J. J. Inteman, A. Ellern and E. M. Jeffries, *J. Org. Chem.*, 2010, **75**, 495-497.

64. G. J. McEntee, P. J. Skabara, F. Vilela, S. Tierney, I. D. W. Samuel, S. Gambino, S. J. Coles, M. B. Hursthouse, R. W. Harrington and W. Clegg, *Chem. Mater.*, 2010, **22**, 3000-3008.

65. A. Tsumura, H. Koezuka and T. Ando, *Appl. Phys. Lett.*, 1986, **49**, 1210-1212.

66. A. Pierre, M. Sadeghi, M. M. Payne, A. Facchetti, J. E. Anthony and A. C. Arias, *Adv. Mater.*, 2014, **26**, 5722-5727.

67. Y. Hu, C. Warwick, A. Sou, L. Jiang and H. Sirringhaus, *J. Mater. Chem. C*, 2014, **2**, 1260-1263.

68. D. Cortizo-Lacalle, S. Arumugam, S. E. T. Elmasly, A. L. Kanibolotsky, N. J. Findlay, A. R. Inigo and P. J. Skabara, *J. Mater. Chem.*, 2012, **22**, 11310-11315.

69. L. Zhang, A. Fonari, Y. Liu, A. L. Hoyt, H. Lee, D. Granger, S. Parkin, T. P. Russell, J. E. Anthony, J. L. Bredas, V. Coropceanu and A. L. Briseno, *J. Am. Chem. Soc.*, 2014, **136**, 9248-9251.

70. X. Guo, S. R. Puniredd, B. He, T. Marszalek, M. Baumgarten, W. Pisula and K. Mullen, *Chem. Mater.*, 2014, **26**, 3595-3598.

71. I. Meager, M. Nikolka, B. C. Schroeder, C. B. Nielsen, M. Planells, H. Bronstein, J. W. Rumer, D. I. James, R. S. Ashraf, A. Sadhanala, P. Hayoz, J.-C. Flores, H. Sirringhaus and I. McCulloch, *Adv. Funct. Mater.*, 2014, **24**, 7109-7115.

72. S.-Y. Jang, I.-B. Kim, J. Kim, D. Khim, E. Jung, B. Kang, B. Lim, Y.-A. Kim, Y. H. Jang, K. Cho and D.-Y. Kim, *Chem. Mater.*, 2014, **26**, 6907-6910.

73. H. Usta, W. C. Sheets, M. Denti, G. Generali, R. Capelli, S. Lu, X. Yu, M. Muccini and A. Facchetti, *Chem. Mater.*, 2014, **26**, 6542-6556.

74. *CRC Handbook of Chemistry and Physics*, 89th edn., 2008.

75. J. Zaumseil and H. Sirringhaus, *Chem. Rev.*, 2007, **107**, 1296-1323.

76. BP, *Statistical Review of World Energy*, 2014.

77. Phillips, 2014.

78. DOE, *Solar Energy Utilization*, 2006.

79. GWEC, *Global Installed Wind Power Capacity*, 2013.

80. *The DESERTEC Concept*, DESERTEC Foundation, 2014.

81. NREL, 2014.

82. NREL, *The Silicon Solar Cell Turns 50*, 2004.

83. *Levelized Cost of Electricity - Renewable Energy Technologies*, Fraunhofer ISE, 2013.

84. NREL, *The Falling Price of Utility-Scale Solar PV Projects*, 2014.

85. NREL, *Best research-cell efficiencies*, 2014.

86. A. L. Dyer, R. H. Bulloch, Y. Zhou, B. Kippelen, J. R. Reynolds and F. Zhang, *Adv. Mater.*, 2014, **26**, 4895-4900.

87. B. Zhao, Z. He, X. Cheng, D. Qin, M. Yun, M. Wang, X. Huang, J. Wu, H. Wu and Y. Cao, *J. Mater. Chem. C*, 2014, **2**, 5077-5082.

88. S. Günes, H. Neugebauer and N. S. Sariciftci, *Chem. Rev.*, 2007, **107**, 1324-1338.

89. L. Lu, T. Xu, W. Chen, E. S. Landry and L. Yu, *Nat. Photon.*, 2014, **8**, 716-722.

90. Z. Li, J. D. A. Lin, H. Phan, A. Sharenko, C. M. Proctor, P. Zalar, Z. Chen, A. Facchetti and T.-Q. Nguyen, *Adv. Funct. Mater.*, 2014, **24**, 6989-6998.

91. S. B. Darling, *Energy Environ. Sci.*, 2009, **2**, 1266-1273.

92. P. W. M. Blom, V. D. Mihailetchi, L. J. A. Koster and D. E. Markov, *Adv. Mater.*, 2007, **19**, 1551-1566.

93. M. C. Scharber, D. Mühlbacher, M. Koppe, P. Denk, C. Waldauf, A. J. Heeger and C. J. Brabec, *Adv. Mater.*, 2006, **18**, 789-794.

94. B. C. Thompson and J. M. J. Fréchet, *Angew. Chem. Int. Ed.*, 2008, **47**, 58-77.

95. B. Kippelen and J.-L. Bredas, *Energy Environ. Sci.*, 2009, **2**, 251-261.

96. L. A. Perez, J. T. Rogers, M. A. Brady, Y. M. Sun, G. C. Welch, K. Schmidt, M. F. Toney, H. Jinnai, A. J. Heeger, M. L. Chabinyc, G. C. Bazan and E. J. Kramer, *Chem. Mater.*, 2014, **26**, 6531-6541.

97. Y. Huang, E. J. Kramer, A. J. Heeger and G. C. Bazan, *Chem. Rev.*, 2014, **114**, 7006-7043.

98. A. Sharenko, D. Gehrig, F. Laquai and T.-Q. Nguyen, *Chem. Mater.*, 2014, **26**, 4109-4118.

99. P. J. Skabara, J.-B. Arlin and Y. H. Geerts, *Adv. Mater.*, 2013, **25**, 1948-1954.

100. L. Fan, R. Cui, X. Guo, D. Qian, B. Qiu, J. Yuan, Y. Li, W. Huang, J. Yang, W. Liu, X. Xu, L. Li and Y. Zou, *J. Mater. Chem. C*, 2014, **2**, 5651-5659.

101. A. Sharenko, C. M. Proctor, T. S. van der Poll, Z. B. Henson, T.-Q. Nguyen and G. C. Bazan, *Adv. Mater.*, 2013, **25**, 4403-4406.

102. J. D. Douglas, M. S. Chen, J. R. Niskala, O. P. Lee, A. T. Yiu, E. P. Young and J. M. J. Fréchet, *Adv. Mater.*, 2014, **26**, 4313-4319.

103. A. a. F. Eftaiha, J.-P. Sun, I. G. Hill and G. C. Welch, *J. Mater. Chem. A.*, 2014, **2**, 1201-1213.

104. Y. Lin and X. Zhan, *Mater. Horiz.*, 2014, **1**, 470-488.

105. Y. Zang, C.-Z. Li, C.-C. Chueh, S. T. Williams, W. Jiang, Z.-H. Wang, J.-S. Yu and A. K. Y. Jen, *Adv. Mater.*, 2014, **26**, 5708-5714.

106. B. Tremolet de Villers, C. J. Tassone, S. H. Tolbert and B. J. Schwartz, *J. Phys. Chem. C*, 2009, **113**, 18978-18982.

107. H. Gao, Y. Li, L. Wang, C. Ji, Y. Wang, W. Tian, X. Yang and L. Yin, *Chem. Commun.*, 2014, **50**, 10251-10254.

108. Z. He, C. Zhong, S. Su, M. Xu, H. Wu and Y. Cao, *Nat. Photon.*, 2012, **6**, 591-595.

109. J. Peet, J. Y. Kim, N. E. Coates, W. L. Ma, D. Moses, A. J. Heeger and G. C. Bazan, *Nat. Mater.*, 2007, **6**, 497-500.

110. R. Xia, D.-S. Leem, T. Kirchartz, S. Spencer, C. Murphy, Z. He, H. Wu, S. Su, Y. Cao, J. S. Kim, J. C. deMello, D. D. C. Bradley and J. Nelson, *Adv. Energy Mater.*, 2013, **3**, 718-723.

111. J. Roncali, *Chem. Rev.*, 1992, **92**, 711-738.

112. J. F. Wolfe, B. H. Loo and F. E. Arnold, *Macromolecules*, 1981, **14**, 915-920.

113. E. C. Carmichael, V. D. Geldart, R. S. McDonald, D. B. Moore, S. Rose, L. D. Colebrook, G. D. Spiropoulos and O. S. Tee, *J. Chem. Soc., Perkin. Trans. 2*, 1997, 2609-2620.

114. V. Benin, A. T. Yeates and D. Dudis, *J. Heterocycl. Chem.*, 2008, **45**, 811-819.

115. T. W. Hagler, K. Pakbaz, K. F. Voss and A. J. Heeger, *Phys. Rev. B*, 1991, **44**, 8652-8666.

116. E. Orgiu, N. Crivillers, J. Rotzler, M. Mayor and P. Samori, *J. Mater. Chem.*, 2010, **20**, 10798-10800.

117. *2-(4-Biphenylyl)-5-phenyl-1,3,4-oxadiazole*, www.sigmaaldrich.com.

118. B. C. Tlach, A. L. Tomlinson, A. G. Ryno, D. D. Knoble, D. L. Drochner, K. J. Krager and E. M. Jeffries, *J. Org. Chem.*, 2013, **78**, 6570-6581.

119. K. R. Graham, C. Cabanetos, J. P. Jahnke, M. N. Idso, A. El Labban, G. O. Ngongang Ndjawa, T. Heumueller, K. Vandewal, A. Salleo, B. F. Chmelka, A. Amassian, P. M. Beaujuge and M. D. McGehee, *J. Am. Chem. Soc.*, 2014, **136**, 9608-9618.

120. J. E. Carle, M. Helgesen, M. V. Madsen, E. Bundgaard and F. C. Krebs, *J. Mater. Chem. C*, 2014, **2**, 1290-1297.

121. J.-G. Kang, H.-G. Cho, S. K. Kang, C. Park, S. W. Lee, G. B. Park, J. S. Lee and I. T. Kim, *J. Photochem. Photobiol. A.*, 2006, **183**, 212-217.

122. A. D. Becke, *J. Chem. Phys.*, 1993, **98**, 5648-5652.

123. T. Yanai, D. P. Tew and N. C. Handy, *Chem. Phys. Lett.*, 2004, **393**, 51-57.

124. Y. Zhao and D. Truhlar, *Theor. Chem. Acc.*, 2008, **120**, 215-241.

125. C. Adamo and V. Barone, *J. Chem. Phys.*, 1998, **108**, 664-675.

126. J.-D. Chai and M. Head-Gordon, *Phys. Chem. Chem. Phys.*, 2008, **10**, 6615-6620.

127. A. D. McLean and G. S. Chandler, *J. Chem. Phys.*, 1980, **72**, 5639-5648.

128. A. Schäfer, H. Horn and R. Ahlrichs, *J. Chem. Phys.*, 1992, **97**, 2571-2577.

129. M. J. Frisch, G. W. Trucks, H. B. Schlegel, G. E. Scuseria, M. A. Robb, J. R. Cheeseman, G. Scalmani, V. Barone, B. Mennucci, G. A. Petersson, H. Nakatsuji, M. Caricato, X. Li, H. P. Hratchian, A. F. Izmaylov, J. Bloino, G. Zheng, J. L. Sonnenberg, M. Hada, M. Ehara, K. Toyota, R. Fukuda, J. Hasegawa, M. Ishida, T. Nakajima, Y. Honda, O. Kitao, H. Nakai, T. Vreven, J. A. Montgomery Jr., J. E. Peralta, F. Ogliaro, M. J. Bearpark, J. Heyd, E. N. Brothers, K. N. Kudin, V. N. Staroverov, R. Kobayashi, J. Normand, K. Raghavachari, A. P. Rendell, J. C. Burant, S. S. Iyengar, J. Tomasi, M. Cossi, N. Rega, N. J. Millam, M. Klene, J. E. Knox, J. B. Cross, V. Bakken, C. Adamo, J. Jaramillo, R. Gomperts, R. E. Stratmann, O. Yazyev, A. J. Austin, R. Cammi, C. Pomelli, J. W. Ochterski, R. L. Martin, K. Morokuma, V. G. Zakrzewski, G. A. Voth, P. Salvador, J. J. Dannenberg, S. Dapprich, A. D. Daniels, Ö. Farkas, J. B. Foresman, J. V. Ortiz, J. Cioslowski and D. J. Fox, *Gaussian 09*, Gaussian, Inc., Wallingford, CT, USA, 2009.

130. M. Cheng, X. Yang, C. Chen, Q. Tan and L. Sun, *J. Mater. Chem. A.*, 2014, **2**, 10465-10469.

131. M. Tsuji, A. Saeki, Y. Koizumi, N. Matsuyama, C. Vijayakumar and S. Seki, *Adv. Funct. Mater.*, 2014, **24**, 28-36.

132. M. Head-Gordon, J. A. Pople and M. J. Frisch, *Chem. Phys. Lett.*, 1988, **153**, 503-506.

133. T. H. Dunning, *J. Chem. Phys.*, 1989, **90**, 1007-1023.

134. A. I. Krylov and P. M. W. Gill, *WIREs. Comput. Mol. Sci.*, 2013, **3**, 317-326.

135. K. Shizu, H. Tanaka, M. Uejima, T. Sato, K. Tanaka, H. Kaji and C. Adachi, *J. Phys. Chem. C*, 2014.

136. S. M. King, R. Matheson, F. B. Dias and A. P. Monkman, *J. Phys. Chem. B*, 2008, **112**, 8010-8016.

137. B. C. Tlach, A. L. Tomlinson, A. Bhuwalka and M. Jeffries-El, *J. Org. Chem.*, 2011, **76**, 8670-8681.

138. F. C. Grozema and L. D. A. Siebbeles, *J. Phys. Chem. Lett.*, 2011, **2**, 2951-2958.

139. A. Riano, P. Mayorga Burrezo, M. J. Mancheno, A. Timalsina, J. Smith, A. Facchetti, T. J. Marks, J. T. Lopez Navarrete, J. L. Segura, J. Casado and R. Ponce Ortiz, *J. Mater. Chem. C*, 2014, **2**, 6376-6386.

140. A. M. Grubb, M. J. Schmidt, A. J. Seed and P. Sampson, *Synthesis*, 2012, **44**, 1026-1029.

141. Y. Li, J. Zou, H.-L. Yip, C.-Z. Li, Y. Zhang, C.-C. Chueh, J. Intemann, Y. Xu, P.-W. Liang, Y. Chen and A. K. Y. Jen, *Macromolecules*, 2013, **46**, 5497-5503.

142. G. He, X. Wan, Z. Li, Q. Zhang, G. Long, Y. Liu, Y. Hou, M. Zhang and Y. Chen, *J. Mater. Chem. C*, 2014, **2**, 1337-1345.

143. C.-Y. Kuo, Y.-C. Huang, C.-Y. Hsiow, Y.-W. Yang, C.-I. Huang, S.-P. Rwei, H.-L. Wang and L. Wang, *Macromolecules*, 2013, **46**, 5985-5997.

144. Y.-X. Xu, C.-C. Chueh, H.-L. Yip, C.-Y. Chang, P.-W. Liang, J. J. Intemann, W.-C. Chen and A. K. Y. Jen, *Poly. Chem.*, 2013, **4**, 5220-5223.

145. A. Saeki, M. Tsuji, S. Yoshikawa, A. Gopal and S. Seki, *J. Mater. Chem. A.*, 2014, **2**, 6075-6080.

146. P. Deng and Q. Zhang, *Poly. Chem.*, 2014, **5**, 3298-3305.

147. D. D. Gunbas, C. Xue, S. Patwardhan, M. C. Fravventura, H. Zhang, W. F. Jager, E. J. R. Sudholter, L. D. A. Siebbeles, T. J. Savenije, S. Jin and F. C. Grozema, *Chem. Commun.*, 2014, **50**, 4955-4958.

148. Y. Li, P. Sonar, S. P. Singh, M. S. Soh, M. van Meurs and J. Tan, *J. Am. Chem. Soc.*, 2011, **133**, 2198-2204.

149. B. Bouthinon, R. Clerc, J. Vaillant, J.-M. Verilhac, J. Faure-Vincent, D. Djurado, I. Ionica, G. Man, A. Gras, G. Pananakakis, R. Gwoziecki and A. Kahn, *Adv. Funct. Mater.*, 2015, In press.

150. L. Torsi, M. Magliulo, K. Manoli and G. Palazzo, *Chem. Soc. Rev.*, 2013, **42**, 8612-8628.

151. C.-H. Kim, H. Hlaing, J.-A. Hong, J.-H. Kim, Y. Park, M. M. Payne, J. E. Anthony, Y. Bonnassieux, G. Horowitz and I. Kymissis, *Adv. Mater. Interfaces*, 2015, **2**, In press.

152. Y. Kuzumoto and M. Kitamura, *Appl. Phys. Express*, 2014, **7**, 035701.

153. G. Lu, J. Blakesley, S. Himmelberger, P. Pingel, J. Frisch, I. Lieberwirth, I. Salzmann, M. Oehzelt, R. Di Pietro, A. Salleo, N. Koch and D. Neher, *Nat. Commun.*, 2013, **4**, 1588.

154. T. Earmme, Y. J. Hwang, S. Subramaniyan and S. A. Jenekhe, *Adv. Mater.*, 2014, **26**, 6080-6085.

155. K. Kim, J.-Y. Choi, T. Kim, S.-H. Cho and H.-J. Chung, *Nature*, 2011, **479**, 338-344.

156. G. Kim, S.-J. Kang, G. K. Dutta, Y.-K. Han, T. J. Shin, Y.-Y. Noh and C. Yang, *J. Am. Chem. Soc.*, 2014, **136**, 9477-9483.

157. B. Gburek and V. Wagner, *Org. Electron.*, 2010, **11**, 814-819.

158. X. Guo, R. P. Ortiz, Y. Zheng, Y. Hu, Y.-Y. Noh, K.-J. Baeg, A. Facchetti and T. J. Marks, *J. Am. Chem. Soc.*, 2011, **133**, 1405-1418.

159. Z. Lu, B. Jiang, X. Zhang, A. Tang, L. Chen, C. Zhan and J. Yao, *Chem. Mater.*, 2014.

160. C.-P. Chen, Y.-C. Chen and C.-Y. Yu, *Poly. Chem.*, 2013, **4**, 1161-1166.

161. C. B. Nielsen, R. S. Ashraf, N. D. Treat, B. C. Schroeder, J. E. Donaghey, A. J. White, N. Stingelin and I. McCulloch, *Adv. Mater.*, 2015, **27**, 948-953.

162. M. Gora, W. Krzywiec, J. Mieczkowski, E. C. Rodrigues Maia, G. Louarn, M. Zagorska and A. Pron, *Electrochim. Acta*, 2014, **144**, 211-220.

163. P. Sonar, E. L. Williams, S. P. Singh and A. Dodabalapur, *J. Mater. Chem.*, 2011, **21**, 10532-10541.

164. G. Dennler, M. C. Scharber and C. J. Brabec, *Adv. Mater.*, 2009, **21**, 1323-1338.

165. A. M. Nardes, M. Kemerink, M. M. de Kok, E. Vinken, K. Maturova and R. A. J. Janssen, *Org. Electron.*, 2008, **9**, 727-734.

166. X. Hu, M. Wang, F. Huang, X. Gong and Y. Cao, *Synth. Met.*, 2013, **164**, 1-5.

167. J. Sun, Y. Zhu, X. Xu, L. Lan, L. Zhang, P. Cai, J. Chen, J. Peng and Y. Cao, *J. Phys. Chem. C*, 2012, **116**, 14188-14198.

168. J. W. Jo, J. W. Jung, H.-W. Wang, P. Kim, T. P. Russell and W. H. Jo, *Chem. Mater.*, 2014, **26**, 4214-4220.

169. Y. Yang, R. Wu, X. Wang, X. Xu, Z. Li, K. Li and Q. Peng, *Chem. Commun.*, 2014, **50**, 439-441.

170. Z. Li, J. Lu, S.-C. Tse, J. Zhou, X. Du, Y. Tao and J. Ding, *J. Mater. Chem.*, 2011, **21**, 3226-3233.

171. K. C. Molloy, P. C. Waterfield and M. F. Mahon, *J. Organomet. Chem.*, 1989, **365**, 61-73.

172. P. Stanetty, M. Schnürch and M. D. Mihovilovic, *J. Org. Chem.*, 2006, **71**, 3754-3761.

173. D. E. Seitz, S.-H. Lee, R. N. Hanson and J. C. Bottaro, *Synth. Commun.*, 1983, **13**, 121-128.

174. L. Biniek, S. Fall, C. L. Chochos, D. V. Anokhin, D. A. Ivanov, N. Leclerc, P. Lévêque and T. Heiser, *Macromolecules*, 2010, **43**, 9779-9786.

175. N. Wang, Z. Chen, W. Wei and Z. Jiang, *J. Am. Chem. Soc.*, 2013, **135**, 17060-17068.

176. X. Guo, R. P. Ortiz, Y. Zheng, M.-G. Kim, S. Zhang, Y. Hu, G. Lu, A. Facchetti and T. J. Marks, *J. Am. Chem. Soc.*, 2011, **133**, 13685-13697.

177. Y. A. Getmanenko, T. A. Purcell, D. K. Hwang, B. Kippelen and S. R. Marder, *J. Org. Chem.*, 2012, **77**, 10931-10937.

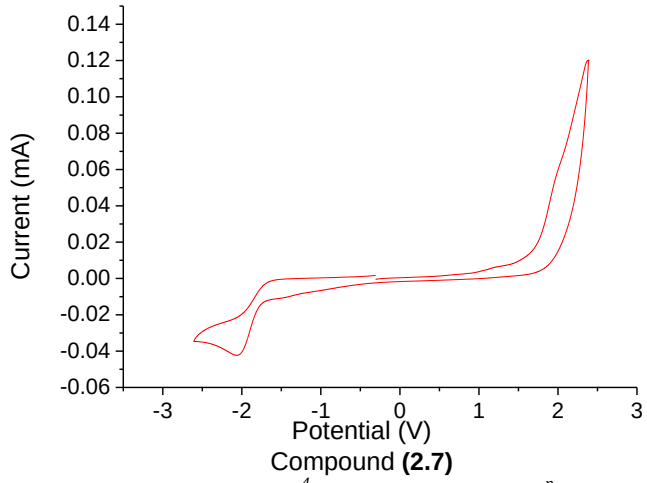

*Appendix 1 - CV of **(2.7)** conducted using a 10^{-4}M solution in CH_2Cl_2/$^nBu_4NPF_6$ (100 mV/s scan rate).*

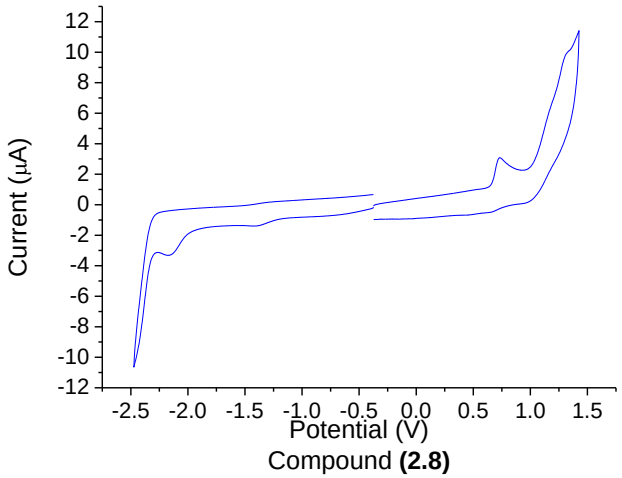

*Appendix 2 - CV of **(2.8)** conducted using a 10^{-4}M solution in CH_2Cl_2/$^nBu_4NPF_6$ (100 mV/s scan rate).*

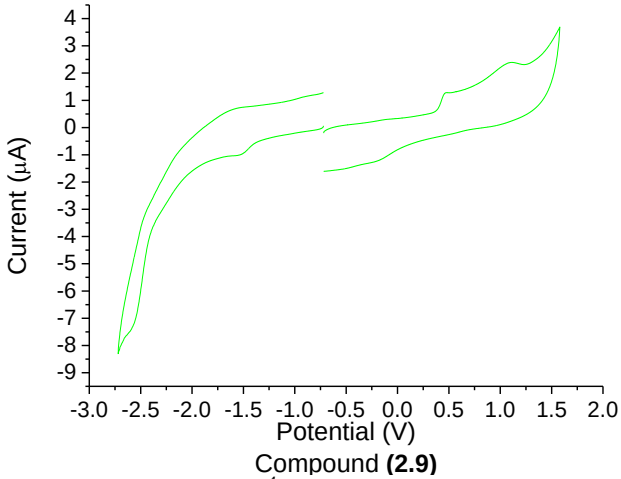

*Appendix 3 - CV of **(2.9)** conducted using a 10^{-4}M solution in CH_2Cl_2/$^nBu_4NPF_6$ (100 mV/s scan rate).*

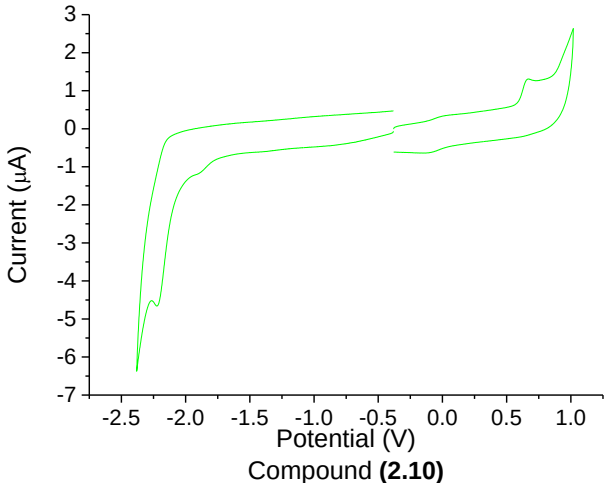

*Appendix 4 - CV of **(2.10)** conducted using a 10^{-4}M solution in CH_2Cl_2/$^nBu_4NPF_6$ (100 mV/s scan rate).*

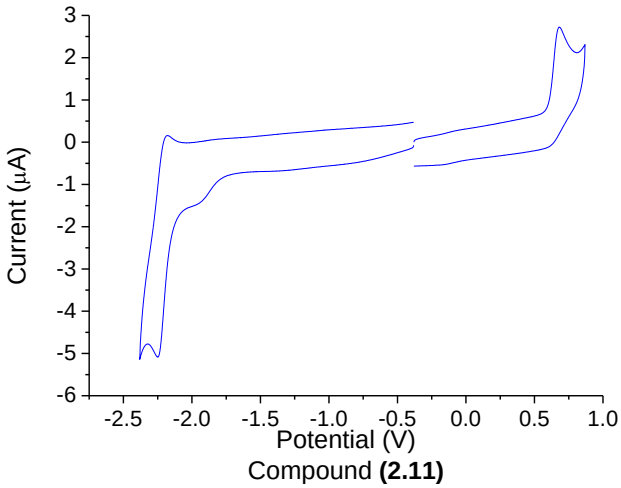

*Appendix 5 – CV of **(2.11)** conducted using a 10^{-4}M solution in CH_2Cl_2/$^nBu_4NPF_6$ (100 mV/s scan rate).*

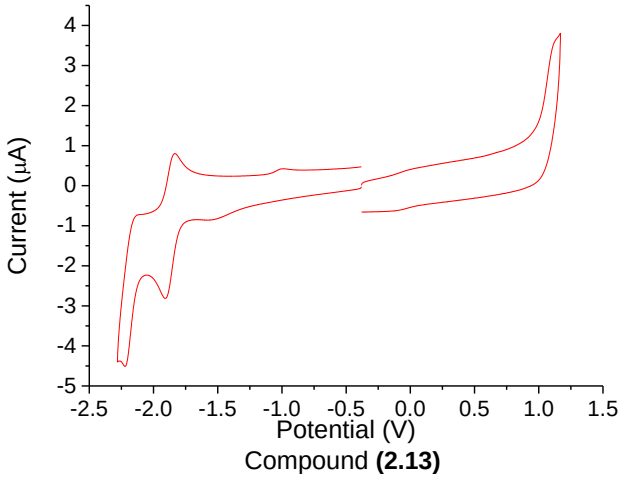

*Appendix 6 - CV of **(2.13)** conducted using a 10^{-4}M solution in CH_2Cl_2/$^nBu_4NPF_6$ (100 mV/s scan rate).*

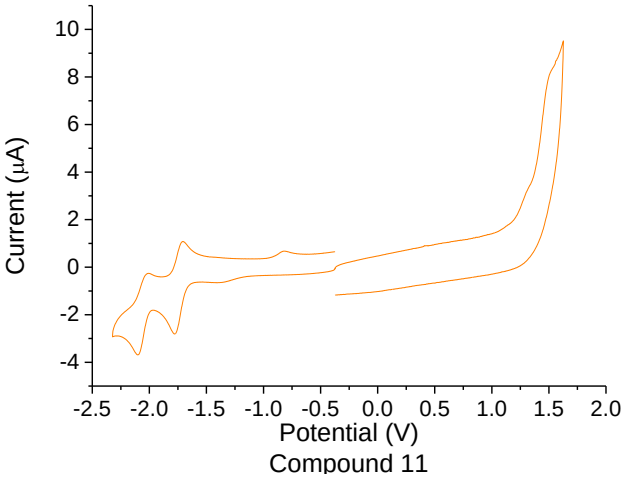

Appendix 7 - CV of ***(2.15)*** *conducted using a 10^{-4}M solution in CH_2Cl_2/$^nBu_4NPF_6$ (100 mV/s scan rate).*

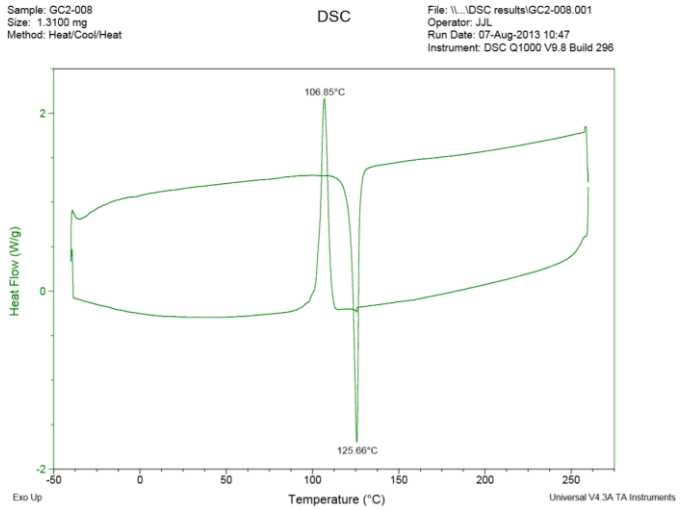

Appendix 8 - DSC thermogram of ***(2.7).***

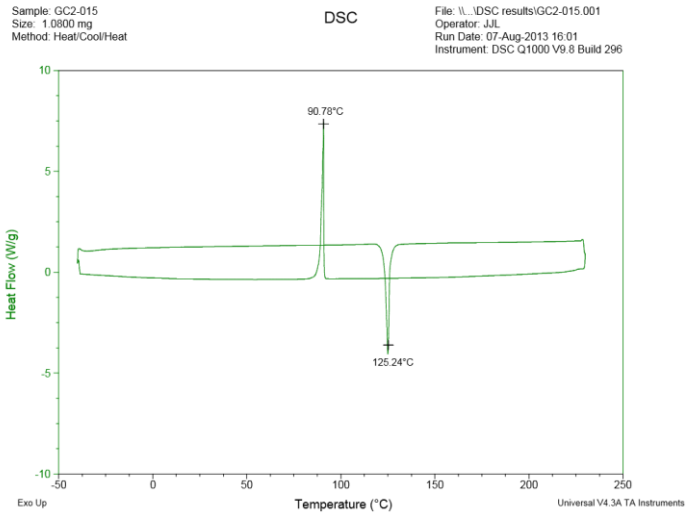

Appendix 9 - DSC thermogram of ***(2.8).***

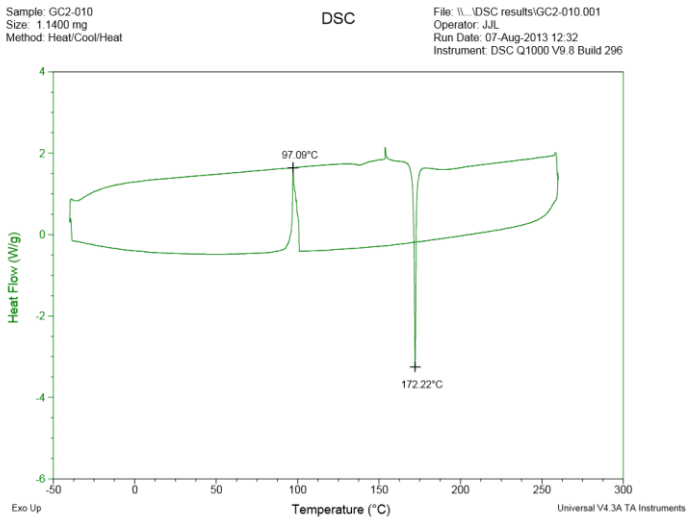

*Appendix 10 - DSC thermogram of **(2.10).***

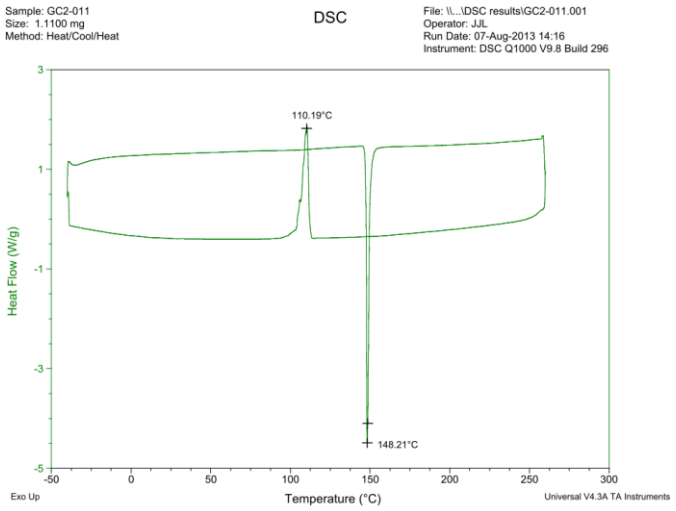

*Appendix 11 - DSC thermogram of **(2.11).***

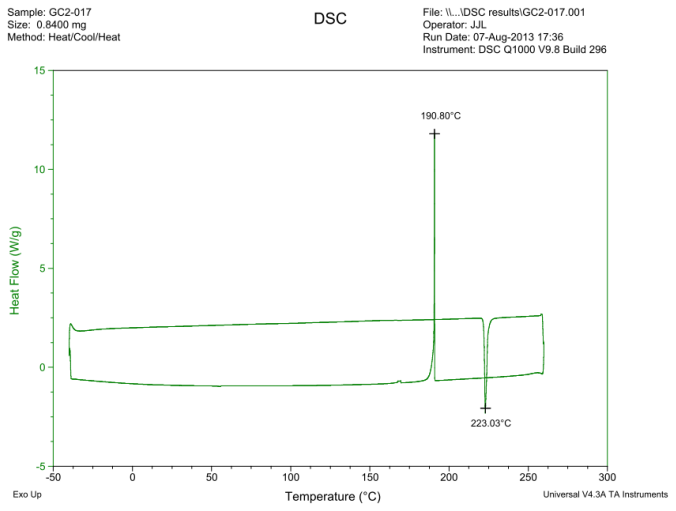

*Appendix 12 - DSC thermogram of **(2.13).***

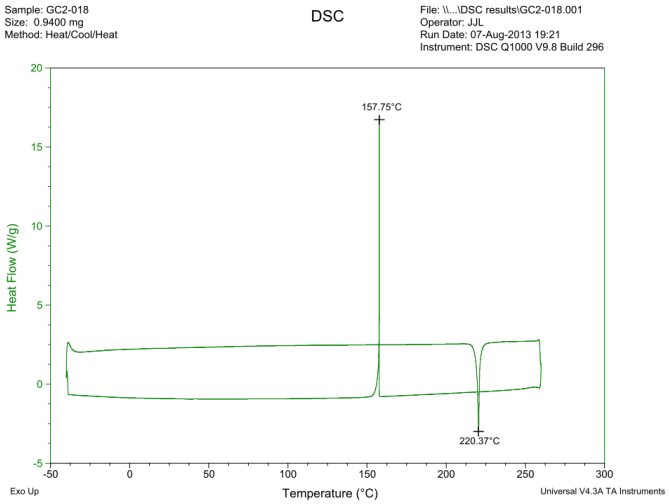

Appendix 13 - DSC thermogram of ***(2.15).***

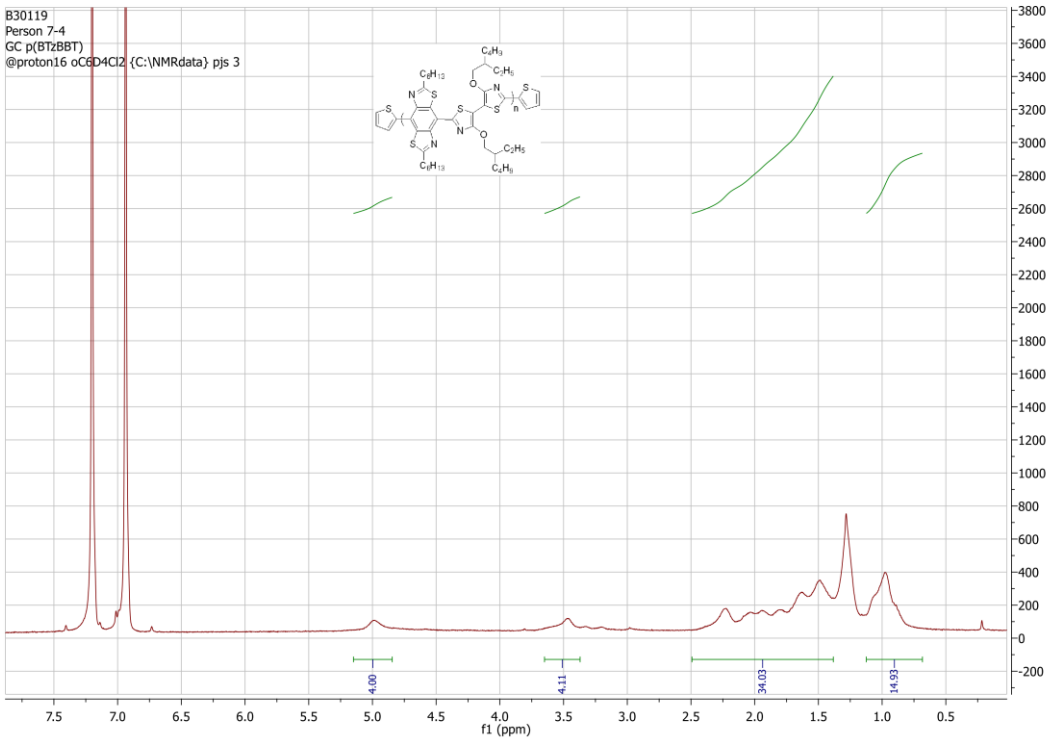

Appendix 14 - 1H NMR of ***p(BTzBBT)*** *in* $C_6D_4Cl_2$.

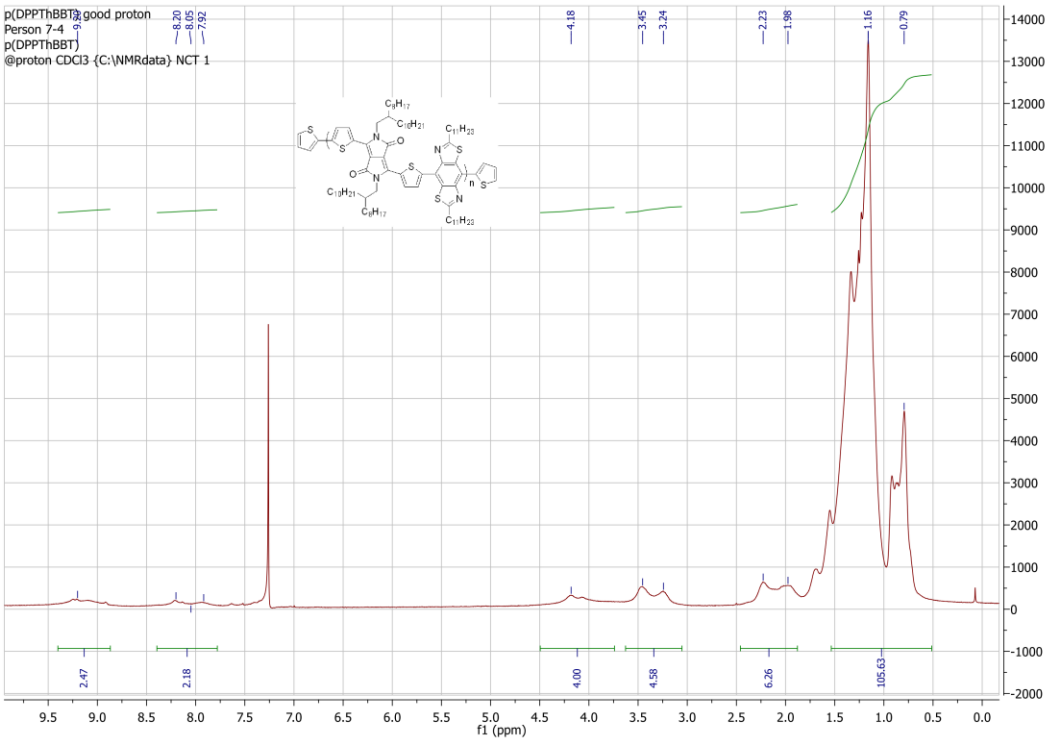

*Appendix 15 - ^{1}H NMR spectra of **p(DPPThBBT)** in $CDCl_3$.*

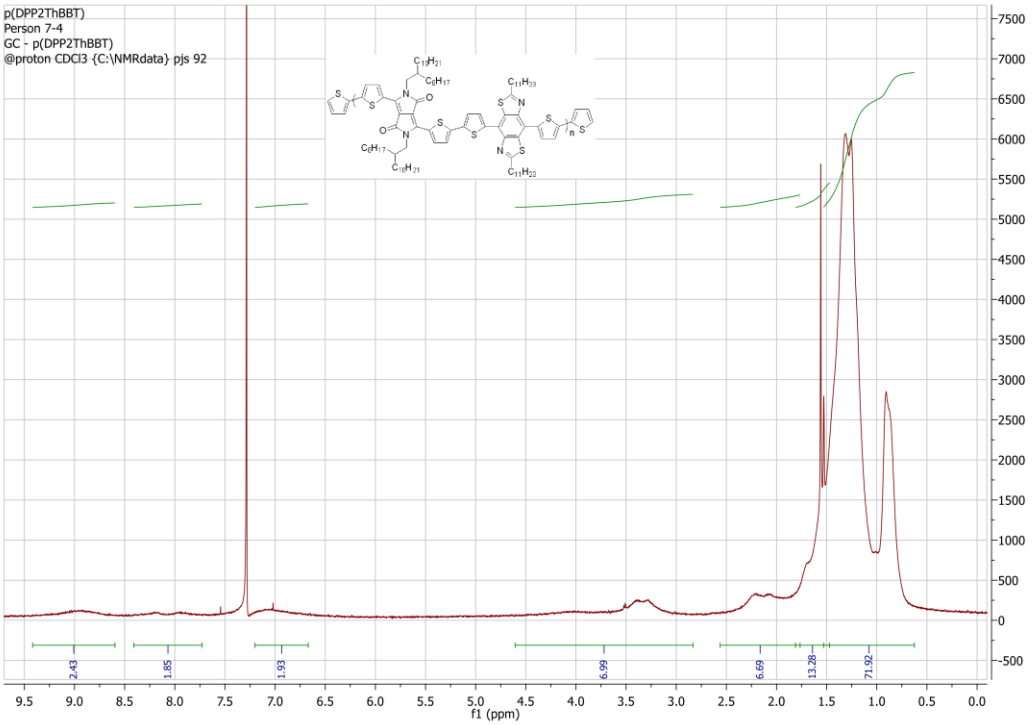

*Appendix 16 - ^{1}H NMR of **p(DPP2ThBBT)** in $CDCl_3$.*

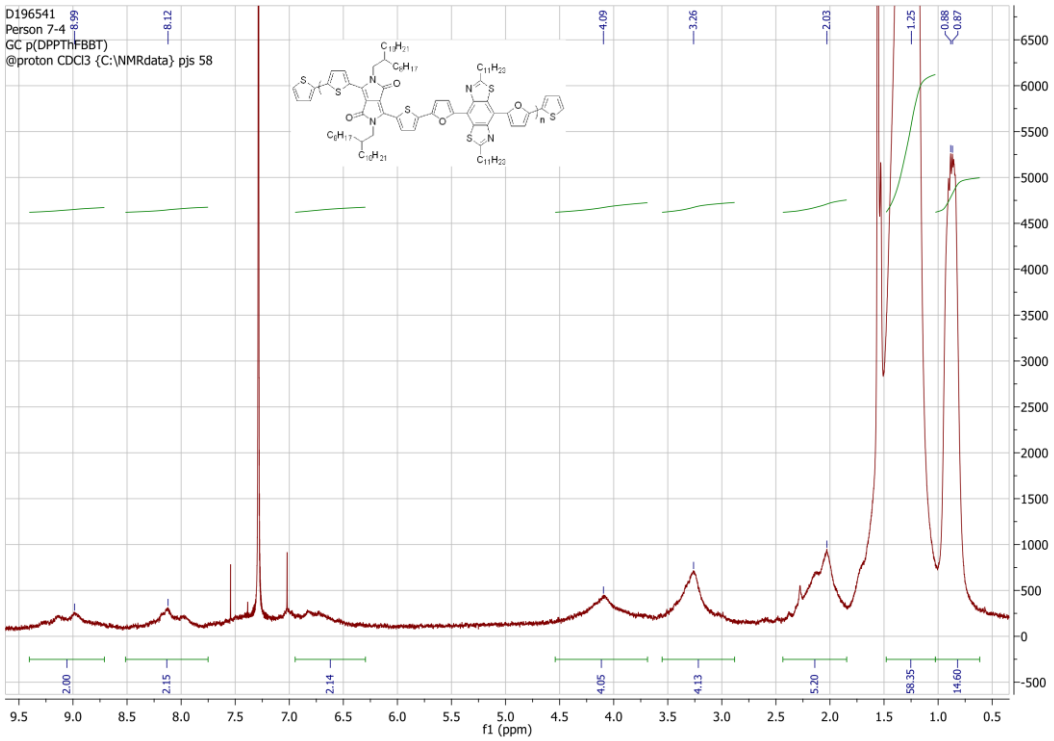

*Appendix 17 - ^{1}H NMR of **p(DPPThFBBT)** in $CDCl_3$.*

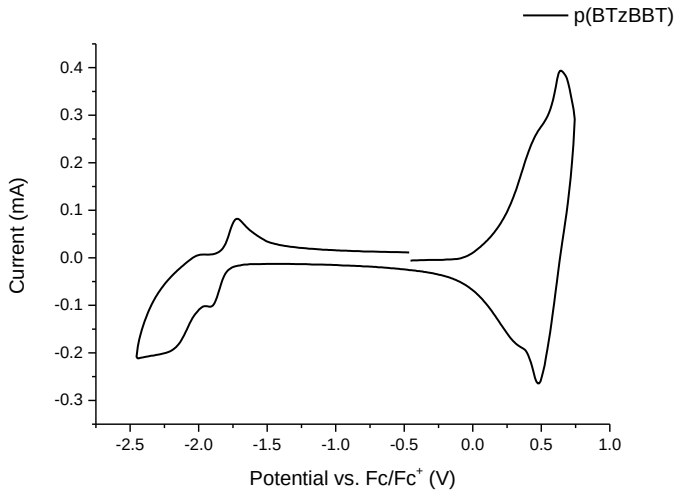

*Appendix 18 - Cyclic voltammogram of **p(BTzBBT)** conducted as a thin-film on platinum disk electrode with MeCN/$^{n}Bu_4NPF_6$ supporting electrolyte (100 mV/s scan rate).*

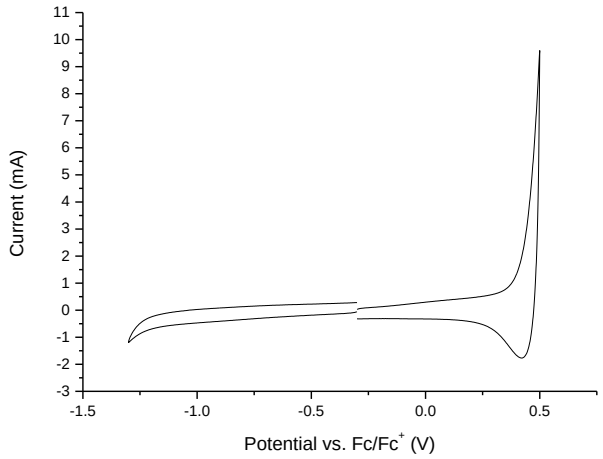

*Appendix 19 - Cyclic voltammogram of **p(DPPThBBT)** conducted as a thin-film on platinum disk electrode with MeCN/$_n$Bu$_4$NPF$_6$ supporting electrolyte (100 mV/s scan rate).*

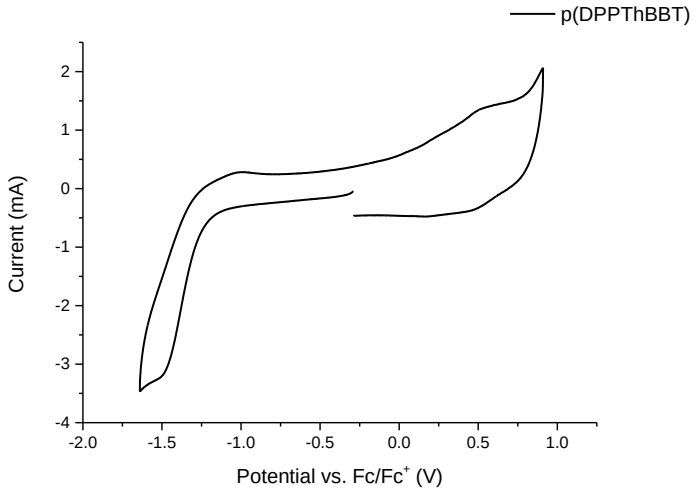

*Appendix 20 - Cyclic voltammogram of **p(DPPThBBT)** conducted using a 0.1 mg/mL solution in CHCl3/$_n$Bu$_4$NPF$_6$ (100 mV/s scan rate).*

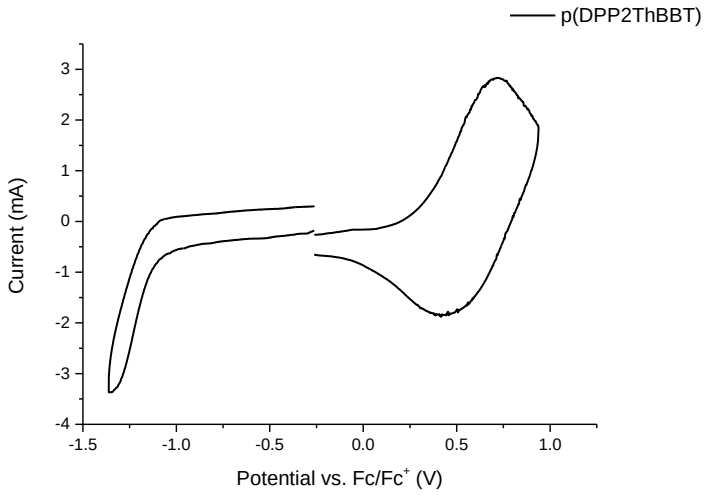

*Appendix 21 - Cyclic voltammogram of **p(DPP2ThBBT)** conducted as a thin-film on platinum disk electrode with MeCN/$_n$Bu$_4$NPF$_6$ supporting electrolyte (100 mV/s scan rate).*

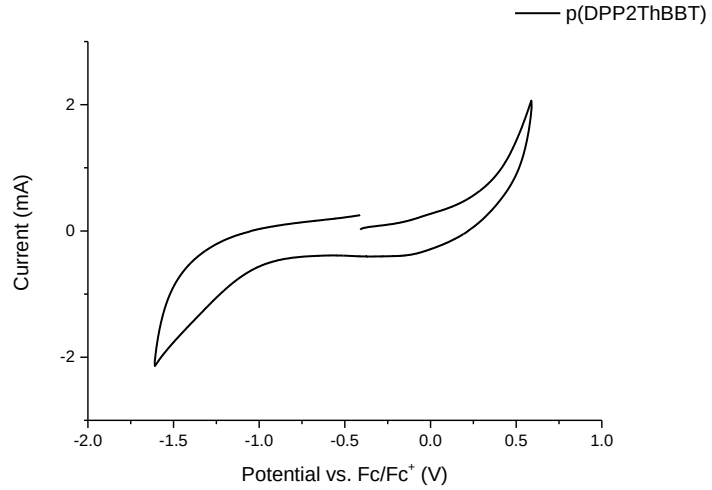

*Appendix 22 - Cyclic voltammogram of **p(DPP2ThBBT)** conducted using a 0.1 mg/mL solution in $CHCl_3$/$^nBu_4NPF_6$ (100 mV/s scan rate).*

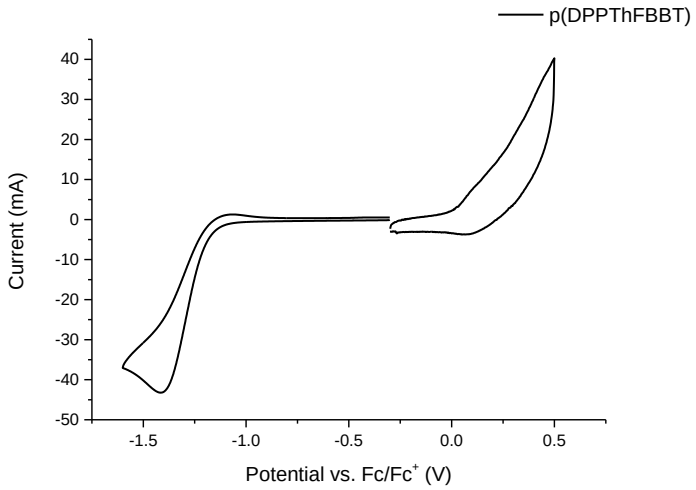

*Appendix 23 - Cyclic voltammogram of **p(DPPThFBBT)** conducted as a thin-film on platinum disk electrode with MeCN/$^nBu_4NPF_6$ supporting electrolyte (100 mV/s scan rate).*

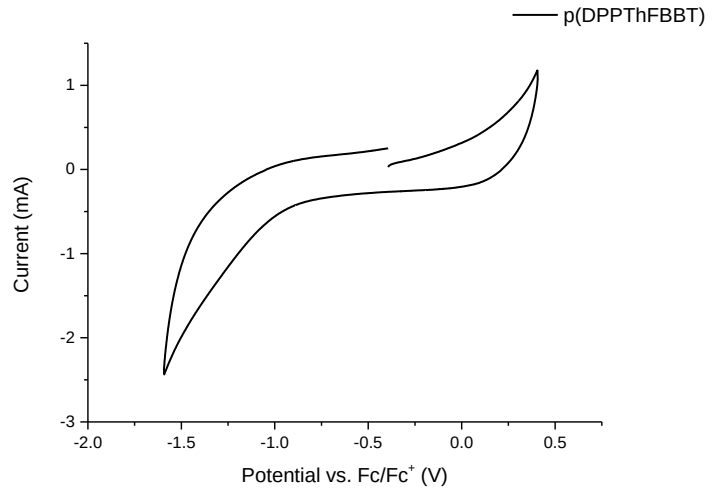

*Appendix 24 - Cyclic voltammogram of **p(DPPThFBBT)** conducted using a 0.1 mg/mL solution in $CHCl_3$/$^nBu_4NPF_6$ (100 mV/s scan rate).*

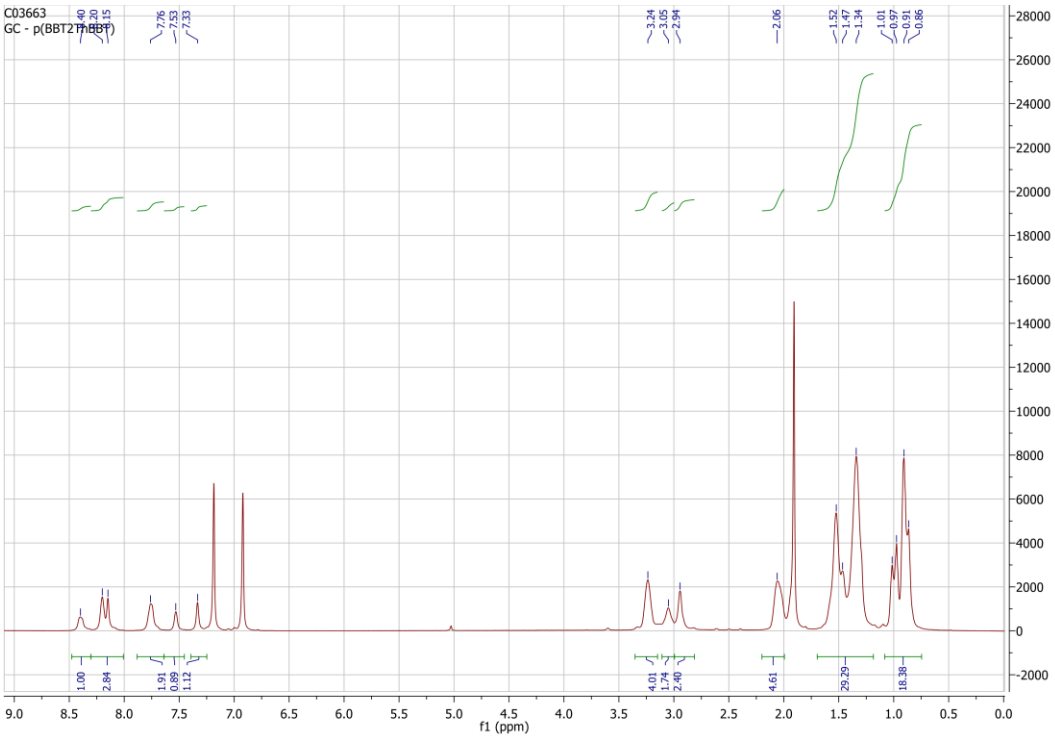

*Appendix 25 - ^{1}H NMR spectrum of **p(BBT2ThBT)** in $C_6D_4Cl_2$.*

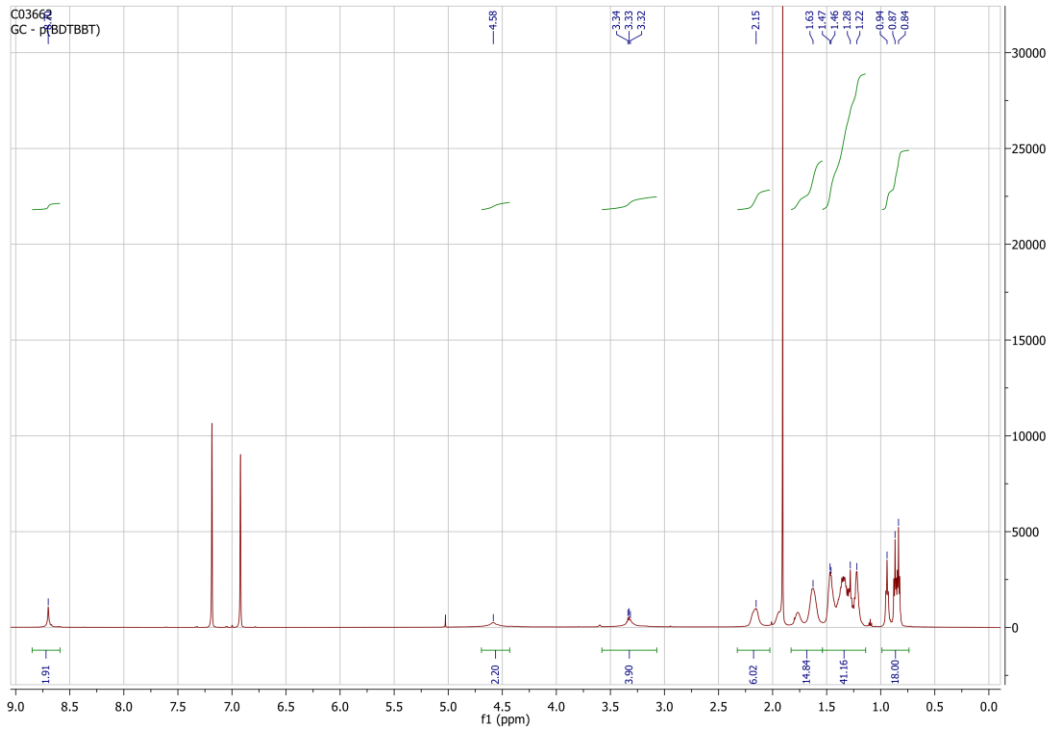

*Appendix 26 - ^{1}H NMR spectrum of **p(BDTBBT)** in $C_6D_4Cl_2$.*

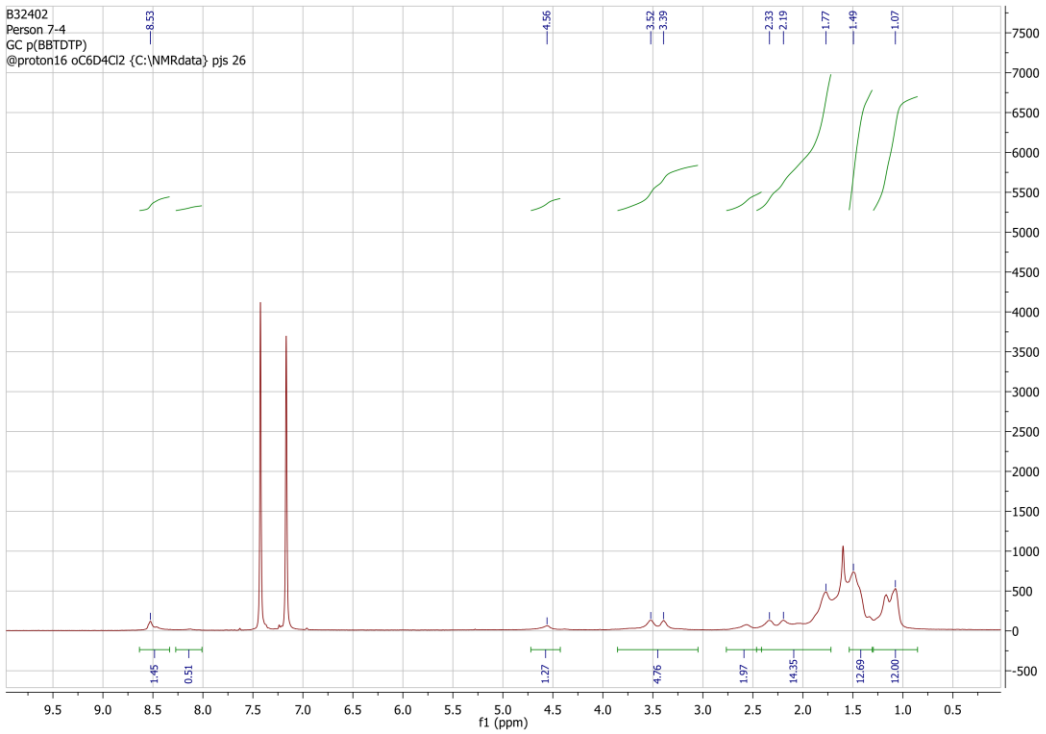

*Appendix 27 - ^{1}H NMR of **p(DTPBBT)** in $C_6D_4Cl_2$.*

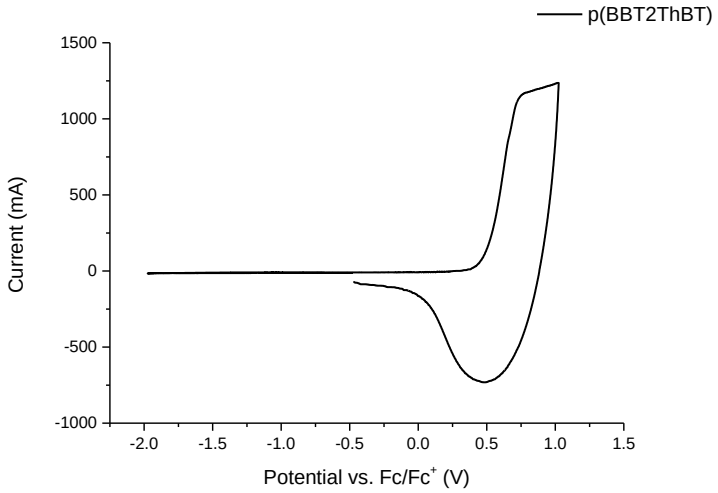

*Appendix 28 - Cyclic voltammogram of **p(BBT2ThBT)** conducted as a thin-film on platinum disk electrode with MeCN/$^{n}Bu_4NPF_6$ supporting electrolyte (100 mV/s scan rate).*

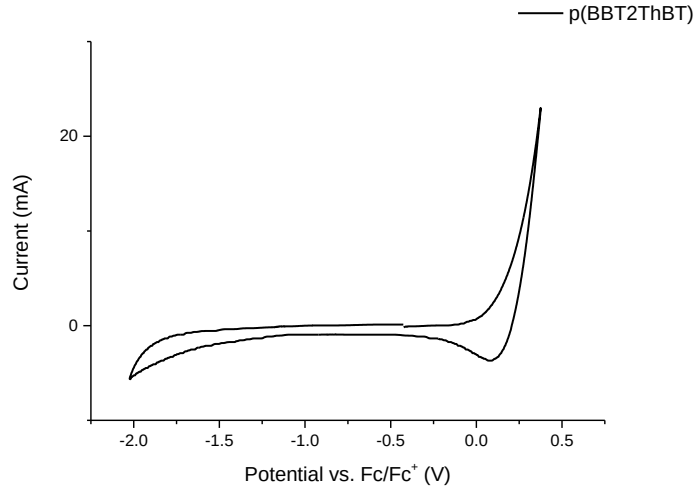

*Appendix 29 - Cyclic voltammogram of **p(BBT2ThBT)** conducted using a 0.1 mg/mL solution in $CHCl_3$/$^nBu_4NPF_6$ (100 mV/s scan rate).*

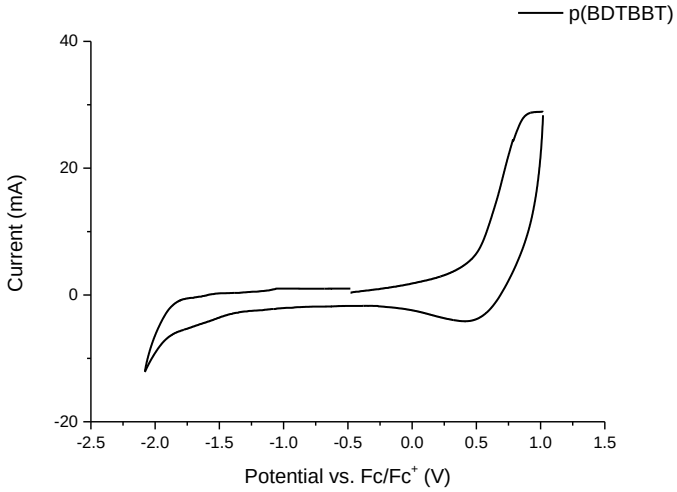

*Appendix 30 - Cyclic voltammogram of **p(BDTBBT)** conducted as a thin-film on platinum disk electrode with MeCN/$^nBu_4NPF_6$ supporting electrolyte (100 mV/s scan rate).*

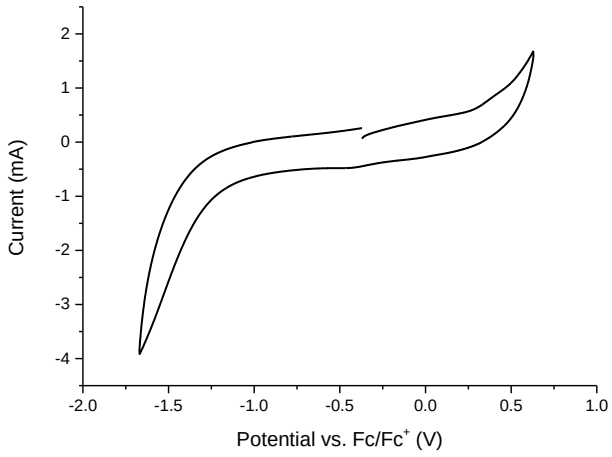

*Appendix 31 - Cyclic voltammogram of **p(BDTBBT)** conducted using a 0.1 mg/mL solution in $CHCl_3$/$^nBu_4NPF_6$ (100 mV/s scan rate).*

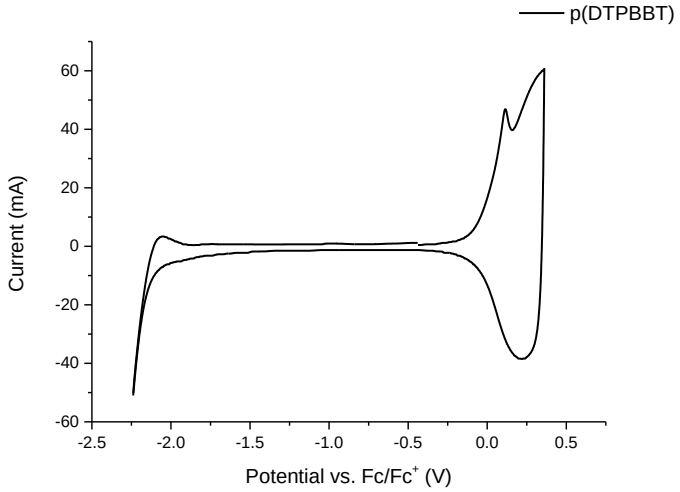

*Appendix 32 - Cyclic voltammogram of **p(DTPBBT)** conducted as a thin-film on platinum disk electrode with MeCN/$^{n}Bu_4NPF_6$ supporting electrolyte (100 mV/s scan rate).*

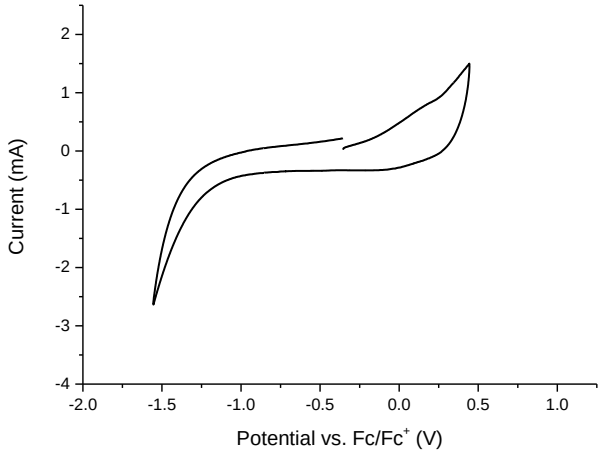

*Appendix 33 - Cyclic voltammogram of **p(DTPBBT)** conducted using a 0.1 mg/mL solution in $CHCl_3$/$^{n}Bu_4NPF_6$ (100 mV/s scan rate).*

Appendix 34 – Crystal structure data for ***(2.7)***

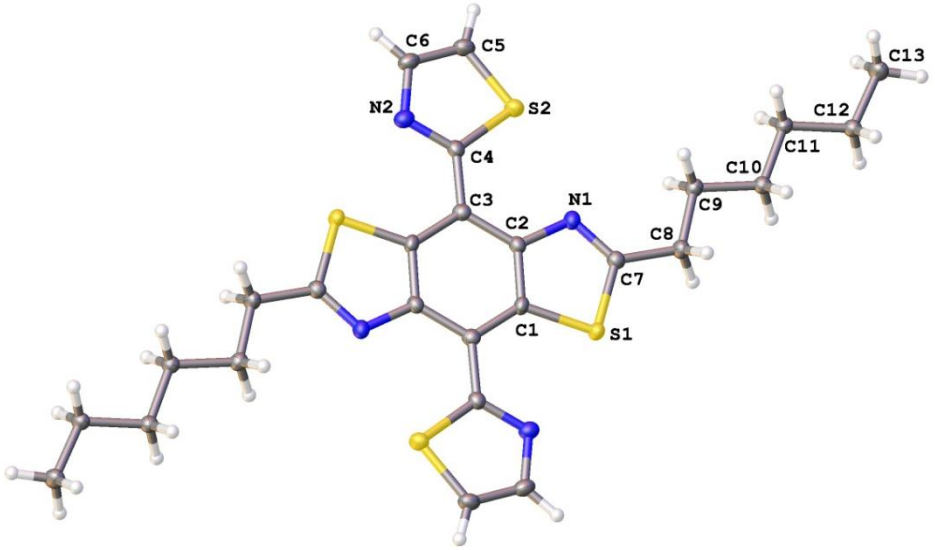

Crystal data and structure refinement details.

Identification code	2013ncs0176
Empirical formula	$C_{26}H_{30}N_4S_4$
Formula weight	526.78
Temperature	100(2) K
Wavelength	0.71075 Å
Crystal system	Triclinic
Space group	*P*–1
Unit cell dimensions	a = 8.5288(11) Å α = 105.144(7)°
	b = 8.7463(11) Å β = 93.192(7)°
	c = 9.9866(14) Å γ = 117.597(8)°
Volume	623.53(14) Å^3
Z	1
Density (calculated)	1.403 Mg / m^3
Absorption coefficient	0.405 mm^{-1}
F(000)	278
Crystal	Plate; Yellow
Crystal size	0.11 × 0.04 × 0.01 mm^3
θ range for data collection	3.13 – 27.48°
Index ranges	$-11 \le h \le 9$, $-8 \le k \le 11$, $-12 \le l \le 11$
Reflections collected	5158

Independent reflections	2823 [R_{int} = 0.0414]
Completeness to θ =	27.48° 99.0 %
Absorption correction	Semi−empirical from equivalents
Max. and min. transmission	1.000 and 0.709
Refinement method	Full-matrix least-squares on F^2
Data / restraints / parameters	2823 / 0 / 155
Goodness-of-fit on F^2	1.050
Final *R* indices [$F^2 > 2\sigma(F^2)$]	*R1* = 0.0453, *wR2* = 0.1047
R indices (all data)	*R1* = 0.0633, *wR2* = 0.1130
Largest diff. peak and hole	0.470 and −0.419 e Å^{-3}

Atomic coordinates [$\times 10^4$], equivalent isotropic displacement parameters [$Å^2 \times 10^3$] and site occupancy factors. U_{eq} is defined as one third of the trace of the orthogonalized U^{ij} tensor.

Atom	*x*	*y*	*z*	U_{eq}	*S.o.f.*
S1	3760(1)	2287(1)	8822(1)	19(1)	1
S2	7683(1)	24(1)	6646(1)	22(1)	1
N1	7250(2)	–1312(2)	8990(2)	19(1)	1
N2	6062(2)	1897(2)	7004(2)	20(1)	1
C1	4565(3)	1010(3)	9370(2)	17(1)	1
C2	6127(3)	–619(3)	9441(2)	17(1)	1
C3	5707(3)	410(3)	8775(2)	17(1)	1
C4	6402(3)	844(3)	7539(2)	17(1)	1
C5	7721(3)	1173(3)	5486(3)	23(1)	1
C6	6806(3)	2080(3)	5843(3)	22(1)	1
C7	2586(3)	2198(3)	10209(2)	18(1)	1
C8	1477(3)	3120(3)	10374(3)	22(1)	1
C9	570(3)	3079(3)	11637(2)	19(1)	1
C10	–492(3)	4085(3)	11637(2)	19(1)	1
C11	–1540(3)	4117(3)	12812(3)	19(1)	1
C12	–2529(3)	5169(3)	12712(3)	20(1)	1
C13	–3619(3)	5271(3)	13840(3)	26(1)	1

Bond lengths [Å] and angles [°].

S1–C1	1.734(2)
S1–C7	1.751(2)
S2–C4	1.733(2)
S2–C5	1.713(2)
N1–C2	1.390(3)
N1–C7^{i}	1.293(3)
N2–C4	1.306(3)
N2–C6	1.363(3)
C1–C2^{i}	1.406(3)
C1–C3	1.397(3)
C2–C1^{i}	1.406(3)
C2–C3	1.402(3)
C3–C4	1.462(3)
C5–H5	0.9300
C5–C6	1.349(3)
C6–H6	0.9300
C7–N1^{i}	1.293(3)
C7–C8	1.493(3)
C8–H8A	0.9700
C8–H8B	0.9700
C8–C9	1.515(3)
C9–H9A	0.9700
C9–H9B	0.9700
C9–C10	1.528(3)
C10–H10A	0.9700
C10–H10B	0.9700
C10–C11	1.516(3)
C11–H11A	0.9700
C11–H11B	0.9700
C11–C12	1.526(3)

C12–H12A	0.9700
C12–H12B	0.9700
C12–C13	1.510(3)
C13–H13A	0.9600
C13–H13B	0.9600
C13–H13C	0.9600

C1–S1–C7	88.91(10)
C5–S2–C4	88.82(11)
$C7^{i}$–N1–C2	110.25(19)
C4–N2–C6	110.89(19)
$C2^{i}$–C1–S1	109.10(16)
C3–C1–S1	128.11(18)
C3–C1–$C2^{i}$	122.78(19)
N1–C2–$C1^{i}$	115.36(19)
N1–C2–C3	123.0(2)
C3–C2–$C1^{i}$	121.64(19)
C1–C3–C2	115.6(2)
C1–C3–C4	121.31(19)
C2–C3–C4	123.11(19)
N2–C4–S2	114.27(17)
N2–C4–C3	121.0(2)
C3–C4–S2	124.75(16)
S2–C5–H5	124.8
C6–C5–S2	110.42(18)
C6–C5–H5	124.8
N2–C6–H6	122.2
C5–C6–N2	115.6(2)
C5–C6–H6	122.2
$N1^{i}$–C7–S1	116.38(16)
$N1^{i}$–C7–C8	125.1(2)

C8–C7–S1	118.48(17)
C7–C8–H8A	108.3
C7–C8–H8B	108.3
C7–C8–C9	116.06(19)
H8A–C8–H8B	107.4
C9–C8–H8A	108.3
C9–C8–H8B	108.3
C8–C9–H9A	109.9
C8–C9–H9B	109.9
C8–C9–C10	108.75(18)
H9A–C9–H9B	108.3
C10–C9–H9A	109.9
C10–C9–H9B	109.9
C9–C10–H10A	108.4
C9–C10–H10B	108.4
H10A–C10–H10B	107.4
C11–C10–C9	115.61(18)
C11–C10–H10A	108.4
C11–C10–H10B	108.4
C10–C11–H11A	109.5
C10–C11–H11B	109.5
C10–C11–C12	110.85(18)
H11A–C11–H11B	108.1
C12–C11–H11A	109.5
C12–C11–H11B	109.5
C11–C12–H12A	108.6
C11–C12–H12B	108.6
H12A–C12–H12B	107.6
C13–C12–C11	114.72(19)
C13–C12–H12A	108.6
C13–C12–H12B	108.6

C12−C13−H13A	109.5
C12−C13−H13B	109.5
C12−C13−H13C	109.5
H13A−C13−H13B	109.5
H13A−C13−H13C	109.5
H13B−C13−H13C	109.5

Anisotropic displacement parameters [$Å^2 \times 10^3$]. The anisotropic displacement factor exponent takes the form: $-2\pi^2[h^2a^{*2}U^{11} + \cdots + 2\,h\,k\,a^*\,b^*\,U^{12}]$.

Atom	U^{11}	U^{22}	U^{33}	U^{23}	U^{13}	U^{12}
S1	21(1)	21(1)	23(1)	12(1)	9(1)	14(1)
S2	25(1)	25(1)	23(1)	12(1)	11(1)	15(1)
N1	18(1)	18(1)	24(1)	9(1)	5(1)	10(1)
N2	21(1)	19(1)	21(1)	9(1)	6(1)	9(1)
C1	17(1)	17(1)	21(1)	9(1)	3(1)	10(1)
C2	14(1)	16(1)	20(1)	6(1)	5(1)	7(1)
C3	16(1)	15(1)	18(1)	5(1)	5(1)	7(1)
C4	15(1)	17(1)	21(1)	7(1)	4(1)	7(1)
C5	22(1)	27(1)	21(1)	12(1)	9(1)	11(1)
C6	22(1)	23(1)	22(1)	12(1)	6(1)	9(1)
C7	17(1)	18(1)	21(1)	7(1)	6(1)	9(1)
C8	24(1)	25(1)	27(1)	14(1)	11(1)	17(1)
C9	21(1)	19(1)	20(1)	9(1)	6(1)	11(1)
C10	19(1)	21(1)	22(1)	10(1)	7(1)	11(1)
C11	18(1)	20(1)	22(1)	10(1)	7(1)	10(1)
C12	21(1)	22(1)	23(1)	11(1)	10(1)	13(1)
C13	30(1)	32(1)	27(1)	14(1)	14(1)	21(1)

Hydrogen coordinates [$\times 10^4$] and isotropic displacement parameters [$Å^2 \times 10^3$].

Atom	*x*	*y*	*z*	U_{eq}	*S.o.f.*
H5	8291	1172	4719	27	1
H6	6692	2783	5330	27	1
H8A	547	2555	9520	26	1
H8B	2249	4384	10444	26	1
H9A	1475	3663	12508	23	1
H9B	–239	1827	11578	23	1
H10A	346	5334	11706	23	1
H10B	–1336	3523	10734	23	1
H11A	–714	4685	13725	23	1
H11B	–2409	2877	12744	23	1
H12A	–1647	6401	12771	24	1
H12B	–3334	4599	11790	24	1
H13A	–4179	5969	13712	39	1
H13B	–2836	5846	14759	39	1
H13C	–4535	4061	13765	39	1

Torsion angles [°].

S1–C1–C3–C2	–179.57(17)
S1–C1–C3–C4	0.5(3)
S1–C7–C8–C9	–176.96(16)
S2–C5–C6–N2	–0.3(3)
N1–C2–C3–C1	–179.66(19)
N1–C2–C3–C4	0.3(3)
$N1^{i}$–C7–C8–C9	3.5(3)
C1–S1–C7–$N1^{i}$	–0.16(19)
C1–S1–C7–C8	–179.75(18)
$C1^{i}$–C2–C3–C1	0.0(3)
$C1^{i}$–C2–C3–C4	179.9(2)
C1–C3–C4–S2	–174.94(17)
C1–C3–C4–N2	4.0(3)
$C2^{i}$–C1–C3–C2	0.0(3)
$C2^{i}$–C1–C3–C4	–179.9(2)
C2–C3–C4–S2	5.1(3)
C2–C3–C4–N2	–175.9(2)
C4–S2–C5–C6	0.40(18)
C4–N2–C6–C5	–0.1(3)
C5–S2–C4–N2	–0.50(18)
C5–S2–C4–C3	178.5(2)
C6–N2–C4–S2	0.4(2)
C6–N2–C4–C3	–178.60(19)
C7–S1–C1–$C2^{i}$	0.11(17)
C7–S1–C1–C3	179.7(2)
$C7^{i}$–N1–C2–$C1^{i}$	0.0(3)
$C7^{i}$–N1–C2–C3	179.8(2)
C7–C8–C9–C10	179.82(19)
C8–C9–C10–C11	178.02(19)
C9–C10–C11–C12	179.50(19)

C10−C11−C12−C13	179.8(2)

*Appendix 35 - Full crystallographic details of **(2.10)**.*

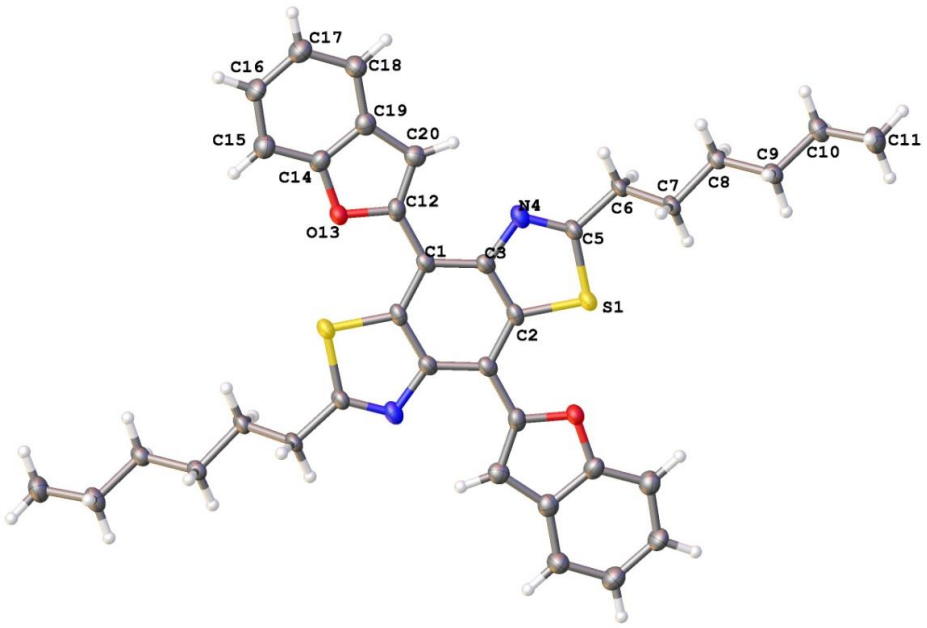

Crystal data and structure refinement details.

Identification code	2013ncs0210	
Empirical formula	$C_{36}H_{36}N_2O_2S_2$	
Formula weight	592.79	
Temperature	100(2) K	
Wavelength	0.68890 Å	
Crystal system	Monoclinic	
Space group	*P*121/*c*1	
Unit cell dimensions	a = 14.575(19) Å	α = 90°
	b = 7.664(9) Å	β = 111.280(14)°
	c = 14.393(19) Å	γ = 90°
Volume	1498(3) Å^3	
Z	2	
Density (calculated)	1.314 Mg / m^3	
Absorption coefficient	0.199 mm^{-1}	
F(000)	628	
Crystal	Platelet; Yellow	
Crystal size	0.05 × 0.03 × 0.01 mm^3	
θ range for data collection	2.770 – 26.609°	

Index ranges	$-18 \leq h \leq 18, -8 \leq k \leq 9, -18 \leq l \leq 17$
Reflections collected	14017
Independent reflections	3413 [R_{int} = 0.1461]
Completeness to θ =	24.415° 99.3 %
Absorption correction	Semi−empirical from equivalents
Max. and min. transmission	1.000 and 0.489
Refinement method	Full-matrix least-squares on F^2
Data / restraints / parameters	3413 / 0 / 191
Goodness-of-fit on F^2	1.136
Final *R* indices [$F^2 > 2\sigma(F^2)$]	*R1* = 0.1099, *wR2* = 0.2872
R indices (all data)	*R1* = 0.1530, *wR2* = 0.3160
Extinction coefficient	n/a
Largest diff. peak and hole	0.909 and −0.573 e Å^{-3}

Atomic coordinates [$\times 10^4$], equivalent isotropic displacement parameters [$Å^2 \times 10^3$] and site occupancy factors. U_{eq} is defined as one third of the trace of the orthogonalized U^{ij} tensor.

Atom	*x*	*y*	*z*	U_{eq}	*S.o.f.*
S1	6449(1)	10589(2)	3884(1)	27(1)	1
O13	2415(3)	8323(5)	4181(3)	27(1)	1
N4	4661(3)	9441(6)	2984(3)	26(1)	1
C1	4028(4)	9358(7)	4367(4)	24(1)	1
C2	5716(4)	10324(7)	4602(4)	25(1)	1
C3	4777(4)	9708(7)	3987(4)	24(1)	1
C5	5467(4)	9848(7)	2840(4)	24(1)	1
C6	5550(4)	9744(8)	1835(4)	25(1)	1
C7	6497(4)	8947(8)	1794(4)	24(1)	1
C8	6498(4)	9072(7)	735(4)	25(1)	1
C9	7438(4)	8421(8)	600(4)	27(1)	1
C10	7449(5)	8912(9)	–427(4)	33(1)	1
C11	8346(5)	8228(10)	–624(5)	41(2)	1
C12	3064(4)	8728(8)	3710(4)	28(1)	1
C14	1578(4)	7687(8)	3442(4)	29(1)	1
C15	739(4)	7091(8)	3584(5)	33(1)	1
C16	–5(4)	6477(8)	2728(4)	31(1)	1
C17	89(4)	6474(9)	1795(5)	36(1)	1
C18	936(4)	7080(8)	1672(4)	34(1)	1
C19	1707(4)	7711(8)	2531(4)	29(1)	1
C20	2674(4)	8396(7)	2717(4)	28(1)	1

Bond lengths [Å] and angles [°].

S1–C2	1.746(5)
S1–C5	1.752(6)
O13–C12	1.385(6)
O13–C14	1.384(7)
N4–C3	1.405(7)
N4–C5	1.302(7)
C1–C2^{i}	1.414(7)
C1–C3	1.414(7)
C1–C12	1.461(8)
C2–C1^{i}	1.414(7)
C2–C3	1.414(8)
C5–C6	1.496(7)
C6–H6A	0.9900
C6–H6B	0.9900
C6–C7	1.530(7)
C7–H7A	0.9900
C7–H7B	0.9900
C7–C8	1.528(7)
C8–H8A	0.9900
C8–H8B	0.9900
C8–C9	1.535(8)
C9–H9A	0.9900
C9–H9B	0.9900
C9–C10	1.532(8)
C10–H10A	0.9900
C10–H10B	0.9900
C10–C11	1.526(8)
C11–H11A	0.9800
C11–H11B	0.9800
C11–H11C	0.9800

C12–C20	1.358(8)
C14–C15	1.389(8)
C14–C19	1.391(8)
C15–H15	0.9500
C15–C16	1.395(8)
C16–H16	0.9500
C16–C17	1.398(9)
C17–H17	0.9500
C17–C18	1.390(8)
C18–H18	0.9500
C18–C19	1.420(8)
C19–C20	1.435(8)
C20–H20	0.9500
C2–S1–C5	89.2(3)
C14–O13–C12	105.7(4)
C5–N4–C3	110.4(5)
$C2^{i}$–C1–C12	124.2(5)
C3–C1–$C2^{i}$	115.3(5)
C3–C1–C12	120.6(5)
$C1^{i}$–C2–S1	128.0(4)
C3–C2–S1	109.2(4)
C3–C2–$C1^{i}$	122.8(5)
N4–C3–C1	123.2(5)
N4–C3–C2	114.8(5)
C1–C3–C2	121.9(5)
N4–C5–S1	116.4(4)
N4–C5–C6	122.3(5)
C6–C5–S1	121.3(4)
C5–C6–H6A	108.1
C5–C6–H6B	108.1
C5–C6–C7	116.7(4)

H6A–C6–H6B	107.3
C7–C6–H6A	108.1
C7–C6–H6B	108.1
C6–C7–H7A	109.7
C6–C7–H7B	109.7
H7A–C7–H7B	108.2
C8–C7–C6	110.0(4)
C8–C7–H7A	109.7
C8–C7–H7B	109.7
C7–C8–H8A	108.4
C7–C8–H8B	108.4
C7–C8–C9	115.4(4)
H8A–C8–H8B	107.5
C9–C8–H8A	108.4
C9–C8–H8B	108.4
C8–C9–H9A	109.3
C8–C9–H9B	109.3
H9A–C9–H9B	108.0
C10–C9–C8	111.4(5)
C10–C9–H9A	109.3
C10–C9–H9B	109.3
C9–C10–H10A	108.8
C9–C10–H10B	108.8
H10A–C10–H10B	107.7
C11–C10–C9	113.9(5)
C11–C10–H10A	108.8
C11–C10–H10B	108.8
C10–C11–H11A	109.5
C10–C11–H11B	109.5
C10–C11–H11C	109.5
H11A–C11–H11B	109.5

H11A–C11–H11C	109.5
H11B–C11–H11C	109.5
O13–C12–C1	115.1(5)
C20–C12–O13	112.0(5)
C20–C12–C1	132.9(5)
O13–C14–C15	125.5(5)
O13–C14–C19	109.7(5)
C15–C14–C19	124.8(6)
C14–C15–H15	122.4
C14–C15–C16	115.2(6)
C16–C15–H15	122.4
C15–C16–H16	118.9
C15–C16–C17	122.2(6)
C17–C16–H16	118.9
C16–C17–H17	119.2
C18–C17–C16	121.6(6)
C18–C17–H17	119.2
C17–C18–H18	121.2
C17–C18–C19	117.5(6)
C19–C18–H18	121.2
C14–C19–C18	118.7(5)
C14–C19–C20	106.8(5)
C18–C19–C20	134.5(5)
C12–C20–C19	105.8(5)
C12–C20–H20	127.1
C19–C20–H20	127.1

Anisotropic displacement parameters [$Å^2 \times 10^3$]. The anisotropic displacement factor exponent takes the form: $-2\pi^2[h^2a^{*2}U^{11} + \cdots + 2\,h\,k\,a^*\,b^*\,U^{12}]$.

Atom	U^{11}	U^{22}	U^{33}	U^{23}	U^{13}	U^{12}
S1	30(1)	34(1)	20(1)	0(1)	13(1)	–2(1)
O13	28(2)	35(2)	22(2)	–3(2)	13(2)	–3(2)
N4	35(2)	23(2)	26(2)	–1(2)	17(2)	1(2)
C1	28(3)	25(3)	21(2)	1(2)	11(2)	5(2)
C2	30(3)	25(3)	23(3)	5(2)	16(2)	2(2)
C3	27(3)	27(3)	20(2)	3(2)	10(2)	4(2)
C5	29(3)	26(3)	20(2)	2(2)	12(2)	–2(2)
C6	29(3)	33(3)	17(2)	0(2)	12(2)	–3(2)
C7	30(3)	27(3)	19(2)	1(2)	14(2)	–3(2)
C8	29(3)	25(3)	21(2)	–1(2)	12(2)	–3(2)
C9	32(3)	30(3)	21(2)	–1(2)	13(2)	–2(2)
C10	42(3)	35(4)	30(3)	–1(2)	21(3)	1(3)
C11	40(3)	54(4)	37(3)	0(3)	23(3)	2(3)
C12	28(3)	30(3)	30(3)	3(2)	16(2)	3(2)
C14	24(3)	31(3)	31(3)	5(2)	9(2)	0(2)
C15	33(3)	34(4)	36(3)	–1(3)	15(2)	–3(2)
C16	27(3)	32(3)	34(3)	–1(2)	12(2)	–9(2)
C17	30(3)	40(4)	38(3)	–2(3)	11(3)	–5(3)
C18	34(3)	40(4)	28(3)	–3(3)	12(2)	–5(3)
C19	29(3)	28(3)	31(3)	1(2)	13(2)	3(2)
C20	29(3)	26(3)	28(3)	–2(2)	11(2)	2(2)

Hydrogen coordinates [$\times 10^4$] and isotropic displacement parameters [$Å^2 \times 10^3$].

Atom	*x*	*y*	*z*	U_{eq}	*S.o.f.*
H6A	5483	10938	1557	30	1
H6B	4987	9053	1393	30	1
H7A	7074	9576	2260	29	1
H7B	6545	7709	2002	29	1
H8A	6392	10306	519	30	1
H8B	5933	8392	287	30	1
H9A	8019	8936	1125	32	1
H9B	7480	7137	678	32	1
H10A	6846	8448	–946	40	1
H10B	7431	10200	–489	40	1
H11A	8310	8603	–1287	62	1
H11B	8355	6951	–591	62	1
H11C	8947	8692	–119	62	1
H15	677	7101	4218	40	1
H16	–596	6046	2781	37	1
H17	–439	6049	1232	44	1
H18	997	7071	1037	40	1
H20	2979	8579	2242	33	1

Torsion angles [°].

S1−C2−C3−N4	0.8(6)
S1−C2−C3−C1	179.5(4)
S1−C5−C6−C7	45.2(7)
O13−C12−C20−C19	−0.6(7)
O13−C14−C15−C16	−178.7(6)
O13−C14−C19−C18	178.9(5)
O13−C14−C19−C20	0.0(7)
N4−C5−C6−C7	−136.6(6)
C1^{i}−C2−C3−N4	−179.0(5)
C1^{i}−C2−C3−C1	−0.3(9)
C1−C12−C20−C19	176.9(6)
C2−S1−C5−N4	0.3(5)
C2−S1−C5−C6	178.6(5)
C2^{i}−C1−C3−N4	178.9(5)
C2^{i}−C1−C3−C2	0.3(9)
C2^{i}−C1−C12−O13	−4.7(8)
C2^{i}−C1−C12−C20	177.9(6)
C3−N4−C5−S1	0.1(6)
C3−N4−C5−C6	−178.2(5)
C3−C1−C12−O13	175.9(5)
C3−C1−C12−C20	−1.5(10)
C5−S1−C2−C1^{i}	179.2(5)
C5−S1−C2−C3	−0.6(4)
C5−N4−C3−C1	−179.2(5)
C5−N4−C3−C2	−0.6(7)
C5−C6−C7−C8	−175.5(5)
C6−C7−C8−C9	176.4(5)
C7−C8−C9−C10	−169.3(5)
C8−C9−C10−C11	−177.4(5)
C12−O13−C14−C15	178.8(6)

C12–O13–C14–C19	–0.4(6)
C12–C1–C3–N4	–1.7(8)
C12–C1–C3–C2	179.8(5)
C14–O13–C12–C1	–177.4(5)
C14–O13–C12–C20	0.6(6)
C14–C15–C16–C17	–0.4(9)
C14–C19–C20–C12	0.3(7)
C15–C14–C19–C18	–0.3(10)
C15–C14–C19–C20	–179.1(6)
C15–C16–C17–C18	0.3(10)
C16–C17–C18–C19	–0.3(10)
C17–C18–C19–C14	0.2(9)
C17–C18–C19–C20	178.7(6)
C18–C19–C20–C12	–178.3(7)
C19–C14–C15–C16	0.3(9)

Hydrogen bonds [Å and °].

D–H···*A*	*d*(*D*–H)	*d*(H···*A*)	*d*(*D*···*A*)	∠(*D*H*A*)
C20–H20···N4	0.95	2.39	2.892(8)	113.0

Appendix 36 - Full crystallographic details of ***(2.11)***.

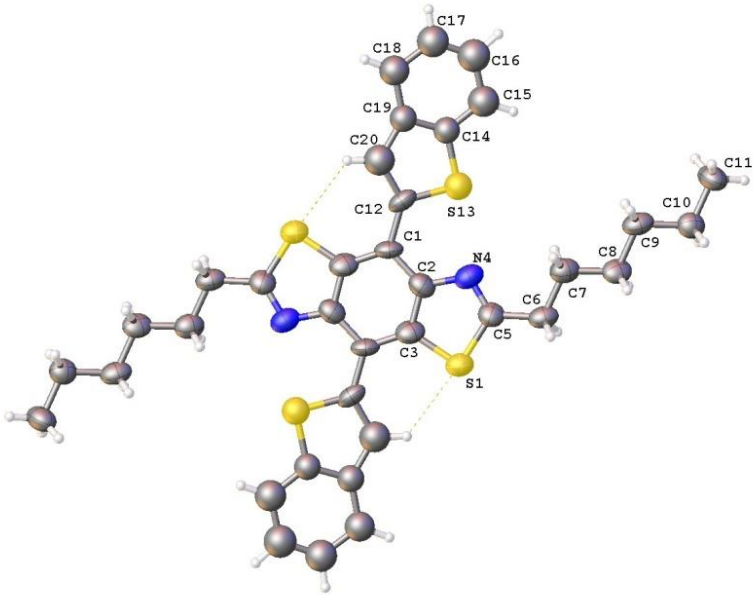

Crystal data and structure refinement details.

Identification code	2013ncs0211	
Empirical formula	$C_{36}H_{36}N_2S_4$	
Formula weight	624.93	
Temperature	100(2) K	
Wavelength	0.71075 Å	
Crystal system	Monoclinic	
Space group	*C*12/*c*1	
Unit cell dimensions	a = 15.349(15) Å	α = 90°
	b = 7.249(7) Å	β = 99.15(2)°
	c = 28.19(3) Å	γ = 90°
Volume	3097(5) Å^3	
Z	4	
Density (calculated)	1.340 Mg / m^3	
Absorption coefficient	0.336 mm^{-1}	
F(000)	1320	
Crystal	Lath; yellow	
Crystal size	0.18 × 0.02 × 0.01 mm^3	

θ range for data collection	2.688 – 24.993°
Index ranges	$-18 \le h \le 17$, $-8 \le k \le 7$, $-33 \le l \le 22$
Reflections collected	6023
Independent reflections	2548 [R_{int} = 0.088]
Completeness to θ =	25.242° 93.7 %
Absorption correction	Semi–empirical from equivalents
Max. and min. transmission	1.000 and 0.280
Refinement method	Full-matrix least-squares on F^2
Data / restraints / parameters	2548 / 12 / 165
Goodness-of-fit on F^2	1.087
Final R indices [$F^2 > 2\sigma(F^2)$]	$R1$ = 0.1512, $wR2$ = 0.3579
R indices (all data)	$R1$ = 0.2375, $wR2$ = 0.4369
Extinction coefficient	0.0032(16)
Largest diff. peak and hole	0.855 and –0.560 e Å^{-3}

Atomic coordinates [$\times 10^4$], equivalent isotropic displacement parameters [$Å^2 \times 10^3$] and site occupancy factors. U_{eq} is defined as one third of the trace of the orthogonalized U^{ij} tensor.

Atom	*x*	*y*	*z*	U_{eq}	*S.o.f.*
S1	1212(2)	209(4)	5388(1)	63(1)	1
S13A	3391(4)	–2969(9)	3703(1)	57(1)	0.65
C20A	2954(17)	280(30)	3824(6)	100(9)	0.65
N4	1844(5)	805(12)	4600(3)	63(2)	1
C8	459(7)	5948(15)	4184(3)	64(3)	1
C10	267(6)	8813(14)	3654(4)	64(3)	1
C19	3434(6)	–1338(13)	3274(3)	67(3)	1
C9	614(6)	6797(15)	3709(4)	68(3)	1
C2	2192(6)	–883(14)	4781(4)	59(3)	1
C11	501(8)	9760(15)	3208(4)	79(3)	1
C6	787(6)	3253(14)	4762(3)	62(3)	1
C5	1313(6)	1465(14)	4872(3)	60(3)	1
C18	3732(7)	–1689(17)	2817(4)	82(3)	1
C12	2981(5)	–1391(10)	4066(3)	58(3)	1
C7	886(7)	4054(16)	4279(4)	69(3)	1
C3	1943(6)	–1416(15)	5222(4)	63(3)	1
C14	3182(6)	406(14)	3361(3)	64(3)	1
C1	2771(6)	–1953(14)	4542(3)	55(3)	1
C16	3444(8)	1493(19)	2616(5)	98(4)	1
C15	3168(8)	1885(18)	3056(5)	89(4)	1
C17	3714(8)	–140(16)	2509(5)	93(4)	1
S13	2790(7)	823(13)	3877(3)	71(3)	0.35
C20	3330(30)	–2290(40)	3695(9)	90(20)	0.35

Bond lengths [Å] and angles [°].

S1–C5	1.742(10)
S1–C3	1.741(11)
S13A–C19	1.699(8)
S13A–C12	1.720(7)
C20A–H20A	0.9500
C20A–C12	1.391(12)
C20A–C14	1.405(13)
N4–C2	1.400(12)
N4–C5	1.298(11)
C8–H8A	0.9900
C8–H8B	0.9900
C8–C9	1.526(13)
C8–C7	1.526(15)
C10–H10A	0.9900
C10–H10B	0.9900
C10–C9	1.555(14)
C10–C11	1.524(13)
C19–C18	1.457(15)
C19–C14	1.356(13)
C19–C20	1.405(13)
C9–H9A	0.9900
C9–H9B	0.9900
C2–C3	1.409(14)
C2–C1	1.427(13)
C11–H11A	0.9800
C11–H11B	0.9800
C11–H11C	0.9800
C6–H6A	0.9900
C6–H6B	0.9900
C6–C5	1.533(13)

C6–C7	1.511(13)
C18–H18	0.9500
C18–C17	1.417(16)
C12–C1	1.487(12)
C12–S13	1.702(9)
C12–C20	1.406(13)
C7–H7A	0.9900
C7–H7B	0.9900
C3–C1^{i}	1.393(14)
C14–C15	1.374(14)
C14–S13	1.688(9)
C1–C3^{i}	1.393(14)
C16–H16	0.9500
C16–C15	1.401(17)
C16–C17	1.305(15)
C15–H15	0.9500
C17–H17	0.9500
C20–H20	0.9500

C5–S1–C3	89.0(5)
C19–S13A–C12	91.2(6)
C12–C20A–H20A	119.4
C12–C20A–C14	121.2(18)
C14–C20A–H20A	119.4
C5–N4–C2	110.1(9)
H8A–C8–H8B	107.7
C9–C8–H8A	108.9
C9–C8–H8B	108.9
C9–C8–C7	113.2(9)
C7–C8–H8A	108.9
C7–C8–H8B	108.9

H10A–C10–H10B	107.8
C9–C10–H10A	109.1
C9–C10–H10B	109.1
C11–C10–H10A	109.1
C11–C10–H10B	109.1
C11–C10–C9	112.6(9)
C18–C19–S13A	124.1(8)
C14–C19–S13A	118.4(8)
C14–C19–C18	117.5(8)
C14–C19–C20	103.3(13)
C20–C19–C18	139.2(13)
C8–C9–C10	111.7(8)
C8–C9–H9A	109.3
C8–C9–H9B	109.3
C10–C9–H9A	109.3
C10–C9–H9B	109.3
H9A–C9–H9B	107.9
N4–C2–C3	114.9(9)
N4–C2–C1	122.2(9)
C3–C2–C1	122.9(9)
C10–C11–H11A	109.5
C10–C11–H11B	109.5
C10–C11–H11C	109.5
H11A–C11–H11B	109.5
H11A–C11–H11C	109.5
H11B–C11–H11C	109.5
H6A–C6–H6B	107.8
C5–C6–H6A	109.1
C5–C6–H6B	109.1
C7–C6–H6A	109.1
C7–C6–H6B	109.1

C7–C6–C5	112.5(8)
N4–C5–S1	116.7(8)
N4–C5–C6	123.5(9)
C6–C5–S1	119.8(7)
C19–C18–H18	122.4
C17–C18–C19	115.2(11)
C17–C18–H18	122.4
C20A–C12–S13A	105.8(10)
C20A–C12–C1	133.6(11)
C1–C12–S13A	120.5(6)
C1–C12–S13	119.3(6)
C20–C12–C1	134.9(11)
C20–C12–S13	105.8(11)
C8–C7–H7A	108.8
C8–C7–H7B	108.8
C6–C7–C8	113.7(9)
C6–C7–H7A	108.8
C6–C7–H7B	108.8
H7A–C7–H7B	107.7
C2–C3–S1	109.1(8)
$C1^{i}$–C3–S1	127.9(8)
$C1^{i}$–C3–C2	122.9(9)
C19–C14–C20A	103.3(12)
C19–C14–C15	126.2(9)
C19–C14–S13	118.3(9)
C15–C14–C20A	130.5(12)
C15–C14–S13	115.4(9)
C2–C1–C12	121.2(9)
$C3^{i}$–C1–C2	114.1(8)
$C3^{i}$–C1–C12	124.5(8)
C15–C16–H16	118.6

C17–C16–H16	118.6
C17–C16–C15	122.7(15)
C14–C15–C16	114.8(11)
C14–C15–H15	122.6
C16–C15–H15	122.6
C18–C17–H17	118.2
C16–C17–C18	123.6(14)
C16–C17–H17	118.2
C14–S13–C12	91.9(7)
C19–C20–C12	120.6(19)
C19–C20–H20	119.7
C12–C20–H20	119.7

Anisotropic displacement parameters [$Å^2 \times 10^3$]. The anisotropic displacement factor exponent takes the form: $-2\pi^2[h^2a^{*2}U^{11} + \cdots + 2\,h\,k\,a^*\,b^*\,U^{12}]$.

Atom	U^{11}	U^{22}	U^{33}	U^{23}	U^{13}	U^{12}
S1	64(2)	73(2)	54(2)	–3(1)	16(1)	–1(1)
S13A	69(3)	64(3)	40(3)	–2(2)	14(2)	4(3)
N4	57(5)	75(6)	56(6)	–18(5)	12(4)	–4(4)
C8	61(6)	89(8)	40(6)	–5(6)	–2(4)	2(5)
C10	59(6)	75(7)	56(7)	2(6)	3(5)	0(5)
C9	65(6)	92(8)	50(7)	–15(6)	14(5)	–3(6)
C2	60(6)	67(7)	48(6)	7(5)	1(5)	–4(5)
C11	108(9)	75(7)	57(7)	8(6)	21(6)	–4(6)
C6	58(6)	83(7)	45(6)	–11(5)	12(4)	–4(5)
C5	66(6)	68(6)	42(6)	–2(5)	1(5)	1(5)
C12	46(5)	70(6)	61(7)	–23(5)	20(4)	–1(5)
C7	63(6)	88(8)	57(7)	–4(6)	10(5)	1(6)
C3	66(6)	83(7)	41(6)	–9(6)	5(5)	1(6)
C1	58(6)	76(7)	35(5)	–5(5)	19(4)	–6(5)

Hydrogen coordinates [$\times 10^4$] and isotropic displacement parameters [$Å^2 \times 10^3$].

Atom	*x*	*y*	*z*	U_{eq}	*S.o.f.*
H20A	2777	1366	3973	120	0.65
H8A	–184	5833	4183	77	1
H8B	699	6789	4450	77	1
H10A	–383	8807	3636	77	1
H10B	520	9529	3942	77	1
H9A	310	6042	3440	82	1
H9B	1253	6784	3693	82	1
H11A	133	9258	2921	119	1
H11B	1125	9540	3189	119	1
H11C	396	11089	3228	119	1
H6A	155	3002	4769	74	1
H6B	990	4172	5016	74	1
H18	3924	–2872	2731	99	1
H7A	618	3193	4024	83	1
H7B	1522	4155	4259	83	1
H16	3434	2455	2386	118	1
H15	2986	3082	3136	107	1
H17	3908	–299	2208	111	1
H20	3486	–3556	3729	104	0.35

Torsion angles [°].

S13A–C19–C18–C17	179.7(9)
S13A–C19–C14–C20A	0.7(16)
S13A–C19–C14–C15	–179.5(9)
S13A–C19–C14–S13	–3.1(13)
S13A–C19–C20–C12	–175(13)
S13A–C12–C1–C2	–160.3(7)
S13A–C12–C1–C3^{i}	15.2(14)
S13A–C12–S13–C14	–2.5(8)
S13A–C12–C20–C19	175(14)
C20A–C12–C1–C2	22(2)
C20A–C12–C1–C3^{i}	–162.0(17)
C20A–C12–S13–C14	11(5)
C20A–C12–C20–C19	–4(4)
C20A–C14–C15–C16	–180.0(18)
C20A–C14–S13–C12	–11(5)
N4–C2–C3–S1	3.0(11)
N4–C2–C3–C1^{i}	–179.6(9)
N4–C2–C1–C12	–4.6(14)
N4–C2–C1–C3^{i}	179.4(8)
C19–S13A–C12–C20A	–2.4(13)
C19–S13A–C12–C1	179.7(8)
C19–S13A–C12–S13	1.2(7)
C19–S13A–C12–C20	–3(10)
C19–C18–C17–C16	–0.7(19)
C19–C14–C15–C16	0.2(18)
C19–C14–S13–C12	3.2(10)
C9–C8–C7–C6	176.3(8)
C2–N4–C5–S1	3.0(11)
C2–N4–C5–C6	–177.0(8)
C11–C10–C9–C8	173.8(9)

C5–S1–C3–C2	–1.1(8)
C5–S1–C3–C1^{i}	–178.3(10)
C5–N4–C2–C3	–3.8(12)
C5–N4–C2–C1	177.6(9)
C5–C6–C7–C8	–173.2(8)
C18–C19–C14–C20A	–179.0(14)
C18–C19–C14–C15	0.8(17)
C18–C19–C14–S13	177.2(9)
C18–C19–C20–C12	–178.5(18)
C12–S13A–C19–C18	–179.2(10)
C12–S13A–C19–C14	1.1(9)
C12–S13A–C19–C20	3(9)
C12–C20A–C14–C19	–3(2)
C12–C20A–C14–C15	177.3(13)
C12–C20A–C14–S13	165(7)
C7–C8–C9–C10	–173.3(8)
C7–C6–C5–S1	–174.3(7)
C7–C6–C5–N4	5.6(14)
C3–S1–C5–N4	–1.1(8)
C3–S1–C5–C6	178.9(8)
C3–C2–C1–C12	176.9(9)
C3–C2–C1–C3^{i}	1.0(16)
C14–C20A–C12–S13A	4(2)
C14–C20A–C12–C1	–178.8(13)
C14–C20A–C12–S13	–164(7)
C14–C20A–C12–C20	4(3)
C14–C19–C18–C17	–0.6(16)
C14–C19–C20–C12	3(5)
C1–C2–C3–S1	–178.4(7)
C1–C2–C3–C1^{i}	–1.1(18)
C1–C12–S13–C14	179.0(8)

C1–C12–C20–C19	179(2)
C15–C14–S13–C12	179.9(9)
C15–C16–C17–C18	2(2)
C17–C16–C15–C14	−1.6(19)
S13–C12–C1–C2	18.2(13)
S13–C12–C1–C3^{i}	−166.3(9)
S13–C12–C20–C19	−1(5)
S13–C14–C15–C16	−176.2(10)
C20–C19–C18–C17	−179(4)
C20–C19–C14–C20A	0(3)
C20–C19–C14–C15	180(3)
C20–C19–C14–S13	−4(3)
C20–C12–C1–C2	−161(3)
C20–C12–C1–C3^{i}	14(4)
C20–C12–S13–C14	−1(3)

Hydrogen bonds [Å and °].

D–H···*A*	*d*(*D*–H)	*d*(H···*A*)	*d*(*D*···*A*)	∠(*D*H*A*)
C20A–H20A···N4	0.95	2.48	3.00(2)	114.8
C20–H20···S1^{i}	0.95	2.74	3.33(2)	121.2

Appendix 37 - Full crystallographic details of ***(2.15).***

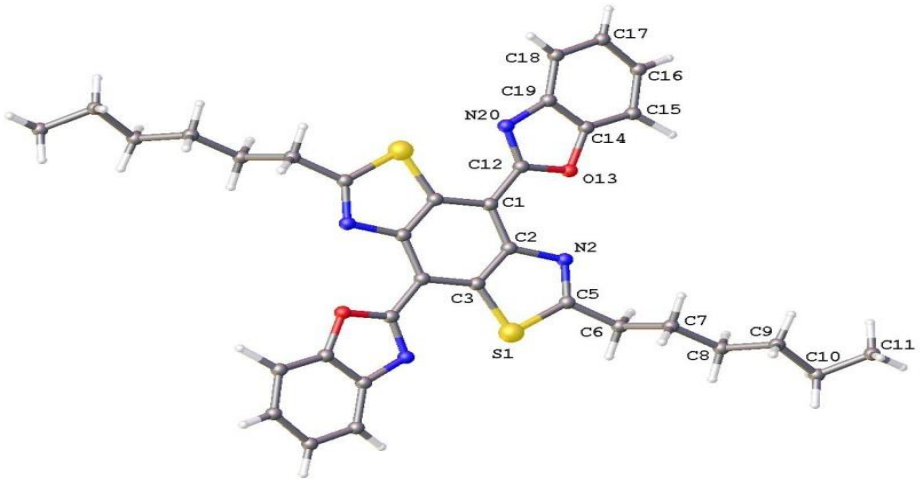

Crystal data and structure refinement details.

Identification code	2013ncs0660	
Empirical formula	$C_{34}H_{34}N_4O_2S_2$	
Formula weight	594.77	
Temperature	100(2) K	
Wavelength	0.71075 Å	
Crystal system	Monoclinic	
Space group	*P*121/*c*1	
Unit cell dimensions	a = 14.526(2) Å	α = 90°
	b = 5.1215(7) Å	β = 109.041(8)°
	c = 20.577(3) Å	γ = 90°
Volume	1447.0(4) Å^3	
Z	2	
Density (calculated)	1.365 Mg / m^3	
Absorption coefficient	0.224 mm^{-1}	
F(000)	628	
Crystal	Block; Yellow	
Crystal size	0.09 × 0.05 × 0.03 mm^3	
θ range for data collection	3.0 – 25.1°	
Index ranges	$-5 \le h \le 6$, $-16 \le k \le 16$, $-23 \le l \le 22$	
Reflections collected	16020	
Independent reflections	2550 [R_{int} = 0.148]	

Completeness to θ =	25.1° 97.2 %
Absorption correction	Semi−empirical from equivalents
Max. and min. transmission	1.000 and 0.617
Refinement method	Full-matrix least-squares on F^2
Data / restraints / parameters	2550 / 291 / 191
Goodness-of-fit on F^2	1.137
Final *R* indices [$F^2 > 2\sigma(F^2)$]	*R1* = 0.1450, *wR2* = 0.3462
R indices (all data)	*R1* = 0.3045, *wR2* = 0.4364
Extinction coefficient	n/a
Largest diff. peak and hole	0.754 and −0.359 e Å^{-3}

Atomic coordinates [$\times 10^4$], equivalent isotropic displacement parameters [$Å^2 \times 10^3$] and site occupancy factors. U_{eq} is defined as one third of the trace of the orthogonalized U^{ij} tensor.

Atom	*x*	*y*	*z*	U_{eq}	*S.o.f.*
S1	6903(2)	–2628(7)	4985(1)	110(2)	1
O13	4632(4)	4638(17)	3492(3)	102(2)	1
N2	6117(5)	1230(20)	4132(3)	90(3)	1
N20	3520(5)	5590(20)	4008(3)	103(3)	1
C1	4644(6)	2070(20)	4494(4)	97(3)	1
C2	5504(7)	680(30)	4553(4)	99(3)	1
C3	5849(7)	–1300(30)	5040(4)	98(3)	1
C5	6836(7)	–410(30)	4341(4)	103(3)	1
C6	7624(7)	–400(30)	4007(6)	121(4)	1
C7	8373(9)	1700(30)	4257(7)	129(4)	1
C8	9070(10)	1590(30)	3839(8)	172(6)	1
C9	9765(11)	3810(30)	3977(8)	168(5)	1
C10	10468(14)	3020(50)	3603(11)	230(9)	1
C11	10786(17)	5620(50)	3471(12)	253(10)	1
C12	4263(7)	4130(30)	4018(4)	94(3)	1
C14	4070(7)	6690(30)	3144(4)	100(3)	1
C15	4135(8)	7940(30)	2551(4)	109(3)	1
C16	3479(7)	9820(30)	2305(5)	107(4)	1
C17	2782(7)	10590(30)	2601(5)	112(4)	1
C18	2743(7)	9270(30)	3187(4)	108(3)	1
C19	3397(7)	7280(30)	3446(4)	102(3)	1

Bond lengths [Å] and angles [°].

S1–C3	1.713(10)
S1–C5	1.725(12)
O13–C12	1.379(10)
O13–C14	1.379(12)
N2–C2	1.456(11)
N2–C5	1.297(12)
N20–C12	1.306(12)
N20–C19	1.407(13)
C1–C2	1.408(13)
C1–C3^{i}	1.428(12)
C1–C12	1.423(15)
C2–C3	1.399(15)
C3–C1^{i}	1.428(12)
C5–C6	1.515(8)
C6–H6A	0.9900
C6–H6B	0.9900
C6–C7	1.498(9)
C7–H7A	0.9900
C7–H7B	0.9900
C7–C8	1.528(9)
C8–H8A	0.9900
C8–H8B	0.9900
C8–C9	1.488(9)
C9–H9A	0.9900
C9–H9B	0.9900
C9–C10	1.521(9)
C10–H10A	0.9900
C10–H10B	0.9900
C10–C11	1.466(10)
C11–H11A	0.9800

C11–H11B	0.9800
C11–H11C	0.9800
C14–C15	1.407(13)
C14–C19	1.353(13)
C15–H15	0.9500
C15–C16	1.333(14)
C16–H16	0.9500
C16–C17	1.399(13)
C17–H17	0.9500
C17–C18	1.400(14)
C18–H18	0.9500
C18–C19	1.376(15)
C3–S1–C5	87.8(5)
C14–O13–C12	103.6(7)
C5–N2–C2	105.2(8)
C12–N20–C19	104.3(8)
C2–C1–C3^{i}	115.3(10)
C2–C1–C12	124.7(9)
C12–C1–C3^{i}	120.0(9)
C1–C2–N2	123.3(10)
C3–C2–N2	114.8(9)
C3–C2–C1	121.9(8)
C1^{i}–C3–S1	126.1(9)
C2–C3–S1	111.1(7)
C2–C3–C1^{i}	122.8(9)
N2–C5–S1	121.1(6)
N2–C5–C6	119.7(10)
C6–C5–S1	119.1(9)
C5–C6–H6A	108.6
C5–C6–H6B	108.6
H6A–C6–H6B	107.6

C7–C6–C5	114.7(9)
C7–C6–H6A	108.6
C7–C6–H6B	108.6
C6–C7–H7A	109.9
C6–C7–H7B	109.9
C6–C7–C8	108.7(10)
H7A–C7–H7B	108.3
C8–C7–H7A	109.9
C8–C7–H7B	109.9
C7–C8–H8A	108.9
C7–C8–H8B	108.9
H8A–C8–H8B	107.7
C9–C8–C7	113.4(12)
C9–C8–H8A	108.9
C9–C8–H8B	108.9
C8–C9–H9A	111.2
C8–C9–H9B	111.2
C8–C9–C10	102.9(13)
H9A–C9–H9B	109.1
C10–C9–H9A	111.2
C10–C9–H9B	111.2
C9–C10–H10A	112.0
C9–C10–H10B	112.0
H10A–C10–H10B	109.7
C11–C10–C9	98.8(16)
C11–C10–H10A	112.0
C11–C10–H10B	112.0
C10–C11–H11A	109.5
C10–C11–H11B	109.5
C10–C11–H11C	109.5
H11A–C11–H11B	109.5

H11A–C11–H11C	109.5
H11B–C11–H11C	109.5
O13–C12–C1	121.0(9)
N20–C12–O13	114.2(9)
N20–C12–C1	124.7(8)
O13–C14–C15	127.0(9)
C19–C14–O13	108.9(9)
C19–C14–C15	124.0(11)
C14–C15–H15	122.7
C16–C15–C14	114.6(10)
C16–C15–H15	122.7
C15–C16–H16	117.7
C15–C16–C17	124.6(10)
C17–C16–H16	117.7
C16–C17–H17	120.8
C16–C17–C18	118.4(11)
C18–C17–H17	120.8
C17–C18–H18	120.8
C19–C18–C17	118.4(10)
C19–C18–H18	120.8
C14–C19–N20	108.9(10)
C14–C19–C18	119.9(10)
C18–C19–N20	131.3(9)

Anisotropic displacement parameters [$Å^2 \times 10^3$]. The anisotropic displacement factor exponent takes the form: $-2\pi^2[h^2a^{*2}U^{11} + \cdots + 2\,h\,k\,a^*\,b^*\,U^{12}]$.

Atom	U^{11}	U^{22}	U^{33}	U^{23}	U^{13}	U^{12}
S1	73(2)	202(4)	64(2)	–2(2)	35(1)	19(2)
O13	70(4)	194(7)	50(3)	4(4)	31(3)	9(4)
N2	53(4)	182(7)	42(3)	–11(4)	24(3)	17(4)
N20	65(5)	199(8)	48(4)	9(4)	25(3)	15(5)
C1	60(5)	193(8)	45(4)	1(5)	26(4)	11(5)
C2	64(5)	200(8)	35(4)	–8(5)	19(4)	11(5)
C3	58(5)	196(9)	44(4)	–6(5)	22(4)	11(5)
C5	77(5)	179(9)	67(5)	–11(5)	41(4)	10(5)
C6	96(7)	185(11)	110(7)	–2(7)	71(6)	21(6)
C7	104(7)	162(11)	149(9)	11(7)	79(7)	20(6)
C8	119(9)	262(15)	171(11)	15(11)	95(9)	22(9)
C9	137(10)	238(14)	151(11)	64(10)	79(9)	32(9)
C10	146(13)	350(20)	234(19)	19(15)	111(13)	3(13)
C11	208(18)	370(20)	194(17)	58(17)	90(14)	–21(16)
C12	56(5)	190(8)	39(4)	–2(4)	20(4)	6(5)
C14	65(5)	188(8)	51(4)	4(5)	24(4)	6(5)
C15	72(6)	202(10)	54(5)	16(5)	25(4)	9(6)
C16	69(6)	196(10)	59(5)	8(5)	22(4)	2(6)
C17	71(6)	209(10)	57(5)	10(6)	23(4)	8(6)
C18	68(6)	200(9)	54(4)	2(5)	18(4)	9(6)
C19	63(5)	197(8)	50(4)	6(5)	25(4)	11(5)

Hydrogen coordinates [$\times 10^4$] and isotropic displacement parameters [$Å^2 \times 10^3$].

Atom	*x*	*y*	*z*	U_{eq}	*S.o.f.*
H6A	7957	–2119	4091	145	1
H6B	7313	–209	3504	145	1
H7A	8739	1437	4750	155	1
H7B	8052	3427	4201	155	1
H8A	9443	–65	3945	207	1
H8B	8684	1570	3343	207	1
H9A	10107	4024	4476	201	1
H9B	9428	5464	3790	201	1
H10A	11015	1955	3897	276	1
H10B	10136	2063	3171	276	1
H11A	11207	5468	3185	379	1
H11B	11149	6455	3909	379	1
H11C	10216	6687	3231	379	1
H15	4607	7474	2343	130	1
H16	3486	10695	1899	129	1
H17	2346	11984	2410	135	1
H18	2276	9727	3400	129	1

Torsion angles [°].

S1−C5−C6−C7	−101.2(12)
O13−C14−C15−C16	177.9(10)
O13−C14−C19−N20	0.3(13)
O13−C14−C19−C18	−179.7(9)
N2−C2−C3−S1	−1.9(12)
N2−C2−C3−C1^{i}	178.7(9)
N2−C5−C6−C7	79.7(14)
C1−C2−C3−S1	179.8(8)
C1−C2−C3−C1^{i}	0.5(18)
C2−N2−C5−S1	0.5(12)
C2−N2−C5−C6	179.6(9)
C2−C1−C12−O13	11.0(16)
C2−C1−C12−N20	−173.0(10)
C3−S1−C5−N2	−1.4(9)
C3−S1−C5−C6	179.6(9)
C3^{i}−C1−C2−N2	−178.6(9)
C3^{i}−C1−C2−C3	−0.5(17)
C3^{i}−C1−C12−O13	−169.6(9)
C3^{i}−C1−C12−N20	6.4(17)
C5−S1−C3−C1^{i}	−179.0(11)
C5−S1−C3−C2	1.7(8)
C5−N2−C2−C1	179.1(9)
C5−N2−C2−C3	0.9(12)
C5−C6−C7−C8	−175.7(11)
C6−C7−C8−C9	172.1(13)
C7−C8−C9−C10	170.8(14)
C8−C9−C10−C11	153.7(17)
C12−O13−C14−C15	−178.8(10)
C12−O13−C14−C19	−1.5(11)
C12−N20−C19−C14	1.1(12)

C12–N20–C19–C18	−178.9(12)
C12–C1–C2–N2	0.9(16)
C12–C1–C2–C3	179.0(10)
C14–O13–C12–N20	2.3(12)
C14–O13–C12–C1	178.7(9)
C14–C15–C16–C17	1.2(17)
C15–C14–C19–N20	177.7(10)
C15–C14–C19–C18	−2.3(18)
C15–C16–C17–C18	−1.9(18)
C16–C17–C18–C19	0.5(17)
C17–C18–C19–N20	−178.6(11)
C17–C18–C19–C14	1.5(17)
C19–N20–C12–O13	−2.1(12)
C19–N20–C12–C1	−178.4(10)
C19–C14–C15–C16	1.0(17)